MCEER
EARTHQUAKE ENGINEERING TO EXTREME EVENTS

ISSN 1520-295X

Seismic Damage Assessment of Low Aspect Ratio Reinforced Concrete Shear Walls

by
Jonathan P. Rivera, Bismarck N. Luna and
Andrew S. Whittaker

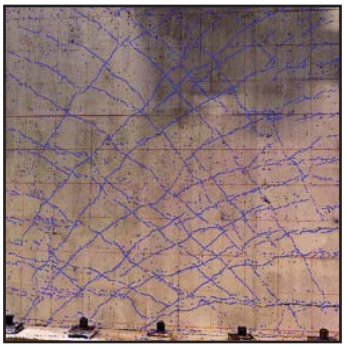

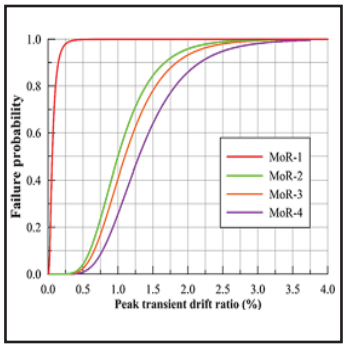

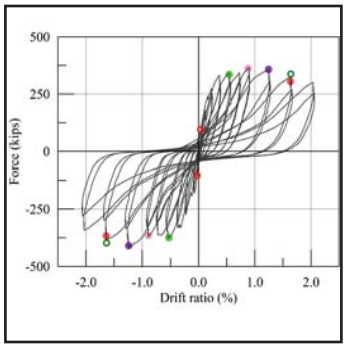

Technical Report MCEER-18-0003

April 16, 2018

This research was conducted at the University at Buffalo, State University of New York, and was supported primarily by the National Science Foundation under Grant Number CMMI-0829978.

NOTICE

This report was prepared by the University at Buffalo, State University of New York, as a result of research sponsored in part by the National Science Foundation under grant number CMMI-0829978. Neither MCEER, associates of MCEER, its sponsors, University at Buffalo, State University of New York, nor any person acting on their behalf:

a. makes any warranty, express or implied, with respect to the use of any information, apparatus, method, or process disclosed in this report or that such use may not infringe upon privately owned rights; or

b. assumes any liabilities of whatsoever kind with respect to the use of, or the damage resulting from the use of, any information, apparatus, method, or process disclosed in this report.

Any opinions, findings, and conclusions or recommendations expressed in this publication are those of the author(s) and do not necessarily reflect the views of MCEER, the National Science Foundation or other sponsors.

Seismic Damage Assessment of Low Aspect Ratio Reinforced Concrete Shear Walls

by

Jonathan P. Rivera,[1] Bismarck N. Luna[2] and Andrew S. Whittaker[3]

Publication Date: April 16, 2018
Submittal Date: November 19, 2017

Technical Report MCEER-18-0003

National Science Foundation Grant Number CMMI-0829978

1 Senior Engineer, Thornton Tomasetti; former Graduate Student, Department of Civil, Structural and Environmental Engineering, University at Buffalo, State University of New York
2 Development Specialist, Praxair; former Graduate Student, Department of Civil, Structural and Environmental Engineering, University at Buffalo, State University of New York
3 SUNY Distinguished Professor and MCEER Director, Department of Civil, Structural and Environmental Engineering, University at Buffalo, State University of New York

MCEER
University at Buffalo, State University of New York
212 Ketter Hall, Buffalo, NY 14260
E-mail: *mceer@buffalo.edu*; Website: *http://buffalo.edu/mceer*

Preface

MCEER is a national center of excellence dedicated to the discovery and development of new knowledge, tools and technologies that equip communities to become more disaster resilient in the face of earthquakes and other extreme events. MCEER accomplishes this through a system of multidisciplinary, multi-hazard research, in tandem with complimentary education and outreach initiatives.

Headquartered at the University at Buffalo, The State University of New York, MCEER was originally established by the National Science Foundation in 1986, as the first National Center for Earthquake Engineering Research (NCEER). In 1998, it became known as the Multidisciplinary Center for Earthquake Engineering Research (MCEER), from which the current name, MCEER, evolved.

Comprising a consortium of researchers and industry partners from numerous disciplines and institutions throughout the United States, MCEER's mission has expanded from its original focus on earthquake engineering to one which addresses the technical and socio-economic impacts of a variety of hazards, both natural and man-made, on critical infrastructure, facilities, and society.

The Center derives support from several Federal agencies, including the National Science Foundation, Federal Highway Administration, Department of Energy, Nuclear Regulatory Commission, and the State of New York, foreign governments and private industry.

The goal of this report is to improve the professional community's ability to collect, document and understand the effects of earthquake damage on low aspect ratio reinforced concrete shear walls. To this end, twelve large-scale specimens were designed, detailed and constructed at the Structural Engineering and Earthquake Simulation Laboratory at the University at Buffalo. The data collected from the reversed cyclic inelastic testing of these 12 walls enabled the development of a first-of-a-kind, non-contact automated tool for processing high-resolution images to obtain and process damage data, including lengths and widths of cracks. The database was also used to correlate observed damage with story drift at peak shear strength, which can be used to inform repair strategies and to update fragility functions in support of performance-based seismic assessment and design.

ABSTRACT

Low aspect ratio reinforced concrete (RC) shear walls provide the lateral strength and stiffness for many low-rise to medium-rise buildings and nearly all safety-related nuclear structures. Low aspect ratio walls are generally shear-critical. In commercial buildings, shear-critical walls are expected to sustain moderate damage in design basis earthquake shaking and severe damage in maximum considered earthquake shaking. In nuclear structures, moderate damage is expected in shear-critical walls in shaking more intense than design basis. The seismic behavior of these shear-critical walls is poorly understood, despite their widespread use. Importantly, there exists no consensus on the level of damage that should trigger repair following an earthquake.

Twelve large-scale low aspect ratio RC walls were constructed and tested at the University at Buffalo as part of a project funded by the National Science Foundation. The goal of the project was to better characterize the seismic performance of low aspect ratio walls in terms of their lateral stiffness, peak lateral strength, post-peak-strength cyclic behavior, and residual lateral strength as a function of damage.

The data collected from the tests of these twelve walls enabled the development and validation of I-Crack: a non-contact, automated tool to document cracks (length, width, location and orientation) in reinforced concrete walls. The tool is suitable for both laboratory and field applications. The Matlab code for the I-Crack tool is provided in the report.

Cracking and crushing (spalling) of concrete was carefully documented at each load step for each wall. Surface cracking of the concrete was mapped using I-Crack and manually, using

drawing sheets and crack gages. Lengths and widths of cracks were documented at peak transient story drift and at zero lateral load in each load step, providing a first-of-a-kind dataset.

The concrete crack data were mined to a) update the Gulec et al. fragility functions for seismic performance assessment, and b) enable an inspector/engineer to judge whether the peak shear strength of a wall has been achieved (in the laboratory or the field), on the basis of crack widths measured at zero lateral loading. Information on whether the peak shear strength of a wall has been reached in the field, during an inspection following an earthquake, will be an important factor in determining whether structural repairs to the wall are needed. This dataset was also mined for crack widths at 1) peak transient displacement, and 2) zero lateral force upon subsequent unloading, to establish crack width ratios at displacements less than, equal to, and greater than that at peak strength, which is important information for future post-earthquake evaluations of low aspect ratio reinforced concrete shear walls.

ACKNOWLEDGMENTS

This research project was funded in part by the United States National Science Foundation (NSF) through the Network for Earthquake Engineering Simulation Research Program, Grant CMMI-0829978. This financial support is gratefully acknowledged.

All of the experiments described in this report were conducted in the Structural Engineering and Earthquake Simulation Laboratory at the University at Buffalo, with technical support of the laboratory staff, including Messrs. Christopher Budden, Jeffrey Cizdziel, Goran Josipovic, the late Duane Kozlowski, Louis Moretta, Mark Pitman, Robert Staniszewski, Scot Weinreber and Christopher Zwierlein. LPCiminelli, Inc. is acknowledged for their assistance in the construction of the Phase II wall specimens. Mr. Joshua Rocks, Ms. Emma Lejeune, Dr. Caglar Goksu, Dr. Joshua Pugh, Dr. Catherine Whyte, Professor Bozidar Stojadinovic and Professor Laura Lowes were involved in different aspects of the NSF project. The authors thank each of these individuals for their contributions to the project.

TABLE OF CONTENTS

Page

TABLE OF CONTENTS (CONT'D)

TABLE OF CONTENTS (CONT'D)

TABLE OF CONTENTS (CONT'D)

LIST OF FIGURES

LIST OF FIGURES (CONT'D)

LIST OF FIGURES (CONT'D)

LIST OF FIGURES (CONT'D)

LIST OF FIGURES (CONT'D)

LIST OF FIGURES (CONT'D)

LIST OF FIGURES (CONT'D)

LIST OF FIGURES (CONT'D)

LIST OF FIGURES (CONT'D)

LIST OF TABLES

LIST OF TABLES (CONT'D)

LIST OF TABLES (CONT'D)

LIST OF TABLES (CONT'D)

SECTION 1
INTRODUCTION

1.1 General

Low aspect ratio reinforced concrete shear walls are widely used in low-rise and medium-rise buildings, infrastructure, and most safety-related nuclear facilities. The height to length ratio for these walls is between 0.3 and 1.0, and their seismic behavior is governed by shear, namely, they are shear-critical.

Seismic framing systems in commercial buildings, such as low aspect ratio reinforced concrete walls, are expected to be damaged in design basis shaking; displacements will be greater than those associated with peak shear strength. The strength and stiffness of shear walls will likely be substantially diminished by design basis shaking and beyond design basis shaking; i.e., maximum considered earthquake shaking per ASCE 7-10 (ASCE, 2010). In nuclear power plants, designed per ASCE 4-16 (ASCE, 2016) and ASCE 43-05 (ASCE, 2005), shear walls are expected to remain elastic for design basis earthquake shaking and sustain the effects of beyond design basis shaking with only moderate damage.

A major challenge confronting design professionals, inspectors and researchers is the effective cataloguing of earthquake damage to reinforced concrete shear walls (and other reinforced concrete components). Post-earthquake inspections of buildings often involve the speedy logging of cracks using photographs, crack gages, and hand sketches, providing an incomplete picture of the extent of the damage and only partial information upon which to base a repair strategy (where the goal is often to return the reinforced concrete component to its pre-earthquake condition). Importantly, inspections in earthquake-damaged buildings entail risk to the

inspector in the event of aftershocks affecting the damaged building. Inspections and documenting of damage to walls tested in a laboratory also entails some risk to those involved, if, as has been the traditional practice, cracks and their widths are logged at peak transient displacements; namely, the wall is still resisting significant lateral loads. An automated, non-contact tool for logging and processing damage data, which could be remotely installed and operated, would be a safe, reliable, and efficient means to collect and process earthquake damage.

Another challenge facing design professionals tasked with post-earthquake evaluation of buildings is to determine whether the earthquake resistance of a building has been compromised; namely, has the displacement associated with the peak shear strength of the building been exceeded? If the earthquake-induced displacement of the wall is less than that associated with its peak shear strength, there may be no reason to perform structural repairs on the wall, which will likely be cracked. However, there is no useful information in the archival literature or in technical reports that enable an engineer to determine whether the displacement associated with the peak shear resistance of a wall has been reached, noting that information on the earthquake loading of a wall, for example, is not available for evaluation after an earthquake. Rather, only information at zero lateral load, such as widths of cracks, spalled concrete, and base sliding is available. An understanding of the extent of damage at zero lateral load (i.e., the post-earthquake condition) corresponding to prior deformation to displacements associated with peak strength would greatly benefit the design professional community.

The ATC-58 project on the performance-based seismic design of buildings, published as FEMA P-58 (FEMA, 2012), provide second-generation tools for performance-based earthquake

engineering. These tools enable calculations of repair cost, as well as business interruption for intensity-, scenario- and time-based assessments. Key to the calculations of loss is fragility functions, which plot the probability of exceeding a damage state (e.g., crack width greater than 0.05") as a function of a demand parameter, which is calculated by analysis of a mathematical model of a building. Each damage state in FEMA P-58 is accompanied by a consequence function, which transforms the damage into a repair measure. Gulec (2009) and his co-workers developed fragility functions for low aspect ratio reinforced concrete shear walls. Gulec used data available in the archival literature to build fragility functions. These data were sparse and not carefully documented. Crack widths, where reported, were limited to maximum values on a component, were often documented as displacements much greater than that associated with peak strength, and were not reported at zero lateral loading, which is the post-earthquake condition encountered by inspectors. Importantly, the areal density of cracking, which is needed for accurate estimates of repair, and associated with cost, was not reported. Fragility functions for low aspect ratio reinforced concrete shear walls, which use observed damage at zero lateral loading (i.e., the post-earthquake basis for repair) as a function of peak transient displacement calculated by analysis, will be more robust than those developed by Gulec.

1.2 Research objectives

The overarching goal of this research is to improve the profession's ability to collect, process, document and understand the effects of damage to low aspect ratio, shear-critical, reinforced concrete shear walls. To this end, the authors undertook the following research tasks:

1. Designed, constructed and tested twelve, large-scale, low aspect ratio reinforced concrete shear walls in partnership with Dr. Luna [as documented in Luna (2015), Luna et al. (2015), Luna et al. (2018)].
2. Documented damage to the twelve walls tested under reversed cyclic loading using traditional means and high-resolution photographs.
3. Developed, documented and validated a non-contact, automated tool (known as I-Crack) for processing high-resolution photographs to obtain detailed information on cracking in reinforced concrete shear walls, including crack length, crack width along length, and areal density of cracking. The source code for I-Crack is written in the MATLAB environment (Mathworks, 2013) and provided in Appendix A of this report. The documentation of I-Crack is also described in Rivera et al. (2015).
4. Correlated the width of cracks in reinforced concrete shear walls as a function of displacement, enabling judgments to be made regarding whether peak shear strength of a wall had been achieved (thus likely requiring repair) as a function of crack width at zero lateral loading (i.e., mimicking the post-earthquake condition).
5. Compared and documented the widths of cracks in given load steps at peak transient displacements and at zero lateral load, at a drift ratio less than that at peak shear strength, the drift ratio at peak shear strength, and at drift ratios greater than that at peak shear strength.

6. Re-assessed the fragility functions developed by Gulec (2009), Gulec and Whittaker (2009) and Gulec et al. (2009), as documented in FEMA P-58, using high-quality data available from the tests of the twelve shear walls.

The research tasks documented in this report complement but do not duplicate prior published work by Rocks (2012), Luna (2015), Luna et al. (2015) and Epackachi and Whittaker (2017). The MS thesis of Rocks (2012), PhD dissertation of Luna (2015), the Luna et al. (2015) journal article, and Chapter 2 of this report document the pre-test analysis, design, construction, instrumentation and testing of 12 large-scale, low aspect ratio reinforced concrete walls. The Luna dissertation presents information on the testing phase of the project not discussed in Chapter 2; the inelastic cyclic responses of the walls; a discussion of the lateral stiffness of the 12 walls, with a focus on displacement less that associated with peak shear strength; information on the strain fields and rebar strains in the 12 walls at the displacement associated with peak shear strength; and equations for predicting the peak shear strength of low aspect ratio walls. Epackachi and Whittaker (2017) present cyclic backbone curves and propose cyclic inelastic models for shear-critical walls, which are informed in part by the data presented in this report and Luna's dissertation.

1.3 Organization of this report

This report is composed of six chapters, a list of references, and two appendices.

Chapter 2 describes the design and construction of twelve large-scale, low aspect ratio reinforced concrete shear walls that were tested at the University at Buffalo. Information is presented on the geometry, material properties, foundation-block design, reinforcement for

selected walls, and construction process for the selected walls. [Other data are reported in Rocks (2012), Luna (2015) and Luna et al. (2015).]

The development of an automated, non-contact tool for documenting cracking in reinforced concrete walls (and other components), known as I-Crack, is detailed in Chapter 3. The means used to validate I-Crack, using data from the tests of eight of the twelve walls tested at the University at Buffalo, is described.

Chapter 4 presents the damage incurred by the twelve walls under reversed cyclic loading, and discusses the degree of damage observed as a function of drifts less than, equal to, and greater than the drift associated with peak shear strength. Cracks widths at peak transient displacement and zero lateral force in the same load step, and the ratios of the crack widths, at drift ratios less than, equal to, and greater than that associated with peak shear strength, are reported. Such data should enable reinterpretation of data from past tests where only crack widths at peak transient displacements were reported.

Fragility functions for low aspect ratio shear walls are discussed in Chapter 5. The functions developed by Gulec (2009), Gulec and Whittaker (2009) and Gulec et al. (2009) are reviewed and updated based on damage collected from the tests of the twelve walls described in Chapter 2.

The studies presented in the report are summarized in Chapter 6. Key conclusions regarding I-Crack, damage to shear walls as a function of story drift, and fragility functions are also presented in this chapter. A list of references follows Chapter 6.

The source code for I-Crack is presented in Appendix A. A tutorial for I-Crack is presented in Appendix B.

SECTION 2
SPECIMEN CONSTRUCTION

2.1 Introduction

Twelve large-scale low aspect ratio reinforced concrete shear walls were designed, detailed and constructed in the Structural Engineering and Earthquake Simulation Laboratory (SEESL) at the University at Buffalo. Construction and testing of these walls was split into two phases: Phase I with seven walls (SW1-SW7) and Phase II with five walls (SW8-SW12). The Phase I walls had varying aspect ratios (height divided-by-length) and equal vertical and horizontal reinforcement ratios. The Phase II walls had an aspect ratio of 0.54 with unequal vertical and horizontal reinforcement ratios; two of the five walls included in-plane boundary elements. The size and reinforcement of these walls was restricted by the capacities of the actuators, strong floor, strong wall and overhead gantry crane in the laboratory.

2.2 Phase I specimens

Complete information on the detailing, materials used and construction of the Phase I walls can be found in Chapter 3 and Chapter 4 of Rocks (2012). These walls were designed with different aspect ratios, horizontal reinforcement ratios (ρ_t), and vertical reinforcement ratios (ρ_l). Two of the specimens, SW2 and SW3, included Type-2 mechanical couplers per ACI 318-14 Section 25.5.7 (ACI, 2014) that joined the vertical reinforcement in the wall to vertical bars in the foundation. Each wall was eight inches thick and 120 inches long. The heights of the walls from the top of the foundation to the centerline of loading were 41 (SW5, SW6, SW7), 65 (SW2, SW3, SW4) and 113 (SW1) inches.

The reinforcement used in walls SW1 and SW4-SW7 was ASTM A615 Grade 60 (ASTM, 2012). The reinforcement used in walls SW2 and SW3 was ASTM A706 Grade 60 (ASTM, 2009).

Tensile tests were performed on random samples using ASTM A370 (ASTM, 2012) to ensure the reinforcement complied with ACI 318-14 Section 20.2.2.5. All reinforcement used for construction of the walls met the requirements of Section 20.2.2.5, namely, the nominal yield strength was between 60 and 78 ksi, and the ratio of tensile to yield strength exceeded 1.25.

Each specimen was cast with normal-weight concrete. Numerous cylinders were cast for compressive-strength testing following ASTM C39 (ASTM, 2012). Compression tests were performed 7, 14, 28, and 56 days after casting and on the day of testing. The compressive strength of the concrete in the walls on the day of testing ranged from 3600 psi to 7800 psi.

The mechanical properties of the Phase I specimens are summarized in Table 2-1. The concrete strengths reported in the last column were obtained on the day of testing. The reinforcement strengths, f_y and f_u, were obtained from tests per ASTM A370. A typical cross-section and plan view of the Phase I specimens are shown in Figure 2-1. Note the use of $90°$ hooks at the ends of the horizontal rebar in the wall. Figure 2-2 shows a typical elevation of the Phase I specimens. Figure 2-1 and Figure 2-2 are reproduced from Chapter 3 of Rocks (2012).

Each Phase I specimen was cast atop a foundation block that was 36 inches wide, 18 inches high and 168 inches long. The reinforcement in the foundation block consisted of ten #8 horizontal bars (five top and five bottom) and vertical reinforcement consisting of four #5 tie sets placed three inches on center. The foundation reinforcement cages were fabricated off-site.

The reinforcement cages were placed into formwork and two-inch diameter pipes were installed at two feet on center. These pipes enabled the installation of the DYWIDAG THREADBAR® used to post-tension the foundation block to the laboratory strong floor. After the reinforcement cages were placed in the formwork and the two-inch diameter pipes were installed, the vertical reinforcement for the walls was placed and the foundation was cast.

Table 2-1. Phase I wall mechanical properties[1]

Wall	h_w/l_w	ρ_l (%)	ρ_t (%)	f_y (ksi)	f_y (ksi)	f'_c (psi)
SW1	0.94	0.67	0.67	67	102	3600
SW2	0.54	1.00	1.00	63	87	7000
SW3		0.67	0.67	63	87	7800
SW4		0.33	0.33	67	102	4200
SW5	0.33	1.00	1.00	67	102	4300
SW6		0.63	0.69	67	102	3800
SW7		0.34	0.38	67	102	3800

1. h_w = height of the wall; l_w = length of the wall; ρ_l = vertical reinforcement ratio; ρ_t = horizontal reinforcement ratio; f_y = yield strength; f_u = ultimate tensile strength; f'_c = concrete compressive strength

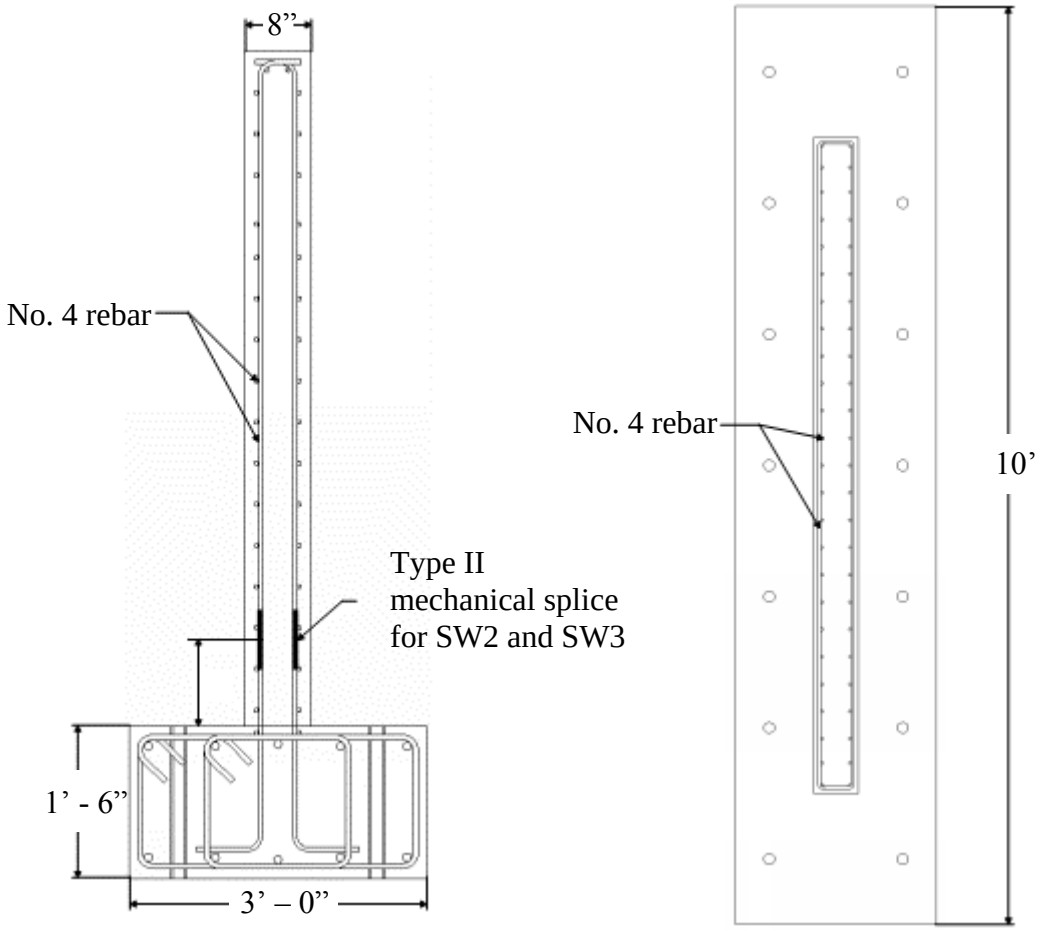

a. cross-section b. plan view

Figure 2-1. Typical Phase I details (Rocks, 2012)

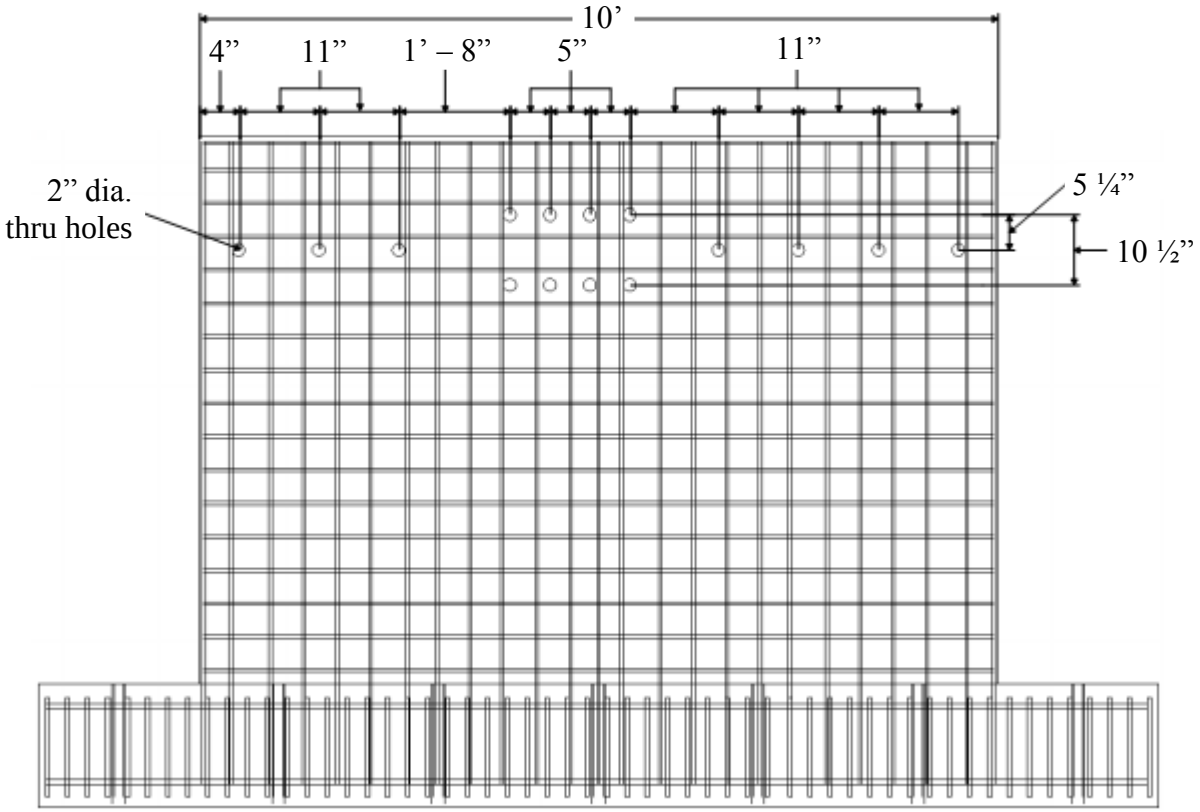

Figure 2-2. Typical Phase I wall elevation (Rocks, 2012)

A typical part elevation and cross-section of the foundation block, reproduced from Rocks (2012), are shown in Figure 2-3 and Figure 2-4, respectively.

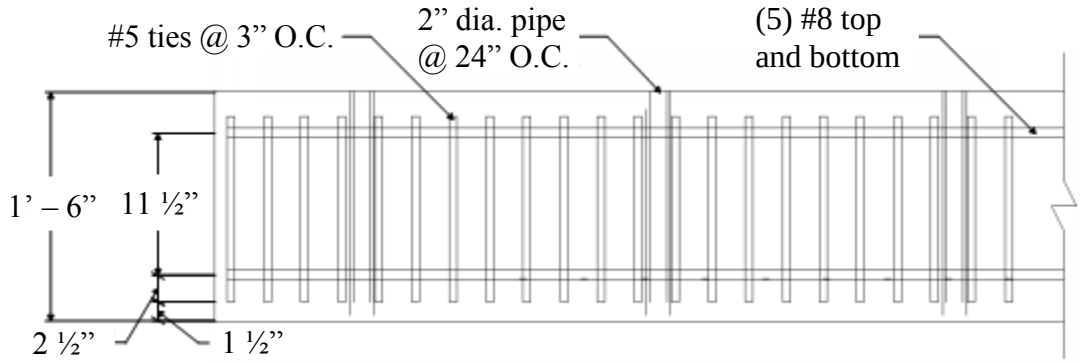

Figure 2-3. Part elevation of the foundation block (Rocks, 2012)

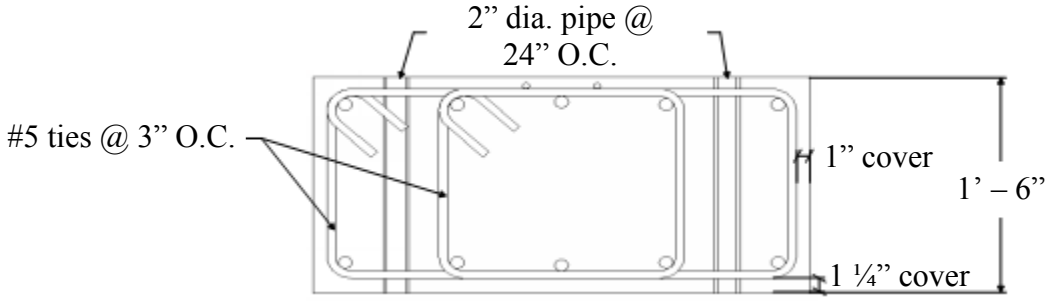

Figure 2-4. Typical cross-section through the foundation block (Rocks, 2012)

2.3 Phase II specimens

The Phase II specimens were detailed and constructed after the Phase I specimens had been tested. These walls were constructed with an aspect ratio of 0.54, and different horizontal and vertical reinforcement ratios. Two specimens, SW11 and SW12, included in-plane boundary elements. Each wall was detailed to be eight inches thick and 120 inches long.

ASTM A615 Grade 60 reinforcement was used in the walls of SW8 through SW12. Material tests were performed to check compliance of the rebar with Section 20.2.2.5 of ACI 318-14 prior to construction. Several rebar samples were tested in accordance with ASTM A370; the test fixture is shown in Figure 2-5. All of the rebar samples tested complied with Section 20.2.2.5 of ACI 318-14, namely, the yield strength of the rebar was between 60 and 78 ksi, and the ratio of tensile to yield strength was greater than 1.25. Figure 2-6 shows typical stress-strain curves for the #4 and #5 rebar.

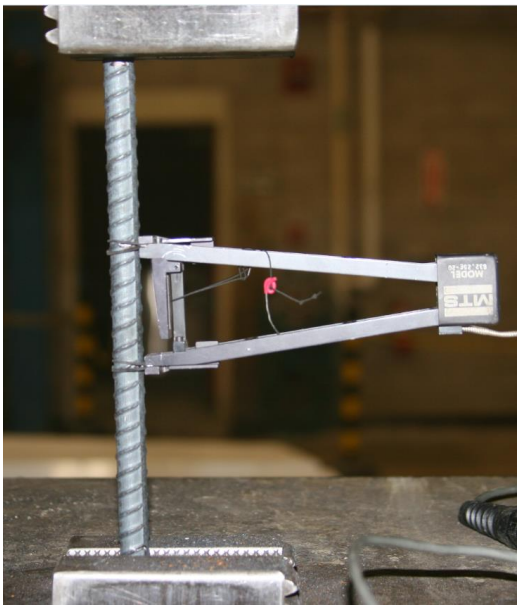

Figure 2-5. Rebar tensile test set-up

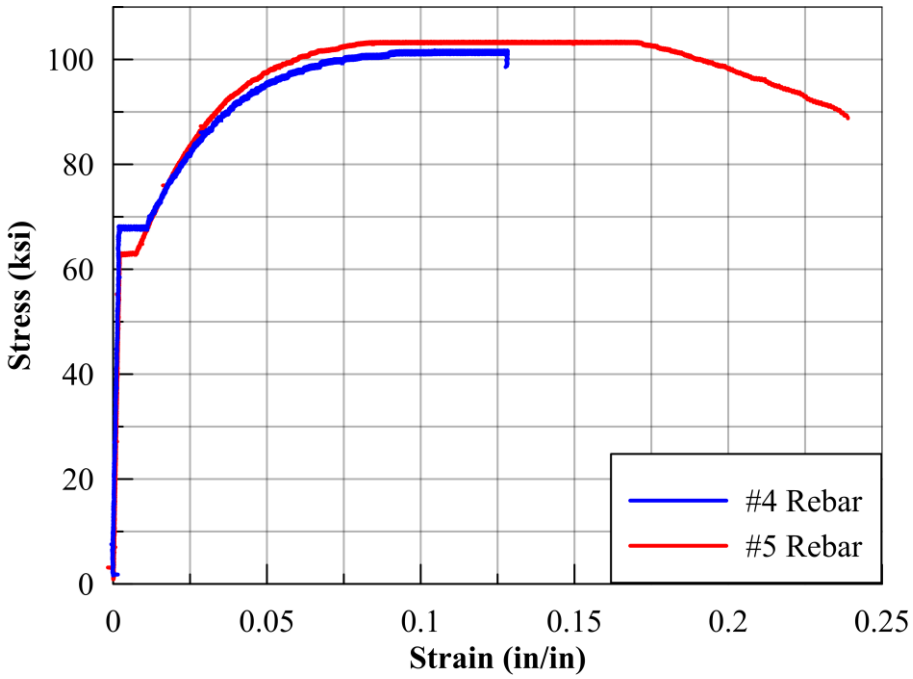

Figure 2-6. Typical stress-strain curves for the samples tested

The concrete mix used in the Phase II specimens was modified based on results from the Phase I walls. The foundations for the Phase II walls were cast with normal-weight concrete with a target compressive strength of 5 ksi to ensure that the strength of the foundation was greater than that of the walls. The concrete mix design included ASTM C150 Portland Cement (ASTM, 2012), ASTM C33 Natural Sand (ASTM, 2011), 1" Coarse Aggregate, MB-AE™ 100 Air-Entraining Admixture and RHEOBUILD® 1000 High-Range Water-Reducing Admixture. The foundation blocks were cast from two truckloads of concrete, and cylinders were cast for testing at a later date to monitor the increase of compressive strength over time. Figure 2-7 shows the increase in compressive strength over time for each truckload.

The Phase II walls were cast with 4 ksi self-compacting concrete (SCC). The components for this SCC mix included ASTM C150 Cement, ASTM C618 Fly Ash (ASTM, 2012), ASTM

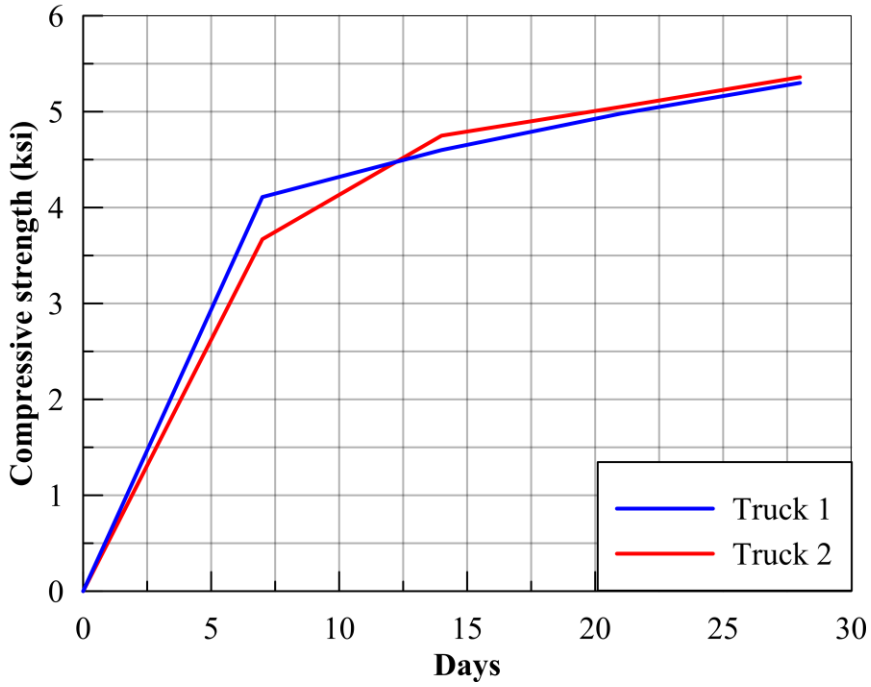

Figure 2-7. Concrete compressive strength test results

C33 Crushed and Natural Gravel (ASTM, 2012), MB-AE™ 100 Air-Entraining Mixture, GLENIUM® 3400 NV High- Reducing Admixture, RHEOMAC® VMA 362 Viscosity-Modifying Admixture, and POZZOLITH® 100 XR Set Retarding Admixture. Similar to the foundations, the walls were cast from two truckloads of concrete. Cylinders were cast to monitor the increase in compressive strength over time. Results are presented in Figure 2-8.

The mechanical properties for the Phase II specimens are summarized in Table 2-2. The concrete compressive strengths shown in last column of Table 2-2 were obtained on the day of testing. The reinforcement strengths, f_y and f_u, were obtained from ASTM A370 compliant tests.

2.3.1 Phase II foundation design

All Phase II specimens were constructed with a modified foundation block because these

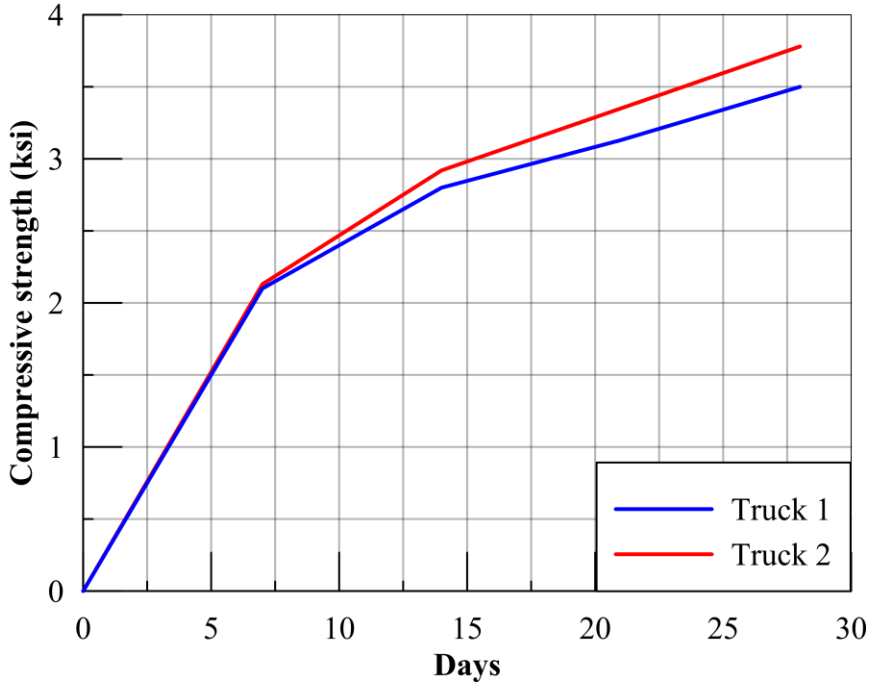

Figure 2-8. Concrete compressive strength results for SCC mixture

Table 2-2. Phase II wall mechanical properties[1]

Wall	h_w/l_w	ρ_l (%)	ρ_t (%)	ρ_{be} (%)	f_y (ksi)	f_u (ksi)	f'_c (psi)
SW8	0.54	1.5	1.5	-	67	102	3500
SW9			0.67	-	63	102	4200
SW10			0.33	-	63	102	4600
SW11		0.63	0.69	1.5	67	102	5000
SW12		0.34	0.38	2.0	67	102	5000

1. h_w = height of the wall; l_w = length of the wall; ρ_l = vertical reinforcement ratio; ρ_t = horizontal reinforcement ratio; ρ_{be} = boundary element reinforcement ratio; f_y = yield strength; f_u = ultimate tensile strength; f'_c = concrete compressive strength

walls were expected to resist greater forces than the Phase I walls. The modified foundation block was 168 inches long, 48 inches wide and 18 inches high. The reinforcement in the Phase II foundation block consisted of five #8 horizontal bars on the top and bottom, and two #4 hoops at four inches on center at the foundation's outer edges and eight inches on center in the foundation's mid-section. Figure 2-9 through Figure 2-11 show the typical details of the foundation blocks used for the Phase II specimens.

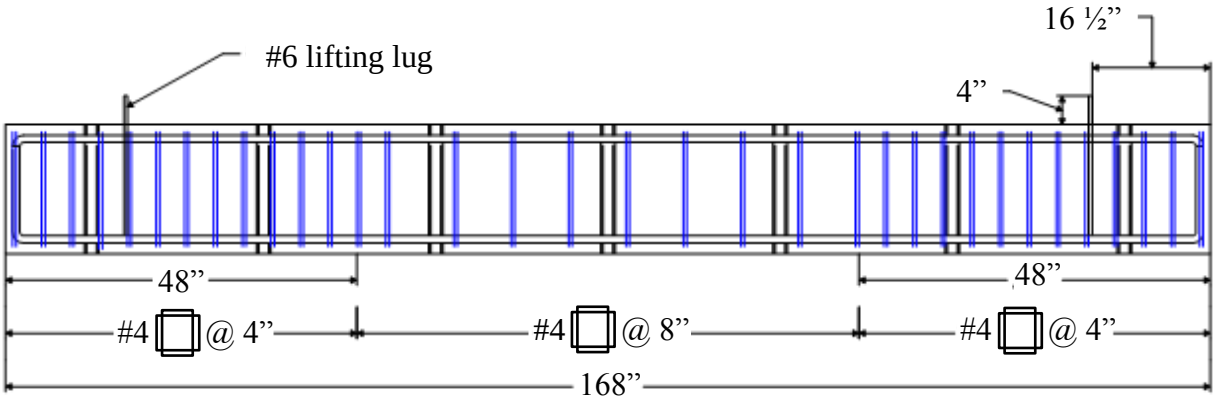

Figure 2-9. Typical elevation view of the Phase II foundation block

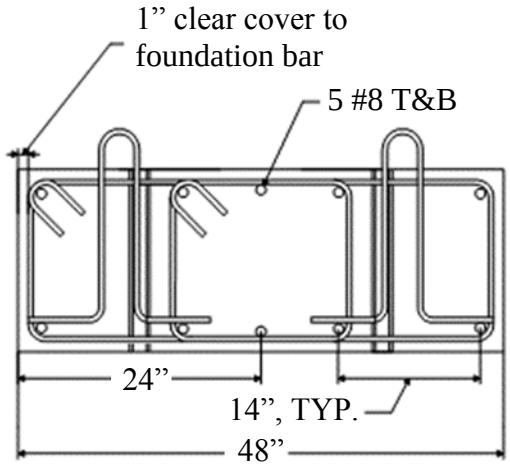

Figure 2-10. Typical cross-section through the Phase II foundation block

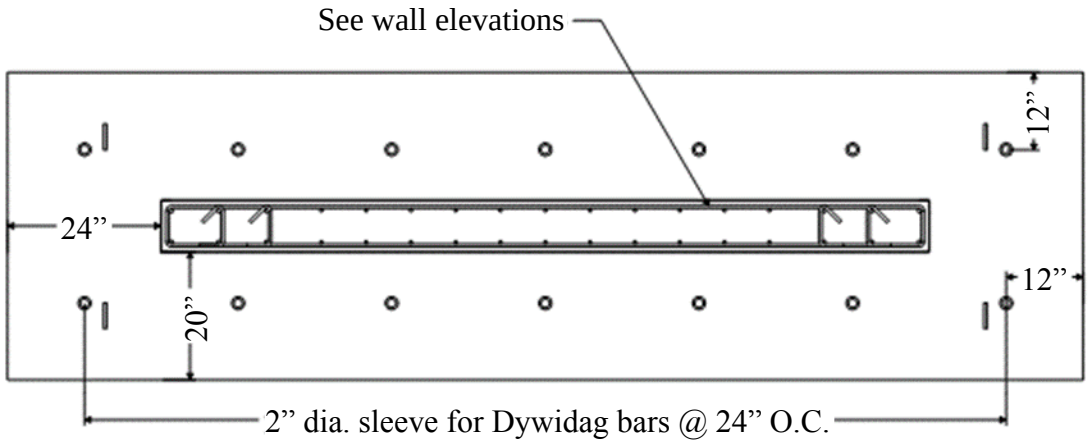

Figure 2-11. Typical plan view of the Phase II foundation block

The foundation block was designed and detailed in accordance with the strut-and-tie procedures of ACI 318-08 (now Chapter 23 of ACI 318-14). Several different strut-and-tie models were considered; 2D and 3D models were prepared and analyzed (shown in Figure 2-12 and Figure 2-13). Several assumptions were made to analyze these models, including:

- An upper bound vertical stress of 90 ksi was assumed in the vertical reinforcement at the edge of the wall. The forces applied using this assumption are 288 kips for SW8-SW10, 167 kips for SW11 and 223 kips for SW12.
- The vertical loads previously mentioned were assumed to be resisted by the two outermost DYWIDAG bars in the 2D model (see Figure 2-12) and the four outermost DYWIDAG bars in the 3D model (see Figure 2-13).
- The node at the bottom of the foundation was located at the center of the wall and 2.5 inches above its base.
- The transverse tie force was resisted by the #4 hoops in the foundation.
- The concrete compressive strength in the foundation was 5 ksi.

- The width of the concrete strut was assumed to be the same width as the DYWIDAG washers (eight inches) for both the 2-D and 3-D models.

Calculations were performed for each wall. The transverse tie forces exceeded the capacity of the #4 transverse reinforcement originally detailed in the foundation. This resulted in additional #4 bars being placed on top of the foundation reinforcement cage. Walls SW8 through SW10 had five additional #4 bars at each end (see Figure 2-14), SW11 had an additional four #4 bars at each end (see Figure 2-15) and SW12 had an additional two #4 bars at each end (see Figure 2-16).

2.3.2 Wall reinforcement layouts

Each Phase II wall was detailed to have a thickness of eight inches, a length of 120 inches and a height from the top of the foundation to the centerline of loading of 65 inches. The thickness and length of the Phase II walls were the same as the Phase I walls. A different reinforcement layout was selected for each Phase II wall; two of the walls included in-plane boundary elements. All of the wall reinforcement was detailed with ACI 318-14 compliant 90-degree hooks.

The Phase II walls were constructed with sixteen 2" diameter PVC sleeves to accommodate the 1.5" diameter B7 threaded rods that attached the loading apparatus to the wall for testing. Figure 2-17 shows the locations of the PVC sleeves.

2.3.3 Reinforcement layout in SW8

The reinforcement ratio in the vertical and horizontal directions of SW8 was 1.5%: two curtains of #4 rebar spaced at 3.25" in each direction, as seen in Figure 2-18.

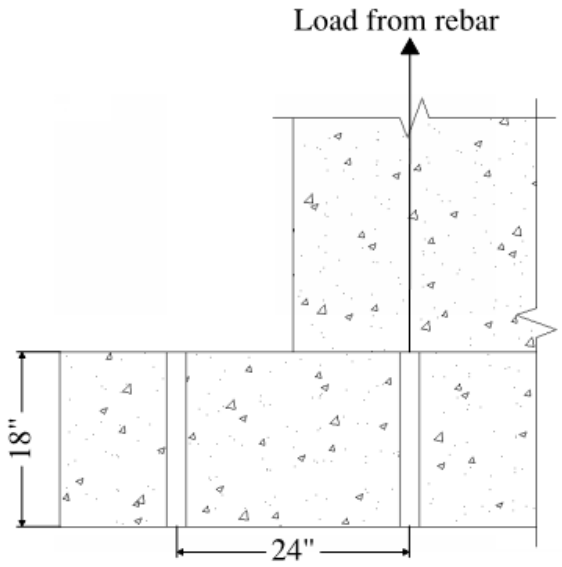

a. side elevation of the 2D strut and tie model

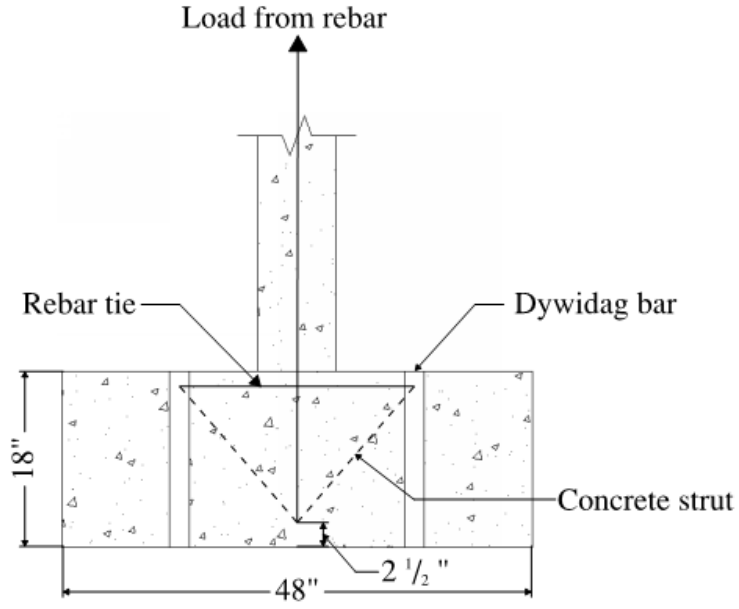

b. front elevation of the 2D strut and tie model

Figure 2-12. 2D strut and tie model

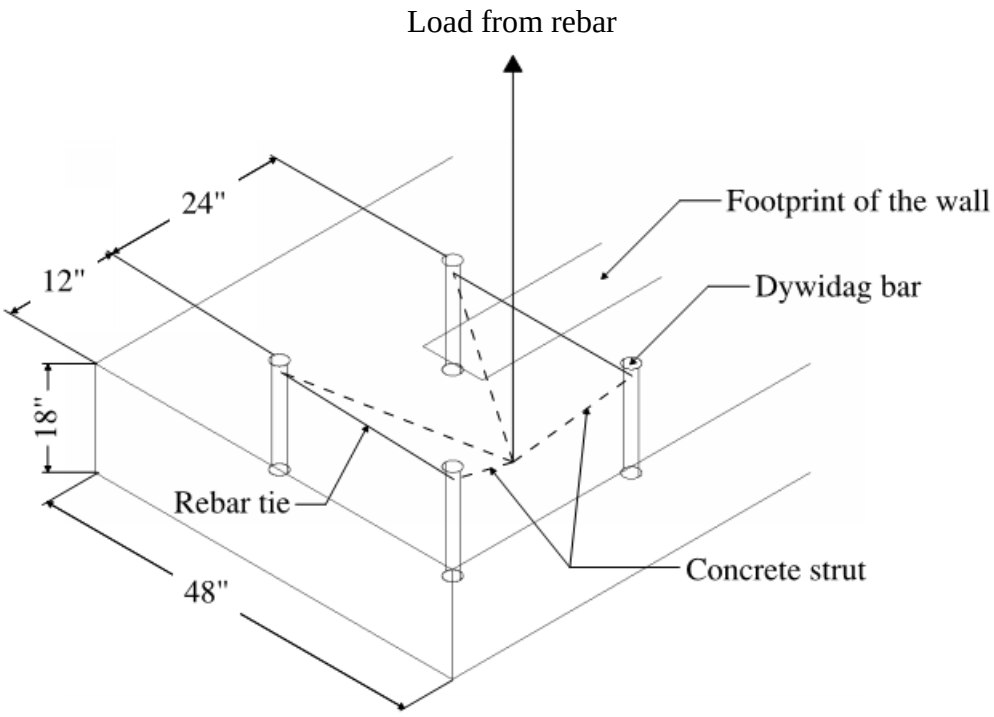

a. isometric view of the 3D strut and tie model

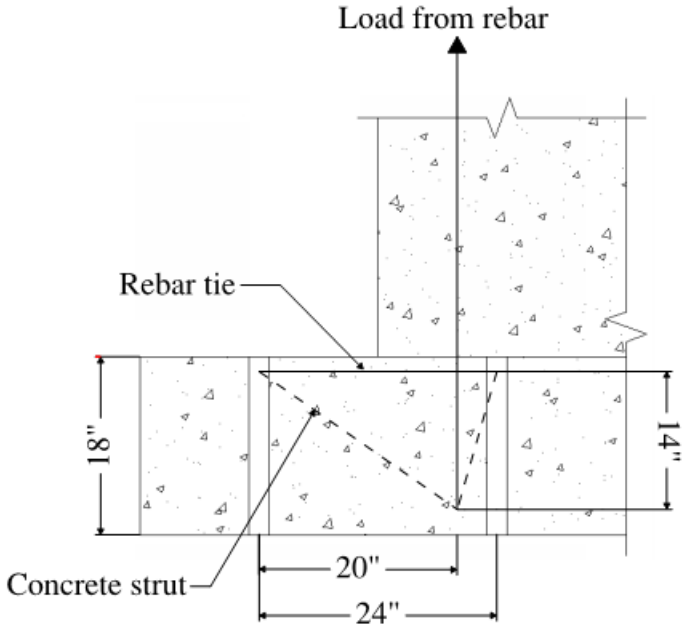

b. side elevation of the 3D strut and tie model

Figure 2-13. 3D strut and tie model

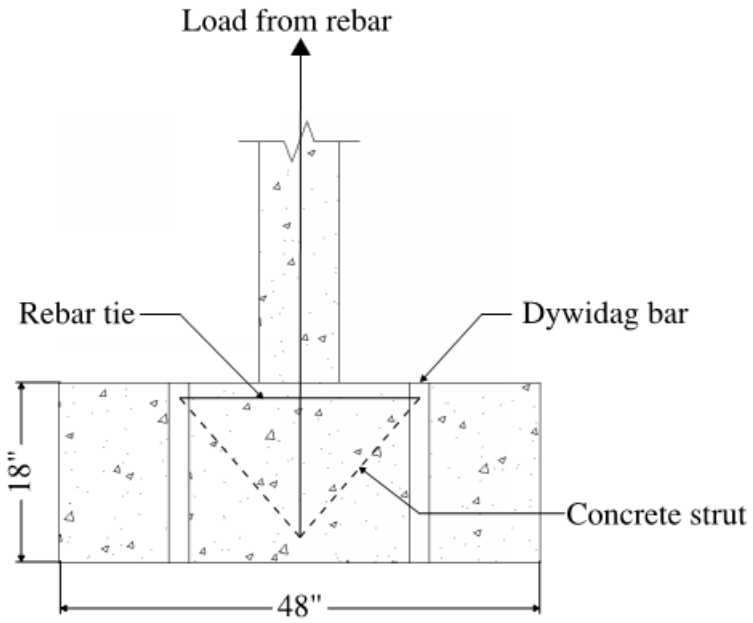

c. front elevation of the 3D strut and tie model

Figure 2-13. 3D strut and tie model (cont.)

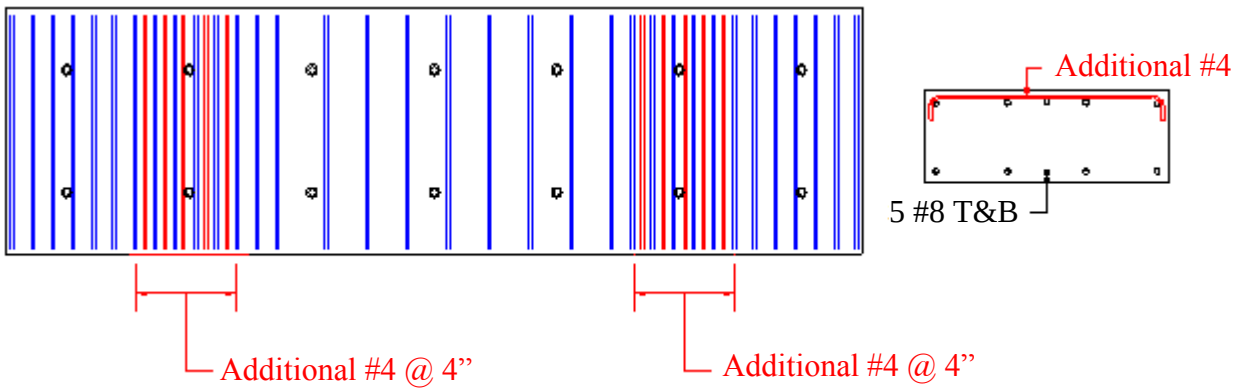

a. schematic

b. as built

Figure 2-14. Additional top rebar in SW8 through SW10

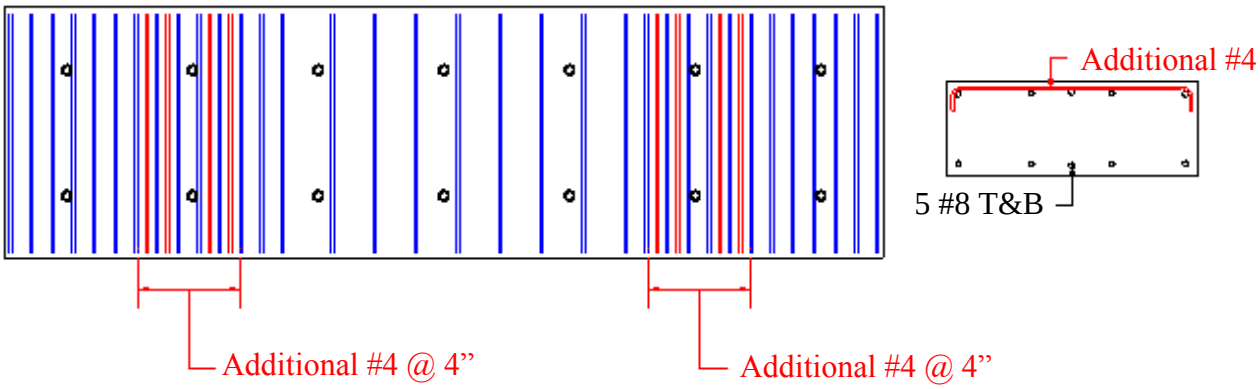

a. schematic

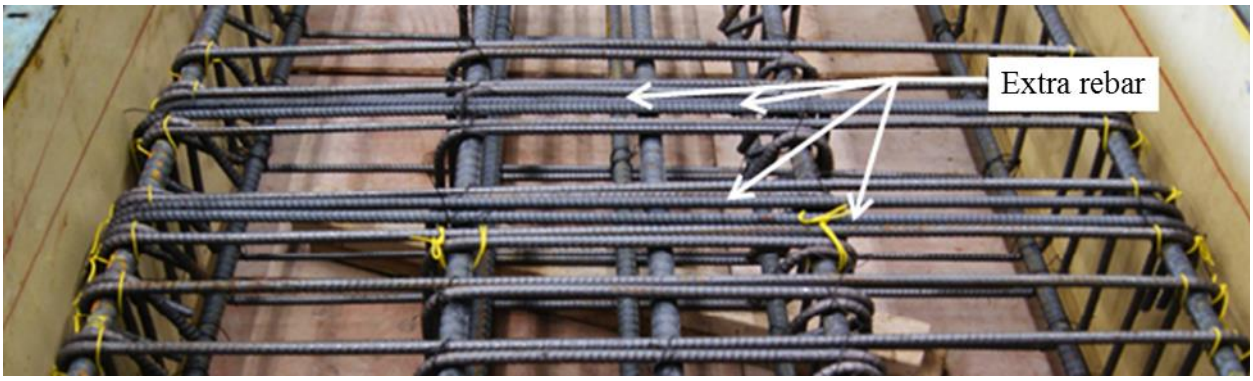

b. as built

Figure 2-15. Additional top rebar in SW11

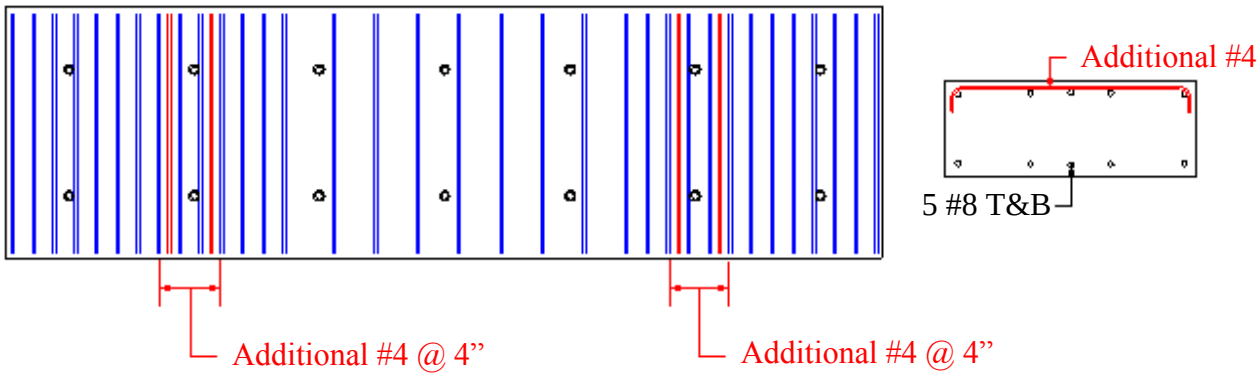

a. schematic

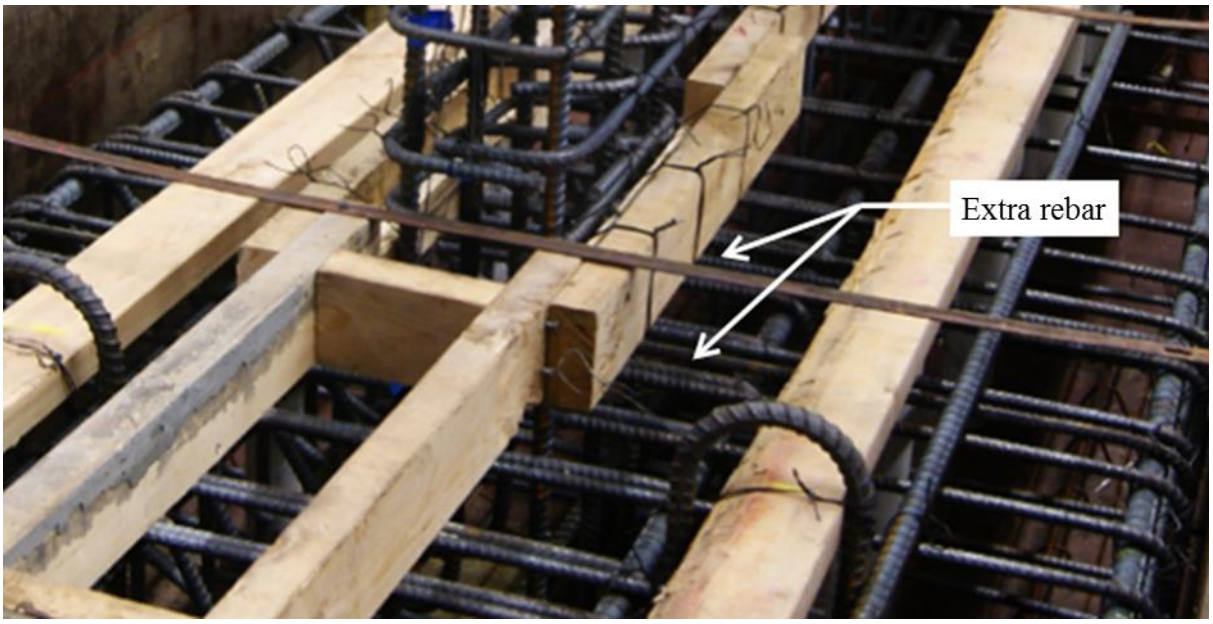

b. as built

Figure 2-16. Additional rebar in SW12

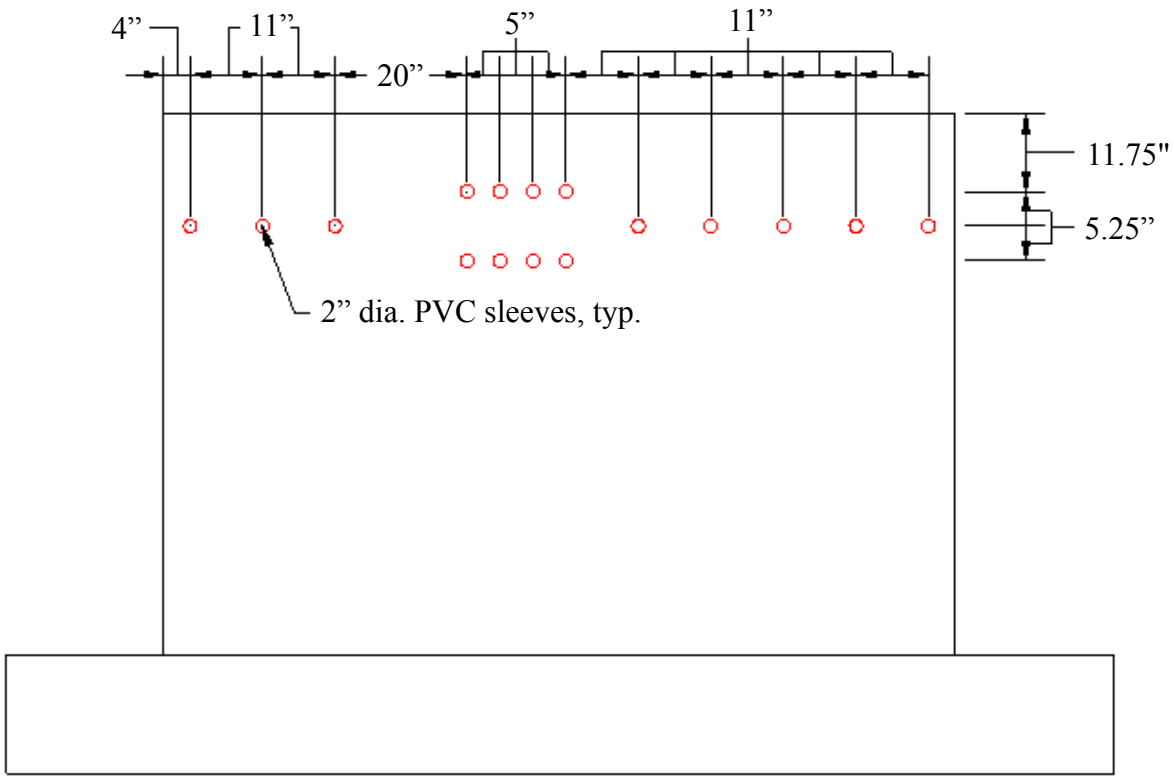

Figure 2-17. Location of 2” dia. PVC sleeves

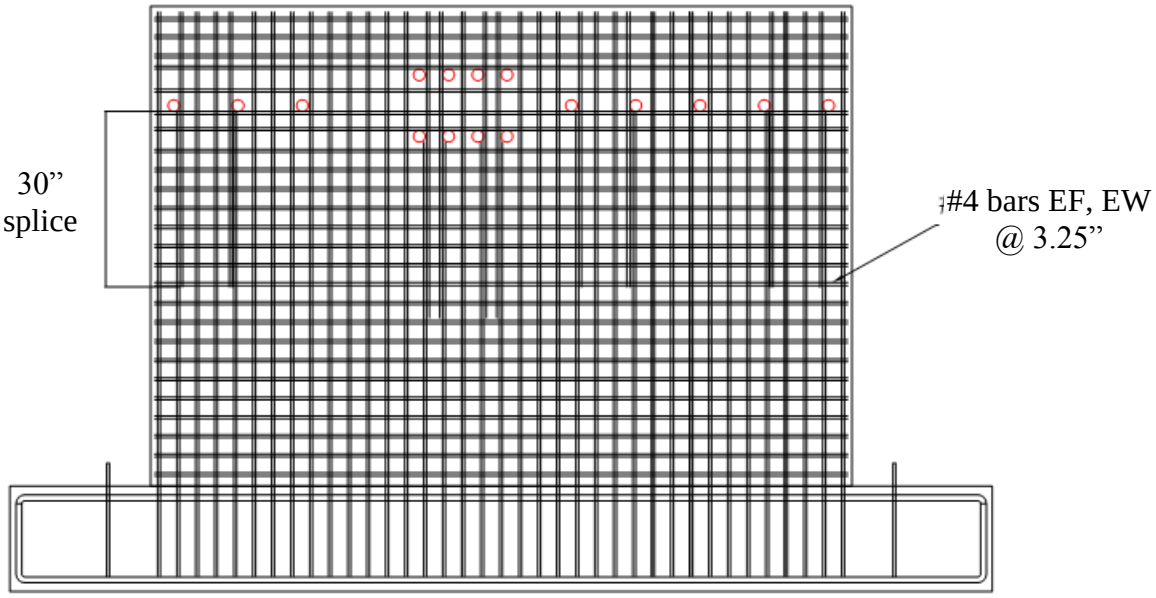

a. elevation view

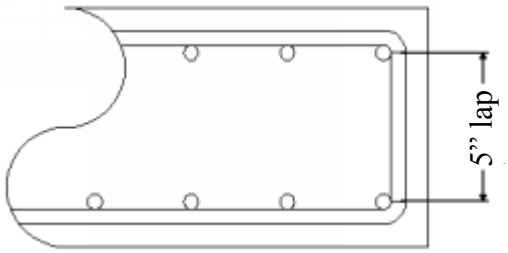

b. section A-A

Figure 2-18. Wall SW8 construction details

2.3.4 Reinforcement layout in SW9 and SW10

SW9 and SW10 had vertical reinforcement ratios of 1.5% but different horizontal reinforcement ratios. SW9 had a horizontal reinforcement ratio of 0.67%: two curtains of #4 rebar spaced at 7". SW10 had a horizontal reinforcement ratio of 0.33%: two curtains of #4 rebar spaced at 15.5". Figure 2-19 and Figure 2-20 are drawings of SW9 and SW10, respectively.

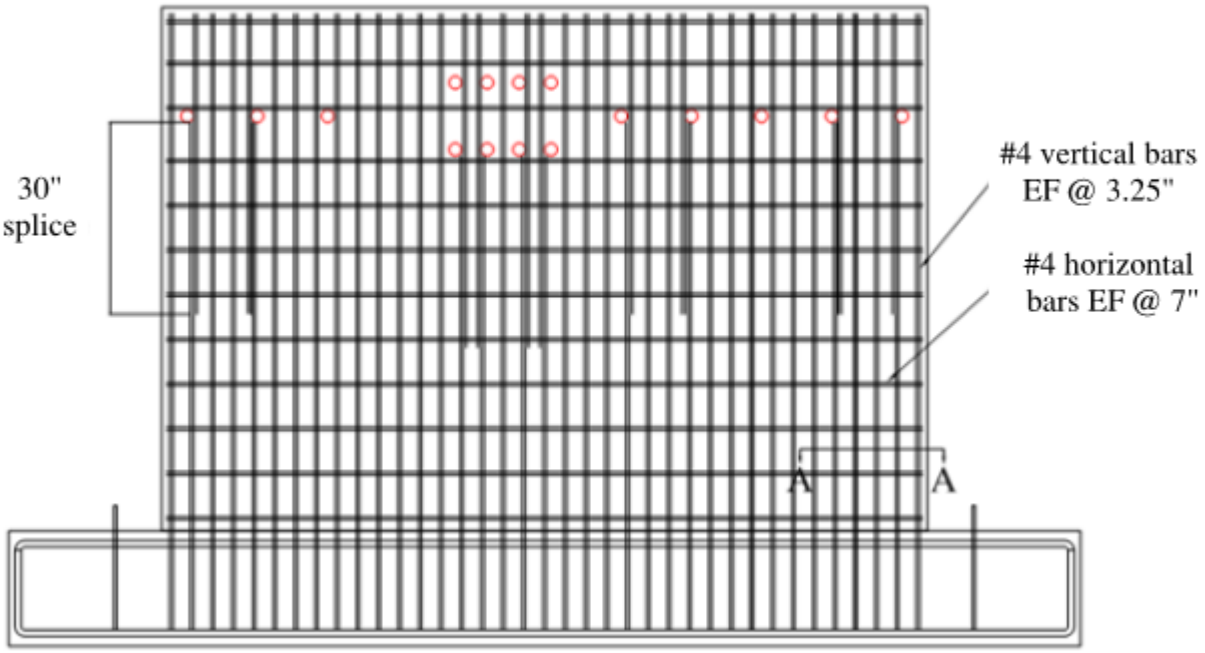

a. elevation view

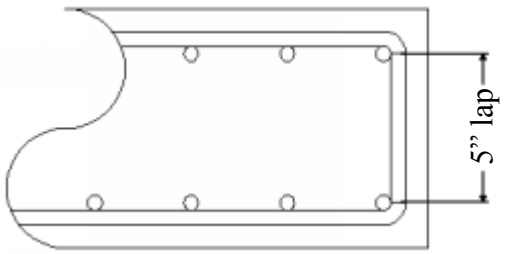

b. section A-A

Figure 2-19. Wall SW9 construction details

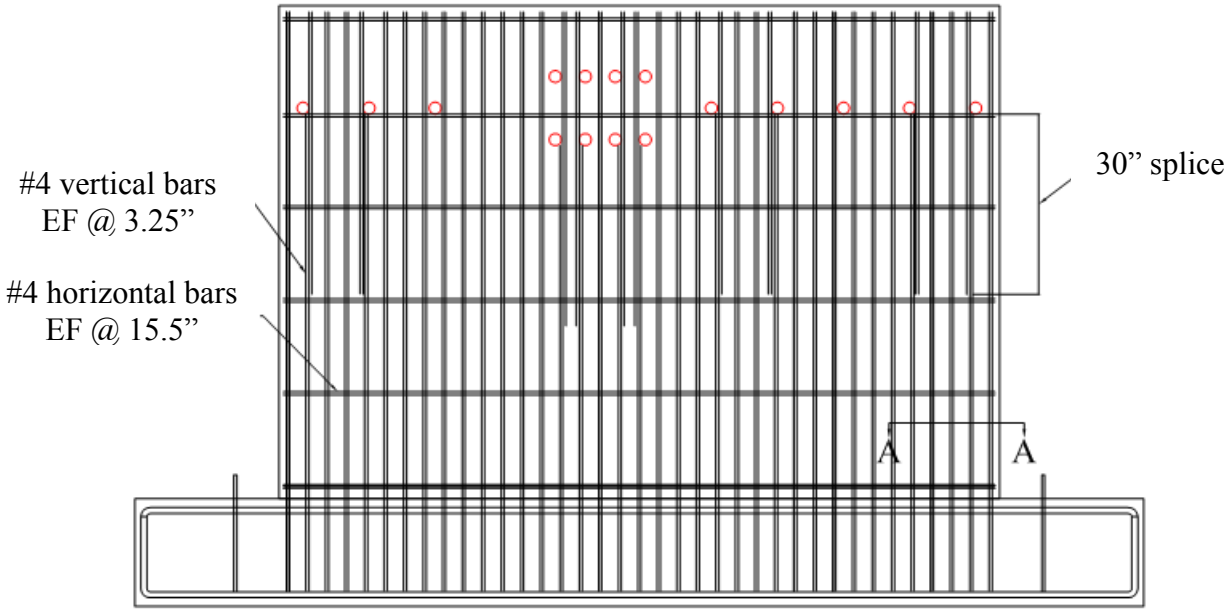

a. elevation view

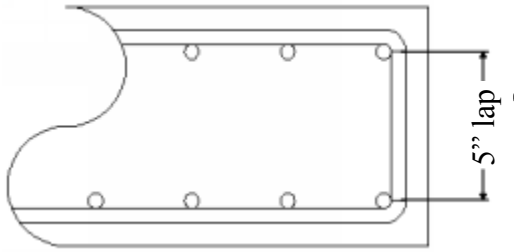

b. section A-A

Figure 2-20. Wall SW10 construction details

2.3.5 Reinforcement layout in SW11 and SW12

Walls SW11 and SW12 included 16”- long boundary elements within the web of the wall. SW11 had web reinforcement ratios of 0.63% (vertical) and 0.69% (horizontal). The web reinforcement ratio in SW11 was achieved with two curtains of #4 horizontal (vertical) bars at 7.25” (7”) on center. SW12 had web reinforcement ratios of 0.34% (vertical) and 0.38% (horizontal). The web reinforcement ratios for SW12 was achieved with two curtains of #4 bars spaced 15.5” and 13” on center horizontally and vertically, respectively.

The boundary elements for these walls consisted of horizontal #4 seismic hoops with cross-ties and #5 vertical bars. For SW11, the boundary element reinforcement ratio was 2.0%: two curtains of #5 bars spaced at 4-5/16”. The horizontal reinforcement ratio in the boundary element was 2.0%: #4 seismic hoops spaced at 2.5”. For SW12, the boundary element reinforcement ratio was 1.5%: two curtains of #5 bars spaced at 6-$7/16$”. The horizontal reinforcement ratio in the boundary element was 1.5%: #4 seismic hoops spaced at 3.5”. Drawings of SW11 and SW12 are presented in Figure 2-21 and Figure 2-22, respectively.

2.4 Phase II construction

The Phase II specimens were constructed by LP Ciminelli Construction in mid-March 2012. Figure 2-23 shows the typical formwork used in the construction of the foundations. Two-inch diameter pucks were screwed into the plywood base at two feet on center to aid with the placement of the two-inch diameter PVC sleeves for the later installation of DYWIDAG bars.

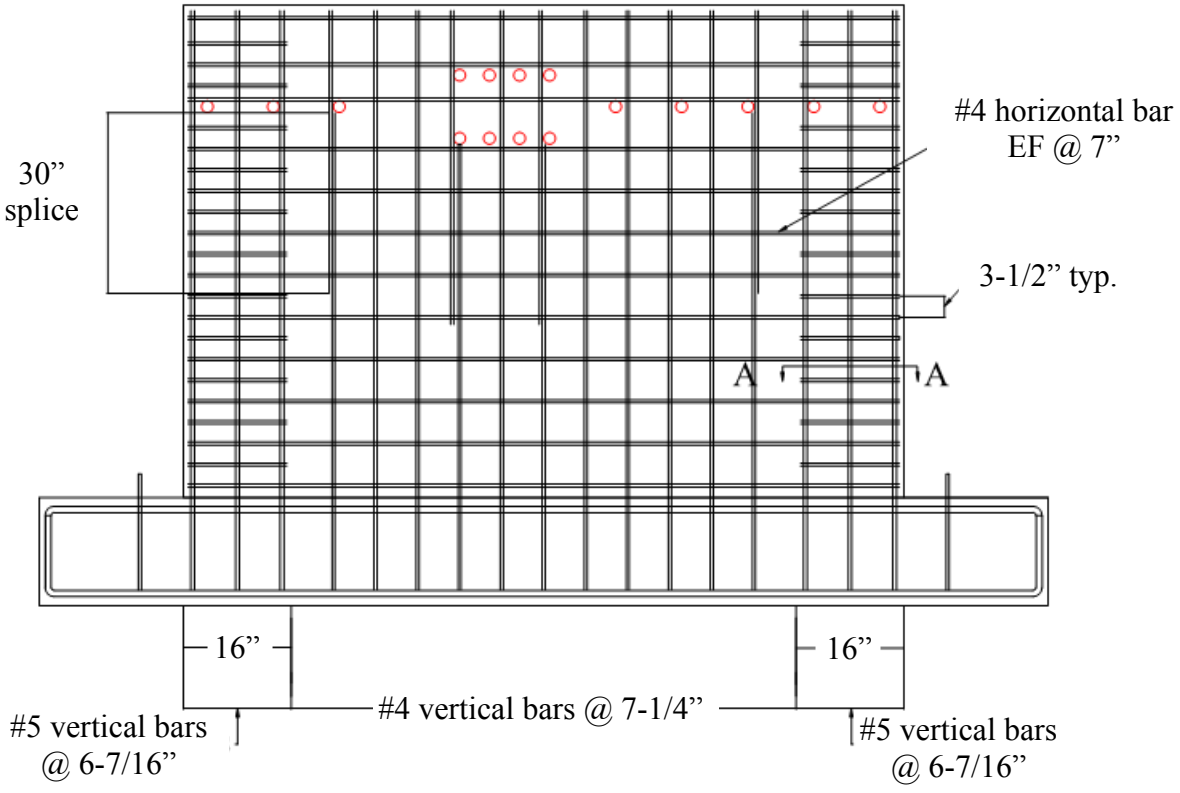

a. elevation view

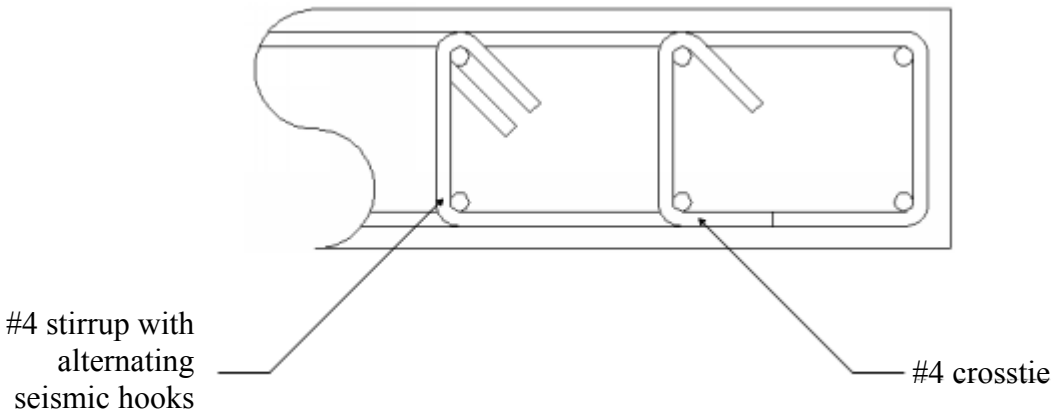

b. section A-A

Figure 2-21. Wall SW11 construction details

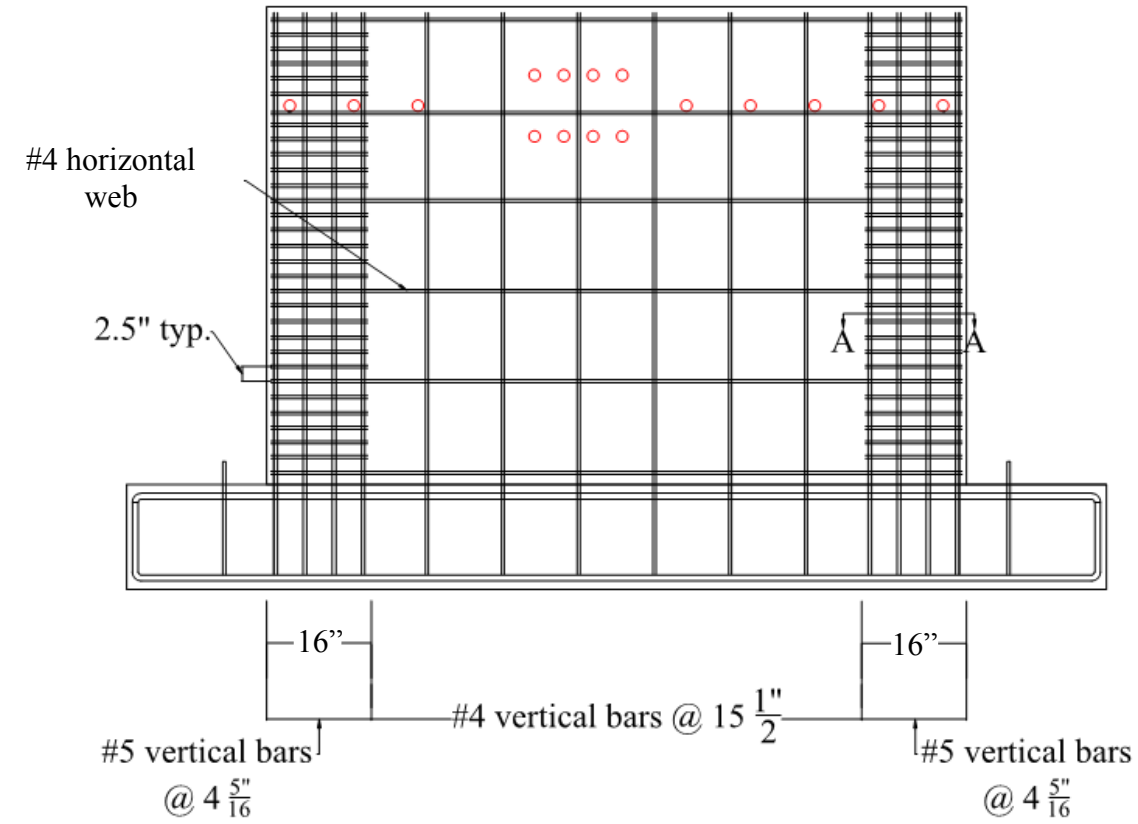

a. elevation view

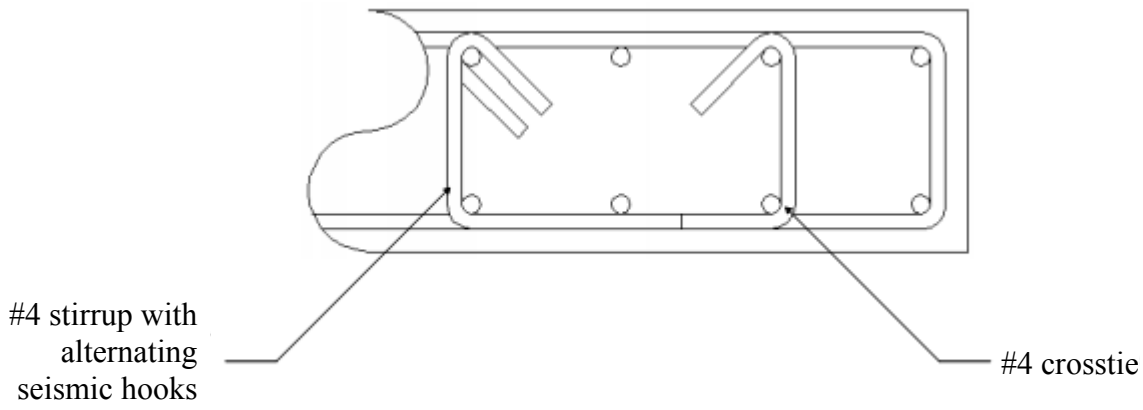

b. section A-A

Figure 2-22. Wall SW12 construction details

Figure 2-23. Typical foundation formwork

The foundation cages were tied on site by iron workers. The process involved setting up the five upper #8 horizontal bars on saw horses to provide a platform for the remainder of the cage. Once the #8 bars were placed, the #4 hoops were hung and then the bottom #8 bars were slid into position. The completed rebar cage was then placed into the formwork on top of two inch high concrete chairs. Figure 2-24 shows the completed rebar cage for SW12

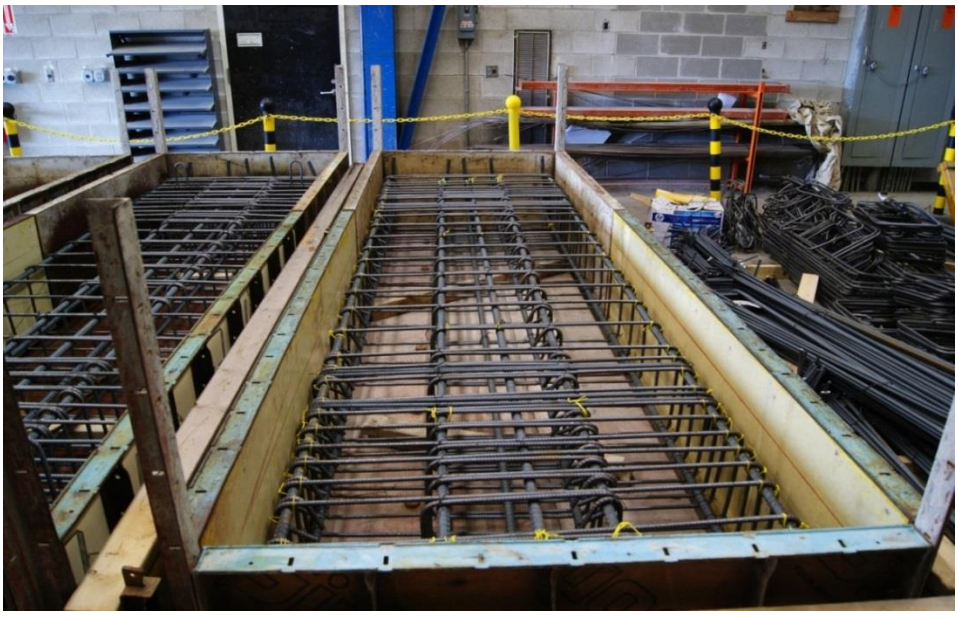

Figure 2-24. SW12 foundation rebar cage

After the foundation rebar cages were placed in the formwork, the vertical PVC sleeves (Figure 2-25) were installed and the wall reinforcement was tied. After the rebar had been placed, the wires leading to the pre-positioned strain gages on the reinforcement were pulled through the wall. The complete rebar cages for specimens SW8 through SW10 are shown in Figure 2-26.

Figure 2-25. Vertical PVC sleeves in the foundation

Figure 2-26. SW8 through SW10 rebar cages

The 5 ksi normal-weight concrete was cast into the foundation formwork via a conveyor belt. The foundations for SW11 and SW12 were cast with concrete from the first truck. The foundation of SW10 was cast with concrete from the first and second trucks. The foundations for walls SW8 and SW9 were cast with concrete from the second truck.

The foundation formwork was stripped one day after casting and then 3/4"- high rebar chairs were then attached to the outer faces of the wall rebar cages. The formwork for one side of the wall was then installed, as shown in Figure 2-27.

One week after the foundations were cast, the walls were cast using 4 ksi self-compacting concrete. The concrete was cast using both a pump truck and a conveyor belt, using two truckloads of concrete. Walls SW10, SW11 and SW12 were cast using a pump, whereas walls SW8 and SW9 were cast using a conveyor belt. Figure 2-28 shows SW11 after the formwork had been stripped. The construction time for the five walls was approximately two weeks.

Figure 2-27. Wall formwork for specimens SW10 through SW12

Figure 2-28. SW11 prior to testing

SECTION 3
AUTOMATED DETECTION AND MEASUREMENT OF CRACKS

3.1 Introduction

The length, width and areal density of cracks are used for damage assessment of reinforced concrete components in the laboratory and field. Damage to reinforced concrete components in buildings and infrastructure after earthquake shaking can be inferred using maximum residual crack widths. Strategies for post-earthquake repair are often based on this information. Cracking of reinforced concrete components during laboratory testing is routinely documented (along with other information) to enable a reconciliation of loss of strength and stiffness with observed damage. Information on the cracking of low aspect ratio reinforced concrete shear walls (Gulec et al., 2010) has been used to generate fragility and consequence functions, which enable an estimate of repair cost per unit area of wall.

Engineers have traditionally identified cracks visually in reinforced concrete components, measuring their widths using a crack-width card (see Figure 3-1), and then transferring that data to drawing sheets. Crack width is either measured at user-determined locations along the length of a crack or a maximum value is reported. Cracks are assigned a width equal to one of the marks on the gage (e.g., 0.005 inch, 0.016 inch, 0.06 inch, see Figure 3-1). Widths of cracks between the marks on a gage can only be estimated. The process is laborious and approximate because uncertainty is introduced in the measurement of crack width, the use of few measurement locations, and the transfer of information to drawing sheets.

Imaging tools provide a means to improve the process of measuring and documenting cracks and their widths, and to substantially improve the quality and accuracy of the results. Non-contact identification and measurements of cracks enables data to be gathered from large-

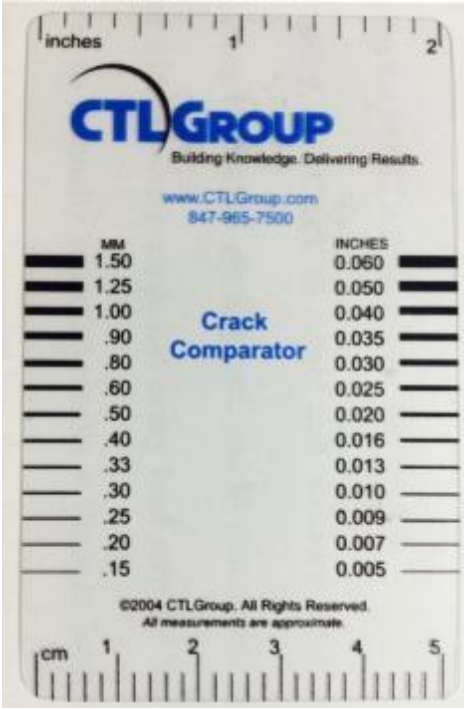

Figure 3-1. Crack gage, full scale (courtesy of CTL Group)

size laboratory tests at instances of peak loading and deformation in a safer and more reliable manner. Gathering information on the length, width and areal density of cracks at instances of peak deformation and zero loading enables estimates to be made of structural damage to components, which are better correlated with peak transient crack widths and lengths than residual crack widths and lengths.

3.2 Literature review

Image-based, crack-detection algorithms have been used primarily to detect cracks on pavement surfaces. Most crack-detection algorithms rely upon edge-detection algorithms to locate cracks. Abdel-Qader et al. (2003) investigated the utility of the Sobel and Canny edge detectors and the Fast Fourier and Fast Haar algorithms to identify cracks within a grayscale (intensity) image. The Sobel and Canny edge detectors locate edges based on the gradient of an image. The

Fast Fourier and Fast Haar algorithms detect edges based on brightness modulation within an image. Each algorithm was applied to 50 640×480 pixel, images. They concluded the Fast Haar algorithm had the highest rate of correct identifications and the Fast Fourier algorithm had the lowest.

The algorithms investigated by Abdel-Qader et al. also detected surface defects such as divots, blemishes and stains, which are present on any concrete component. Fujita et al. (2006) addressed the presence of surface defects using two pre-processing techniques: 1) image subtraction, and 2) line emphasis. Image subtraction is similar to matrix subtraction because the pixel value (a number that describes the pixel brightness) of one image was subtracted from the pixel value of another image. Image subtraction removed minor irregularities (e.g., shading and some lighting irregularities) and more clearly defined the cracks. A line emphasis filter was then used to better define edges and separate surface defects from the cracks. These two pre-processing steps were applied to 50 images of concrete surfaces with irregular lighting and blemishes. Fujita et al. concluded that these two pre-processing steps were effective.

Although edge detection and noise removal were necessary steps in detecting cracks on concrete surfaces, they did not provide sufficient information for damage assessment. Miyamoto et al. (2007) developed a method to measure crack widths. Crack widths were determined by using the difference in pixel brightness between cracks and surrounding surfaces. This method involved detection of cracks, approximating the cracks as a straight line, applying calibration factors and then detecting the difference in pixel brightness. They evaluated the method using multiple images and manually measured crack widths. Miyamoto et al. showed the results of this method compared reasonably well to the measurements taken manually.

Yamaguchi et al. (2008) processed images using a percolation model for crack detection. In the percolation-based process, the central pixel in a window of $N \times N$ pixels (where N was defined by the user) was selected and the brightness of that pixel was set as the initial threshold. The neighboring pixels were then evaluated individually based on their brightness. If the brightness was less than the threshold, the neighboring pixel was added to the central pixel to form a two-dimensional cluster; otherwise, the pixel was ignored. If the brightness of each of the neighboring pixels was greater than the threshold, then only the darkest neighboring pixel was added to the central pixel. The process of selecting neighboring pixels and evaluating them was repeated until the cluster reached the boundary of the $N \times N$ window. After reaching the boundary, the window size was increased and the threshold updated. The threshold was updated by selecting the brightest pixel in the cluster and using its brightness as the new threshold. Additional pixels were then added to the cluster and evaluated based on the updated threshold. The process of incrementally increasing the window size, updating the threshold, and adding pixels to the cluster was continued until a predefined maximum window size was reached. The cluster was then evaluated based on a ratio of its area to its length (i.e., its circularity) to determine if it was part of a crack. Every pixel in the original image was evaluated by shifting the origin of the $N \times N$ window and repeating the above process. Figure 3 of Yamaguchi et al. (reproduced here as Figure 3-2) illustrates the percolation process. Figure 3-2a shows the propagation of the two-dimensional cluster when no cracks are present in the image. Figure 3-2b shows the propagation of the two-dimensional cluster within the crack when the central pixel of the $N \times N$ window is inside the crack. The process was applied to 50 480×480 pixel images and to a single image of 3040×2008 pixels. Yamaguchi et al. concluded this method could satisfactorily detect a crack in an image.

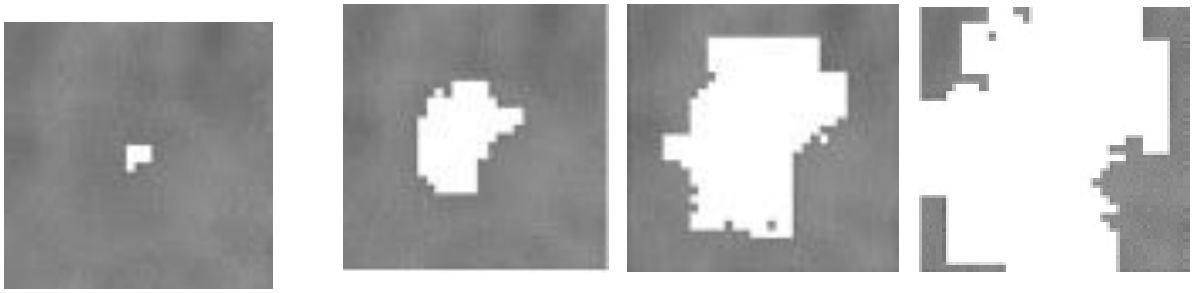

Iteration 1 Iteration 5 Iteration 10 Termination

a. background only

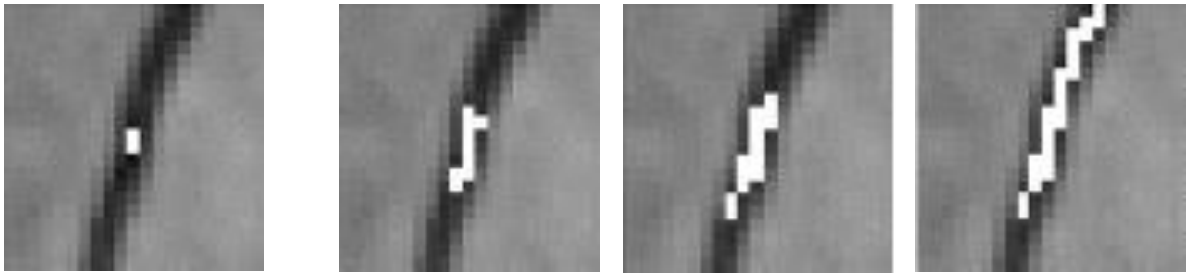

Iteration 1 Iteration 5 Iteration 10 Termination

b. crack present

Figure 3-2. Examples of the percolation process from Yamaguchi et al. (2008)

Choudhary and Dey (2012) used fuzzy logic and neural network models to detect cracks. RGB images were converted to grayscale images and a Sobel edge detection algorithm was used to locate the edges of the cracks and the surface defects. Morphological operations were then used to fill the space between the detected edges and to remove some of the surface defects. Two parameters (area and major-minor axes length ratio) were then extracted from the cracks or surface defects using subroutines available in MATLAB (Matworks, 2013). These parameters were then entered into the neural network model or fuzzy logic model where the object was classified as a crack or not a crack. The neural network model provided better results than the fuzzy logic model.

For a non-contact damage assessment algorithm to be useful in the field or for large scale testing, it must be able to a) identify cracks in concrete components, b) accurately monitor crack width and propagation under changing amplitudes of loading, c) enable measurement of crack width for the purpose of establishing damage and repair measures, d) be capable of handling high-resolution images of an entire specimen, and e) remove image irregularities due to shadows and lighting. None of the algorithms described above can accomplish these goals.

3.3 Digital imaging of damaged concrete walls

High-resolution images must be used for automated detection and measurement of cracks because cracks represent a very small fraction of the concrete surface. A digital SLR camera and a robotic panohead were used to capture high-resolution images of nine reinforced concrete shear walls described in Chapter 2. The camera was a Canon EOS 60D with a resolution of 18 megapixels and a maximum image size of 5200×3462 pixels. This camera could not image an entire wall in sufficient detail and was therefore mounted on a GigaPan Epic robotic panohead to enable the assembly of a gridded set of high-resolution images at a given load step. This combination of the Canon EOS 60D and GigaPan Epic robotic panohead allowed cracks as narrow as 0.01 inch to be detected by I-Crack (likely sufficient for most applications) and corresponded to 200 pixels per inch of concrete surveyed. (The detection of even narrower cracks would require a greater number of pixels per inch). Figure 3-3 is a set of raw images of specimen SW8 at LS6. The high-resolution panorama of Figure 3-4 was created by aligning and blending each image using GigaPan Stitch software (GigaPan Systems, 2013). The panorama of the wall shown in Figure 3-4 is not an exact rectangle. The top and bottom of the wall are curved slightly and the edges of the wall are not exactly vertical. This fish-eye effect is due to the digital camera rotating

about a fixed point, with slightly different distances between the camera and the center of each of the raw images of Figure 3-3. If important, and it is not for the small distortions seen here, the fish-eye effect could be eliminated or mitigated by a) additional image procession (eliminate), b) moving the camera further away from the wall (mitigate), or c) mounting the camera on a frame that would allow the camera to traverse the elevation of the wall, horizontally and vertically (eliminate).

Figure 3-3. Raw images of SW8, LS6

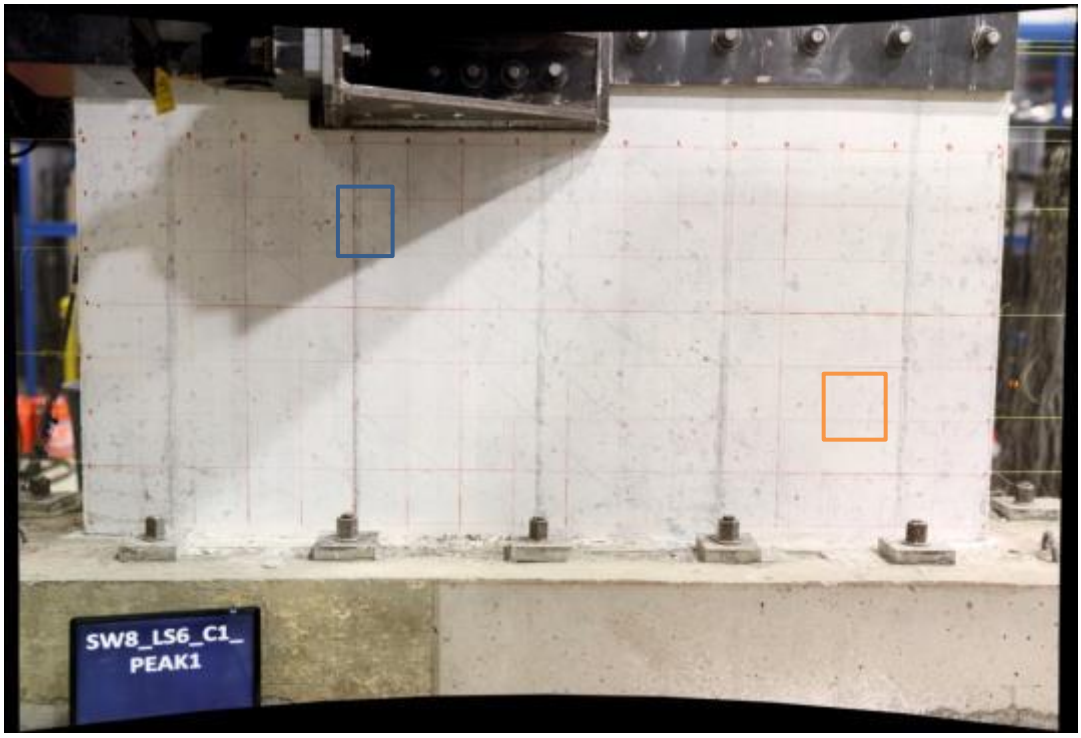

Figure 3-4. Assembled high-resolution panorama of SW8, LS6

During testing, damage in the form of spalled concrete, crack initiation, propagation and width, and rebar buckling and fracturing were monitored at each displacement increment. Cracks were identified by 1) visual inspection (with crack widths measured by hand using the gage of Figure 3-1), and 2) using an automated process (known as I-Crack) based on digital imaging and processing, as described in the following sections. High-resolution panoramas were collected for every wall at every displacement increment for the development and validation of I-Crack. Data from SW8 was used to develop I-Crack, and data from SW1, SW2, SW3, SW5, SW6, SW7, SW9 and SW12 were used to validate I-Crack.

I-Crack was developed to detect and measure cracks in reinforced concrete components using high-resolution panoramas, as described in Section 3.4. These panoramas could also be used to identify other types of damage, including crushed concrete, buckled reinforcement, and base

sliding. Image processing algorithms could be developed to automatically identify these types of damage. Alternately, and likely more efficiently, the high-resolution panorama could be visually inspected for evidence of other damage.

3.4 Automatic detection and measurement of cracks

I-Crack was constructed around algorithms found in MATLAB. The building blocks of I-Crack are 1) an edge detection algorithm, 2) morphological operations that fill cracks, 3) operations that distinguish and separate cracks from surface defects, and 4) measurement of crack widths. Each step is shown in Figure 3-5. The computer code is presented in Appendix A.

3.4.1 Image pre-processing and pixel length calibration

Image pre-processing precedes the implementation of I-Crack and is unique for each panorama analyzed. The need for pre-processing is dependent upon the quality of the panorama, which is determined in part by the environment where it was captured. Ideally, the component being surveyed will be uniformly lit to avoid shadows and this should be possible for many field applications. The laboratory setting was less than ideal because the testing equipment cast shadows and the ambient lighting varied over the duration of a test. Initial attempts to process the panoramas from SW8 identified two hurdles: 1) overexposure of the panoramas, and 2) shadows on the specimen surface. Overexposure produces areas within the panorama that are extremely light compared to the remainder of the image. A crack propagating through an overexposed region is difficult to detect; as highlighted in the open orange box of Figure 3-4 and enlarged in Figure 3-6a.

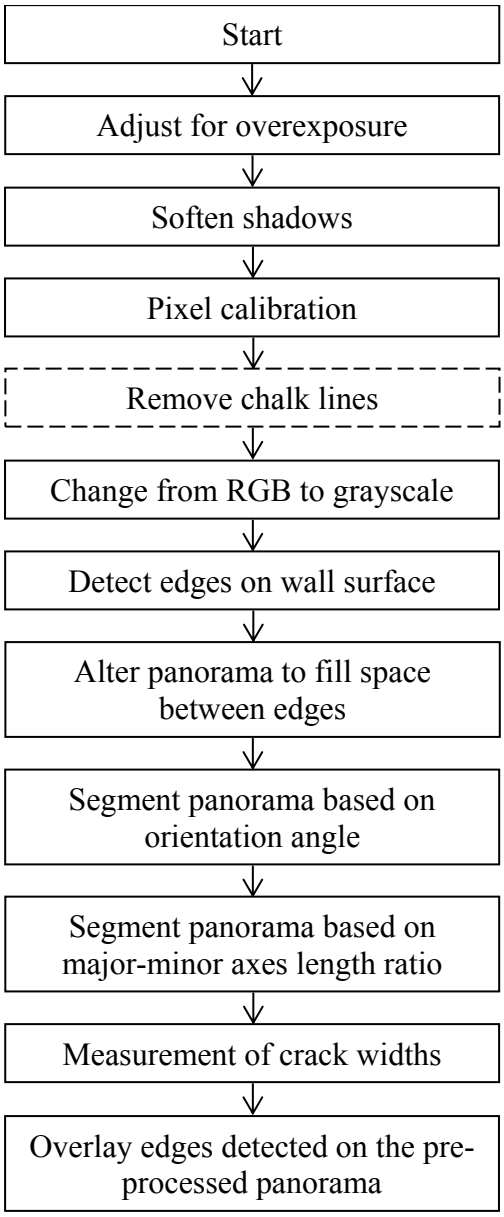

Figure 3-5. I-Crack flowchart

Image-processing software [e.g., Adobe Photoshop Elements (Adobe Systems Inc, 2010) or FastStone Image Viewer (FastStone Soft, 2013)] can be used to adjust a panorama. The Auto-Adjust Colors option in the FastStone Image Viewer was used here to reduce the overexposure in the image, with results shown in Figure 3-6b.

After a panorama is processed for overexposure, the shadows present on the wall should be softened to improve crack detection. An example is enclosed in the open blue box in Figure 3-4 and enlarged in Figure 3-7a. Shadow softening is preferred to shadow removal because the image manipulation required to completely remove a shadow will overexpose the areas where no shadows are present. The Adjust Lighting option in the FastStone Image Viewer was used to soften the shadows, as seen in Figure 3-7b. (A component must be evenly lit if no shadows are permissible.)

A completely pre-processed panorama of SW8 is shown in Figure 3-8. The area enclosed in the open red box of Figure 3-8 was used to develop I-Crack and this area is discussed in the following sections.

A calibration factor is determined from the pre-processed panorama. The factor is required because I-Crack initially predicts crack properties based on the number of pixels present within a feature (crack or surface defect). To obtain a useable measurement (inch or $inch^2$), a measurement in pixels is multiplied by the corresponding calibration factor. The calibration factor can be determined several ways and is unique for each specimen imaged. Within each panorama an object must be present that has a known length or area. Using image segmentation, that object is changed to white and the rest of the panorama is changed to black. MATLAB interprets a black and white image as a matrix full of zeroes and ones; black and white, respectively. The length can then be determined by summing along the row or column of the matrix; the area can be determined by

summing all of the elements in the matrix. The calibration factor is determined by dividing the object's length or area by the number of pixels.

The specimens used to develop I-Crack were rectangular walls with a known geometry. The wall was used as the object in the panorama to calculate the calibration factor. The panorama was loaded into MATLAB and changed to a black and white image using the function im2bw. The wall was changed to white and the background to black, thus locating the wall in the panorama; see Figure 3-9. The number of pixels in the wall length was determined by summing along one of

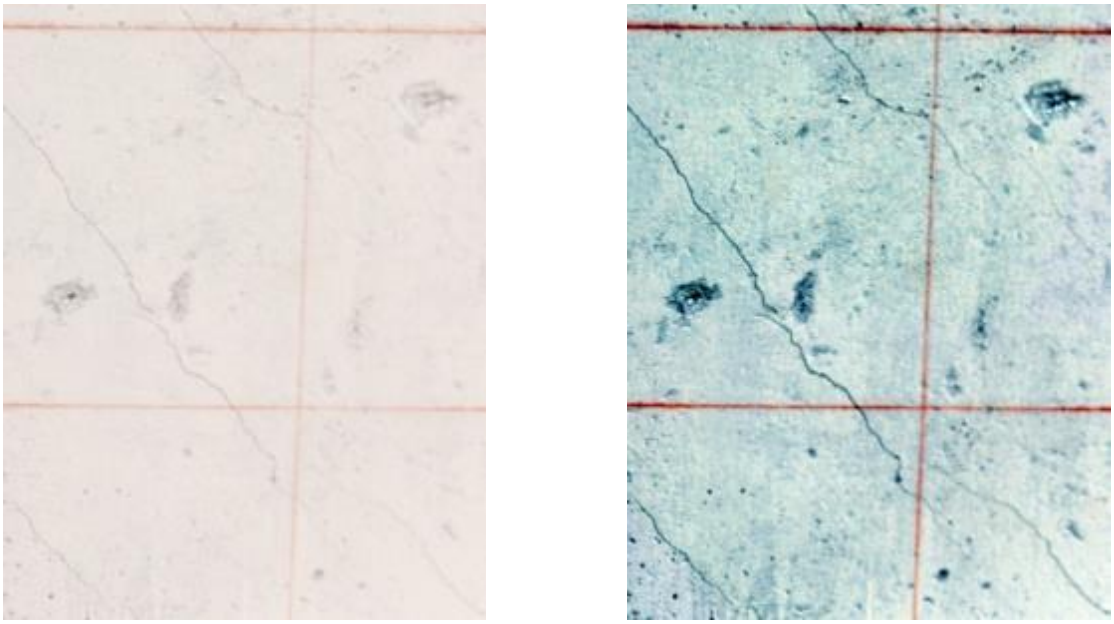

a. overexposed image b. image after preprocessing

Figure 3-6. Correction for overexposure, SW8, LS6

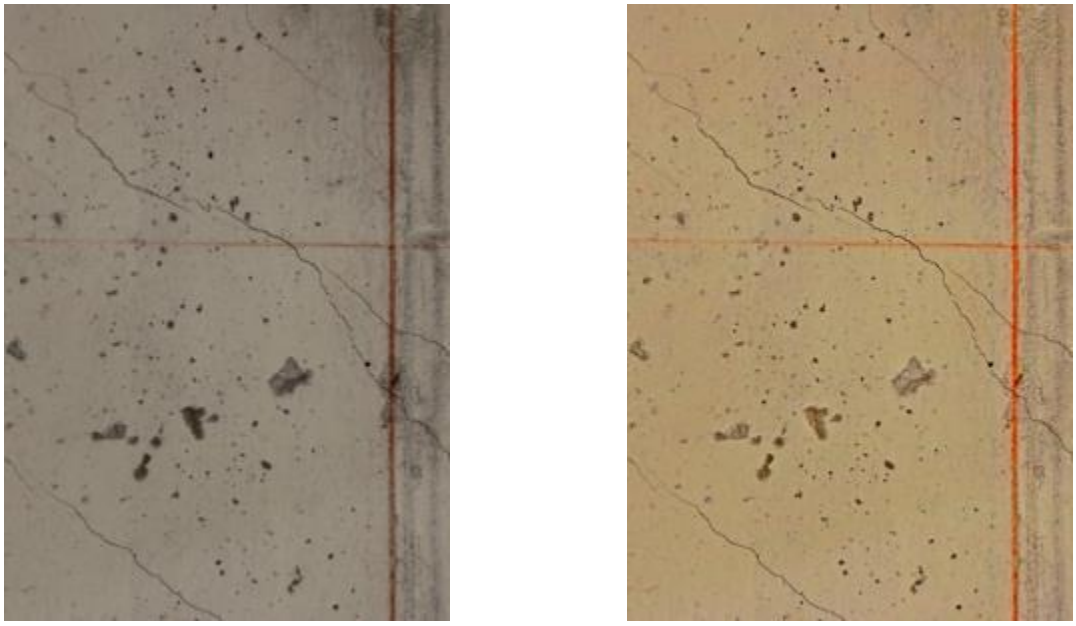

a. shadows present b. image after pre-processing

Figure 3-7. Correction for shadows, SW8, LS6

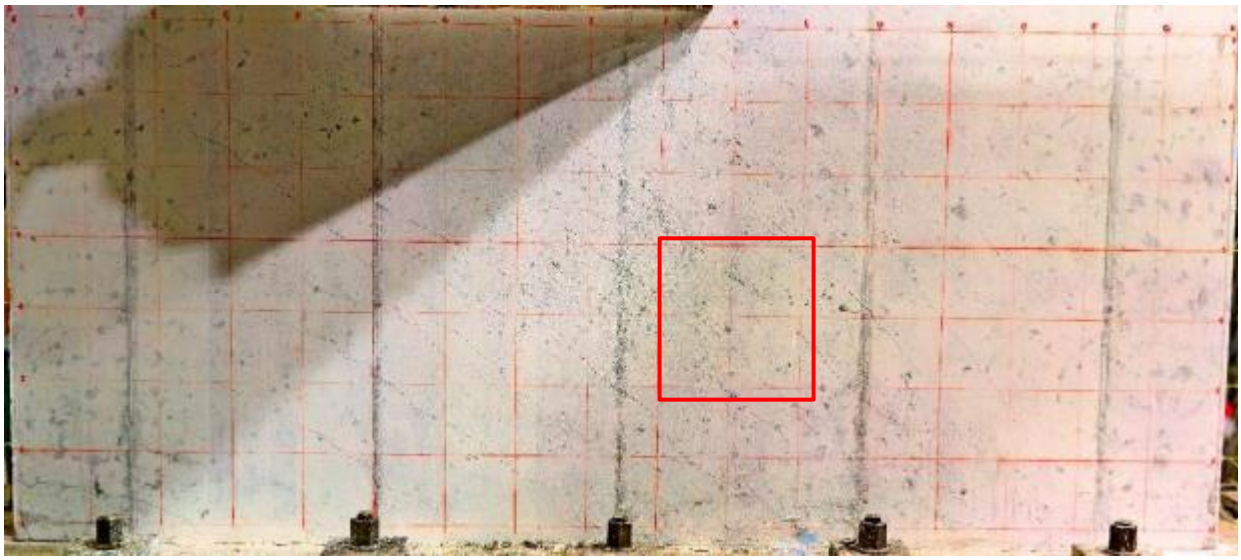

Figure 3-8. Pre-processed panorama SW8, LS6

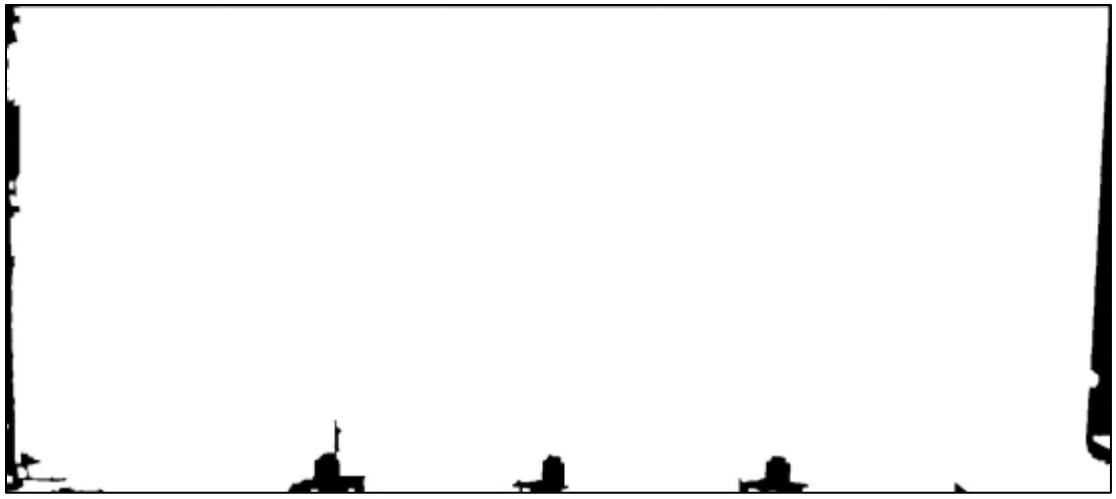

Figure 3-9. Black and white image used for pixel calibration

the rows. The calibration factor was calculated by dividing the length of the wall by the number of pixels. For field applications, a fine scale ruler could be attached to the specimen being surveyed for the purpose of establishing a calibration factor.

3.4.2 Block processing

I-Crack is implemented once a panorama has been pre-processed and a calibration factor has been determined. The panorama is loaded into MATLAB using a RGB color scheme, which is stored as a set of three matrices. Each matrix is used to define the presence of red, blue and green in each pixel. The dimensions of each matrix are equal to the number of horizontal and vertical pixels in the panorama (e.g., a panorama with an image size of 24000×6000 pixels will require three matrices with 24000 rows and 6000 columns). High-resolution panoramas require significant computational resources for processing.

MATLAB provides block processing (blockproc) to execute scripts and decrease processing time for larger images. Block processing divides the panorama into smaller sub-images

(blocks), which are individually processed by the script. The sub-image sizes used in I-Crack were 500×500 pixels or 2000×2000 pixels (Figure 3-10); resulting in 1130 and 70 blocks for SW8, respectively. These sub-image sizes were selected based on outputs obtained during the development of I-Crack and can be chosen by the user.

3.4.3 Gridline removal

Both faces of every wall tested in the NEES facility were marked with a grid of red chalk lines (Figure 3-8 and Figure 3-11a) to facilitate the location and documentation of cracks. Although the chalk lines were useful for visual inspection of the walls, they are problematic for I-Crack analysis because a pixel gradient is present at each chalk line, causing I-Crack to detect and record many unnecessary edges. Gridline removal is (obviously) not needed if gridlines are not marked on a specimen.

Removal of these unnecessary edges is accomplished with a script written to replace the chalk lines with a pixel similar to the surrounding surface: an averaged pixel. The script uses a thresholding technique based on the contribution of red to each pixel. If the contribution of red in a pixel reaches the threshold that pixel is replaced with an averaged pixel. By replacing the pixel with an averaged pixel, the gradient between the surface and the chalk line is reduced. The edge detection algorithm should not detect edges of the chalk line after these pixels are replaced (see Figure 3-11b).

3.4.4 Edge detection

I-Crack uses rgb2gray to change the panorama from a RGB color scheme to grayscale to enable edge detection. All of the edge detection algorithms in MATLAB (Roberts, Sobel, Prewitt,

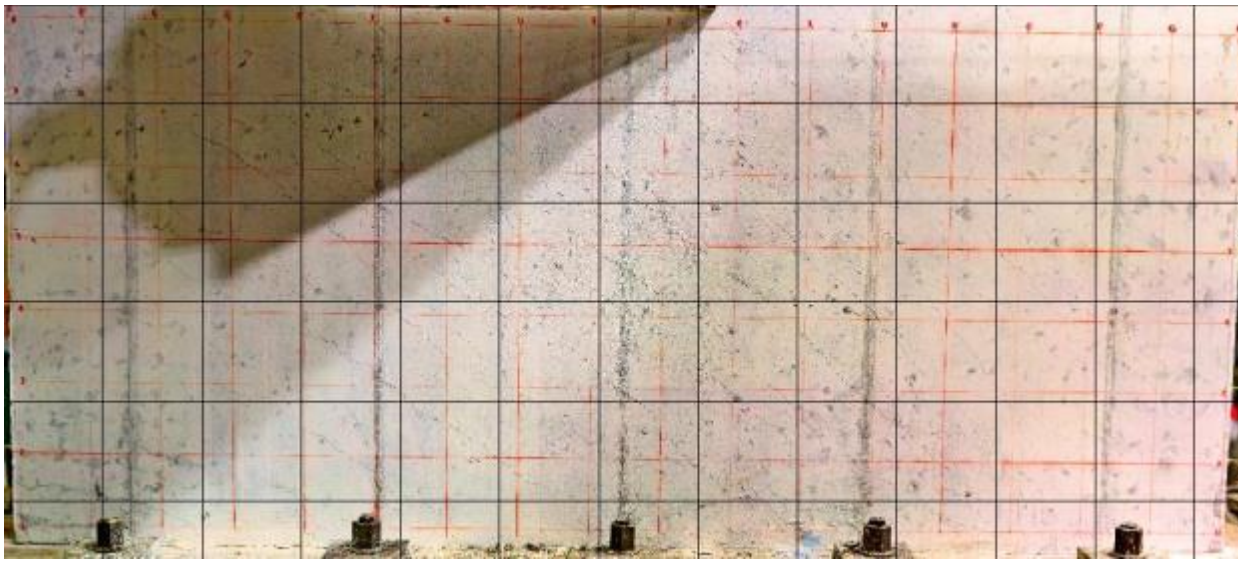

Figure 3-10. SW8, LS6 panorama divided by block processing

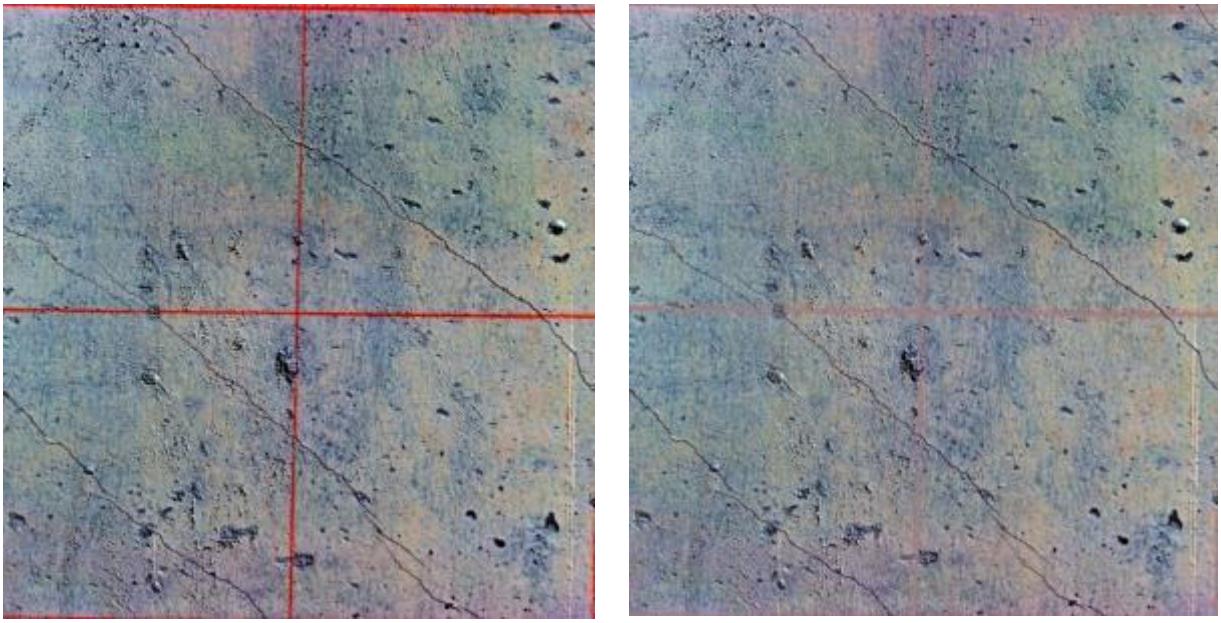

a. chalk lines present b. chalk lines replaced

Figure 3-11. Removal of chalk lines on SW8, LS6

Canny and Laplacian of Gaussian) require a grayscale image as input.

The Roberts, Sobel and Prewitt algorithms involve the convolution of the image with two matrices that determine the gradient of each pixel in the horizontal and the vertical directions. The size and composition of these matrices depend on which algorithm is chosen. The magnitude of the gradient for each pixel is then calculated as the square root sum of the squares of the gradients in the vertical and horizontal directions. A threshold is then applied to the magnitude and determines if an edge has been detected. If the magnitude is greater than the threshold, the algorithm has detected an edge and returns a value of 1; if not, 0 is returned. The threshold can be set automatically by MATLAB or defined by the user. MATLAB calculates a threshold as the square root of the average of the pixel gradients across the entire image. Since it was impossible to select one threshold that was applicable to every panorama, MATLAB was used to automatically calculate the threshold for each panorama. The result from these edge detection algorithms is a black and white image.

Another gradient-based edge detector available in MATLAB is the Canny algorithm. This algorithm applies a Gaussian filter to an image to reduce noise. The gradient in the horizontal and vertical directions, and the magnitude of the gradient of every pixel is then determined as described previously. Non-maximum suppression is then used to remove spurious pixels after the gradients in each direction and the magnitude of the gradient have been determined for each pixel. Non-maximum suppression removes spurious pixels based on the magnitude of that pixel and the magnitudes of its neighboring pixels: a spurious pixel is removed if the magnitude of that pixel is less than the magnitude of its neighboring pixels. The Canny edge detector then uses upper and lower thresholds to remove additional spurious pixels. If the magnitude of the gradient is greater than the upper threshold, then an edge is detected and a value of 1 is returned. If the magnitude of

the gradient is less than the lower threshold, then no edge is detected and a value of 0 is returned. If the magnitude of the gradient lies between the two thresholds, a value of 1 is returned if that pixel is connected to another pixel that is already considered an edge, otherwise a value of 0 is returned. The result of the Canny algorithm is also a black and white image.

Another edge detecting algorithm available in MATLAB is the Laplacian of Gaussian. The Laplacian of Gaussian applies a Gaussian filter to reduce the noise in the images, creating a "smoothed" image, which is then convolved with a Laplacian filter. The Laplacian filter is a matrix of partial second-order derivatives that determines the gradient at every pixel. The pixel is part of an edge if the convolution of the matrix and the image is zero; otherwise the pixel is not part of an edge. The product of this edge detector is a black and white image.

Each of these algorithms was applied to Figure 3-12a to determine the algorithm that best identified the edges of cracks and surface defects. The Roberts, Sobel and Prewitt algorithms detected the edges of the features in Figure 3-12a but the Roberts and Sobel algorithms recorded additional edges associated with the shading present on the wall surface. The Prewitt algorithm detected the edges of the cracks and the surface defects with fewer edges associated with shading. Both the Canny and Laplacian of Gaussian algorithms detected spurious edges. Accordingly, the Prewitt edge detection algorithm was chosen for I-Crack, although the code is written to accommodate any of the MATLAB edge detection algorithms. The results for each edge detection algorithm are shown in panel b. through panel e. of Figure 3-12.

3.4.5 Morphological operations

After edge detection, the panorama is manipulated to fill the space between the detected edges for image segmentation and measurement. MATLAB provides several morphological

operations to accomplish this task: 1) bridge: changes black pixels to white if there are two neighboring white pixels, 2) fill: changes isolated black pixels to white, 3) close: changes black pixels to white pixels based on a matrix of ones and zeroes, 3) bwareaopen: removes connected objects in a black and white image with pixels less than a set threshold, 5) imfill: fills in a region of the image based on the connectivity of the pixels within that region, and 6) imclose: dilates and then erodes the image. Figure 3-13 shows the cracks and surface defects after all of these morphological operations were applied to Figure 3-12c.

3.4.6 Image segmentation

Cracks and surfaces defects are separated after applying morphological operations. The process of separating cracks and surface defects is accomplished through image segmentation: the separation of objects based on their properties (e.g., color, area and perimeter). I-Crack segments the image using scripts based on two criteria, 1) orientation angle, and 2) the major-minor axes length ratio. Both criteria are determined using the regionprops routine in MATLAB, which measures the properties of image features; such as area, centroid, orientation angle and perimeter.

The first script, orientationFilter, used to segment the panorama, is based on the orientation angle of each crack or surface defect. Orientation angle is selected as a criterion because many cracks are inclined, whereas surface defects are often horizontal or vertical. MATLAB determines the orientation angle of the crack or surface defect based on the "…angle between the x-axis and the major axis of an ellipse that has the same second moment at the region." Figure 3-14 illustrates this process. Figure 3-14a shows four white pixels enclosed by an ellipse; the four white pixels and the ellipse have the same second moment. The second moment for a two-dimensional dataset is the covariance matrix. The covariance matrix fits a multivariate normal distribution to the region

a. specimen image

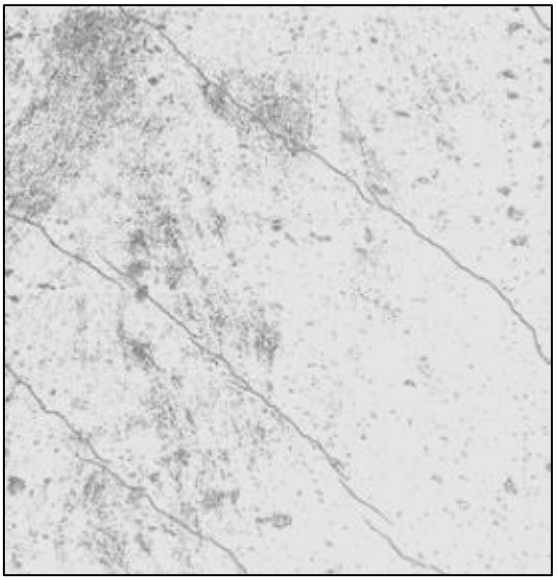

b. Roberts

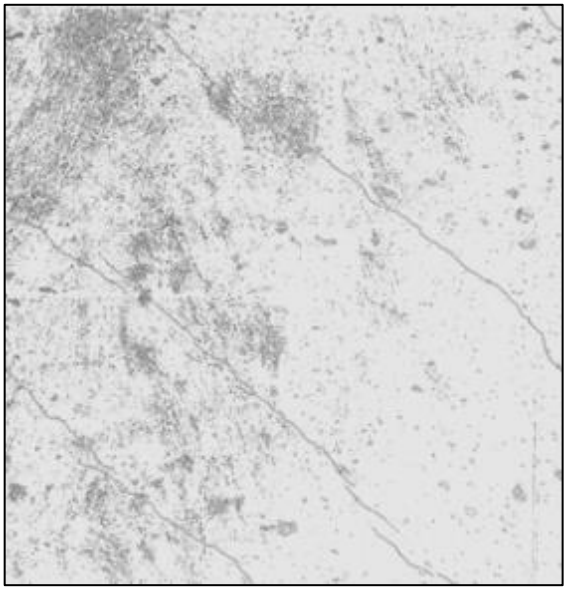

c. Sobel

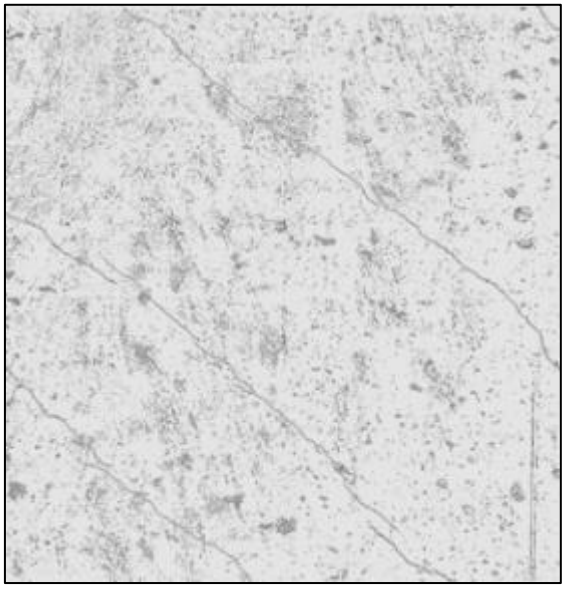

c. Prewitt

Figure 3-12. Edge detection algorithms applied to SW8, LS6

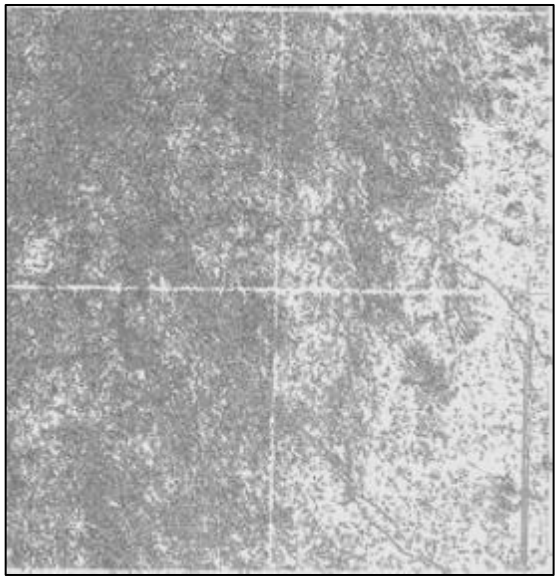

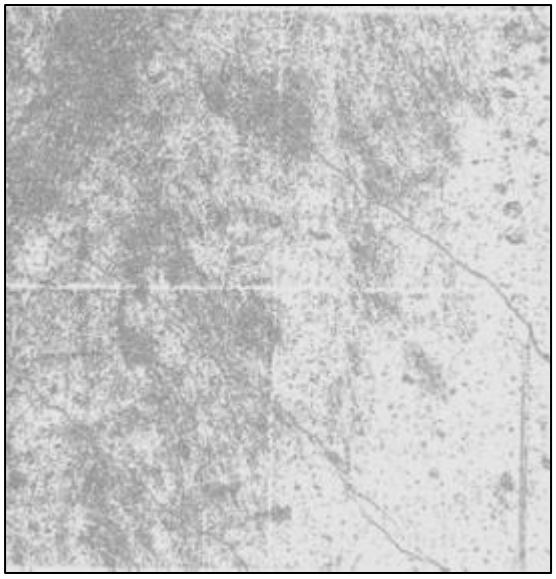

d. Canny e. Laplacian of Gaussian

Figure 3-12. Edge detection algorithms applied to SW8, LS6 (cont.)

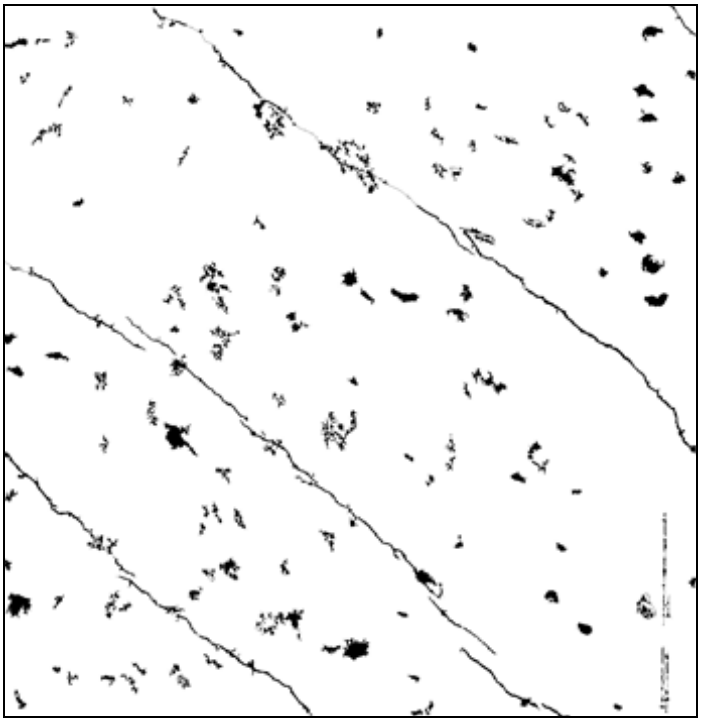

Figure 3-13. Cracks and surface defects filled after applying morphological operations

and takes the shape of an ellipse. The eigenvalues of the covariance matrix are the lengths of the major and minor axes of the ellipse. Figure 3-14b shows the ellipse; lines a and b are the major and minor axes of the ellipse, respectively. The orientation angle is defined as the angle between the horizontal and line a.

The second script, CrackLabel, used to segment the panorama, is based on the ratio of the major axis length to the minor axis length. This ratio is selected as a criterion for image segmentation based on observations made during the development of the script. Cracks have a much longer major axis (length) than minor axis (width), resulting in a ratio much greater than one. Surface defects will have a ratio much closer to one because many are circular or ellipsoidal in shape.

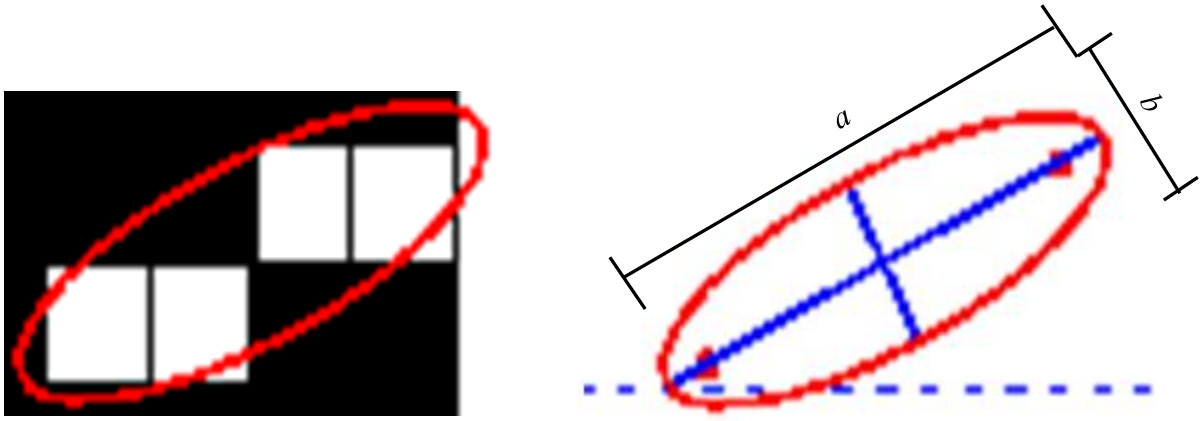

a. generic image b. major and minor axes lengths labeled

Figure 3-14. Parameter extraction

3.4.7 Crack width measurement

The width of each crack is determined after the panorama is segmented (Figure 3-15), but crack widths are not measured directly in I-Crack. Rather, the MATLAB sub-routine regionprops is used to measure area by counting the number of pixels within a crack or surface defect. Since

only the area can be measured using regionprops, two area measurements are required; 1) the area of the crack, and 2) the area of the crack after it has been altered to have a unit width (i.e., length).

The area of a crack is calculated by calling regionprops and measuring area. The area of each crack is then stored in an array for subsequent use. The entire panorama is then altered using the morphological operator skel, which "…removes pixels on the boundaries of objects but does not allow objects to break apart." The product is a panorama of cracks that have unit width and are located on the centerline of the detected areas. Regionprops is then called to measure the length of the centerline of the areas detected in the altered panorama. The width of a crack is determined by

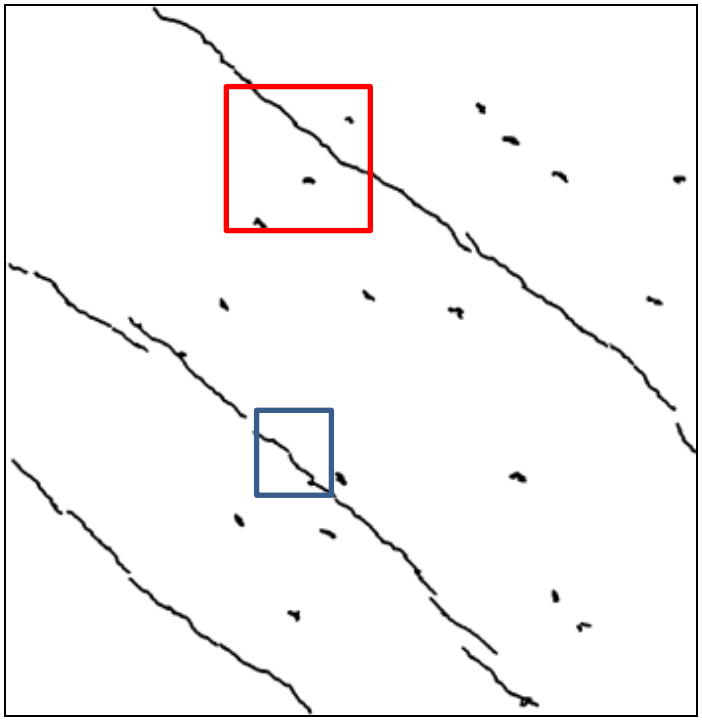

Figure 3-15. Cracks after image segmentation, SW8, LS6

dividing its area by its centerline length, and so is an averaged value over the centerline length. Each crack is assigned a label to allow the user to extract width and area. As an example, Figure 3-16 identifies the cracks in the open red box of Figure 3-15 that are detected and labelled by I-Crack. The red box has a side dimension of three inches.

Cracks are then color coded based on their width to enable further processing. The color coding scheme could be based on the method of repair associated with the width of crack. Blemishes (e.g., numbers 9, 10, 17 and 27 in Figure 3-16) would not be included by the user in the calculation of crack lengths. All of the cracks in Figure 3-17 are in one color (purple) because two ranges were chosen for post-processing crack width, w, $0.02 \le w \le 0.125$ inch and $w > 0.125$ inch, but no crack had a width greater than 0.125 inch.

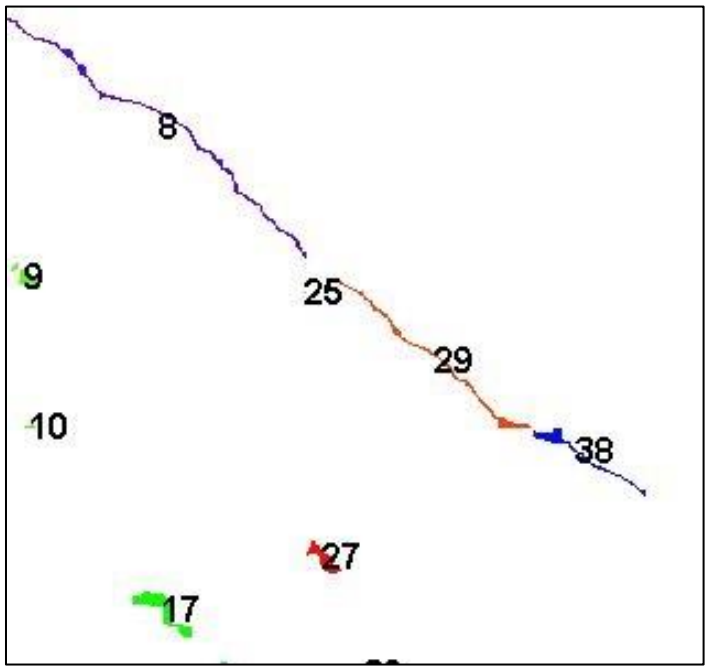

Figure 3-16. Crack width labels of boxed region in Figure 3-15, SW8, LS6

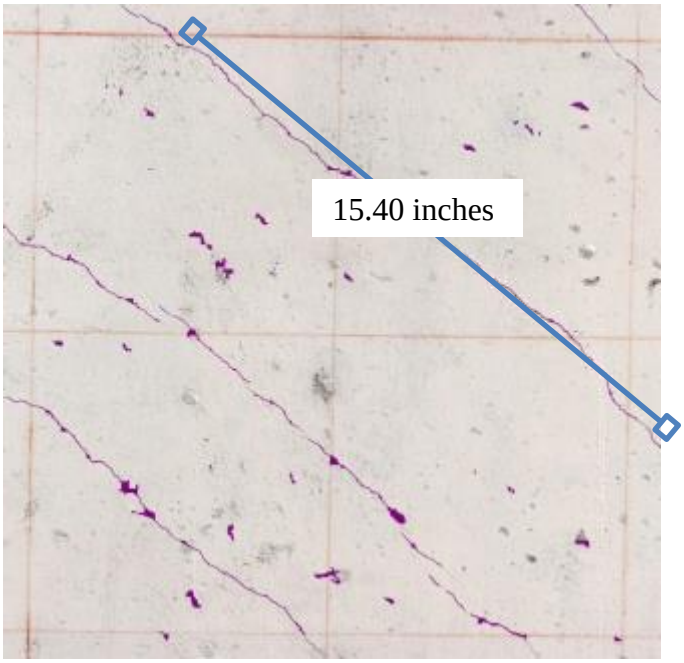

Figure 3-17. Measuring crack length and color coding cracks, SW8, LS6

3.4.8 Crack length measurement

Crack lengths are measured in I-Crack using the imdistline tool in the MATLAB Image Processing Toolbox, which provides the user with a "…draggable, resizable line," that is superimposed on an image to measure the distance between two endpoints. Figure 3-17 shows a line generated with imdisline superimposed on the wall surface. The endpoints (open blue boxes in Figure 3-17) are selected by the user and could correspond to a) initiation of a crack, or b) a crack of a given width (e.g., 0.02 inch) or greater.

The imdistline tool provides the user with a manual method of measuring crack lengths instead of an automatic procedure. An automated procedure to measure crack lengths in I-Crack would a) provide the user with only a total length of crack across the entire surface of the wall (instead of individual crack lengths), and b) rely on the morphological operator skel. The total

length of a crack in a panorama is predicted by calling regionprops to measure the detected area after skel has been applied to the panorama.

The result of applying skel to the open blue box in Figure 3-15 is shown in Figure 3-18. In Figure 3-18, a main crack and multiple "branches" can be seen (enclosed in the blue boxes of Figure 3-18). For each crack there could be thousands of "branches," each with a finite length. The finite length of each "branch" added to the length of the crack causes an automated procedure to overestimate the total length of crack on the surface of the wall. An automated procedure to measure crack length is therefore not included in I-Crack.

3.5 Validation of I-Crack

I-Crack was evaluated using crack patterns and crack widths collected manually from the tests of SW1, SW2, SW3, SW5, SW6 SW7, SW9 and SW12. Wall SW2 was first used to evaluate

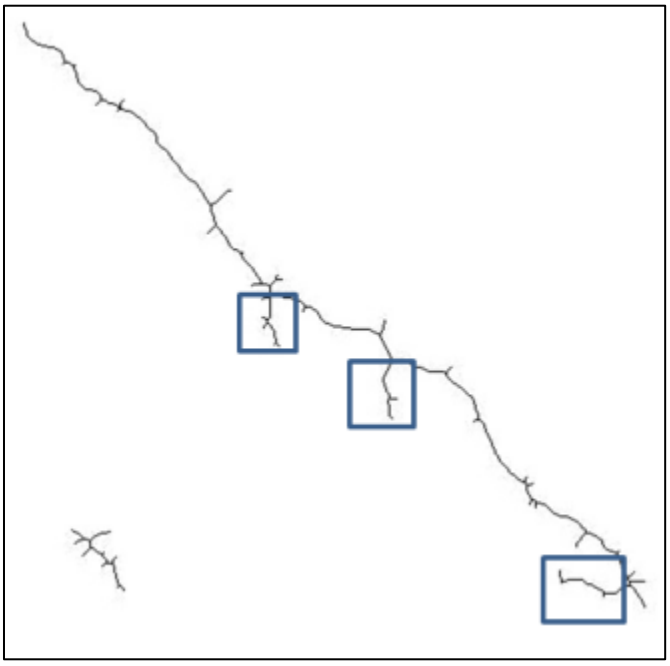

Figure 3-18. Close-up view of the blue box in Figure 3-15 after the skel operator

I-Crack because it had the same geometry and a similar cracking pattern as SW8. Figure 3-19 shows SW2, LS10 after pre-processing and Figure 3-20 shows the cracks detected by I-Crack. A composite of Figure 3-19 and Figure 3-20 is shown in Figure 3-21. A close-up of the area enclosed in the open red and blue boxes can be seen in Figure 3-22, which shows I-Cracks can detect cracks accurately.

Crack widths predicted by I-Crack are compared to data collected manually at the locations denoted by the letters in Figure 3-23 and Figure 3-24 for SW2 at peak displacements for LS10 and LS11, respectively. A comparison of I-Crack predictions and manual measurements is presented in Table 3-1. The peak displacement in LS10 was 0.82 inch (story drift angle of 1.26%) and is the displacement associated with peak shearing strength. The peak displacement in LS11 was 1.45 inch (story drift angle of 2.23%) and greater than the displacement associated with peak shearing strength. The manually measured and I-Crack results are comparable at both displacements, noting that the variability in manually measuring and locating cracks is unknown and the intervals of the crack gage are not uniform and range from 0.005 inch to 0.0625 inch (see Figure 3-1). For LS10 the greatest difference in crack width is 0.047 inch at Crack J, which is less than the interval for widths greater than 0.0625 inch. For LS11 the greatest difference in crack width is 0.043 inch, which also occurs on Crack J.

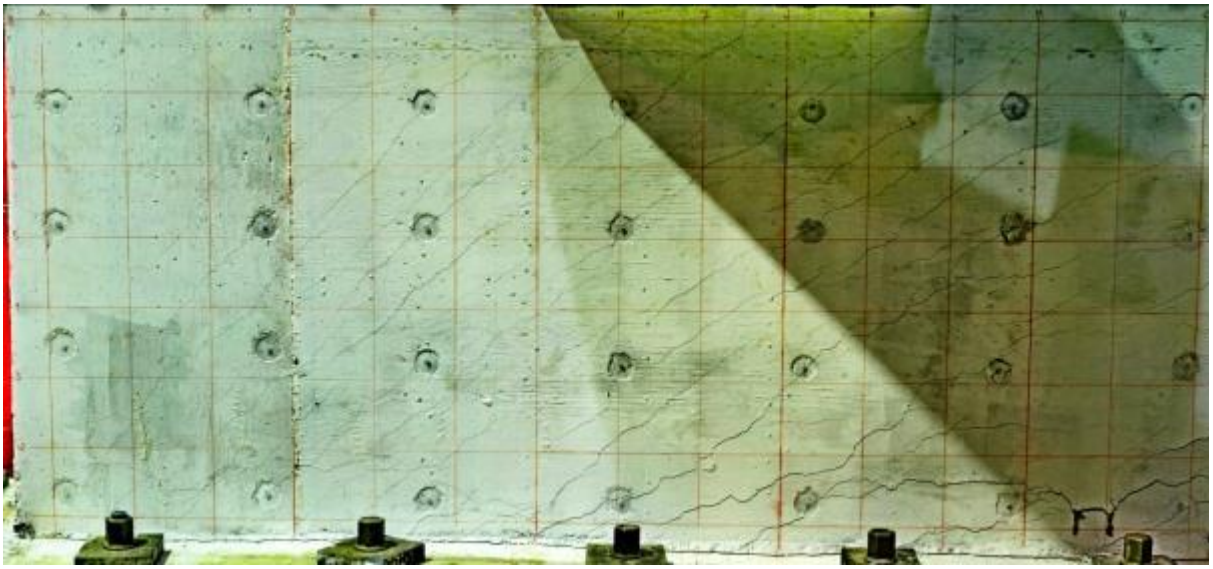

Figure 3-19. Pre-processed image of SW2, LS10

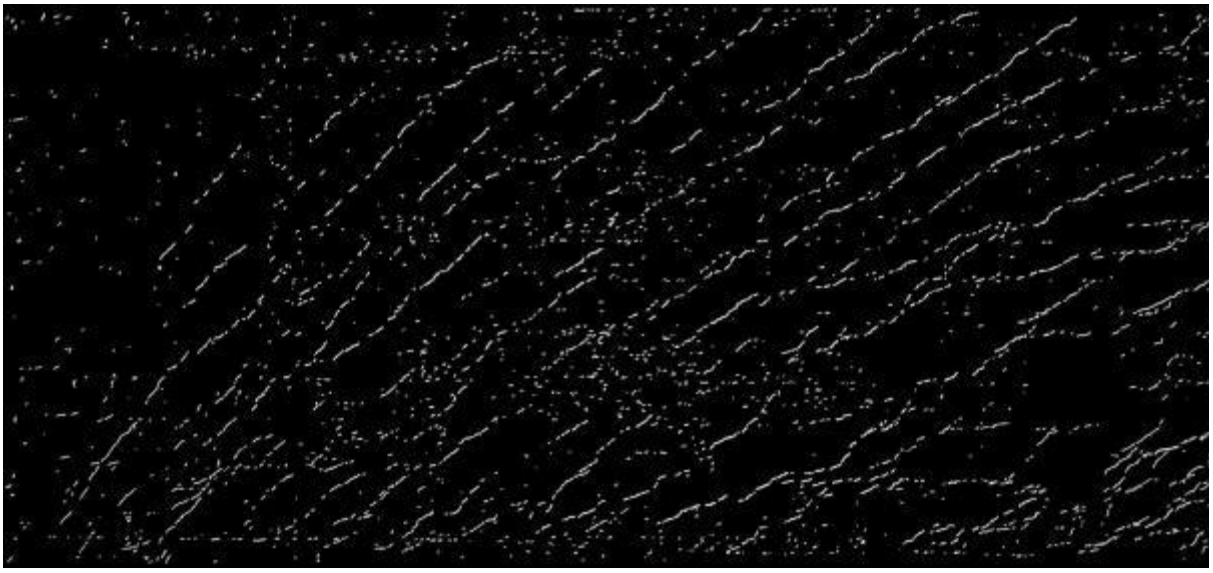

Figure 3-20. Predicted crack locations for SW2, LS10

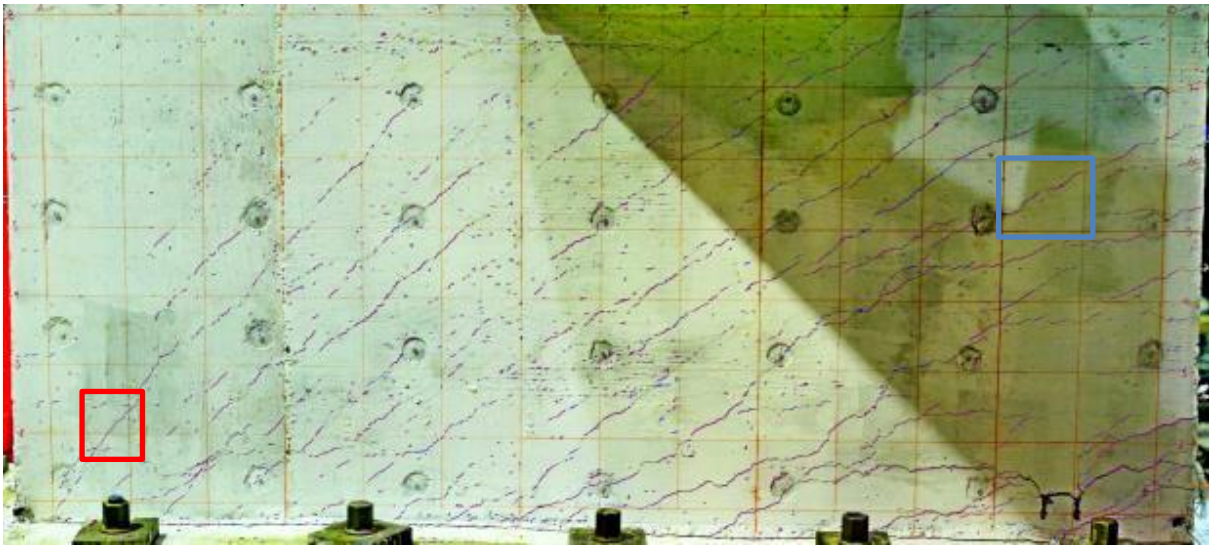

Figure 3-21. Composite image of SW2, LS10

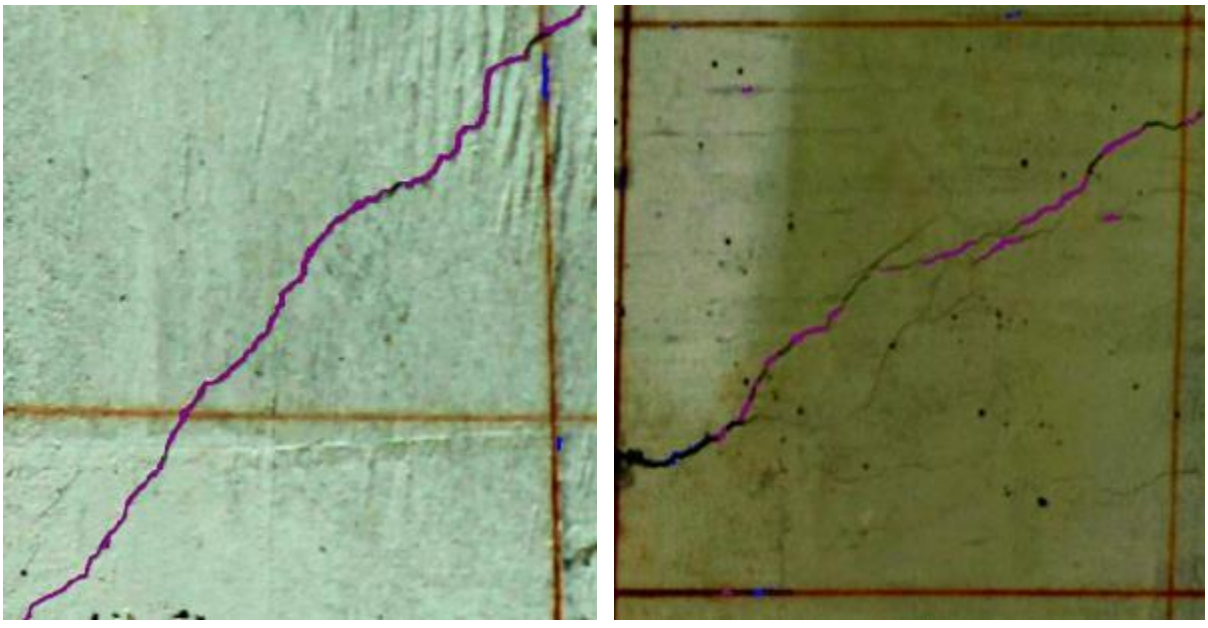

a. red box b. blue box

Figure 3-22. Close up of the boxed areas in Figure 3-21, SW2, LS10

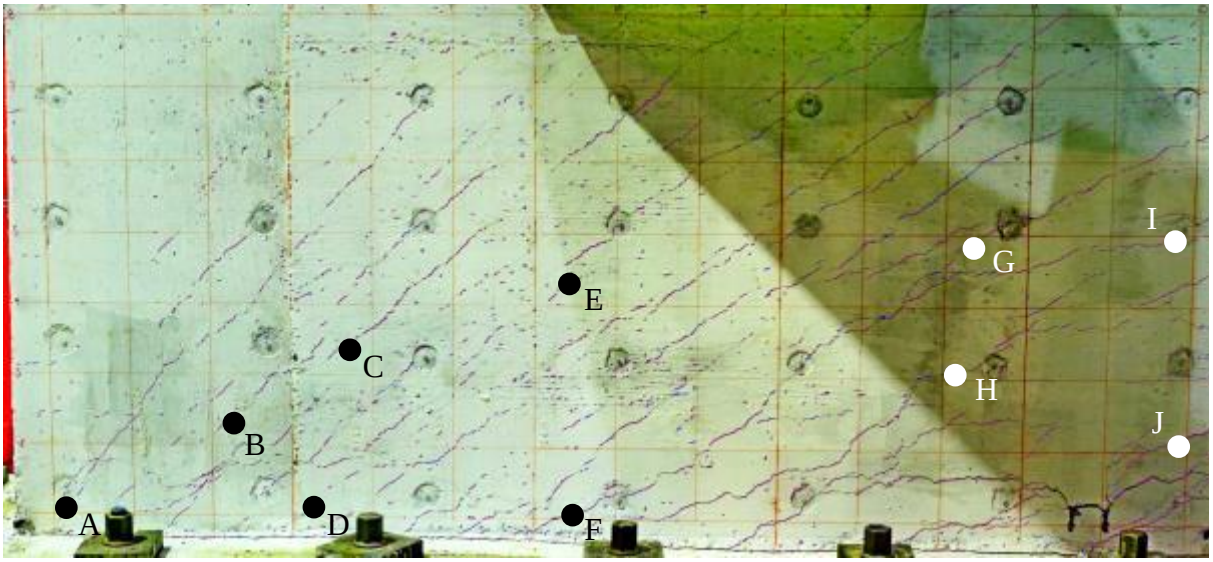

Figure 3-23. Composite image of SW2, LS10

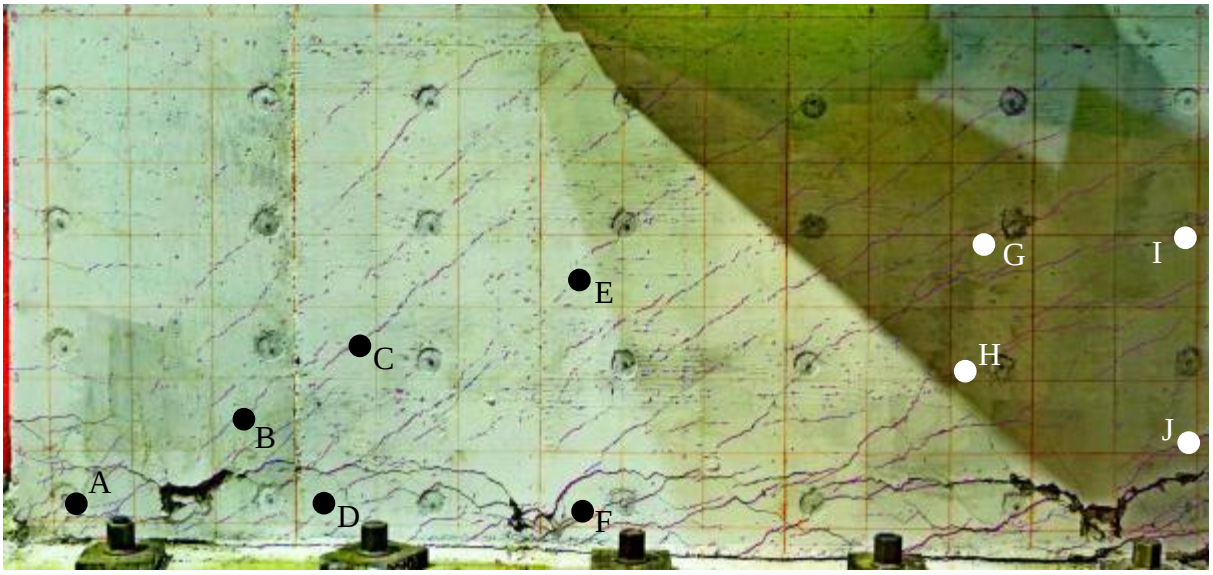

Figure 3-24. Composite image of SW2, LS11

Table 3-1. Crack width data for SW2

	Measurement (inch)			
	LS10		LS11	
Crack ID	Manual	I-Crack	Manual	I-Crack
A	0.020	0.027	0.040	0.040
B	0.016	0.024	0.016	0.017
C	0.016	0.033	0.020	0.024
D	0.025	0.031	0.025	0.029
E	0.020	0.038	0.020	0.030
F	0.050	0.039	0.050	0.051
G	0.016	0.019	0.016	0.027
H	0.020	0.023	0.020	0.032
I	0.020	0.033	0.020	0.026
J	0.125	0.078	0.125	0.082

Figure 3-25 and Figure 3-26 show the locations, denoted by letters, where data were collected manually and compared to predictions by I-Crack for SW1 at load steps LS9 and LS10. Table 3-2 enables a comparison of crack widths for SW1. The peak displacement for LS9 was 1.46 inches (story drift angle of 1.3%) and corresponds to peak shearing strength. The peak displacement of LS10 was 2.38 inches (story drift angle of 2.1%) and corresponds to a displacement greater than peak shearing strength. For LS9, the greatest difference in crack width is 0.029 inch on Crack G. For LS10, the greatest different in crack width is 0.054 inch on Crack D, which is less than the interval on the crack gage for widths greater than 0.0625 inch. For Cracks E, F, G, H and I, the manual and I-Crack measurements detected a decrease in crack width from LS9 to LS10. The reduction in crack width could be attributed to the change of the load-resisting mechanism after peak shear strength was attained.

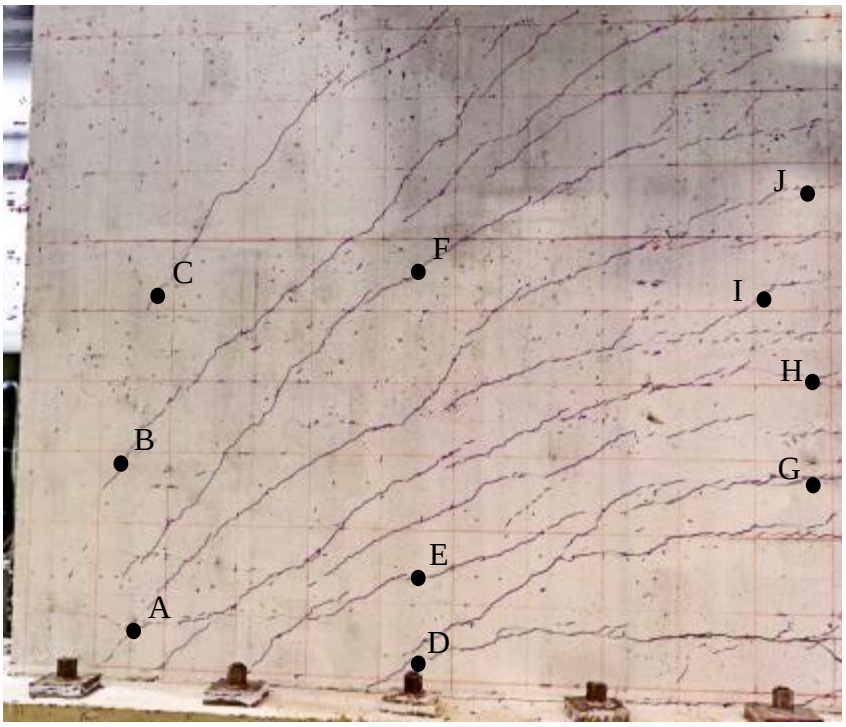

Figure 3-25. Composite image of SW1, LS9

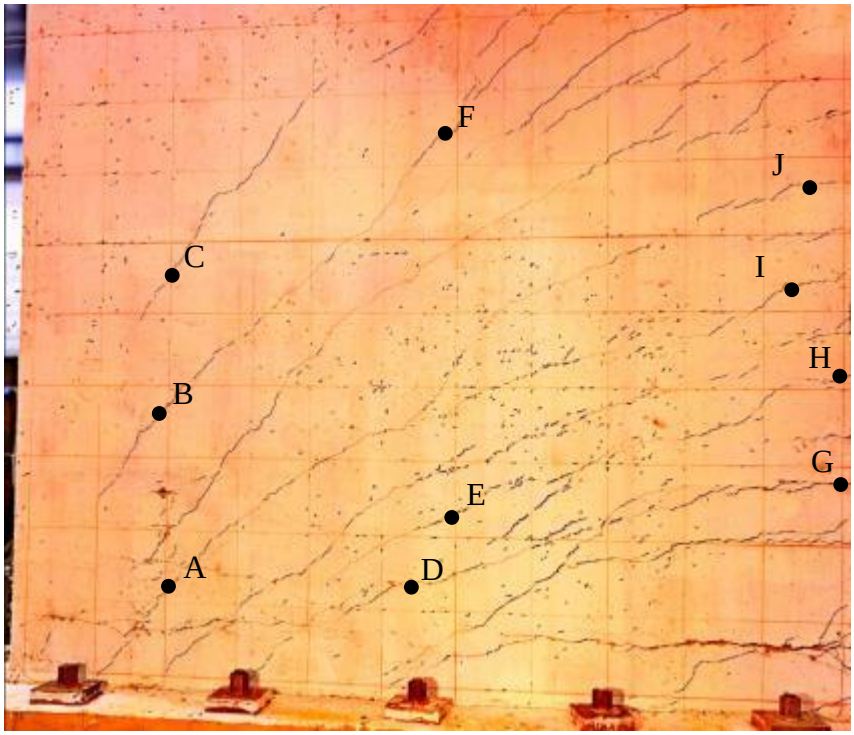

Figure 3-26. Composite image of SW1, LS10

Table 3-2. Crack width data for SW1

	Measurement (inch)			
	LS9		LS10	
Crack ID	Manual	I-Crack	Manual	I-Crack
A	0.016	0.031	0.060	0.039
B	0.016	0.033	0.016	0.040
C	0.005	0.032	0.005	0.031
D	0.050	0.054	0.060	0.114
E	0.060	0.065	0.040	0.031
F	0.040	0.062	0.020	0.037
G	0.125	0.096	0.125	0.074
H	0.025	0.036	0.025	0.036
I	0.025	0.032	0.020	0.047
J	0.013	0.018	0.013	0.046

Figure 3-27, Figure 3-28 and Figure 3-29 show SW3 at displacements corresponding to approximately half peak shear strength (LS7), peak shear strength (LS12) and beyond peak shear strength (LS13), respectively. The peak displacements for LS7, LS12 and LS13 were 0.15 inch (story drift ratio of 0.23%), 1.36 inches (story drift ratio of 2.1%) and 1.9 inches (story drift ratio of 2.9%), respectively. Table 3-3 shows the predicted and manually measured crack widths for SW3. The greatest difference in crack width for SW3 is 0.033 inch on Crack B for LS12.

Figure 3-30 and Figure 3-31 show SW5 at peak displacements in load steps LS5 and LS8, respectively. Load step LS5 had a peak displacement of 0.12 inch (story drift angle of 0.3%) and corresponds to approximately half of the peak shear strength. Load step LS8 had a peak displacement of 0.51 inch (story drift angle of 1.3%) and corresponds to a displacement beyond peak shear strength. Table 3-4 presents the predicted and manual measurements of crack widths for SW5. The greatest difference in crack width is 0.023 inches on Crack E for LS8.

The locations for crack widths at peak displacements on SW6 are denoted by letters in Figure 3-32 (LS8) and Figure 3-33 (LS10). The peak displacement for LS8 was 0.32 inch (story

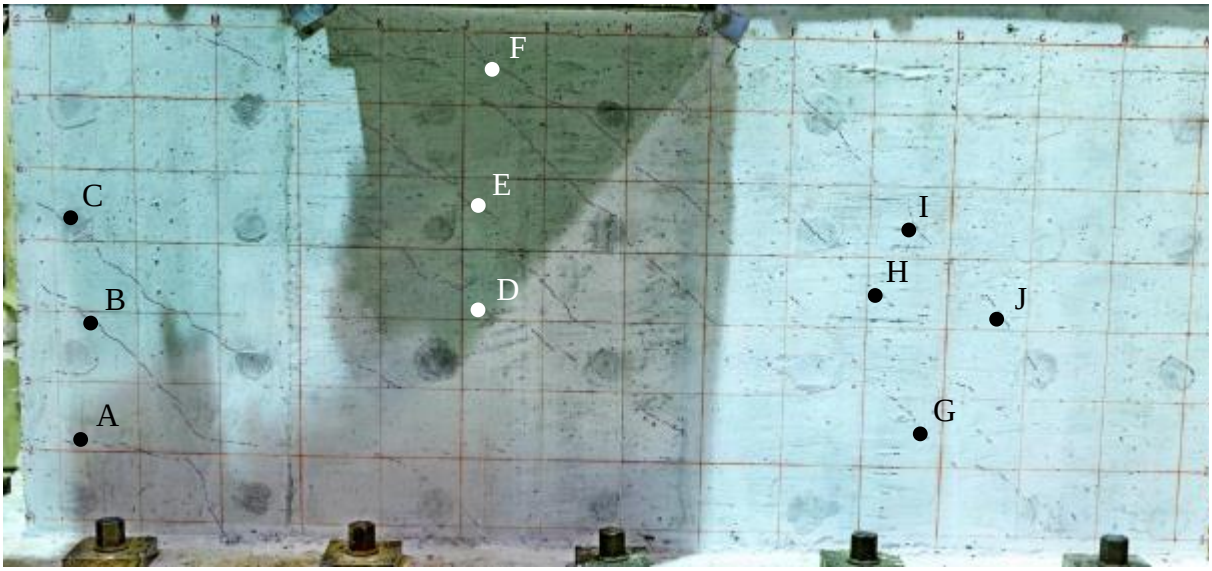

Figure 3-27. Composite image of SW3, LS7

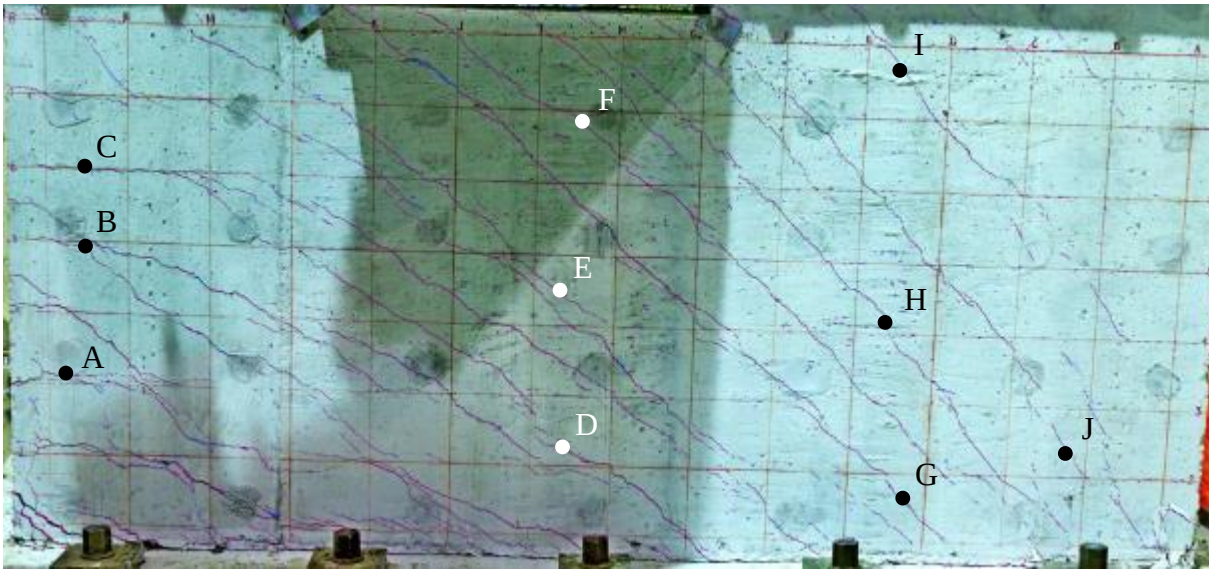

Figure 3-28. Composite image of SW3, LS12

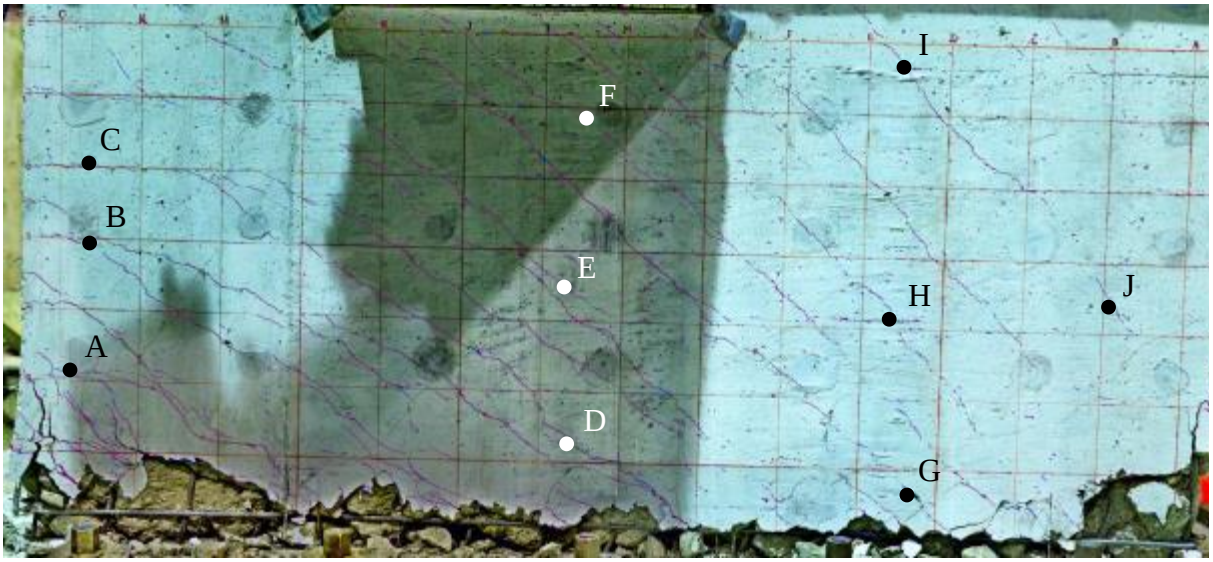

Figure 3-29. Composite image of SW3, LS13

Table 3-3. Crack width data for SW3

	Measurement (inch)					
	LS7		LS12		LS13	
Crack ID	Manual	I-Crack	Manual	I-Crack	Manual	I-Crack
A	0.009	0.019	0.060	0.037	0.040	0.025
B	0.013	0.020	0.060	0.027	0.050	0.027
C	0.013	0.020	0.035	0.037	0.050	0.032
D	0.010	0.028	0.060	0.050	0.035	0.035
E	0.010	0.024	0.030	0.038	0.040	0.043
F	0.009	0.029	0.025	0.039	0.040	0.031
G	0.009	0.021	0.035	0.035	0.030	0.016
H	0.010	0.028	0.035	0.035	0.035	0.034
I	0.010	0.023	0.035	0.030	0.035	0.029
J	0.005	0.022	0.030	0.022	0.016	0.024

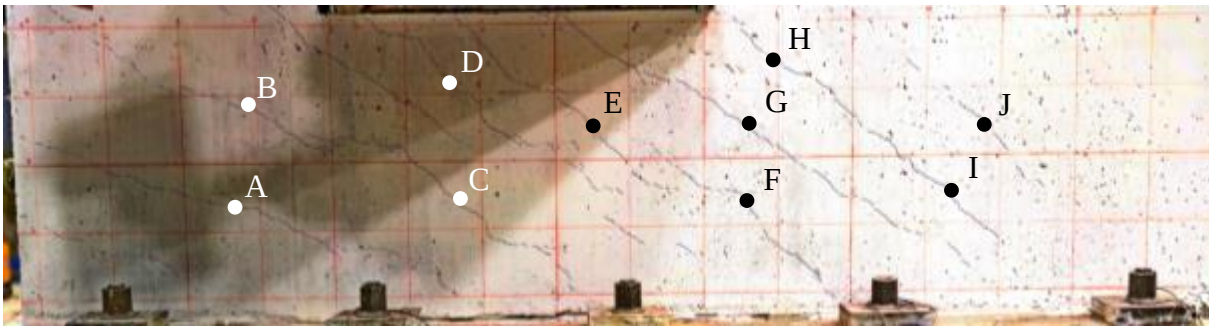

Figure 3-30. Composite image of SW5, LS5

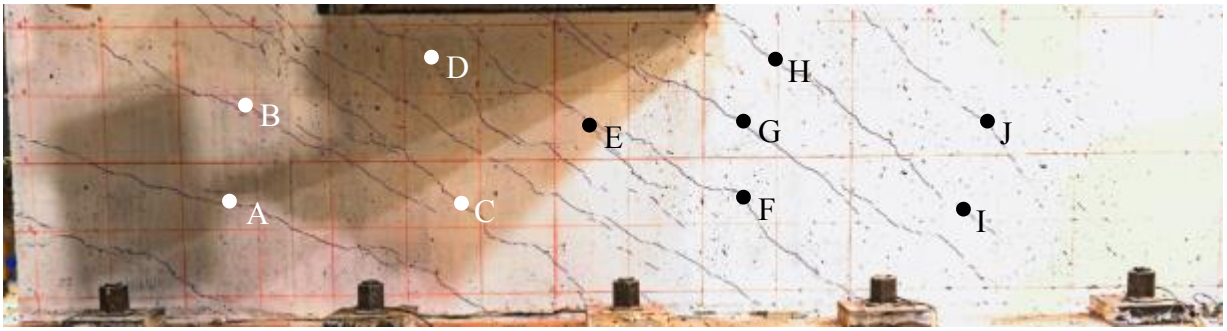

Figure 3-31. Composite image of SW5, LS8

Table 3-4. Crack width data for SW5

	Measurement (inch)			
	LS5		LS8	
Crack ID	Manual	I-Crack	Manual	I-Crack
A	0.013	0.019	0.050	0.034
B	0.010	0.025	0.040	0.029
C	0.013	0.024	0.016	0.026
D	0.010	0.023	0.040	0.030
E	0.010	0.023	0.050	0.027
F	0.013	0.019	0.050	0.032
G	0.013	0.021	0.030	0.028
H	0.010	0.019	0.020	0.032
I	0.010	0.022	0.030	0.026
J	0.013	0.021	0.020	0.026

drift angle of 0.8%) and is associated with peak shear strength. The peak displacement for LS10 was 0.67 inch (story drift angle of 1.7%) and is a displacement beyond that associated with peak shear strength. The manual and predicted crack widths for SW6 are shown in Table 3-5. The greatest difference between manual and I-Crack measurements is 0.026 inches on Crack I during LS10.

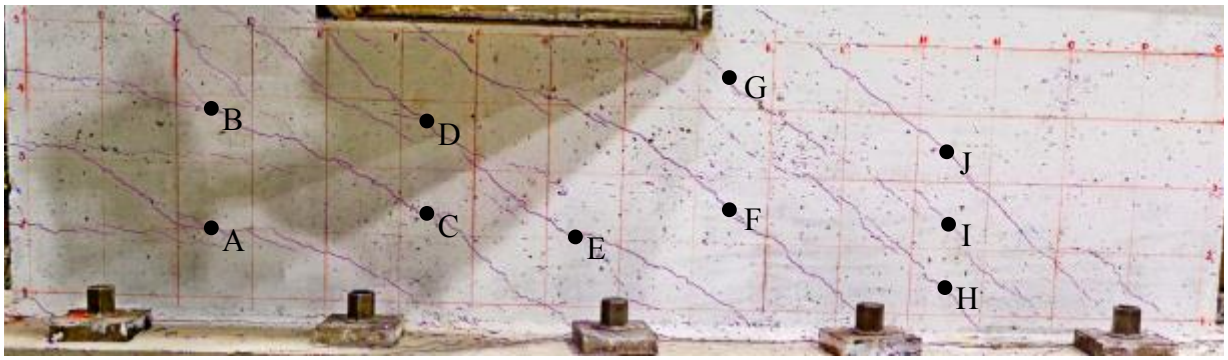

Figure 3-32. Composite image of SW6, LS8

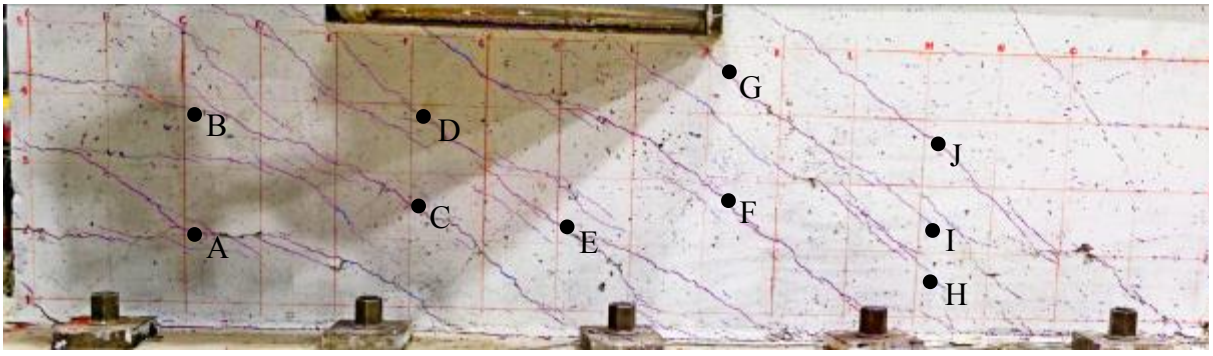

Figure 3-33. Composite image of SW6, LS10

Table 3-5. Crack width data for SW6

	Measurement (inch)			
	LS8		LS10	
Crack ID	Manual	I-Crack	Manual	I-Crack
A	0.060	0.038	0.125	0.138
B	0.035	0.033	0.050	0.048
C	0.050	0.039	0.125	0.109
D	0.063	0.040	0.060	0.045
E	0.035	0.030	0.060	0.044
F	0.060	0.039	0.063	0.045
G	0.030	0.031	0.035	0.034
H	0.035	0.026	0.025	0.028
I	0.035	0.022	0.050	0.024
J	0.020	0.022	0.035	0.034

The letters on Figure 3-34 (LS3), Figure 3-35 (LS7), and Figure 3-36 (LS10) identify the locations used to compare crack widths for SW7. Load step LS3 had a peak displacement of 0.05 inch (story drift ratio of 0.1%) and corresponded to approximately half of the peak shear strength. The peak displacement for LS7 was 0.18 inch (story drift ratio of 0.5%) and is associated with peak shear strength. Load step LS10 had a peak displacement approximately twice the displacement associated with peak shear strength: 0.34 inch (story drift angle 0.9%). Table 3-6 presents the manual and predicted crack widths for SW7. The greatest difference between the manual and I-Crack measurements is 0.025 inch on Crack D in LS7.

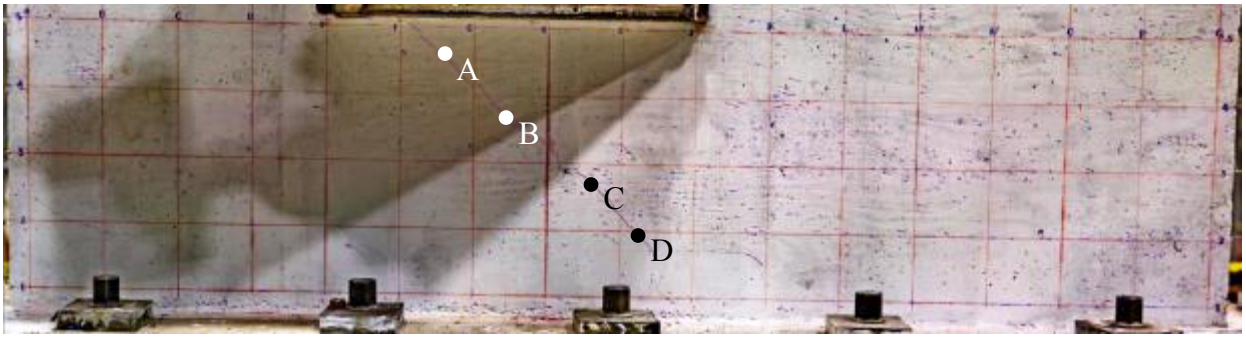

Figure 3-34. Composite image of SW7, LS3

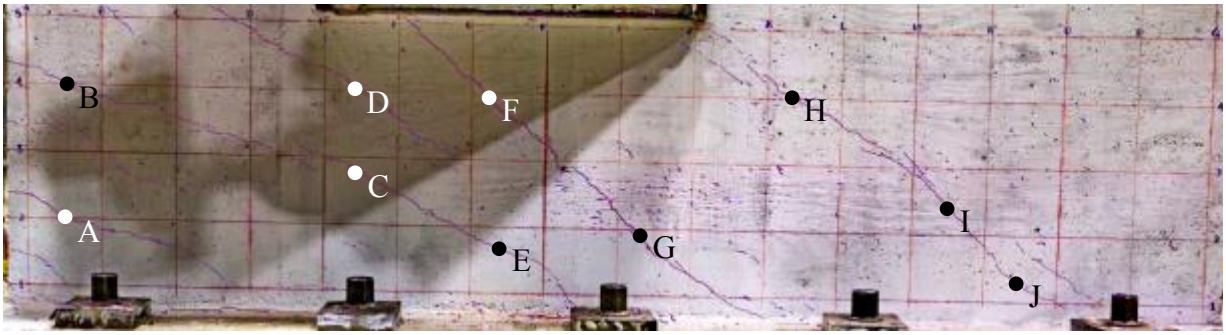

Figure 3-35. Composite image of SW7, LS7

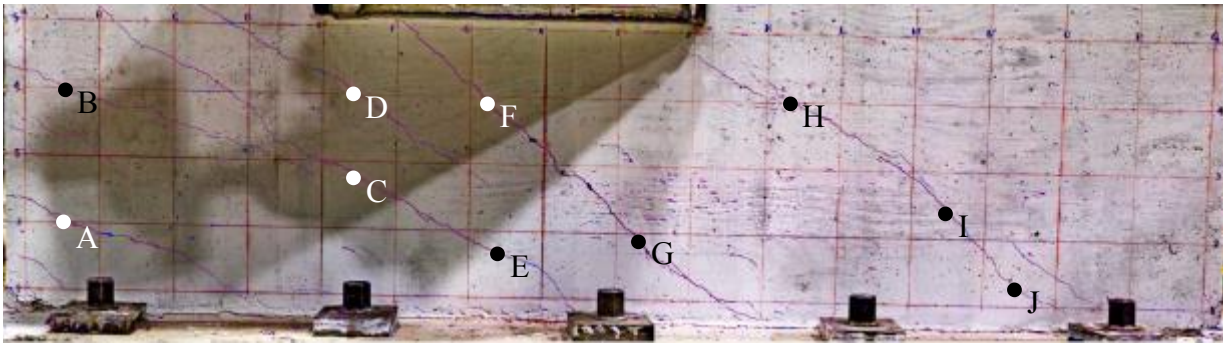

Figure 3-36. Composite image of SW7, LS10

Table 3-6. Crack width data for SW7

	Measurement (inch)					
	LS3		LS7		LS10	
Crack ID	Manual	I-Crack	Manual	I-Crack	Manual	I-Crack
A	0.025	0.035	0.050	0.046	0.050	0.047
B	0.025	0.030	0.020	0.027	0.010	0.035
C	0.020	0.028	0.030	0.043	0.050	0.043
D	0.020	0.024	0.016	0.041	0.025	0.036
E	-	-	0.040	0.033	0.030	0.033
F	-	-	0.035	0.043	0.063	0.049
G	-	-	0.063	0.045	0.063	0.045
H	-	-	0.016	0.038	0.025	0.033
I	-	-	0.040	0.043	0.040	0.044
J	-	-	0.025	0.031	0.020	0.027

Figure 3-37, Figure 3-38 and Figure 3-39 show SW9 at peak displacements in load steps LS3, LS7 and LS8, respectively. The peak displacement for LS3 was 0.14 inch (story drift angle of 0.2%) and was associated with approximately half of the peak shear strength. Load step LS7 had a peak displacement of 0.50 inch (story drift angle of 0.8%) and is the displacement at peak shear strength. Load step LS8 had a peak displacement of 0.80 inch (story drift angle of 1.2%), which was greater than the displacement associated with peak shear strength. Measured and predicted crack widths for SW9 are shown in Table 3-7 are comparable except for Crack E during LS8. Given the consistency of the manual measurements and the I-Crack calculations at other locations, there is much higher confidence in the crack width (=0.043 inch) predicted by I-Crack.

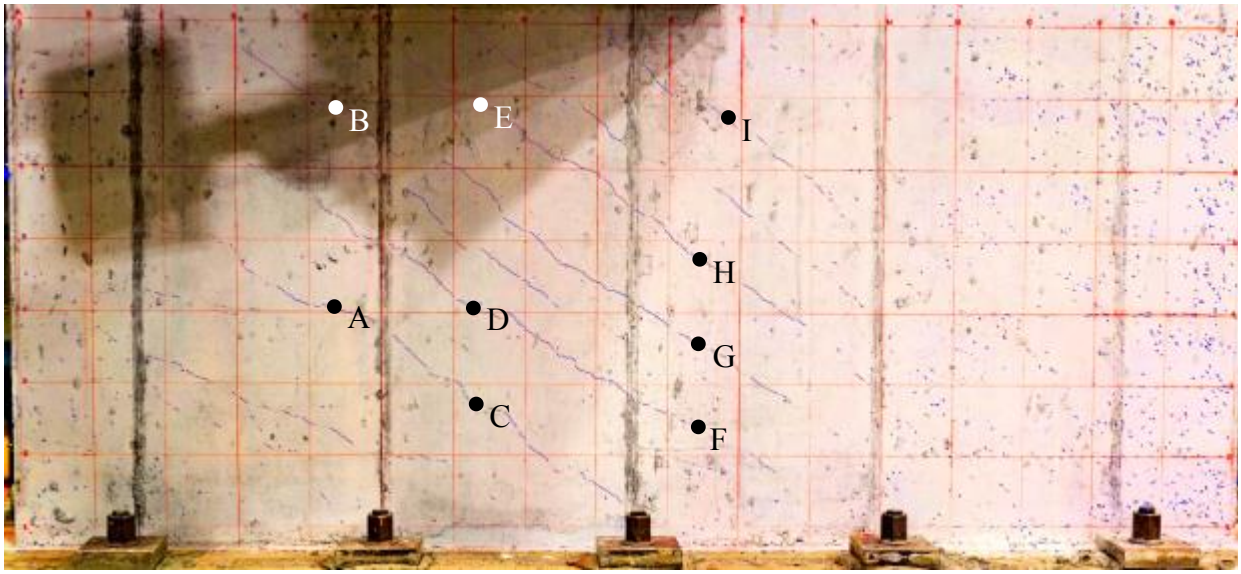

Figure 3-37. Composite image of SW9, LS3

Figure 3-40, Figure 3-41 and Figure 3-42 show SW12 at peak displacement in load steps LS3, LS8 and LS9, respectively. Load step LS3 had a peak displacement of 0.15 inch (story drift ratio of 0.2%) and is associated with approximately three-quarters of peak shear strength. Load

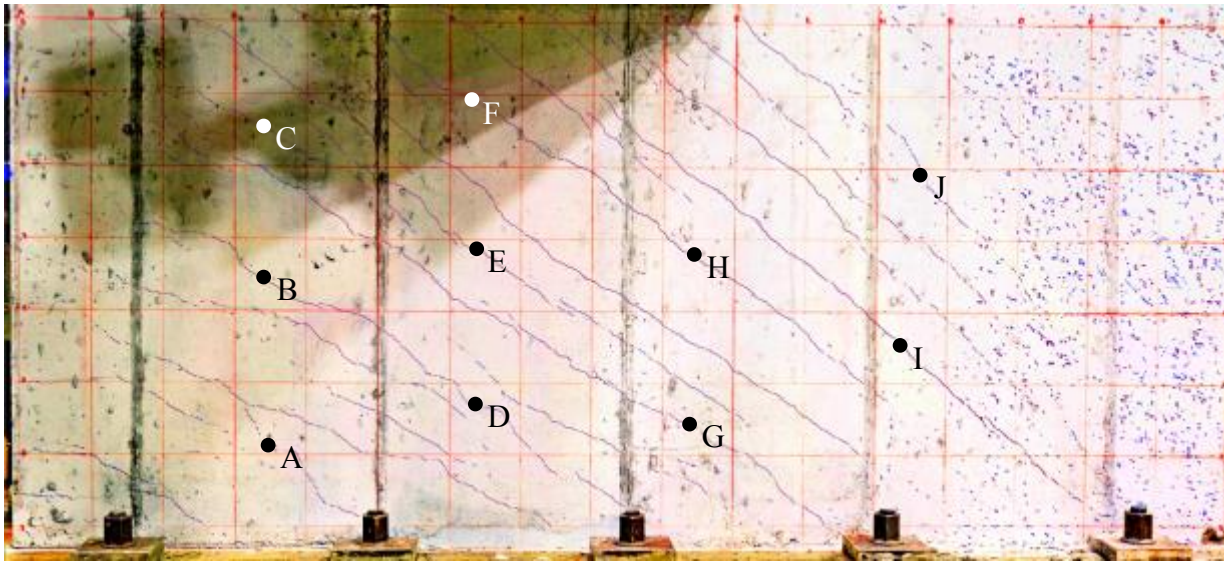

Figure 3-38. Composite image of SW9, LS7

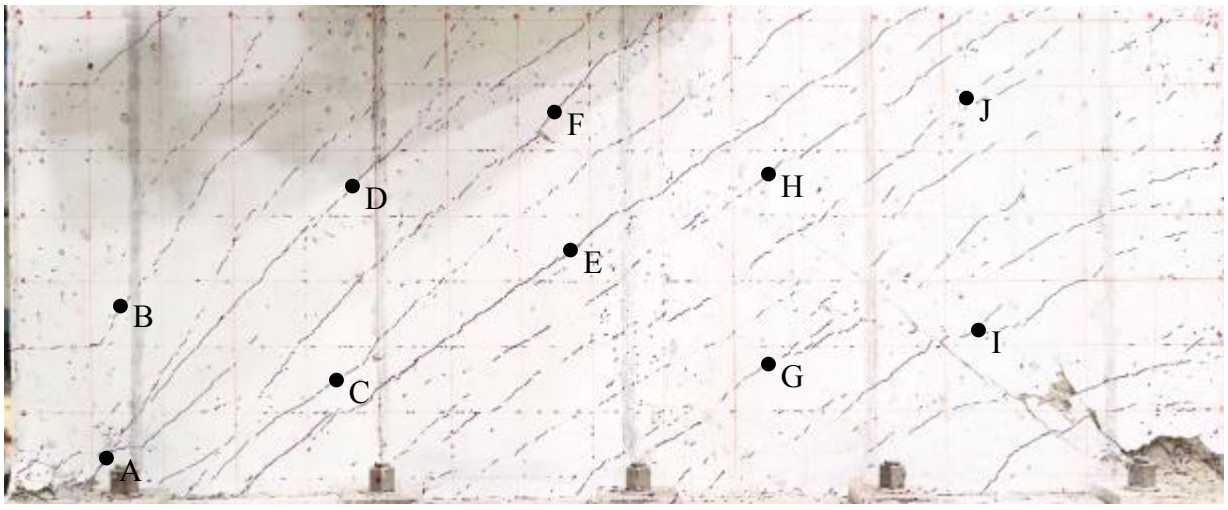

Figure 3-39. Composite image of SW9, LS8

Table 3-7. Crack width data for SW9

	Measurement (inch)					
	LS3		LS7		LS8	
Crack ID	Manual	I-Crack	Manual	I-Crack	Manual	I-Crack
A	0.007	0.018	0.013	0.029	0.050	0.043
B	0.009	0.026	0.020	0.026	0.013	0.019
C	0.007	0.020	0.030	0.028	0.040	0.030
D	0.007	0.018	0.007	0.019	0.030	0.032
E	0.010	0.023	0.016	0.028	0.125	0.043
F	0.009	0.018	0.030	0.029	0.040	0.037
G	0.010	0.018	0.025	0.025	0.025	0.024
H	0.010	0.020	0.030	0.033	0.040	0.037
I	0.007	0.018	0.060	0.040	0.030	0.027
J	-	-	0.020	0.032	0.016	0.024

step LS8 had a peak displacement of 0.58 inch (story drift ratio of 0.9%) and is associated with peak shear strength. The peak displacement for LS9 was 1.07 inch (story drift ratio of 1.6%) and is greater than the displacement associated with peak shear strength. Table 3-8 shows the crack widths measured manually and predicted by I-Crack for SW12. The greatest difference in crack width occurred at Crack A for LS9 and LS10 and is 0.065 inch, which is equivalent to the interval on the crack gage for widths greater than 0.0625 inch. The difference between manual and predicted measurements is due to the width of Crack A varying greatly along its length. For all other measurements the largest difference is 0.029 inch.

3.6 Length and areal density of cracks

Damage to reinforced concrete components can be measured in terms of peak crack width (a traditional measure reported by researchers), length of crack with a width greater than a user-specified limit [often tied to a method of repair, see Gulec et al. (2010)], and areal density of cracks (e.g., length of crack with a width greater than a threshold divided by the area of the component being surveyed).

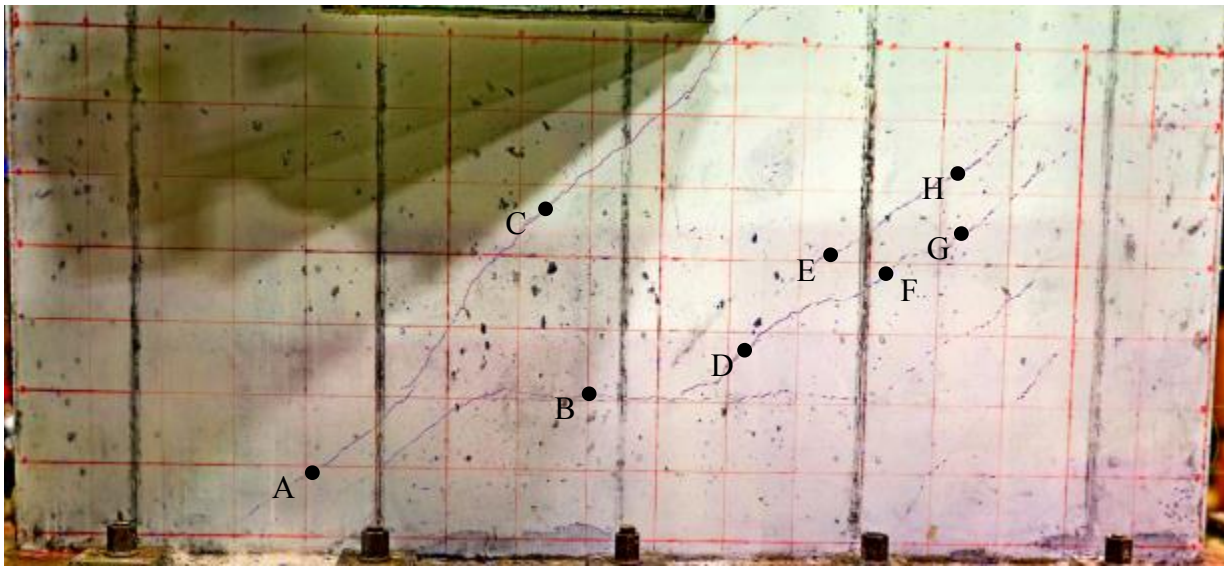

Figure 3-40. Composite image of SW12, LS3

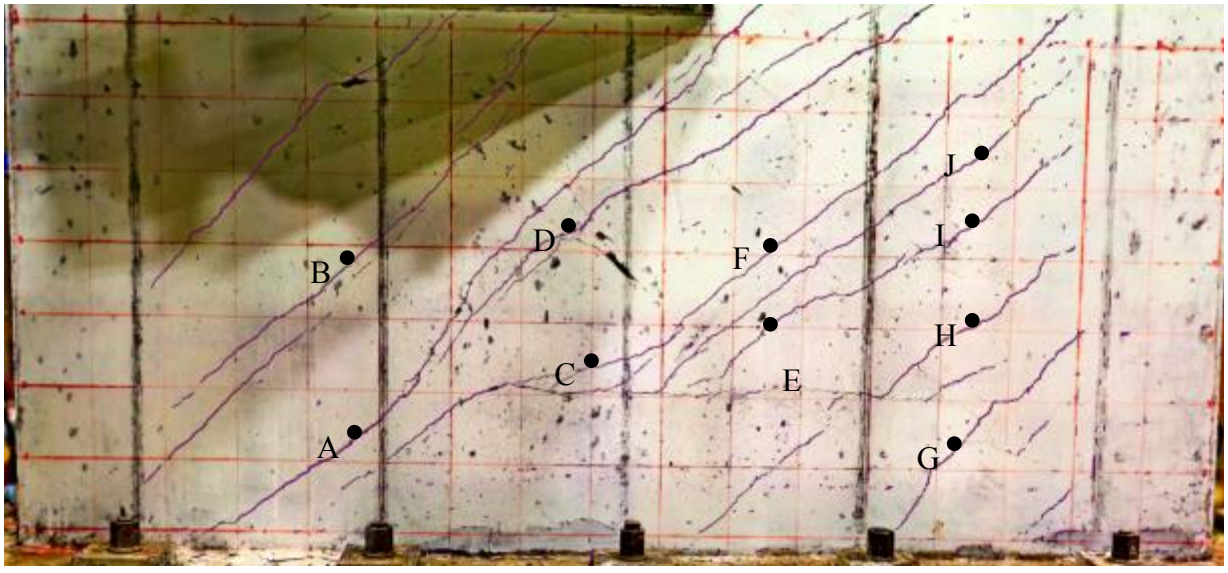

Figure 3-41. Composite image of SW12, LS8

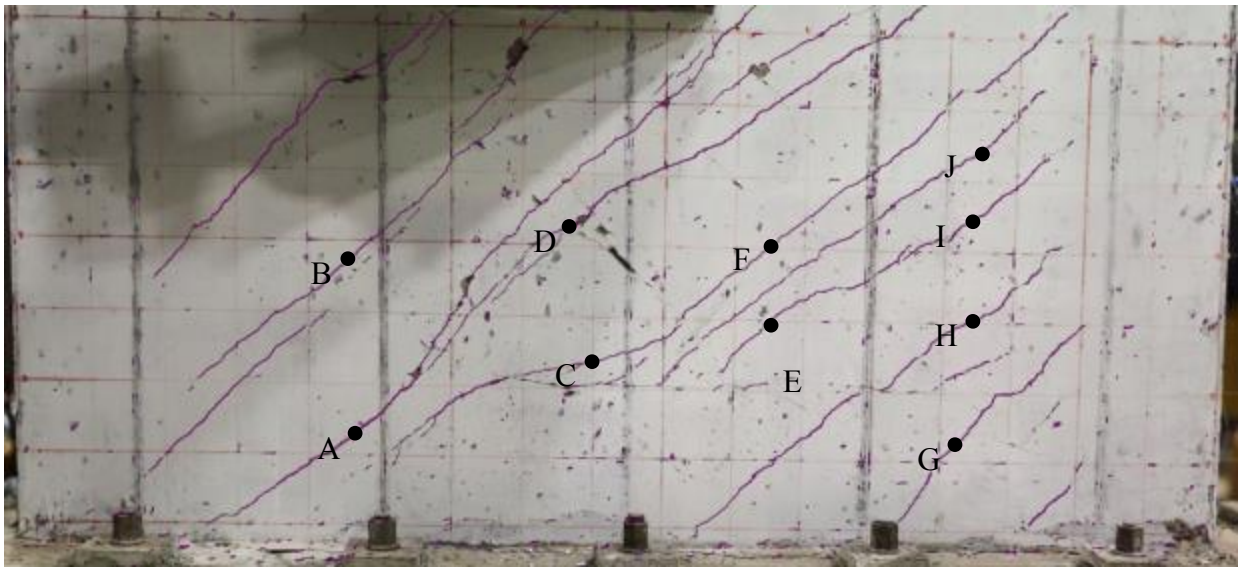

Figure 3-42. Composite image of SW12, LS9

Table 3-8. Crack width data for SW12

	Measurement (inch)					
	LS3		LS8		LS9	
Crack ID	Manual	I-Crack	Manual	I-Crack	Manual	I-Crack
A	0.016	0.029	0.125	0.060	0.125	0.060
B	0.013	0.026	0.063	0.049	0.063	0.048
C	0.025	0.035	0.040	0.047	0.050	0.044
D	0.020	0.029	0.060	0.058	0.050	0.058
E	0.016	0.029	0.030	0.038	0.040	0.048
F	0.013	0.018	0.035	0.042	0.035	0.045
G	0.013	0.022	0.016	0.046	0.040	0.056
H	0.016	0.023	0.025	0.052	0.030	0.050
I	-	-	0.030	0.054	0.030	0.049
J	-	-	0.025	0.051	0.020	0.049

For this example, the user-specified limits for crack widths are 0.02 inch and 0.125 inch. Results are presented in Table 3-9 for two ranges of peak transient crack width: $0.02 \le w \le 0.125$ inch and $w > 0.125$ inch. These data could be used to characterize damage and estimate repair costs, noting that field calculations will employ residual rather than peak transient data.

Table 3-9. Crack length and areal density data

Wall	Load step	Crack width, w	Crack length (inch)	Areal density (in/ft^2)
SW1	LS9	$0.02 \text{ in} \leq w < 0.125 \text{ in}$	760	8.07
		$w \geq 0.125 \text{ in}$	25.0	0.27
	LS10	$0.02 \text{ in} \leq w < 0.125 \text{ in}$	817	8.68
		$w \geq 0.125 \text{ in}$	34.0	0.36
SW2	LS10	$0.02 \text{ in} \leq w < 0.125 \text{ in}$	1170	21.6
		$w \geq 0.125 \text{ in}$	7.00	0.13
	LS11	$0.02 \text{ in} \leq w < 0.125 \text{ in}$	1464	27.0
		$w \geq 0.125 \text{ in}$	7.00	0.13
SW3	LS7	$0.02 \text{ in} \leq w < 0.125 \text{ in}$	388	7.16
		$w \geq 0.125 \text{ in}$	0.00	0.00
	LS12	$0.02 \text{ in} \leq w < 0.125 \text{ in}$	828	15.3
		$w \geq 0.125 \text{ in}$	14.0	0.26
	LS13	$0.02 \text{ in} \leq w < 0.125 \text{ in}$	710	13.1
		$w \geq 0.125 \text{ in}$	15.0	4.15
SW5	LS5	$0.02 \text{ in} \leq w < 0.125 \text{ in}$	314	9.19
		$w \geq 0.125 \text{ in}$	0.00	0.00
	LS8	$0.02 \text{ in} \leq w < 0.125 \text{ in}$	415	12.1
		$w \geq 0.125 \text{ in}$	0.00	0.00
SW6	LS8	$0.02 \text{ in} \leq w < 0.125 \text{ in}$	400	11.7
		$w \geq 0.125 \text{ in}$	0.00	0.00
	LS10	$0.02 \text{ in} \leq w < 0.125 \text{ in}$	445	13.1
		$w \geq 0.125 \text{ in}$	8.00	0.23
SW7	LS3	$0.02 \text{ in} \leq w < 0.125 \text{ in}$	57.0	1.67
		$w \geq 0.125 \text{ in}$	0.00	0.00
	LS7	$0.02 \text{ in} \leq w < 0.125 \text{ in}$	222	6.50
		$w \geq 0.125 \text{ in}$	0.00	0.00
	LS10	$0.02 \text{ in} \leq w < 0.125 \text{ in}$	222	6.50
		$w \geq 0.125 \text{ in}$	0.00	0.00
SW9	LS3	$0.02 \text{ in} \leq w < 0.125 \text{ in}$	101	1.87
		$w \geq 0.125 \text{ in}$	0.00	0.00
	LS7	$0.02 \text{ in} \leq w < 0.125 \text{ in}$	741	13.7
		$w \geq 0.125 \text{ in}$	0.00	0.00
	LS9	$0.02 \text{ in} \leq w < 0.125 \text{ in}$	811	15.0
		$w \geq 0.125 \text{ in}$	0.00	0.00

Table 3-9. Crack length and areal density data (cont.)

SW12	LS3	0.02 in $\leq w <$ 0.125 in	224	4.14
		$w \geq$ 0.125 in	0.00	0.00
	LS8	0.02 in $\leq w <$ 0.125 in	554	10.2
		$w \geq$ 0.125 in	0.00	0.00
	LS9	0.02 in $\leq w <$ 0.125 in	512	9.45
		$w \geq$ 0.125 in	14.0	0.26

3.7 Summary

An automated, non-contact procedure (I-Crack), to measure and document crack widths in reinforced concrete components was developed, deployed and validated. I-Crack could replace traditional methods of collecting data with crack gages, which are labor intensive and approximate.

I-Crack was developed and validated using data from the cyclic tests of nine low-aspect ratio reinforced concrete shear walls in the NEES facility at the University at Buffalo. The processing techniques and algorithms were developed using data from one wall and validated using data from eight other walls.

I-Crack requires pre-processing to reduce overexposure and shadows in the high-resolution panoramas. The image resolution to detect cracks as narrow as 0.01 inch is 200 pixels per inch of concrete surveyed. Once pre-processing was completed, the panorama is loaded into I-Crack where an edge-detection algorithm and morphological operations are used to detect cracks and surface defects. The Prewitt algorithm and morphological operations, as implemented in MATLAB, are recommended for use. I-Crack uses image segmentation to separate the cracks from surface defects. The two parameters used for image segmentation are the major-minor axes length ratio and the orientation angle. Crack widths are measured using the MATLAB regionprops sub-routine after the panorama is segmented. The lengths of individual cracks are measured using the MATLAB imdistline sub-routine.

The utility of I-Crack to detect and measure crack widths was evaluated using data collected a) using traditional crack gages, and b) transferred manually to drawing sheets. Crack locations and widths were recorded at every load step for the nine shear walls. I-Crack results were compared to manually recorded results at discrete locations on every wall at two or three load steps, one at a peak displacement less than that associated with peak strength, one at a peak displacement associated with peak shear strength, and/or one at a peak displacement greater than that associated with peak strength. I-Crack recovered well the crack widths in the eight shear walls used to validate the algorithm and this provides confidence that the I-Crack algorithm is robust.

Appendix A provides the MATLAB code to implement I-Crack. Appendix B presents a tutorial for the use of I-Crack.

SECTION 4
CHARACTERIZING DAMAGE AND STRENGTH LOSS IN REINFORCED CONCRETE WALLS

4.1 General

Post-earthquake repair strategies for damaged structural components are often based on visual inspection. Several documents [e.g., FEMA 306 (ATC, 1998), FEMA 308 (ATC, 1998) and ACI 546R-04 (ACI, 2004)] describe damage states and repair methods for buildings with reinforced concrete walls. Gulec (2009) selected damage states and corresponding repair methods for low aspect ratio reinforced concrete shear walls using observations from experimental programs and expert opinion. These damage states include 1) onset of visible cracking, 2) cracks with a maximum width of 0.02 inch, 3) cracks with a maximum width of 0.04 inch, 4) concrete crushing in toe regions, 5) vertical cracking in toe regions, 6) sliding at the base, 7) wide diagonal cracks (crack widths greater than 0.125 inch), 8) widespread crushing of concrete, 9) buckling of reinforcement, and 10) reinforcement fracture.

Using these damage states, Gulec and Whittaker (2009) developed fragility functions for FEMA P-58 Guidelines for Seismic Performance Assessment of Buildings (FEMA, 2012). The experimental data available to Gulec and Whittaker (2009) reported damage states at instances of peak transient displacement. However, only damage at displacements associated with zero lateral load is available to an engineer/inspector after an earthquake. This chapter documents damage states and characterizes strength loss for walls SW1 through SW12 when the wall is in its unloaded condition to a) build a body of knowledge to be used by others performing post-earthquake damage assessments, and b) update Gulec's fragility functions.

4.2 Damage states for SW1 through SW12

Damage states at times of a) peak transient displacement, and b) subsequent displacement at zero lateral loading were carefully documented for walls SW1 through SW12. At each of these displacements, a low-resolution photograph was taken of the wall and crack patterns were transferred by hand to drawing sheets with crack widths measured using a crack width gage (see Figure 3-1). Additionally, a high-resolution panorama of the wall was taken at each instant of peak transient displacement (see Chapter 3). The documentation of damage at peak transient displacements and subsequent displacements at zero lateral load creates a unique dataset to characterize damage and strength loss in low aspect ratio reinforced concrete shear walls.

Two tables and three figures are provided for each wall. The first table (Damage summary for SW*) identifies damage states defined using information at displacements at zero lateral load: onset of visible cracking, crack width between specified limits, onset of concrete crushing, formation of wide diagonal cracks, and sliding at the base of the wall. Information beneath the title provides data on the wall, including the peak shear strength (see below) and the load step in which it was recorded. The load step, peak transient drift ratio, average shear force $\left(V_{ave}\right)$, average shear force normalized by peak shear strength $\left(V_{ave}/V_{\max}\right)$, average shear stress $\left(V_{ave}/A_w\right)$, and normalized average shear stress $\left(V_{ave}/\left[A_w\sqrt{f_c'}\right]\right)$ reported in the table are calculated from the complete cycle of loading (load step) that preceded the damage reported at zero lateral load. The peak shear strength of the wall is the greater of the maximum values recorded in the first and third quadrants of loading. The average shear force in a given load cycle is the average maximum resistance recorded in the first and third quadrants of loading. The area of the wall, A_w, is 960 in^2.

The first crossing of a limit on width by any (not all) crack in the wall triggered a report in the table. The crack width limits of 0.02 inch, 0.04 inch, and 0.125 inch were based on a) cracks with a width of less than 0.02 inch will generally require only cosmetic repair, b) cracks with a width between 0.02 inch and 0.125 inch will require epoxy injection to recover pre-earthquake strength, and c) walls with cracks with a width of greater than 0.125 inch cannot be repaired by epoxy injection alone to recover pre-earthquake strength and partial wall demolition and replacement is required. Information is also provided for a crack width of 0.04 inch if the reader considers 0.02 inch to be too small a threshold for repair by epoxy injection. Crushing of concrete at the toes of a wall will require partial wall demolition and replacement. Sliding at the base of the wall will likely require demolition and reconstruction of the entire wall panel.

The second table (Length and areal density data for cracks in SW* at zero lateral load following LS* and LS**) provides additional damage data, which could aid in the development of consequence functions. The load steps for which data are reported are a) the load cycle associated with crack widths crossing the threshold limit of 0.02 inch or peak shear strength, and b) two load cycles after peak shear strength or the last load cycle in the test, whichever came first; except SW12, which utilized the load step immediately after peak shear strength. The crack lengths reported in the table were calculated using I-Crack (see Chapter 3) for walls SW1 – SW3, SW5 – SW9 and SW12 at the peak transient displacement in the load step. For walls SW4, SW10 and SW11, the crack lengths at instances of peak transient displacement in the load step were calculated using low-resolution images and the software Bluebeam Revu (Bluebeam Software, Inc. 2016), which is a PDF reader and editor. The width of each crack (which typically varied along its length)

was calculated using a crack gage at the end of the load step (zero lateral force). The areal density reported in the table was calculated by dividing the crack length, parsed by width at the displacement associated with zero lateral load, by the surface area of the wall (one face only).

The first figure (Force-drift relationship for SW*) presents the cyclic response of the wall, measured in terms of in-plane lateral force and the in-plane drift ratio (displacement divided by the distance between the centerline of loading and the base of the wall). The load steps associated with the onset of damage, as described above, are identified on the figure. The other two figures presented for each wall are composite images, corresponding to load steps in the second table. The base images for walls SW1 – SW3, SW5 – SW9 and SW12 were provided by the Gigapan system, which was used for I-Crack measurements. The base images for walls SW4, SW10 and SW11 shows cracks drawn using Bluebeam Revu. The color coding of the cracks identifies the width of the cracks at the displacement associated with zero lateral load (end of the load step): blue indicates a crack width of less than or equal to 0.02 inch; purple indicates a crack width between 0.02 and 0.125 inch; red indicates a crack width of greater than 0.125 inch.

Table 4-1. Damage summary for SW1[1]

$\left(h_w/l_w = 0.94, r_l = 0.67\%, r_t = 0.67\%, f_c' = 3600 \text{ psi}, V_{max} = 253 \text{ kips in LS9}\right)$

Damage at zero lateral load[2]	Load step (LS)	Drift ratio (%)	V_{ave} (kips)	$\frac{V_{ave}}{V_{max}}$	$\frac{V_{ave}}{A_w}$ (psi)	$\frac{V_{ave}}{A_w\sqrt{f_c'}}$
Visible cracking	1	0.06	69	0.27	72	1.20
0.02 in $\leq w <$ 0.04 in	7	0.61	231	0.91	241	4.01
0.04 in $\leq w \leq$ 0.125 in	8	0.84	237	0.94	247	4.11
Concrete crushing in toe regions	10	1.68	233	0.92	243	4.05
$w >$ 0.125 in	10	1.68	233	0.92	243	4.05
Sliding at the base	10	2.60	140	0.55	146	2.43

1. Peak transient drift ratio prior to damage measured at a zero lateral load
2. Damage states not observed during testing of this wall: vertical cracking in the toe regions and widespread crushing of concrete

Table 4-2. Crack length and areal density for SW1 at zero lateral load following LS7 and LS10

Load step	Drift ratio[1] (%)	Crack width, w	Crack length (inch)	Areal density (in/ft^2)
LS7[2]	0.61	w $\leq$ 0.02 in	1695	18.0
		0.02 in $< w <$ 0.125 in	0	0.0
LS10[3]	1.68	w $\leq$ 0.02 in	1470	15.6
		0.02 in $< w <$ 0.125 in	517	5.5

1. Peak transient drift ratio
2. Load step related to crack widths crossing the threshold of 0.02 inch
3. Final load step

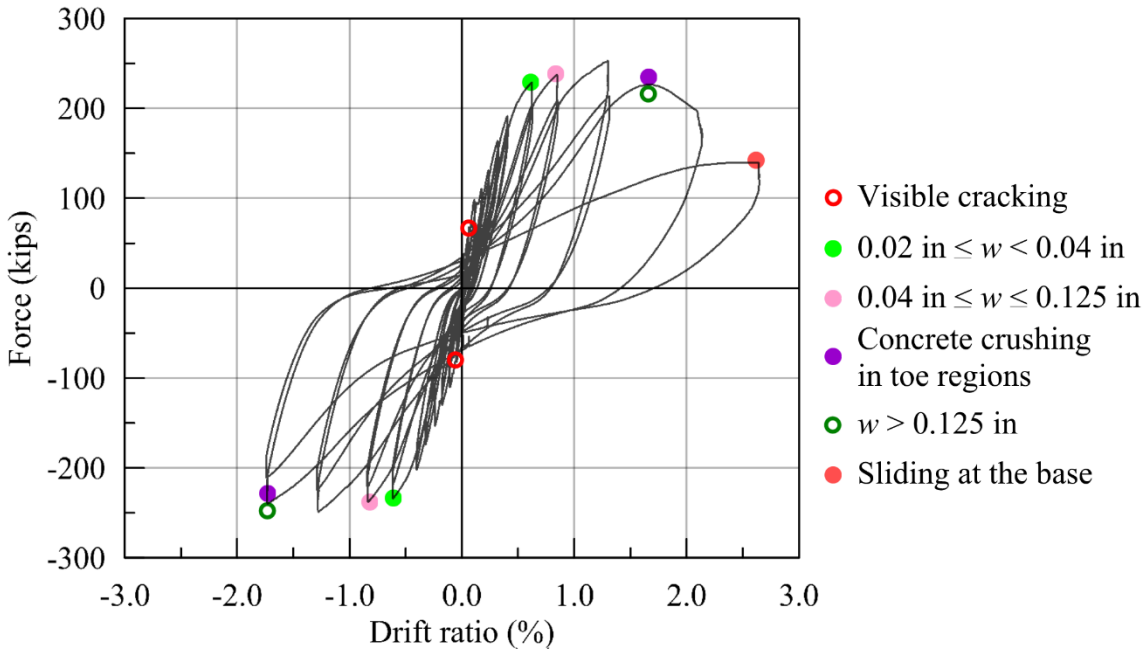

Figure 4-1. Force-drift relationship for SW1

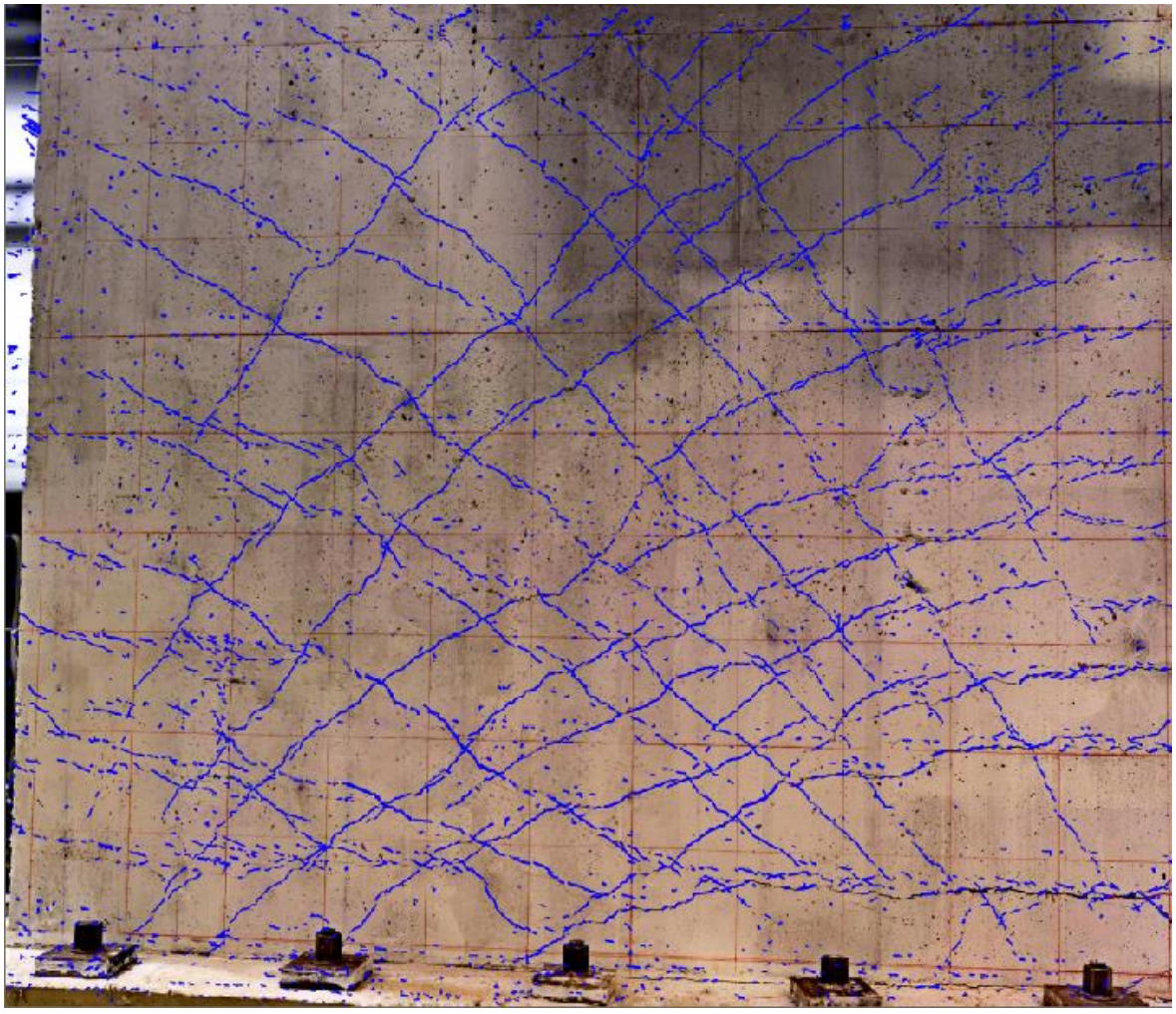

Figure 4-2. SW1 after load step LS7, peak transient drift ratio of 0.61%

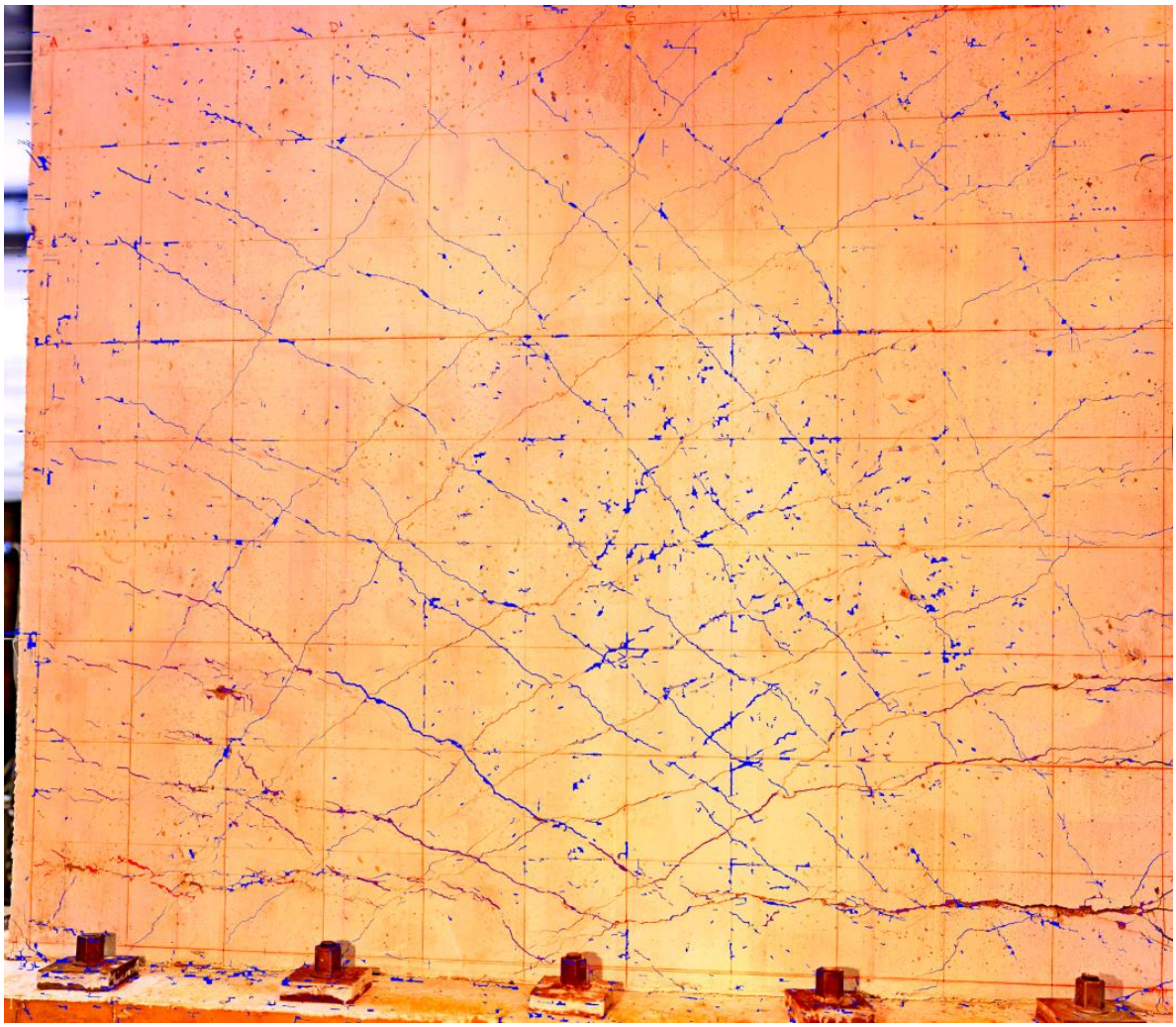

Figure 4-3. SW1 after load step LS10, final load step, peak transient drift ratio of 1.68%

Table 4-3. Damage summary for SW2[1]

$\left(h_w/l_w = 0.54, \rho_l = 1.00\%, \rho_t = 1.00\%, f_c^{'} = 7000 \text{ psi}, V_{max} = 563 \text{ kips at LS10}\right)$

Damage at zero lateral load[2]	Load step (LS)	Drift ratio (%)	V_{ave} (kips)	$\frac{V_{ave}}{V_{max}}$	$\frac{V_{ave}}{A_w}$ (psi)	$\frac{V_{ave}}{A_w\sqrt{f_c^{'}}}$
Visible cracking	2	0.08	164	0.29	171	2.04
0.02 in $\leq w <$ 0.04 in	9	0.78	509	0.90	530	6.34
0.04 in $\leq w \leq$ 0.125 in	10	1.26	521	0.93	543	6.49
Concrete crushing in toe regions	11	1.68	461[3]	0.82	480	5.74

1. Peak transient drift ratio prior to damage measured at zero lateral load
2. The following damage states were not observed during testing: cracks with widths greater than 0.125 inch, vertical cracks in the toe regions, widespread crushing of concrete and sliding at the base
3. Shear strength based on first quadrant force only

Table 4-4. Crack length and areal density for SW2 at zero lateral load following LS9 and LS11

Load step	Drift ratio[1] (%)	Crack width, w	Crack length (inch)	Areal density (in/ft^2)
LS9[2]	0.78	w $\leq$ 0.02 in	1116	20.6
		0.02 in $< w <$ 0.125 in	0	0.0
LS11[3]	1.68	w $\leq$ 0.02 in	1092	20.2
		0.02 in $< w <$ 0.125 in	167	3.1

1. Peak transient drift ratio
2. Load step related to crack widths crossing the threshold of 0.02 inch
3. Final load step

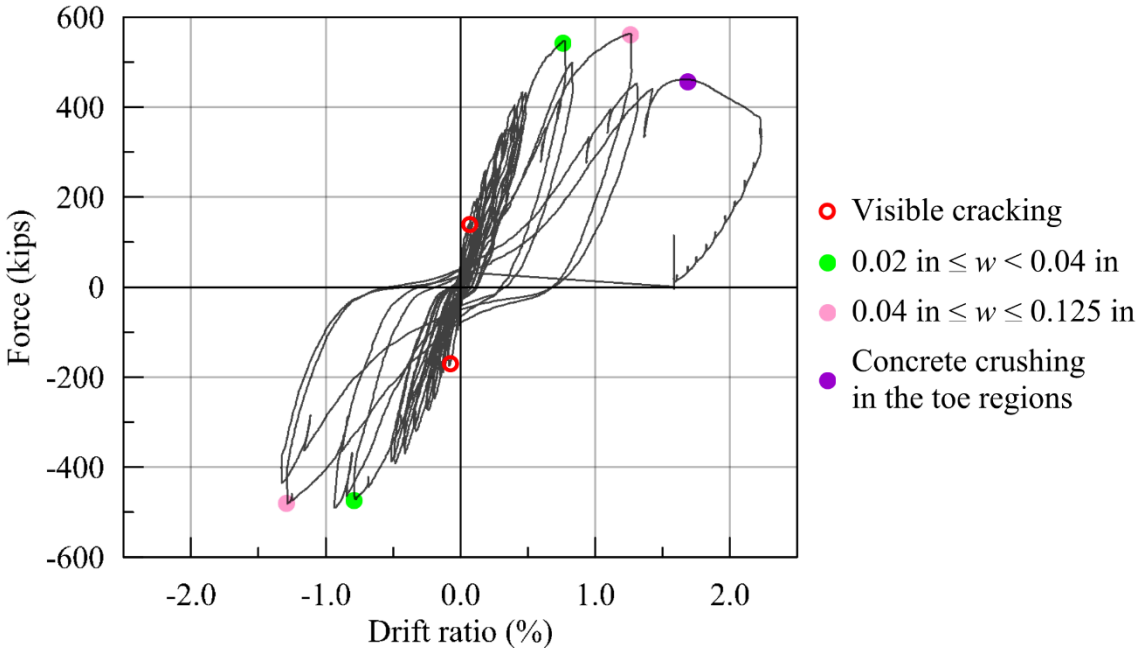

Figure 4-4. Force-drift relationship for SW2

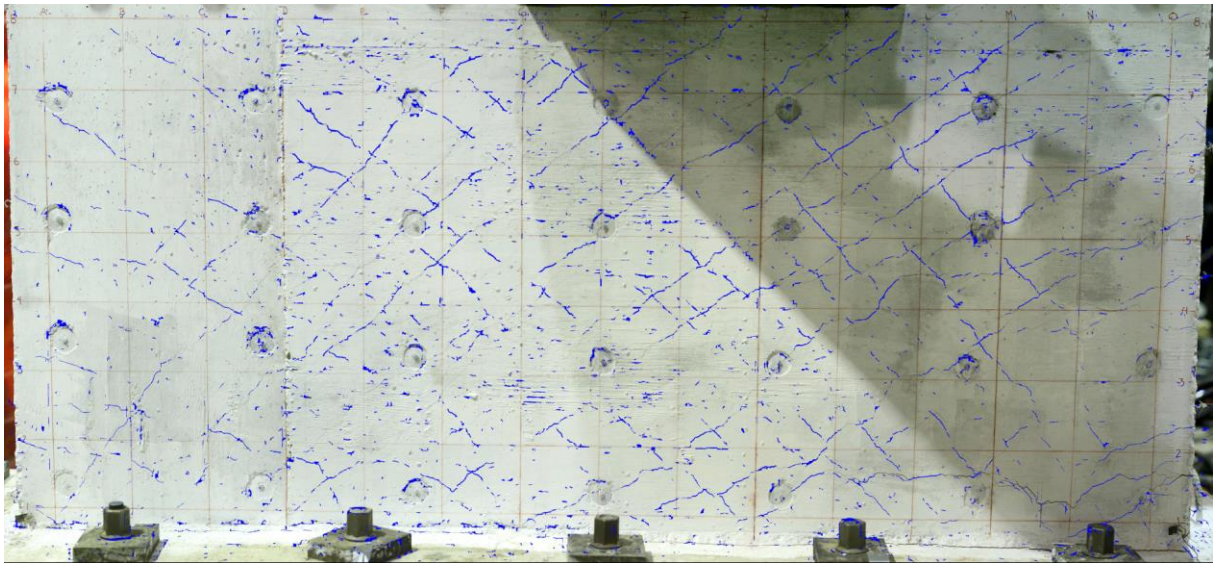

Figure 4-5. SW2 after load step LS9, peak transient drift ratio of 0.78%

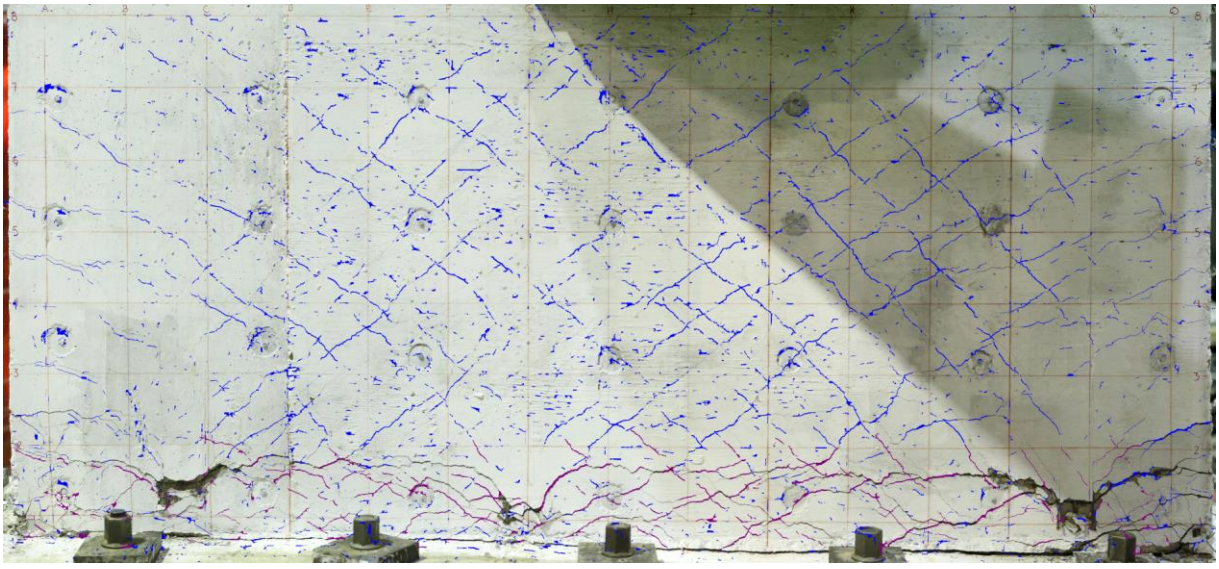

Figure 4-6. SW2 after load step LS11, final load step, peak transient drift ratio of 1.68%

Table 4-5. Damage summary for SW3[1]

$\left(h_w/l_w = 0.54, \rho_l = 0.67\%, \rho_t = 0.67\%, f_c^{'} = 7800 \text{ psi}, V_{max} = 468 \text{ kips at LS12}\right)$

Damage at zero lateral load[2]	Load step (LS)	Drift ratio (%)	V_{ave} (kips)	$\frac{V_{ave}}{V_{max}}$	$\frac{V_{ave}}{A_w}$ (psi)	$\frac{V_{ave}}{A_w\sqrt{f_c^{'}}}$
Visible cracking	3	0.06	132	0.28	138	1.56
0.02 in $\leq w <$ 0.04 in	10	0.75	397	0.85	414	4.68
0.04 in $\leq w \leq$ 0.125 in	12	1.82	403	0.86	420	4.75
Concrete crushing in toe regions	12	2.09	277	0.59	289	3.27
Sliding at the base	12	2.09	277	0.59	289	3.27

1. Peak transient drift ratio prior to damage measured at a zero lateral load
2. The following damage states were not observed during testing: cracks with widths greater than 0.125 inch, vertical cracks in the toe regions and widespread crushing of concrete

Table 4-6. Length and areal density for SW3 at zero lateral load following LS10 and LS13

Load step	Drift ratio[1] (%)	Crack width, w	Crack length (inch)	Areal density (in/ft^2)
LS10[2]	0.75	w $\leq$ 0.02 in	1125	20.8
		0.02 in $< w <$ 0.125 in	0	0.0
LS13[3]	2.95	w $\leq$ 0.02 in	295	5.4
		0.02 in $< w <$ 0.125 in	899	16.6

1. Peak transient drift ratio
2. Load step related to crack widths crossing the threshold of 0.02 inch
3. Final load step

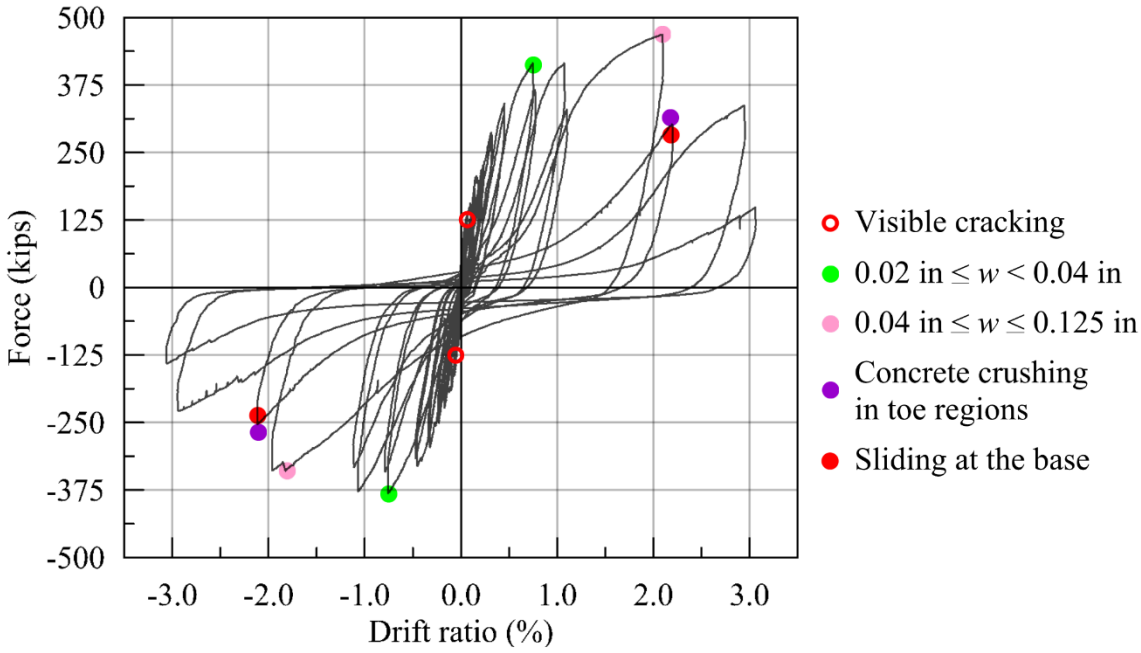

Figure 4-7. Force-drift relationship for SW3

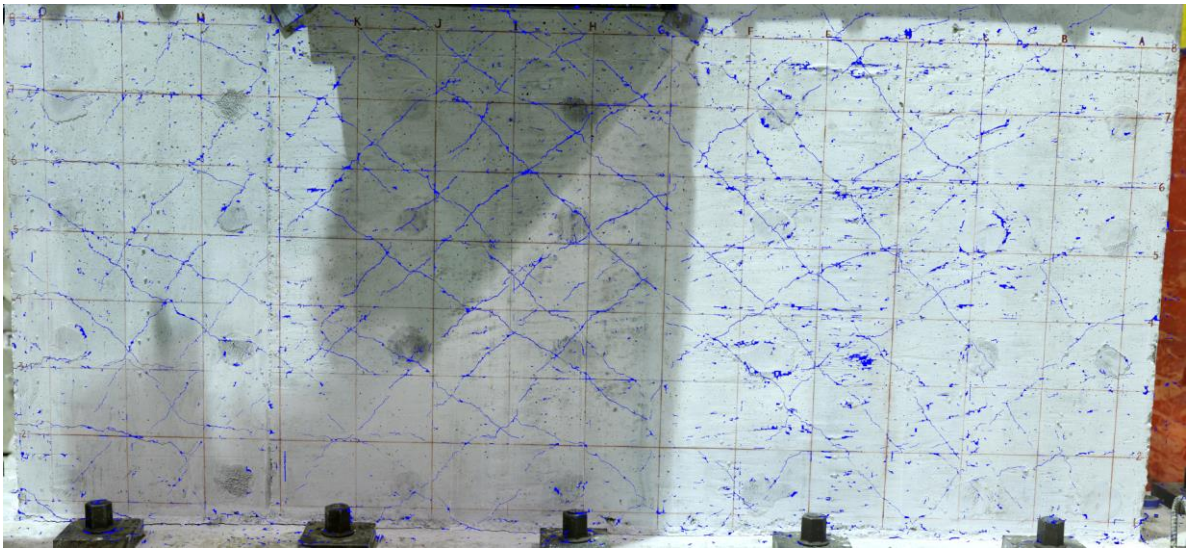

Figure 4-8. SW3 after load step LS10, peak transient drift ratio of 0.75%

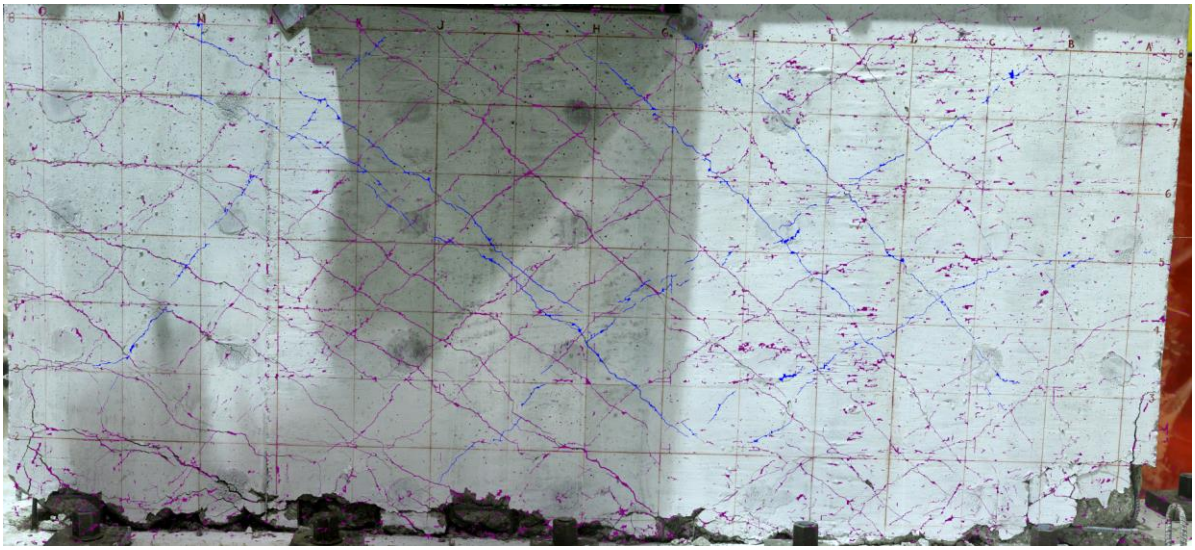

Figure 4-9. SW3 after load step LS13, final load step, peak transient drift ratio of 2.95%

Table 4-7. Damage summary for SW4[1]

$\left(h_w/l_w = 0.54, \rho_l = 0.33\%, \rho_t = 0.33\%, f_c^{'} = 4200 \text{ psi}, V_{max} = 226 \text{ kips at LS12}\right)$

Damage at zero lateral load[2]	Load step (LS)	Drift ratio[1] (%)	V_{ave} (kips)	$\frac{V_{ave}}{V_{max}}$	$\frac{V_{ave}}{A_w}$ (psi)	$\frac{V_{ave}}{A_w\sqrt{f_c^{'}}}$
Visible cracking	3	0.04	80	0.35	83	1.29
0.02 in $\leq w <$ 0.04 in	9	0.41	193	0.85	201	3.10
Vertical cracks in the toe regions	10	0.60	205	0.91	214	3.29
0.04 in $\leq w \leq$ 0.125 in	11	0.75	208	0.92	217	3.34
Concrete crushing in toe regions	12	1.08	220	0.97	229	3.54
Sliding at the base	13	1.50	211	0.93	220	3.39

1. Peak transient drift ratio prior to damage measured at a zero lateral load
2. The following damage states were not observed during testing: cracks with widths greater than 0.125 inch and widespread crushing of concrete

Table 4-8. Length and areal density for SW4 at zero lateral load following LS9 and LS14[1]

Load step	Drift ratio[2] (%)	Crack width, w	Crack length $\left(\text{inch}\right)$	Areal density $\left(\text{in}/\text{ft}^2\right)$
LS9[3]	0.41	w $\leq$ 0.02 in	323	6.0
		0.02 in $< w <$ 0.125 in	0	0.0
LS14[4]	2.29	w $\leq$ 0.02 in	414	7.6
		0.02 in $< w <$ 0.125 in	191	3.5

1. Crack lengths measured using Bluebeam Revu
2. Peak transient drift ratio
3. Load step related to crack widths crossing the threshold of 0.02 inch
4. Final load step

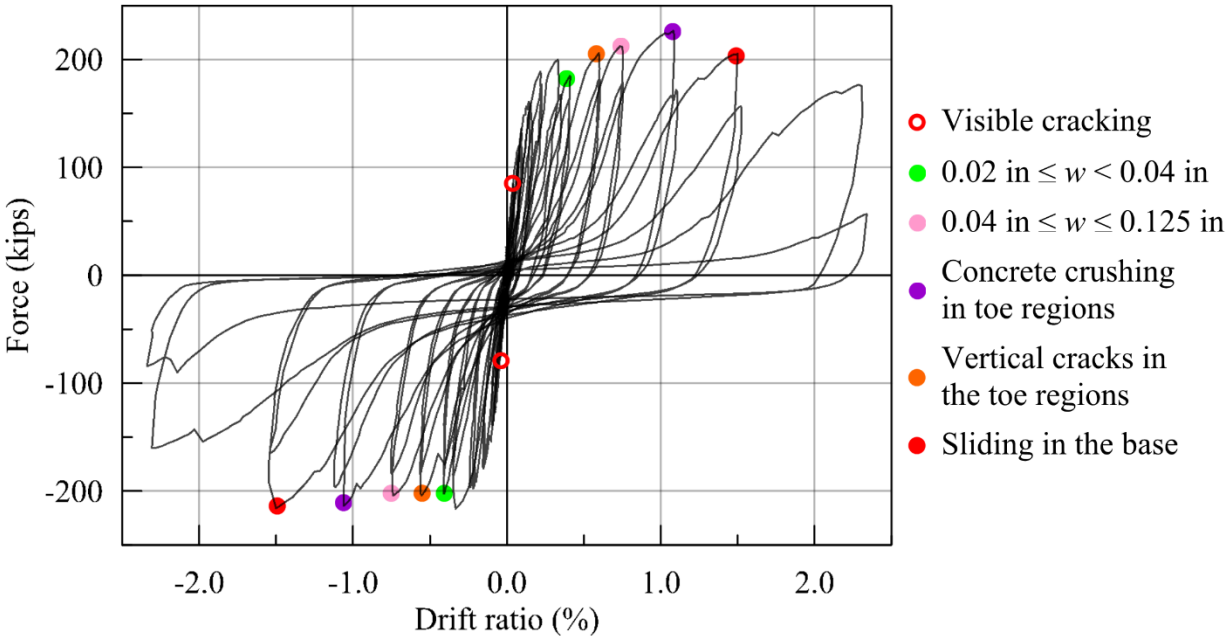

Figure 4-10. Force-drift relationship for SW4

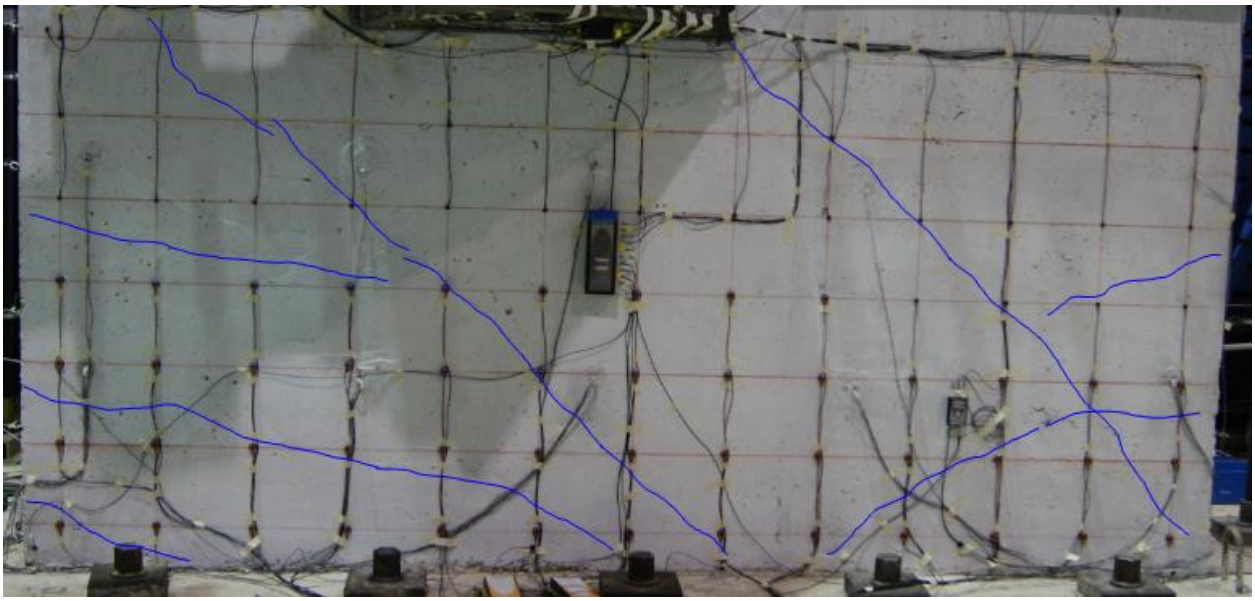

Figure 4-11. SW4 after load step LS9, peak transient drift ratio of 0.41%

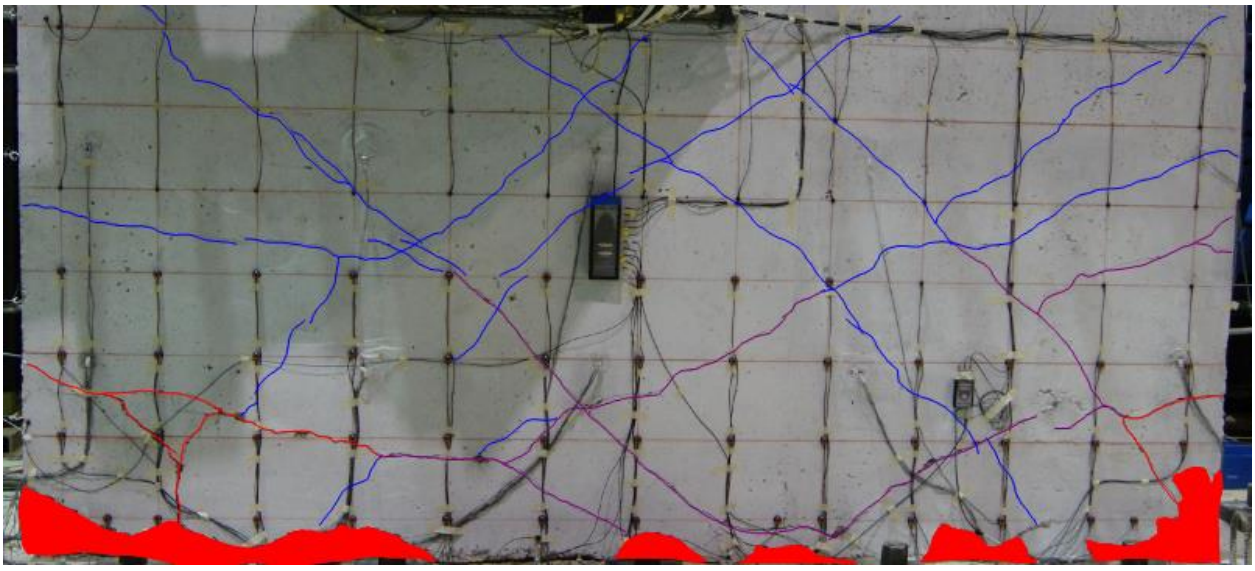

Figure 4-12. SW4 after load step LS14, final load step, peak transient drift ratio of 2.29%

Table 4-9. Damage summary for SW5[1]

$\left(h_w/l_w = 0.33, \rho_l = 1.00\%, \rho_t = 1.00\%, f_c^{'} = 4300 \text{ psi}, V_{max} = 726 \text{ kips at LS8}\right)$

Damage at zero lateral load[2]	Load step (LS)	Drift ratio (%)	V_{ave} (kips)	$\frac{V_{ave}}{V_{max}}$	$\frac{V_{ave}}{A_w}$ (psi)	$\frac{V_{ave}}{A_w\sqrt{f_c^{'}}}$
Visible cracking	1	0.02	63	0.09	66	1.00
0.02 in $\leq w <$ 0.04 in	7	0.67	600	0.83	625	9.53
0.04 in $\leq w \leq$ 0.125 in	8	0.89	636	0.88	663	10.10
Concrete crushing in the toe regions	8	0.89	636	0.88	663	10.10
Sliding near the base[3]	8	0.89	373	0.51	389	5.92
$w >$ 0.125 in	8	0.89	636	0.88	663	10.10
Widespread crushing of concrete	8	0.89	636	0.88	663	10.10

1. Peak transient drift ratio prior to damage measured at a zero lateral load
2. The following damage states were not observed during testing: vertical cracks in the toe region
3. Sliding along a plane approximately seven inches above the base of the wall

Table 4-10. Length and areal density for SW5 at zero lateral load following LS7 and LS8

Load step	Drift ratio[1] (%)	Crack width, w	Crack length $\left(\text{inch}\right)$	Areal density $\left(\text{in}/\text{ft}^2\right)$
LS7[2]	0.67	w $\leq$ 0.02 in	679	19.9
		0.02 in $< w <$ 0.125 in	10	0.3
LS8[3]	0.89	w $\leq$ 0.02 in	632	18.5
		0.02 in $< w <$ 0.125 in	99.4	2.9

1. Peak transient drift ratio
2. Load step related to crack widths crossing the threshold of 0.02 inch
3. Final load step and load step at peak shear strength

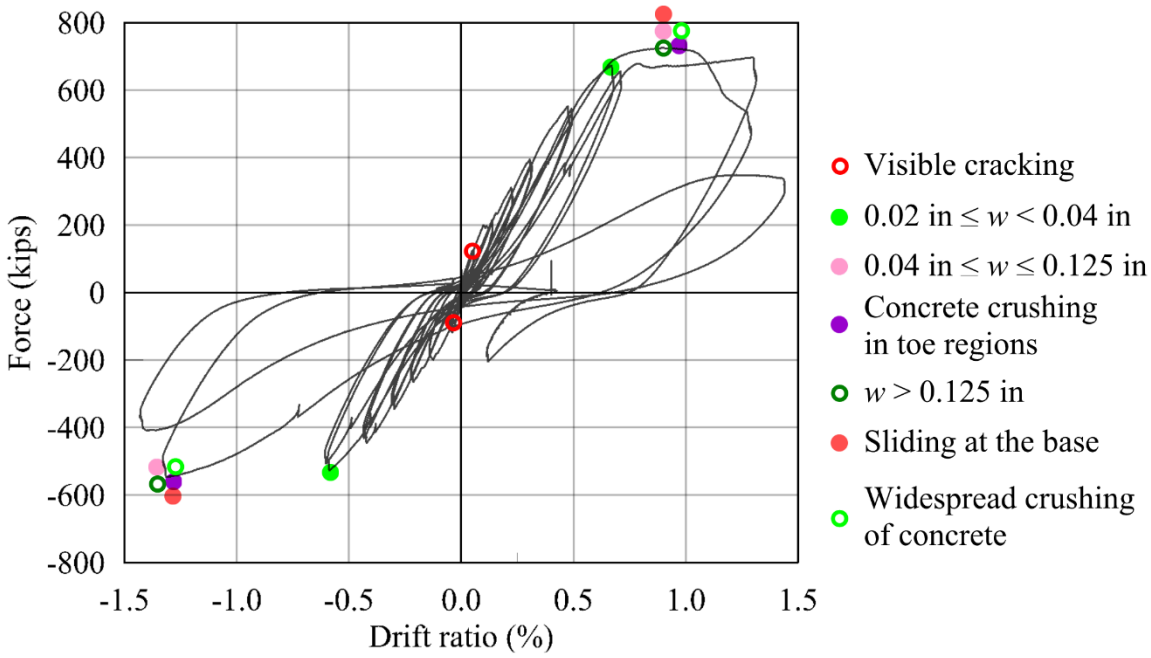

Figure 4-13. Force-drift relationship for SW5

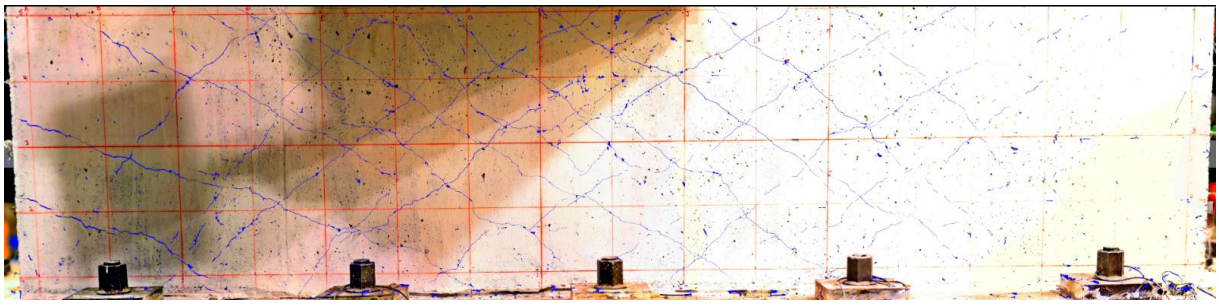

Figure 4-14. SW5 after load step LS7, peak transient drift ratio of 0.67%

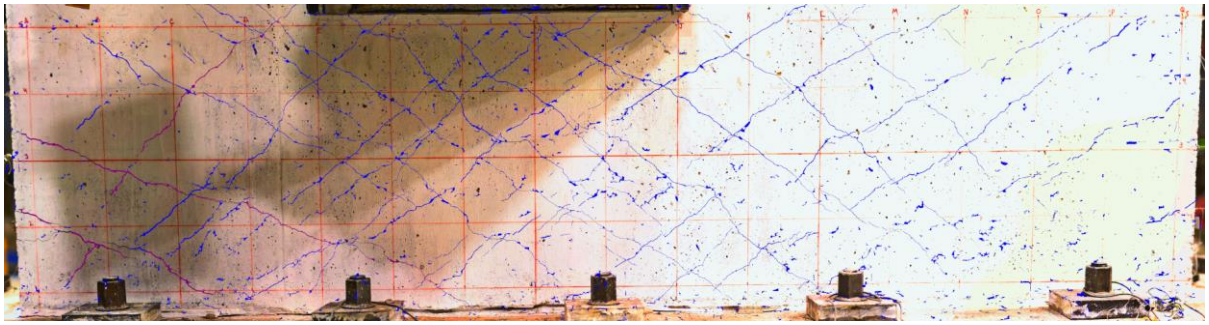

Figure 4-15. SW5 after load step LS8, final load step and load step at peak shear strength, peak transient drift ratio of 0.89%

Table 4-11. Damage summary for SW6[1]

$\left(h_w/l_w = 0.33, \rho_l = 0.63\%, \rho_t = 0.69\%, f_c^{'} = 3800 \text{ psi}, V_{max} = 570 \text{ kips at LS8}\right)$

Damage at zero lateral load[2]	Load step (LS)	Drift ratio[1] (%)	V_{ave} (kips)	$\frac{V_{ave}}{V_{max}}$	$\frac{V_{ave}}{A_w}$ (psi)	$\frac{V_{ave}}{A_w\sqrt{f_c^{'}}}$
Visible cracking	2	0.04	121	0.21	126	2.04
0.02 in $\leq w <$ 0.04 in	8	0.81	491	0.86	512	8.30
0.04 in $\leq w \leq$ 0.125 in	9	1.07	473	0.83	493	7.99
Concrete crushing in toe regions	9	1.07	473	0.83	493	7.99
$w >$ 0.125 in	10	1.69	450	0.79	469	7.60
Sliding at the base	10	1.81	330	0.58	344	5.58

1. Peak transient drift ratio prior to damage measured at zero lateral load
2. The following damage states were not observed during testing: vertical cracks in the toe region and widespread crushing of concrete

Table 4-12. Length and areal density for SW6 at zero lateral load following LS8 and LS10

Load step	Drift ratio[1] (%)	Crack width, w	Crack length $\left(\text{inch}\right)$	Areal density $\left(\text{in}/\text{ft}^2\right)$
LS8[2]	0.81	w $\leq$ 0.02 in	637	18.6
		0.02 in $< w <$ 0.125 in	71	2.1
LS10[3]	1.69	w $\leq$ 0.02 in	193	5.6
		0.02 in $< w <$ 0.125 in	506	14.8

1. Peak transient drift ratio
2. Load step related to crack widths crossing the threshold of 0.02 inch and load step at peak shear strength
3. Two load steps after peak shear strength

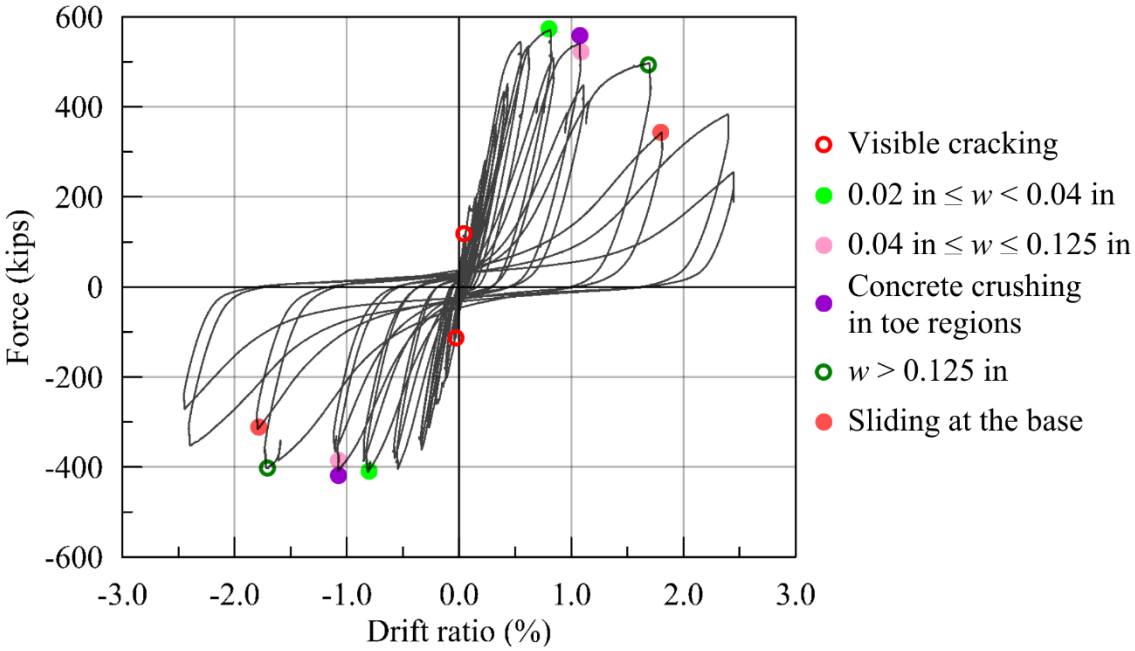

Figure 4-16. Force-drift relationship for SW6

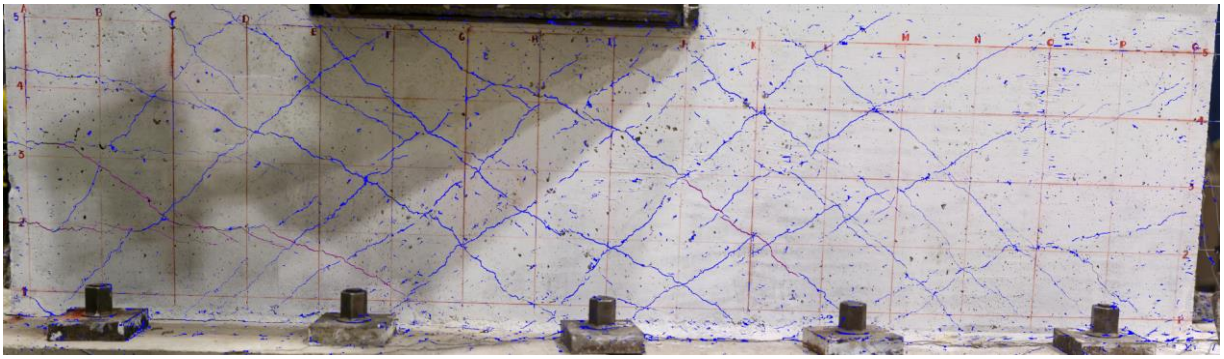

Figure 4-17. SW6 after load step LS8, load step at peak shear strength, peak transient drift ratio of 0.81%

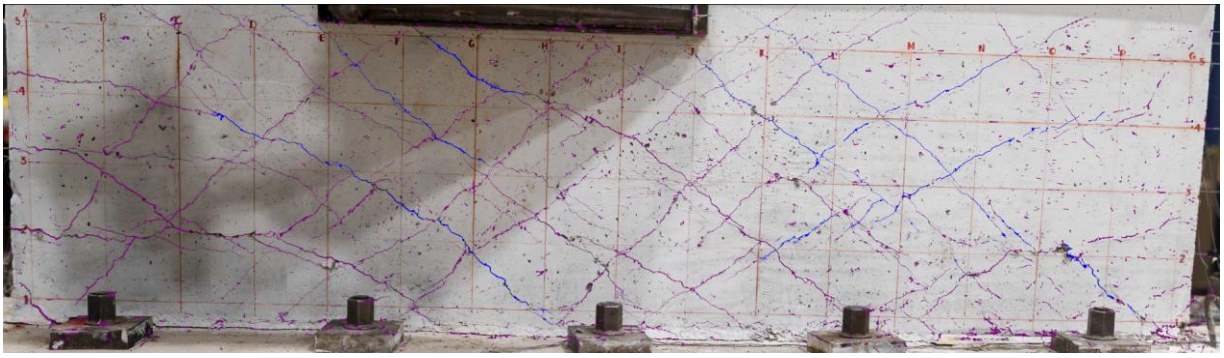

Figure 4-18. SW6 after load step LS10, peak transient drift ratio of 1.69%

Table 4-13. Damage summary for SW7[1]

$\left(h_w/l_w = 0.33, \rho_l = 0.34\%, \rho_t = 0.38\%, f_c^{'} = 3800 \text{ psi}, V_{max} = 318 \text{ kips at LS7}\right)$

Damage at zero lateral load[2]	Load step (LS)	Drift ratio[1] (%)	V_{ave} (kips)	$\frac{V_{ave}}{V_{max}}$	$\frac{V_{ave}}{A_w}$ (psi)	$\frac{V_{ave}}{A_w\sqrt{f_c^{'}}}$
Visible cracking	2	0.08	137	0.43	143	2.31
0.02 in $\leq w <$ 0.04 in	7	0.45	298	0.94	310	5.04
Vertical cracks in toe regions	9	0.70	256	0.81	267	4.33
Sliding at the base	9	0.70	256	0.81	267	4.33
Concrete crushing in toe regions	10	0.85	237	0.75	247	4.01
0.04 in $\leq w \leq$ 0.125 in	13	1.94	234	0.74	244	3.95

1. Peak transient drift ratio prior to damage measured at a zero lateral load
2. The following damage states were not observed during testing: cracks with widths greater than 0.125 inch and widespread crushing of concrete

Table 4-14. Length and areal density SW7 at zero lateral load following LS7 and LS9

Load step	Drift ratio[1] (%)	Crack width, w	Crack length $\left(\text{inch}\right)$	Areal density $\left(\text{in}/\text{ft}^2\right)$
LS7[2]	0.45	w $\leq$ 0.02 in	440	12.9
		0.02 in $< w <$ 0.125 in	0	0.0
LS9[3]	0.70	w $\leq$ 0.02 in	529	15.5
		0.02 in $< w <$ 0.125 in	0	0.0

1. Peak transient drift ratio
2. Load step related to crack widths crossing the threshold of 0.02 inch and load step at peak shear strength
3. Two load steps after peak shear strength

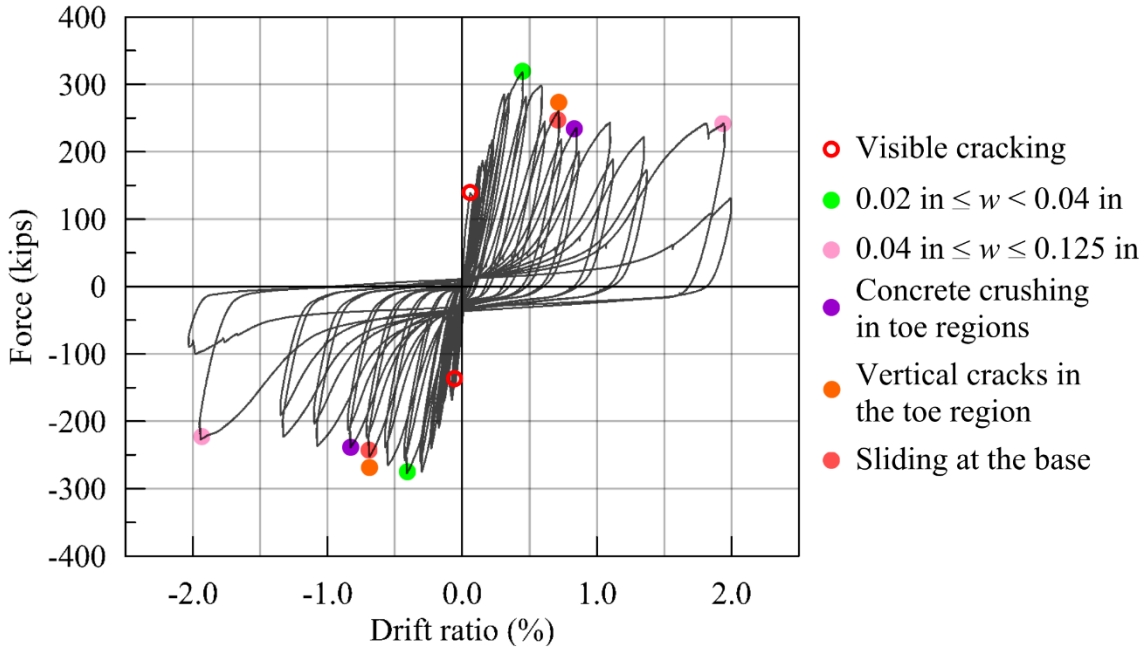

Figure 4-19. Force-drift relationship for SW7

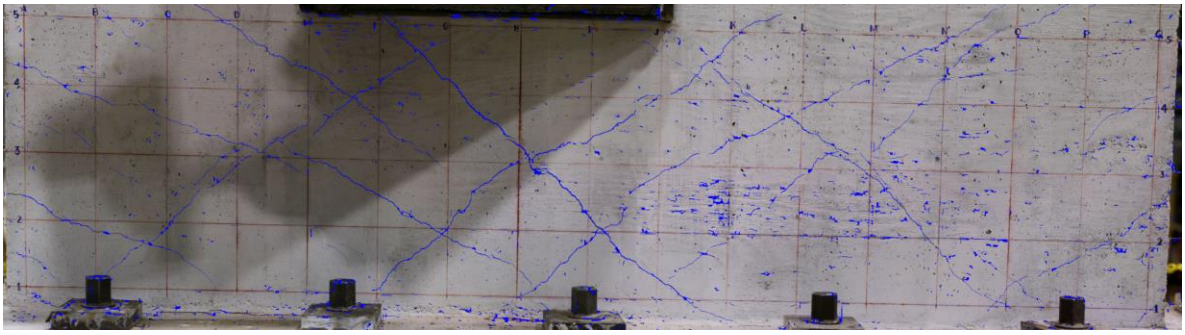

Figure 4-20. SW7 after load step LS7, load step at peak shear strength, peak transient drift ratio of 0.45%

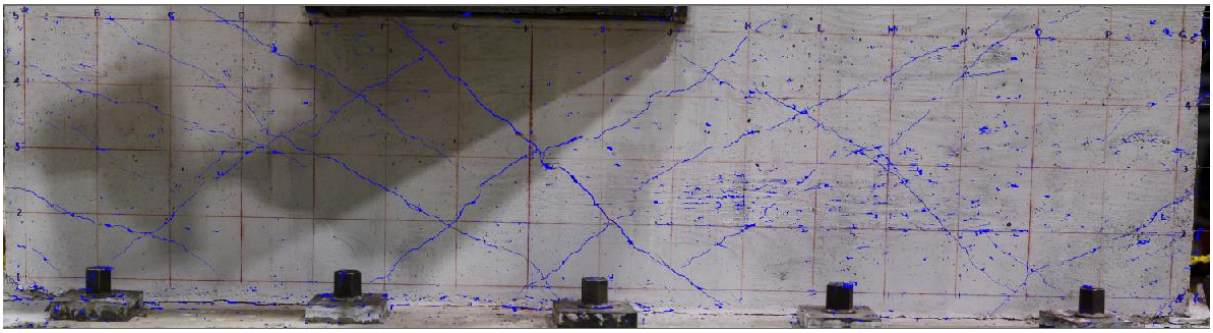

Figure 4-21. SW7 after load step LS9, peak transient drift ratio of 0.90%

Table 4-15. Damage summary for SW8[1]

$\left(h_w/l_w = 0.54, \rho_l = 1.50\%, \rho_t = 1.50\%, f_c^{'} = 3500 \text{ psi}, V_{max} = 623 \text{ kips at LS6}\right)$

Damage at zero lateral load[2]	Load step (LS)	Drift ratio[1] (%)	V_{ave} (kips)	$\frac{V_{ave}}{V_{max}}$	$\frac{V_{ave}}{A_w}$ (psi)	$\frac{V_{ave}}{A_w\sqrt{f_c^{'}}}$
Visible cracking	4	0.34	468	0.75	488	8.24
0.02 in $\leq w <$ 0.04 in	7	0.88	515	0.83	537	9.07
Concrete crushing in toe regions	7	0.88	515	0.83	537	9.07
Vertical cracks in toe regions	7	0.88	515	0.83	537	9.07
Sliding at the base	8	1.33	465	0.75	484	8.19
Widespread crushing of concrete	10	2.34	338	0.54	352	5.95

1. Peak transient drift ratio prior to damage measured at a zero lateral load
2. The following damage states were not observed during testing: cracks with widths greater than 0.04 inch

Table 4-16. Length and areal density for SW8 at zero lateral load following LS6 and LS8

Load step	Drift ratio[1] (%)	Crack width, w	Crack length (inch)	Areal density (in/ft^2)
LS6[2]	0.70	w $\leq$ 0.02 in	1150	21.2
		0.02 in $< w <$ 0.125 in	0	0.0
LS8[3]	1.34	w $\leq$ 0.02 in	1346	24.9
		0.02 in $< w <$ 0.125 in	0	0.0

1. Peak transient drift ratio
2. Load step at peak shear strength
3. Two load steps after peak shear strength

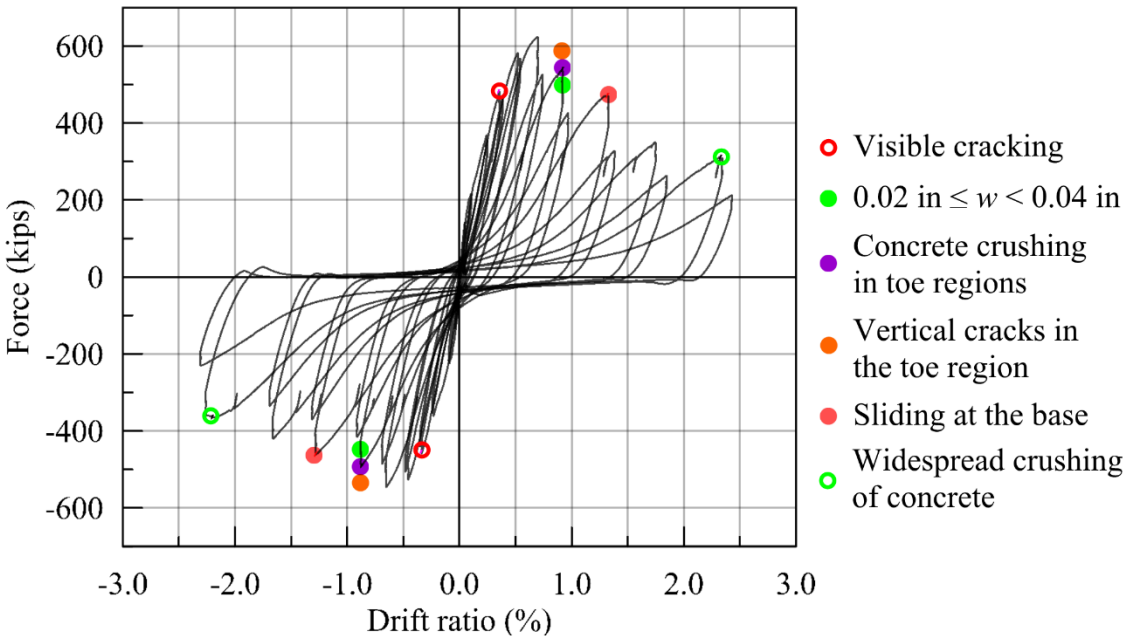

Figure 4-22. Force-drift relationship for SW8

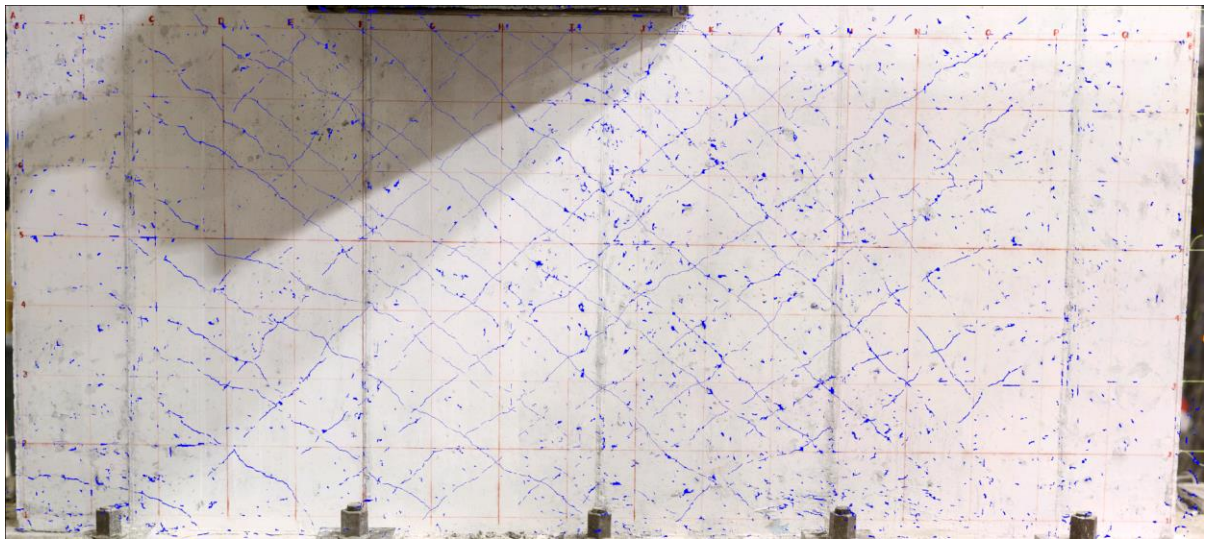

Figure 4-23. SW8 after load step LS6, load step at peak shear strength, peak transient drift ratio of 0.70%

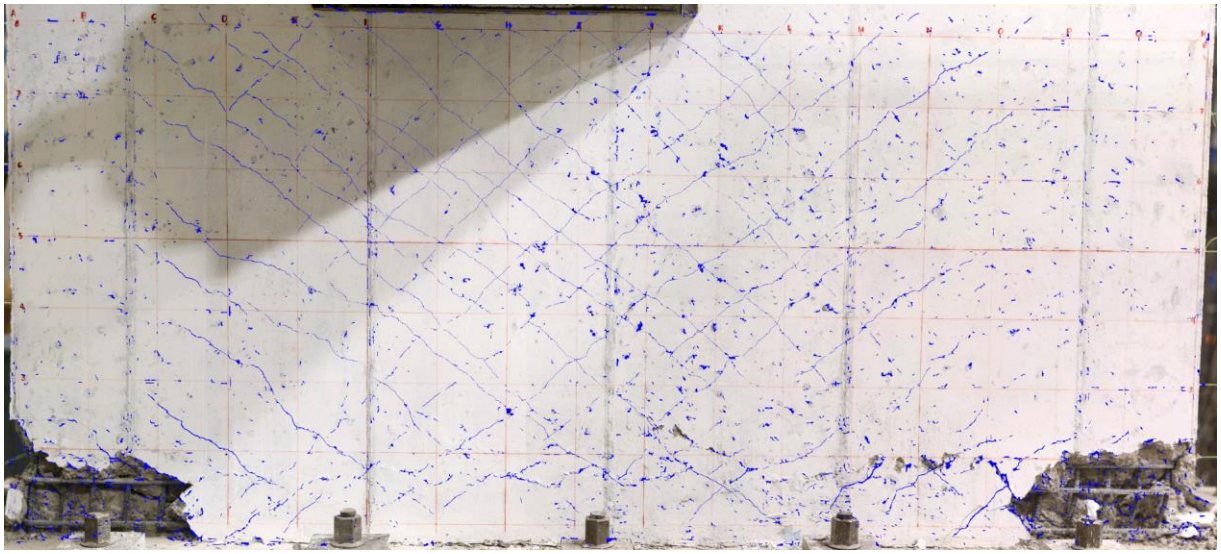

Figure 4-24. SW8 after load step LS8, peak transient drift ratio of 1.33%

Table 4-17. Damage summary for SW9[1]

$\left(h_w/l_w = 0.54, \rho_l = 1.50\%, \rho_t = 0.67\%, f_c^{'} = 4300 \text{ psi}, V_{max} = 633 \text{ kips at LS7}\right)$

Damage at zero lateral load[2]	Load step (LS)	Drift ratio[1] (%)	V_{ave} (kips)	$\frac{V_{ave}}{V_{max}}$	$\frac{V_{ave}}{A_w}$ (psi)	$\frac{V_{ave}}{A_w\sqrt{f_c^{'}}}$
Visible cracking	2	0.07	227	0.36	237	3.61
0.02 in $\leq w <$ 0.04 in	7	0.76	627	0.99	653	9.96
0.04 in $\leq w \leq$ 0.125 in	8	1.23	526	0.83	548	8.36
Concrete crushing in toe regions	8	1.23	526	0.83	548	8.36
Sliding at the base	8	1.35	326	0.52	340	5.18

1. Peak transient drift ratio prior to damage measured at a zero lateral load
2. The following damage states were not observed during testing: cracks with widths greater than 0.125 inch, vertical cracks in the toe region and widespread crushing of concrete

Table 4-18. Length and areal density for SW9 at zero lateral load following LS7 and LS9

Load step	Drift ratio[1] (%)	Crack width, w	Crack length $(inch)$	Areal density (in/ft^2)
LS7[2]	0.76	w $\leq$ 0.02 in	1062	19.6
		0.02 in $< w <$ 0.125 in	42	0.8
LS9[3]	1.72	w $\leq$ 0.02 in	1409	26.0
		0.02 in $< w <$ 0.125 in	203	3.8

1. Peak transient drift ratio
2. Load step related to crack widths crossing the threshold of 0.02 inch and load step at peak shear strength
3. Two load steps after peak shear strength

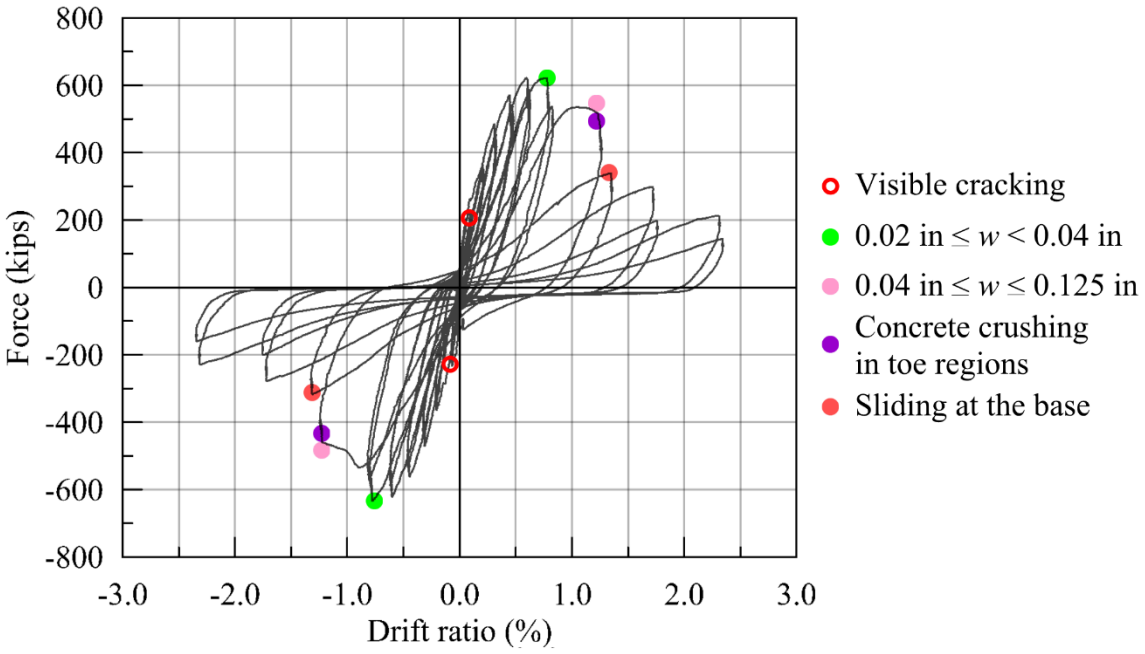

Figure 4-25. Force-drift relationship for SW9

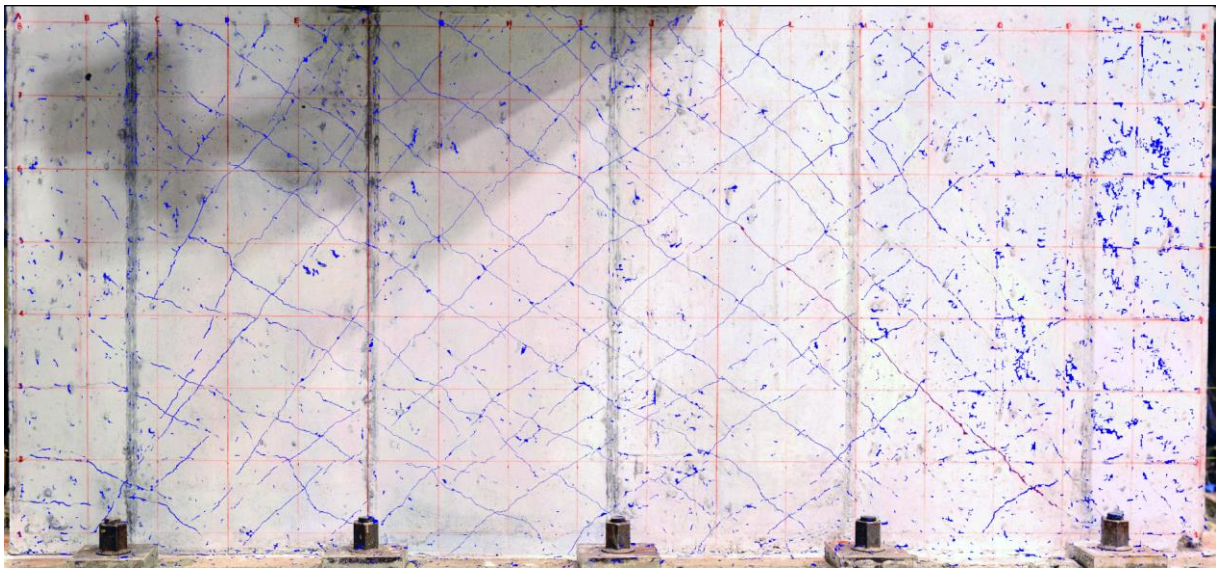

Figure 4-26. SW9 after load step LS7, load step at peak shear strength, peak transient drift ratio of 0.76%

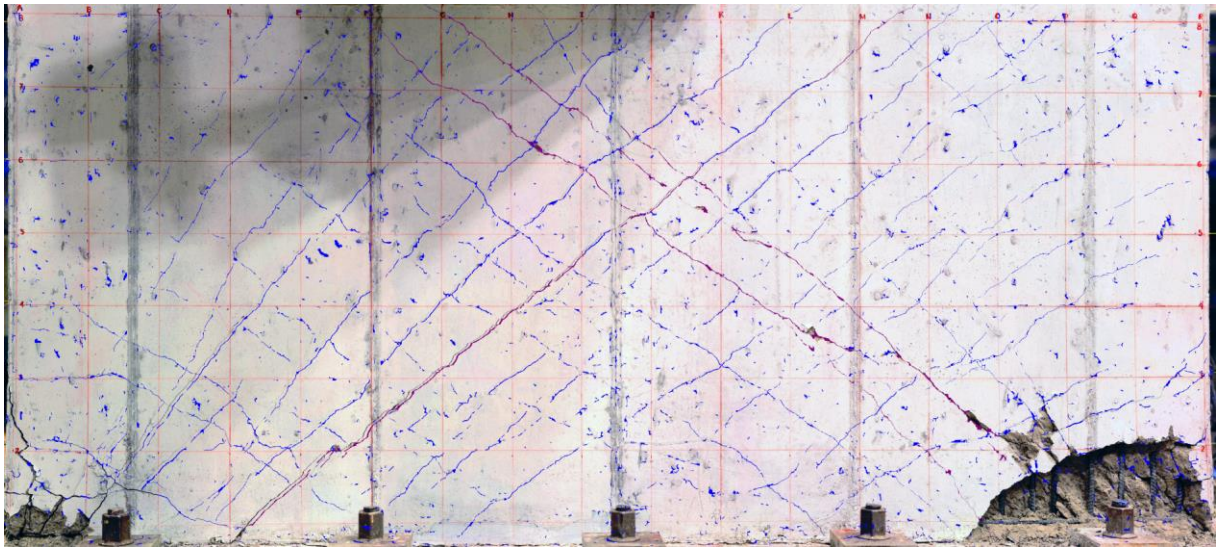

Figure 4-27. SW9 after load step LS9, peak transient drift ratio of 1.72%

Table 4-19. Damage summary for SW10[1]

$\left(h_w/l_w = 0.54, \rho_l = 1.50\%, \rho_t = 0.33\%, f_c^{'} = 4600 \text{ psi}, V_{\max} = 528 \text{ kips at LS6}\right)$

Damage at zero lateral load[2]	Load step (LS)	Drift ratio[1] (%)	V_{ave} (kips)	$\frac{V_{ave}}{V_{max}}$	$\frac{V_{ave}}{A_w}$ (psi)	$\frac{V_{ave}}{A_w\sqrt{f_c^{'}}}$
Visible cracking	2	0.09	218	0.41	227	3.35
0.02 in $\leq w <$ 0.04 in	5	0.42	500	0.95	521	7.68
0.04 in $\leq w \leq$ 0.125 in	5	0.42	500	0.95	521	7.68
$w >$ 0.125 in	6	0.59	507	0.96	528	7.79
Concrete crushing in toe regions	7	0.75	488	0.92	508	7.49
Widespread crushing of concrete	7	0.75	488	0.92	508	7.49
Sliding at the base	8	0.95	242	0.46	252	3.72

1. Peak transient drift ratio prior to damage measured at a zero lateral load
2. The following damage states were not observed during testing: vertical cracks in the toe region

Table 4-20. Length and areal density for SW10 at zero lateral load following LS5 and LS8[1]

Load step	Drift ratio[2] (%)	Crack width, w	Crack length $(inch)$	Areal density (in/ft^2)
LS5[3]	0.42	w $\leq$ 0.02 in	1041	19.2
		0.02 in $< w <$ 0.125 in	93	1.7
LS8[4]	0.95	w $\leq$ 0.02 in	705	13.0
		0.02 in $< w <$ 0.125 in	170	3.1

1. Crack lengths measured using Bluebeam Revu
2. Peak transient drift ratio
3. Load step related to crack widths crossing the threshold of 0.02 inch
4. Final load step

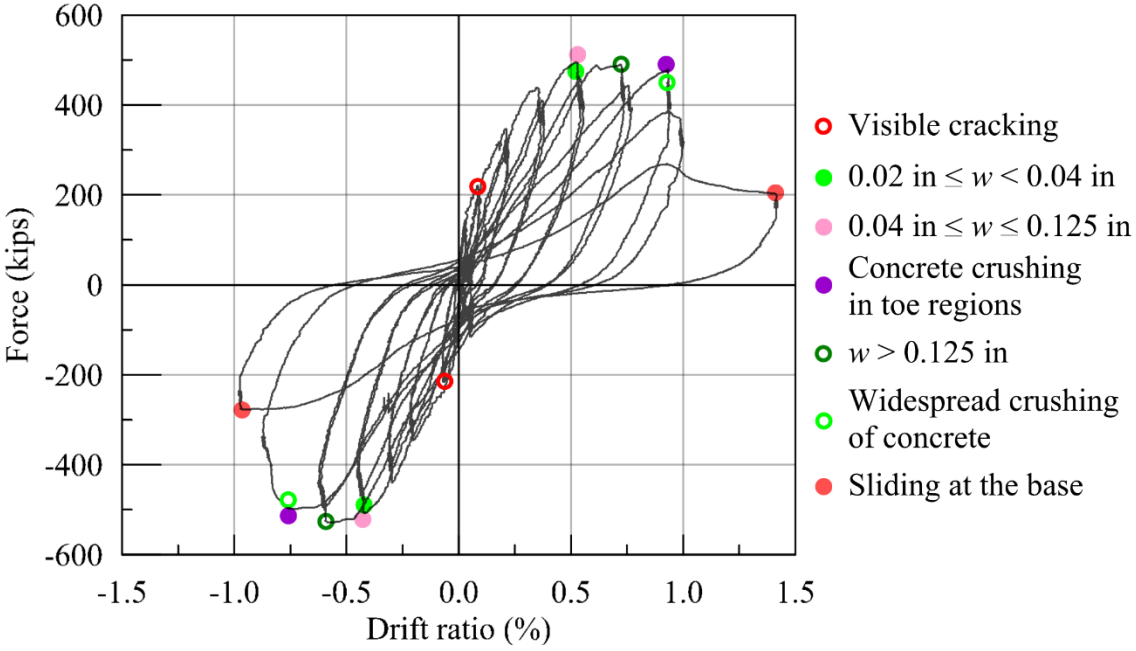

Figure 4-28. Force-drift relationship for SW10

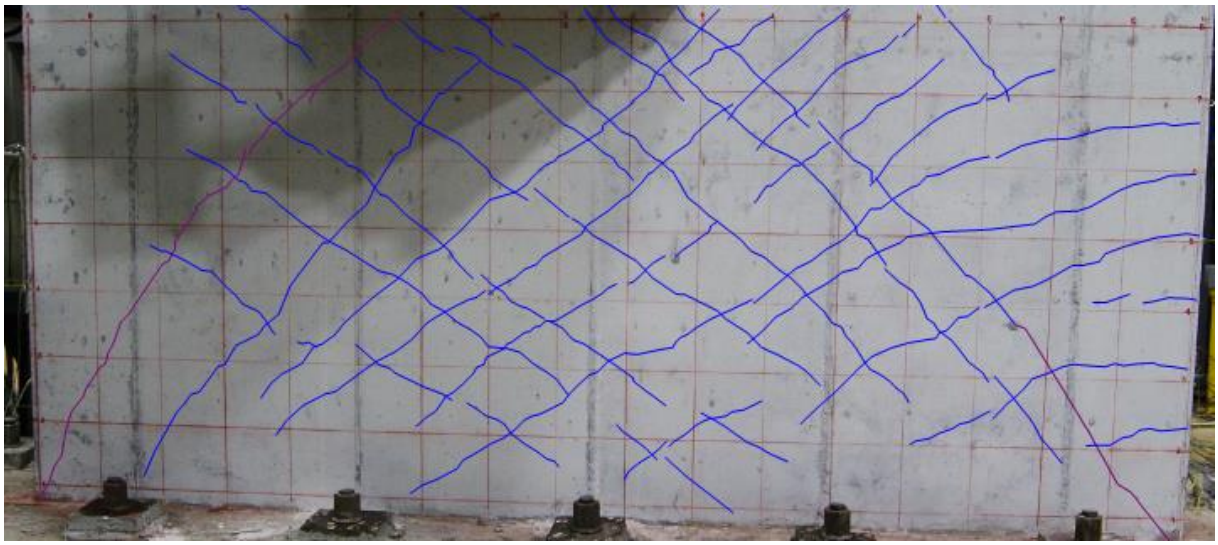

Figure 4-29. SW10 after load step LS5, load step at peak shear strength, peak transient drift ratio of 0.42 %

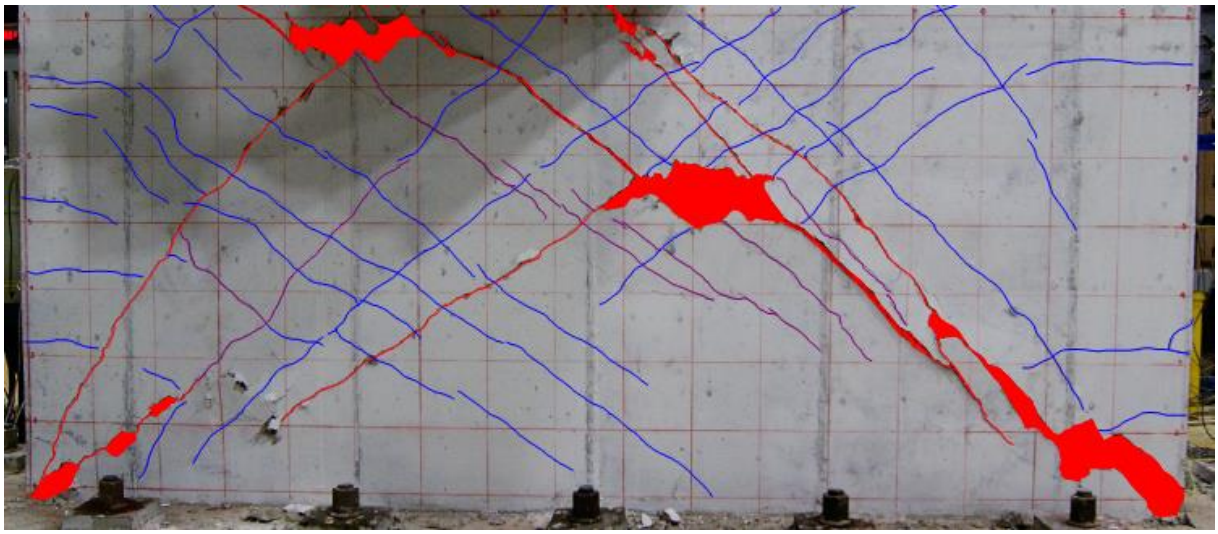

Figure 4-30. SW10 after load step LS8, final load step, peak transient drift ratio of 0.95 %

Table 4-21. Damage sustained by SW11[1]

$\left(h_w/l_w = 0.54, \rho_l = 0.67\%, \rho_t = 0.67\%, \rho_{be} = 1.50\%, f_c^{'} = 5000 \text{ psi}, V_{max} = 424 \text{ kips at LS5}\right)$

Damage at zero lateral load[2]	Load Step (LS)	Drift ratio[1] (%)	V_{ave} (kips)	$\frac{V_{ave}}{V_{max}}$	$\frac{V_{ave}}{A_w}$ (psi)	$\frac{V_{ave}}{A_w\sqrt{f_c^{'}}}$
Visible cracking	2	0.09	208	0.50	217	3.06
0.02 in $\leq w <$ 0.04 in	5	0.57	415	0.98	432	5.99
0.04 in $\leq w \leq$ 0.125 in	6	0.75	407	0.96	424	6.00
Vertical cracks in toe regions	7	0.93	394	0.93	410	5.80
Concrete crushing in toe regions	8	1.30	403	0.95	420	5.94
Sliding at the base	9	1.82	272	0.64	283	4.01

1. Peak transient drift ratio prior to damage measured at a zero lateral load
2. The following damage states were not observed during testing: cracks with widths greater than 0.125 inch and widespread crushing of concrete

Table 4-22. Length and areal density for SW11 at zero lateral load following LS5 and LS7[1]

Load step	Drift ratio[2] (%)	Crack width, w	Crack length $(inch)$	Areal density (in/ft^2)
LS5[3]	0.57	w $\leq$ 0.02 in	1215	22.4
		0.02 in $< w <$ 0.125 in	0	0.0
LS7[4]	0.93	w $\leq$ 0.02 in	1284	23.7
		0.02 in $< w <$ 0.125 in	38	0.7

1. Crack lengths measured using Bluebeam Revu
2. Peak transient drift ratio
3. Load step related to crack widths crossing the threshold of 0.02 inch and peak shear strength
4. Two load steps after peak shear strength

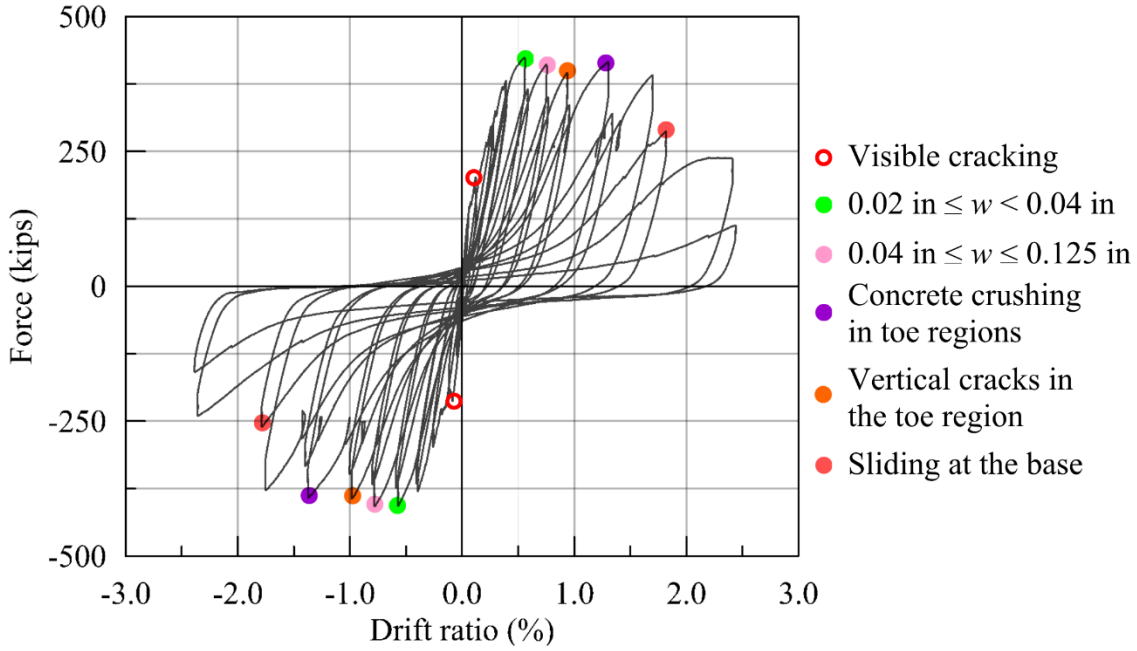

Figure 4-31. Force-drift relationship for SW11

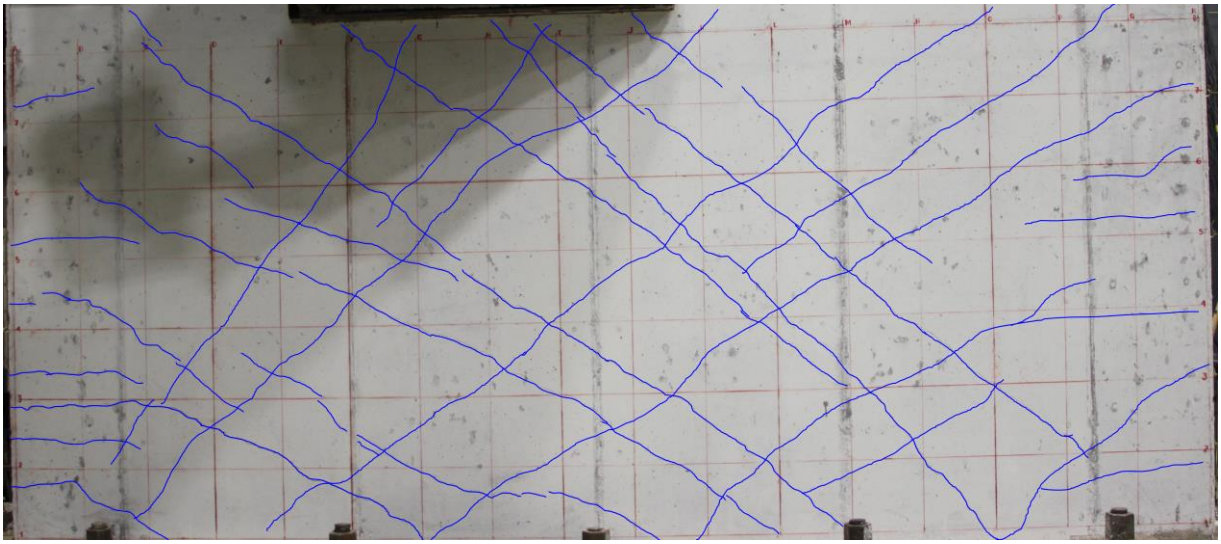

Figure 4-32. SW11 after load step LS5, load step at peak shear strength, peak transient drift ratio of 0.54%

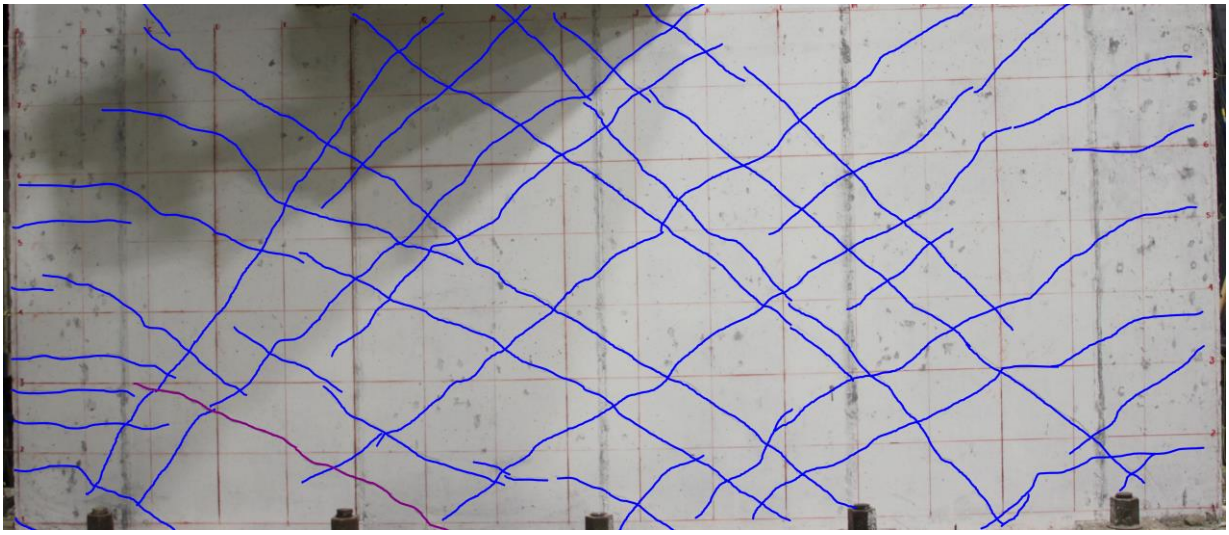

Figure 4-33. SW11 after load step LS7, peak transient drift ratio of 0.93%

Table 4-23. Damage summary for SW12[1]

$\left(h_w/l_w = 0.54, \rho_l = 0.33\%, \rho_t = 0.33\%, \rho_{be} = 2.00\%, f_c^{'} = 5000 \text{ psi}, V_{max} = 416 \text{ kips at LS8}\right)$

Damage at zero lateral load[2]	Load Step (LS)	Drift ratio[1] (%)	V_{ave} (kips)	$\frac{V_{ave}}{V_{max}}$	$\frac{V_{ave}}{A_w}$ (psi)	$\frac{V_{ave}}{A_w\sqrt{f_c^{'}}}$
Visible cracking	1	0.03	102	0.25	106	1.50
0.02 in $\leq w <$ 0.04 in	5	0.54	358	0.86	373	5.27
0.04 in $\leq w \leq$ 0.125 in	7	0.90	366	0.88	381	5.39
Concrete crushing in toe regions	8	1.27	384	0.92	400	5.66
Sliding at the base	9	1.64	353	0.85	368	5.20
$w >$ 0.125 in	9	1.64	353	0.85	368	5.20

1. Peak transient drift ratio prior to damage measured at a zero lateral load
2. The following damage states were not observed during testing: vertical cracks in toe regions and widespread crushing of concrete

Table 4-24. Length and areal density for SW12 at zero lateral load following LS5 and LS9

Load step	Drift ratio[1] (%)	Crack width, w	Crack length (inch)	Areal density (in/ft^2)
LS5[2]	0.54	$w < 0.02$ in	752	13.9
		0.02 in $\leq w <$ 0.125 in	0	0.00
LS9[3]	1.64	$w < 0.02$ in	497	8.70
		0.02 in $\leq w <$ 0.125 in	382	7.05

1. Peak transient drift ratio
2. Load step related to crack widths crossing the threshold of 0.02 inch
3. One load step after peak shear strength

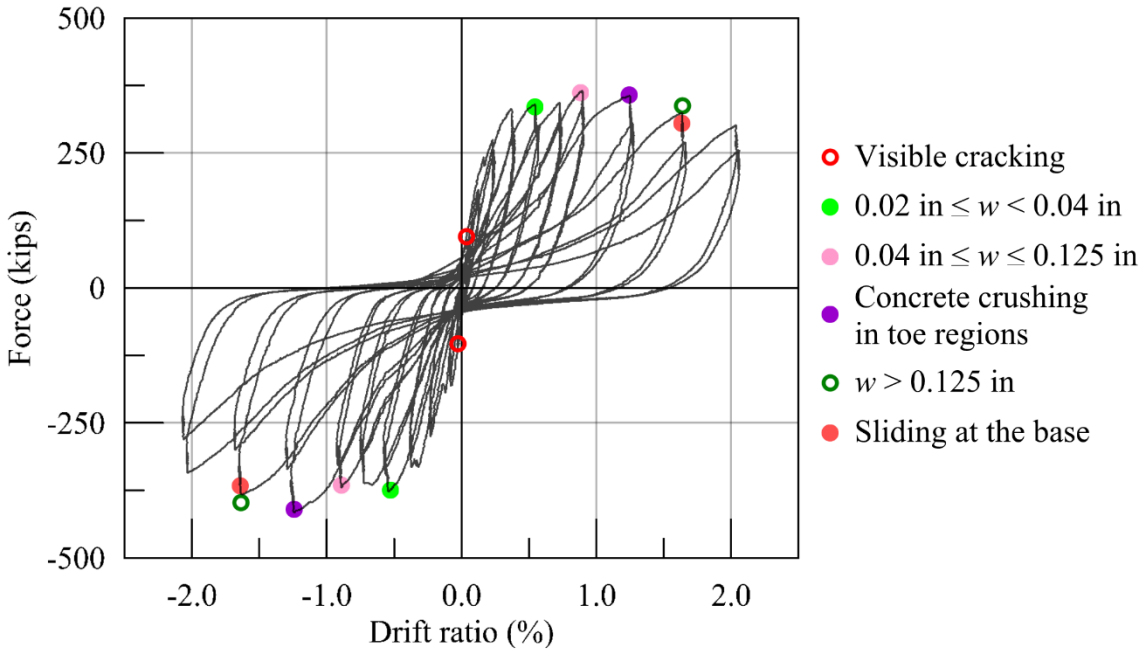

Figure 4-34. Force-drift relationship for SW12

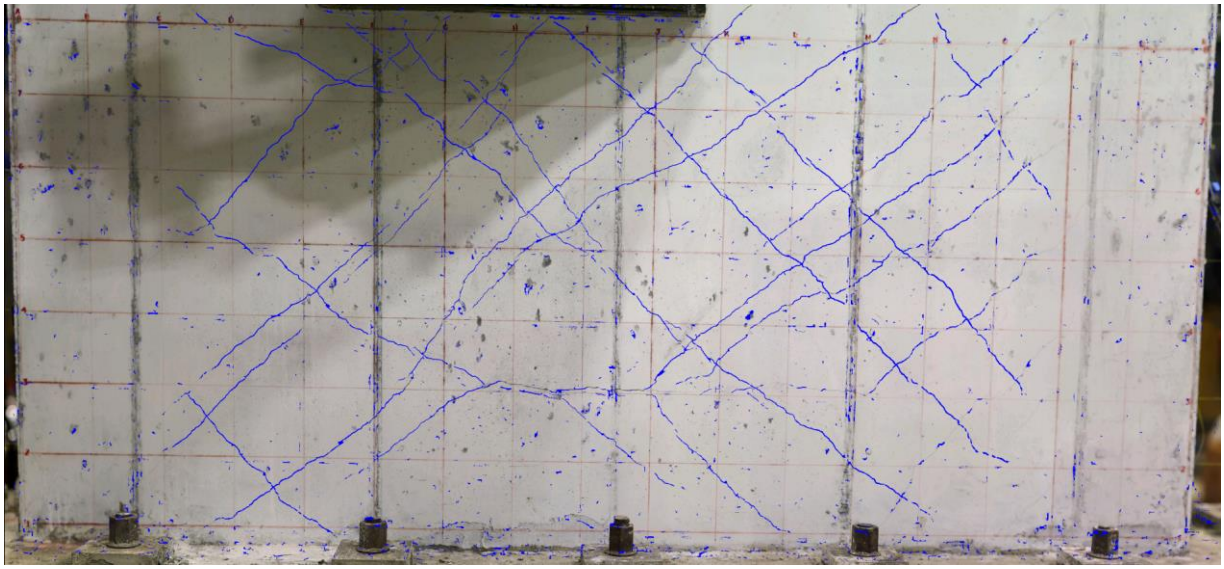

Figure 4-35. SW12 after load step LS5, peak transient drift ratio of 0.54%

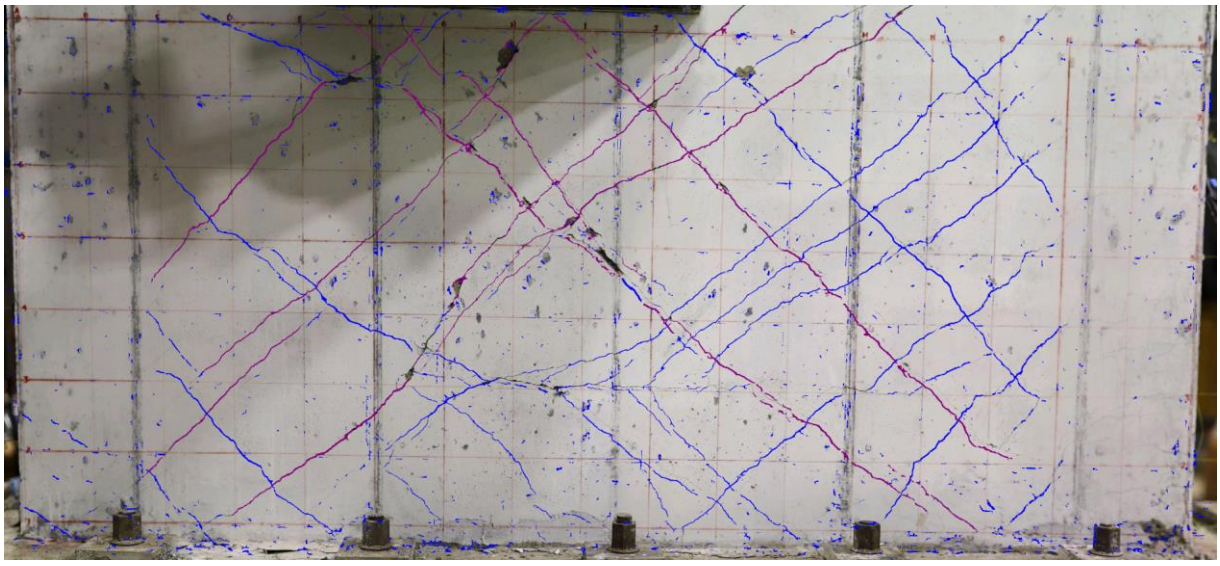

Figure 4-36. SW12 after load step LS9, peak transient drift ratio of 1.64%

4.3 Relating damage states to shear strength

A goal of repairing an earthquake-damaged wall is to restore its pre-earthquake strength and stiffness. The challenge facing the engineer inspecting an earthquake-damaged wall is to determine whether the strength and stiffness of the wall has been compromised, namely, has the deformation associated with peak strength been exceeded. If peak strength has not been achieved (or the earthquake-induced drift was smaller than that associated with peak strength), there is likely no reason to execute a structural repair. Prior to this test program there are no data relating observed damage to pre-peak- and post-peak-strength response.

This section correlates damage observed on walls SW1 through SW12 at zero lateral force (mimicking the post-earthquake condition), the shear force resisted in the load cycle prior to the reported displacement associated with zero lateral load and the peak transient drift ratio immediately prior to the displacement associated with zero lateral load when the damage state is reported. The peak transient drift ratio is reported to aid in the development of fragility functions, see Chapter 5.

Damage observed at zero lateral loading in SW1 through SW12 included 1) visible cracking, 2) cracks with width greater than or equal to 0.02 inch, 3) cracks with width greater than or equal to 0.04 inch, 4) crushing of concrete in the toe regions, and 5) sliding at the base of the wall. Three damage states: wide diagonal cracks (cracks with width greater than 0.125 inch), widespread crushing of concrete, and vertical cracking in the toe regions, were observed in five, three and two walls, respectively. These damage states occurred at drift ratios associated with peak shear strength or post-peak shear strength and require a repair method to restore the wall to its pre-earthquake

condition. Buckling of reinforcement and reinforcement fracture were not observed in any specimen and so are associated with drift ratios greater than those associated with peak strength, for which repair is needed to restore the pre-earthquake condition.

4.3.1 Onset of visible cracking

The damage observed first for all specimens was visible cracking and it occurred prior to peak shear strength in all walls. Most of these cracks were inclined at approximately 45 degrees to the horizontal and observed at mid-length of the wall (see Figure 4-37). Some walls also developed flexural cracks: see the photograph of the flexure-critical wall SW1 in Figure 4-38. Figure 4-39 presents the ratio of the average shear force (V_{ave}) to the peak shear force (V_{max}), as defined previously in Section 4.2, at the onset of visible cracking. The range is 0.1 to 0.5, with an average value of 0.3. The outlier in Figure 4-39 is wall SW8, which had vertical and horizontal reinforcement ratios of 1.5%. Webs of walls with high vertical and horizontal reinforcement ratios, and closely spaced reinforcement, are expected to develop many more but much narrower cracks than walls with low reinforcement ratios. Accordingly, the drift at the onset of visible cracking in SW8 is substantially greater than that for the other walls tested.

4.3.2 Crack widths at zero lateral load of greater than or equal to 0.02 inch

The second state of damage observed in all of the walls was cracks with a width upon unloading (i.e., at zero lateral load) of greater than or equal to 0.02 inch. This lower bound (0.02 inch) is one of two thresholds given by Gulec et al. (2009) for epoxy-resin injection. The damage

state was associated with one or more cracks on a wall with a width at zero lateral force of 0.02 inch or greater. Cracks with a width in the unloaded condition of 0.02 inch were observed in load

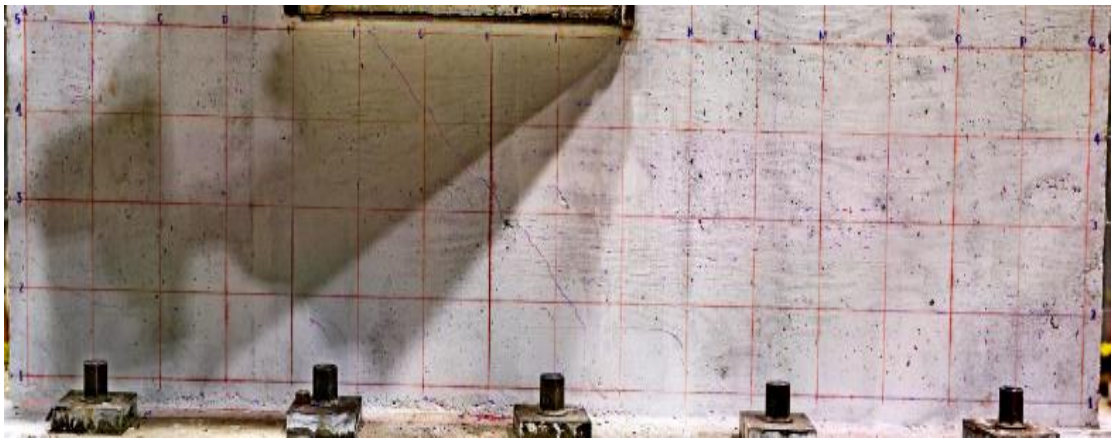

Figure 4-37. Onset of visible cracks, SW7, after LS3 (peak transient drift ratio of 0.08%)

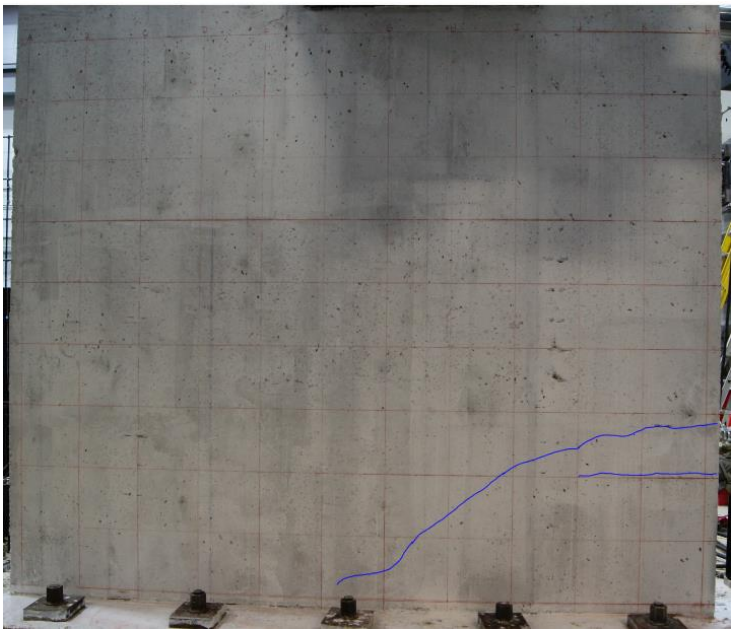

Figure 4-38. Shear and flexural cracks, SW1, after LS2 (peak transient drift ratio of 0.06%)

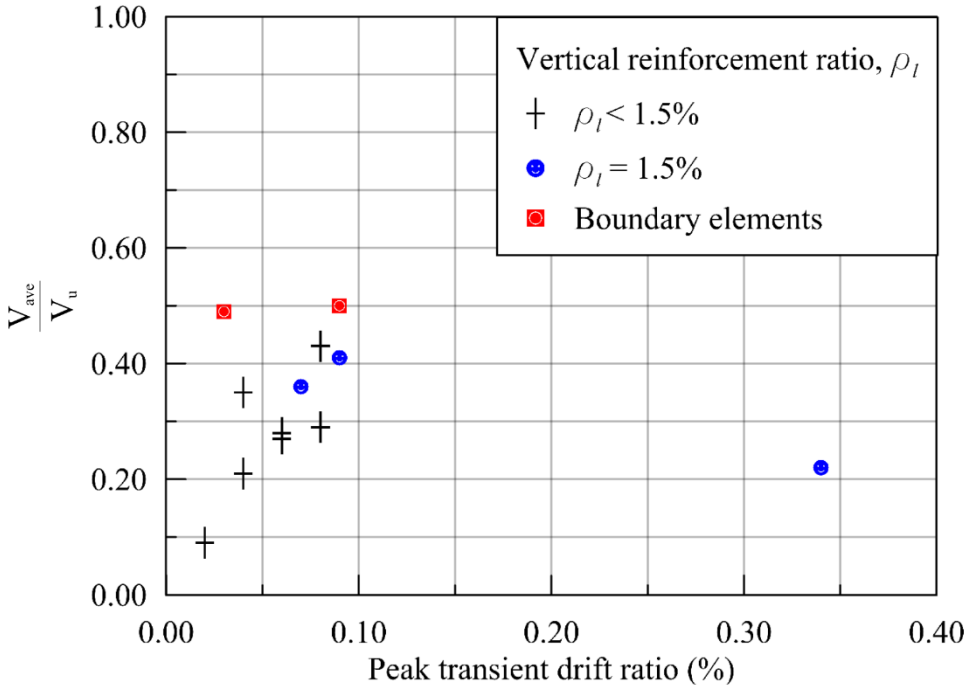

Figure 4-39. Damage data at the onset of visible cracking

steps at or less than that associated with peak shear strength in 11 of the 12 walls. Figure 4-40 presents the ratio of the average shear force (V_{ave}) to the peak shear force (V_{max}) as a function of peak transient drift ratio for cracks with width of greater than or equal to 0.02 inch in the unloaded condition for walls SW1 to SW7 and SW9 to SW12. Data for SW8 is not shown in Figure 4-40 because this damage state was observed at a displacement greater than that associated with peak shear strength. (Cracks widths in SW8 were narrower than in the other 11 walls for the reason given in the Section 4.3.1.) The data presented in Figure 4-40 is parsed by web vertical reinforcement ratio (ρ_l) and the presence of in-plane boundary elements.

Cracks with a width of greater than or equal to 0.02 inch in the unloaded condition were first observed at pre-peak loads between $0.83V_{max}$ and $0.99V_{max}$ for walls SW1 – SW7, SW9 and

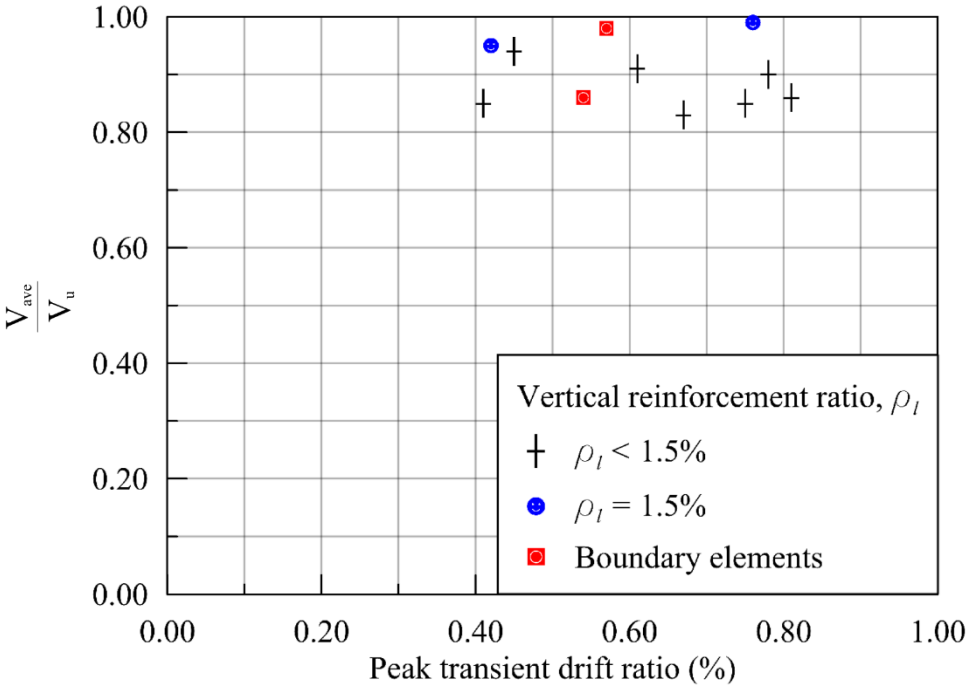

Figure 4-40. Damage data for first crack width greater than or equal to 0.02 inch

SW10. The pre-peak loads that produced cracks with width of 0.02 inch and greater in walls SW11 and SW12 (i.e., walls with in-plane boundary elements) were $0.98V_{max}$ and $0.86V_{max}$ respectively. The average value of the lateral load that triggered this limit state was $0.90V_{max}$

4.3.3 Crack widths at zero lateral load of greater than or equal to 0.04 inch

Another threshold used by the design professional community for the epoxy-resin injection is crack width of 0.04 inch. Cracks with width greater than or equal to 0.04 inch at zero lateral loading were first observed at displacements near or at those associated with peak shear strength. In walls SW1, SW4, SW11 and SW12, cracks with width greater than 0.04 inch in the unloaded condition were first observed prior peak shear strength. In walls SW2, SW3, SW5 and SW10, cracks with width greater than or equal to 0.04 inch in the unloaded condition were first observed

in the load step associated with peak shear strength. For walls SW6, SW7 and SW9, such cracks in the unloaded condition were first observed in the load steps following that to peak shear strength. The widths of the cracks in SW8 were less than 0.04 inch in the unloaded condition in all load steps.

Figure 4-41 presents the ratio of the average shear force (V_{ave}) to the peak shear force (V_{max}) as a function of peak transient drift ratio for cracks with width of greater than or equal to 0.04 inch in the unloaded condition for walls SW1 to SW7 and SW9 to SW12. The data of Figure 4-41 is parsed by loading stage at which this damage was first observed.

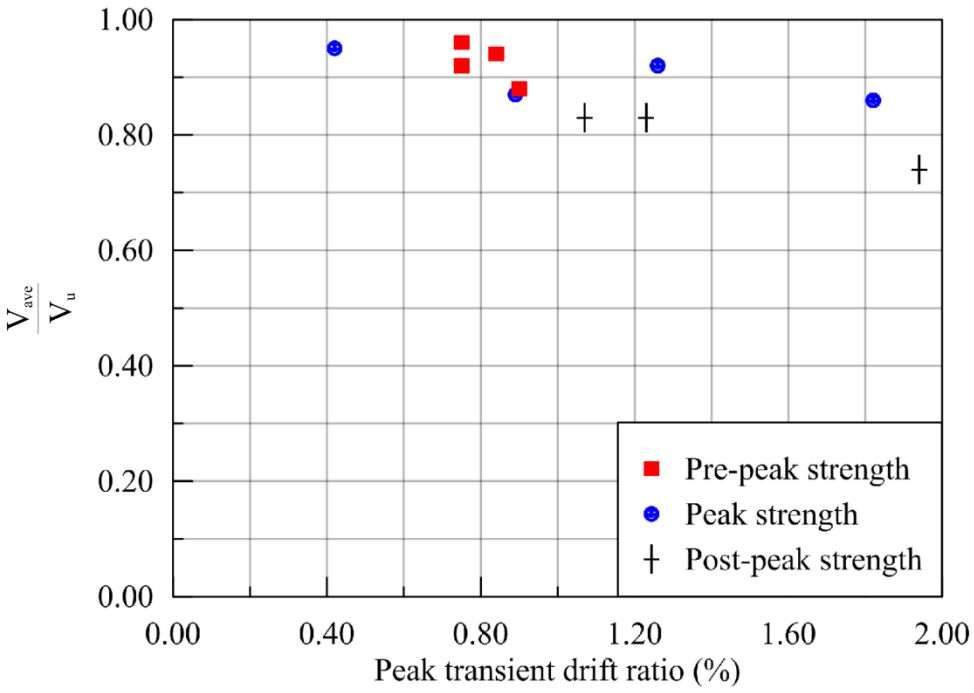

Figure 4-41. Damage data for first crack width greater than 0.04 inch

4.3.4 Concrete crushing in the toe regions

Crushing of concrete in the toe regions was observed in all walls. This damage was observed in load steps immediately prior to, at, or following the load step to peak strength. Figure 4-42 presents the ratio of average (V_{ave}) to peak $(V_{\max})$ shear force versus peak transient drift ratio for the first crushing of concrete. The data are parsed by web vertical reinforcement ratio (ρ_l). For the walls with a vertical reinforcement ratio of less than 1.5% (walls SW1 to SW7), this damage was first observed at displacements greater than that associated with peak shear strength. Crushing of concrete in walls SW8, SW9 and SW10, each with a vertical web reinforcement ratio of 1.5%, was first observed in load steps prior to that associated with peak shear strength. Concrete crushing was observed in the walls with boundary elements, SW11 and SW12, at displacements greater than those associated with peak shear strength.

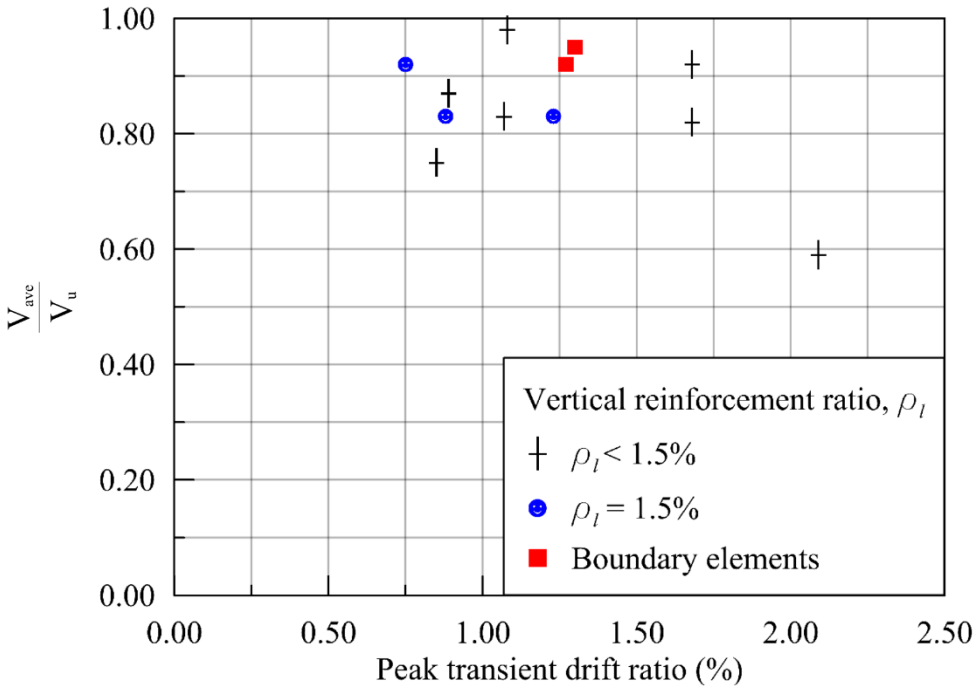

Figure 4-42. Damage data for crushing of concrete in toe regions

4.3.5 Sliding at the base

Sliding of the wall panel atop its foundation was observed in 11 of the 12 walls. Sliding was identified by observation and/or evaluation of the shape of the global force-drift hysteresis loops. Typical physical evidence included a single large crack and/or significant spalling along the base of the wall. High-resolution images were also used to determine whether sliding had taken place. Lateral force-displacement relationships with near-zero stiffness at zero lateral displacement (drift) were associated with sliding. None of the walls slid at the base before peak shear strength was achieved.

Figure 4-43 presents the ratio of average (V_{ave}) to peak $(V_{\max})$ shear force versus peak transient drift ratio at the first occurrence of sliding. The data is parsed by wall web vertical reinforcement ratio (ρ_l).

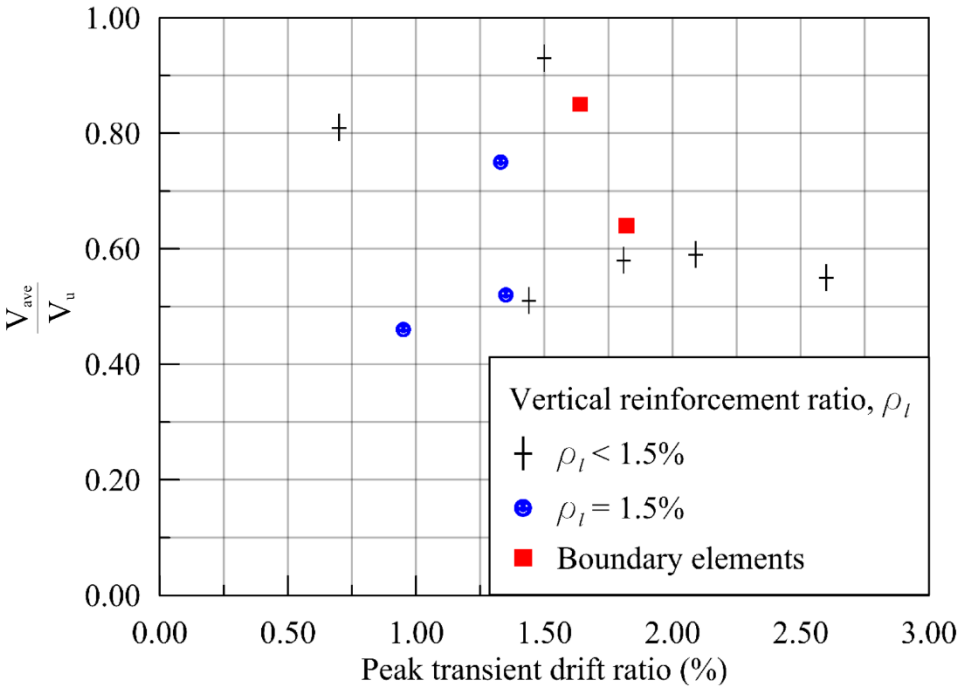

Figure 4-43. Damage data for initiation of base sliding

4.4 An investigation of crack propagation in SW1 to SW12

Reporting of previous experimental programs has included widths of cracks at peak transient displacement or a maximum crack width without specifying the corresponding loading. Missing from these experimental programs is the reporting of a) cracks and widths at multiple locations on the wall and b) crack widths at displacements associated with zero lateral loading. Information on crack width at zero lateral loading is important because this mimics the post-earthquake condition of a wall.

This section investigates the relationship between widths of cracks at 1) peak transient displacement, and 2) the displacement associated with zero lateral force upon subsequent unloading. Cracks and their widths were measured at these displacements for all 12 walls. The locations where measurements were taken varied as a function of load step.

One table and four or five figures are provided for each wall. The table (Crack width data, in inch, for SW*) presents crack widths at peak transient displacement and the subsequent displacement associated with zero loading. The information below the title of the table provides information regarding the mechanical and geometric properties of the wall, the peak shear force and the load step when the peak shear force occurred. The load steps chosen for each wall correspond to 1) approximately half of the displacement associated with peak shear strength, 2) the displacement associated with peak shear strength, and 3) approximately two to three times the displacement associated with peak shear strength or the final load step. Information at a load step beyond peak strength is not provided for SW5 because testing was terminated immediately following the cycles to peak strength. The table presents the ratio of the crack width at peak

transient displacement to the crack width at the subsequent displacement associated with zero lateral loading, w_p / w_r, which is denoted as crack width ratio. The average of this ratio is presented for each load step and for each wall.

The first figure (First quadrant of the force-drift relationship for SW*) presents the first quadrant of the cyclic response for each wall, as measured in terms of in-plane lateral force versus the in-plane drift ratio (lateral displacement divided by the height from centerline of loading to top the foundation block). Highlighted in purple are the first quadrant responses corresponding to the load steps identified in the table. The open and solid circles on the *x* axis in each force-drift ratio relationship identifies the displacements at which crack widths were measured during testing.

The remaining figures presented for each wall highlight the crack patterns for each load stage during peak transient displacement. Cracks highlighted in blue have a width less than 0.02 inch. Cracks highlighted in purple have a width between 0.02 inch and 0.125 inch. Cracks highlighted in red have a width greater than 0.125 inch. Areas of significant spalled of concrete are shaded in red. The letters on each figure identify monitoring locations where crack widths were measured and reported in the table for each wall.

Table 4-25. Crack width data, in inch, for SW1

$\left(h_w/l_w = 0.94, r_l = 0.67\%, r_t = 0.67\%, f_c' = 3600 \text{ psi}, V_{max} = 253 \text{ kips in LS9}\right)$

	LS7[1]			LS9[2]			LS10[3]		
Crack ID[4]	$w_{p,7}$[5]	$w_{r,7}$[6]	$\frac{w_{p,7}}{w_{r,7}}$	$w_{p,9}$[5]	$w_{r,9}$[6]	$\frac{w_{p,9}}{w_{r,9}}$	$w_{p,10}$[5]	$w_{r,10}$[6]	$\frac{w_{p,10}}{w_{r,10}}$
A	0.016	0.007	2.29	0.031	0.005	6.20	0.039	0.005	7.80
B	0.010	0.007	1.43	0.033	0.005	6.60	0.040	0.005	8.00
C	0.010	0.005	2.00	0.032	0.005	6.40	0.031	0.005	6.20
D	0.007	0.005	1.40	0.054	0.020	2.70	0.114	0.020	5.70
E	0.025	0.005	5.00	0.065	0.020	3.25	0.031	0.016	1.94
F	0.030	0.005	6.00	0.060	0.005	12.00	0.037	0.005	7.40
G	0.125	0.040	3.13	0.096	0.050	1.93	0.074	0.125	0.59
H	0.035	0.009	3.89	0.036	0.016	2.25	0.036	0.007	5.14
I	0.016	0.005	3.20	0.032	0.005	6.40	0.047	0.005	9.40
J	0.010	0.005	2.00	0.018	0.005	3.60	0.046	0.005	9.20
Average			3.03			5.13			6.14

1. Peak transient drift ratio = 0.63%
2. Peak transient drift = 1.30% (at peak shear strength)
3. Peak transient drift ratio = 2.10%
4. Monitoring location varies as a function of load step; see Figure 4-45 to Figure 4-47
5. Crack width at peak transient drift ratio
6. Crack width at zero lateral force in the same half cycle of loading (see Figure 4-44)

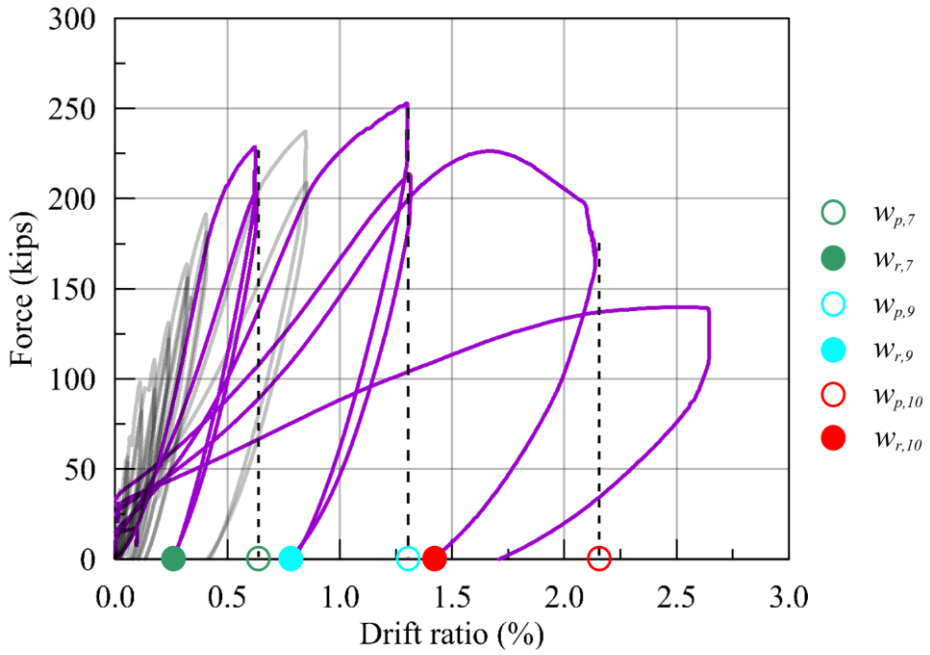

Figure 4-44. First quadrant of the force-drift relationship for SW1

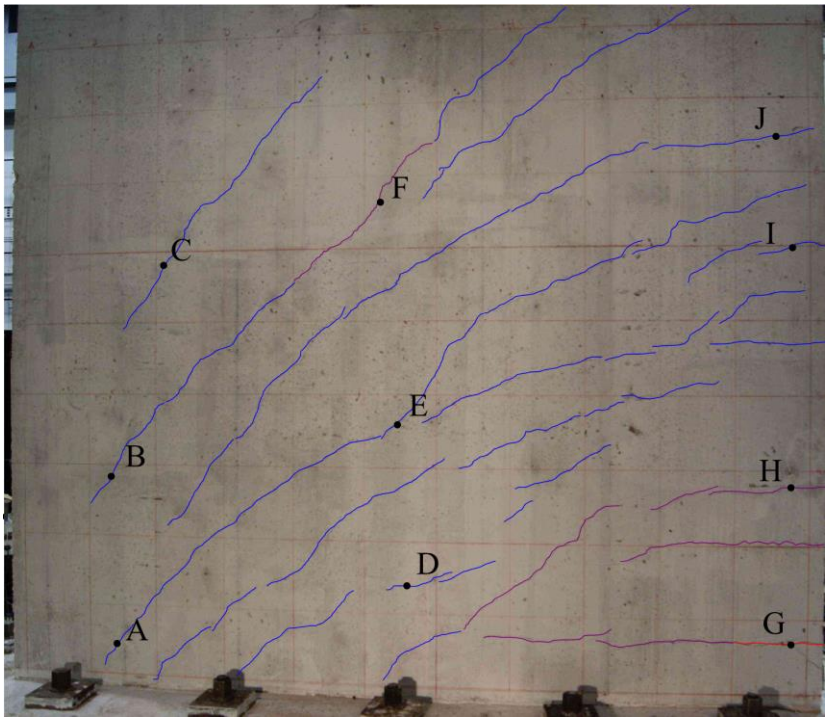

Figure 4-45. Crack width measurement locations SW1, LS7

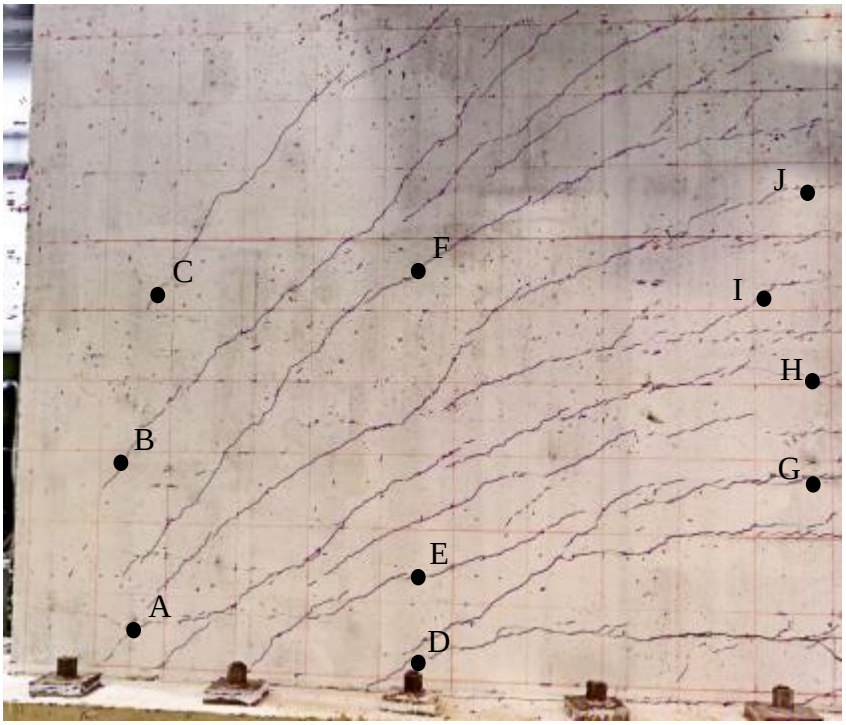

Figure 4-46. Crack width measurement locations for SW1, LS9

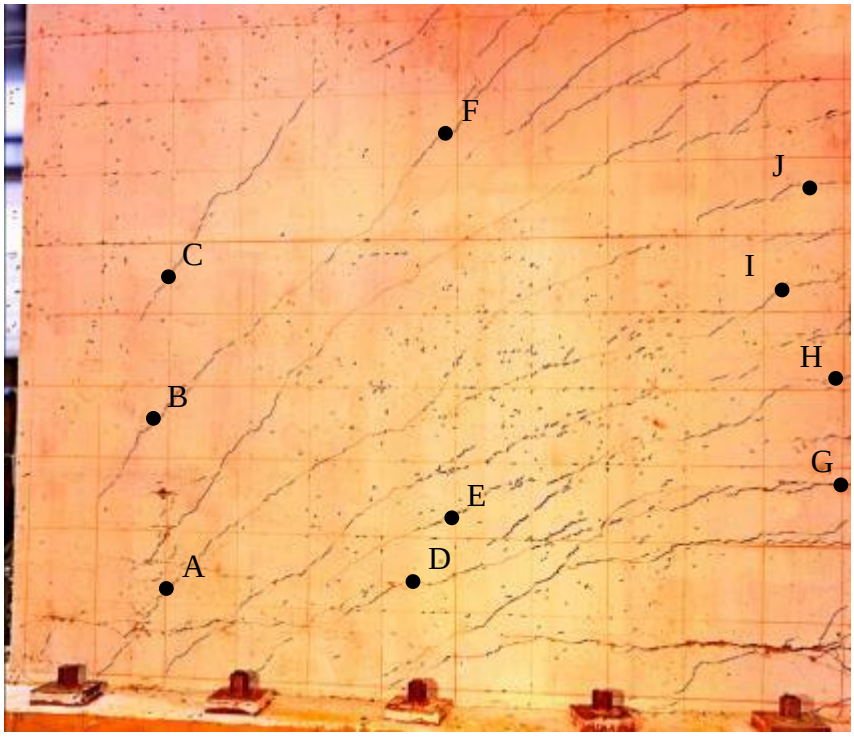

Figure 4-47. Crack width measurement locations for SW1, LS10

Table 4-26. Crack width data, in inch, for SW2

$\left(h_w/l_w = 0.54, \rho_l = 1.00\%, \rho_t = 1.00\%, f_c^{'} = 7000 \text{ psi}, V_{max} = 563 \text{ kips at LS10}\right)$

Crack ID[4]	LS8[1]			LS10[2]			LS11[3]		
	$w_{p,8}$[5]	$w_{r,8}$[6]	$\frac{w_{p,8}}{w_{r,8}}$	$w_{p,10}$[5]	$w_{r,10}$[6]	$\frac{w_{p,10}}{w_{r,10}}$	$w_{p,11}$[5]	$w_{r,11}$[6]	$\frac{w_{p,11}}{w_{r,11}}$
A	0.009	0.005	1.80	0.027	0.005	5.40	0.040	0.005	8.00
B	0.010	0.005	2.00	0.024	0.005	4.80	0.017	0.005	3.40
C	0.016	0.005	3.20	0.033	0.005	6.60	0.024	0.007	3.43
D	0.009	0.005	1.80	0.031	0.005	6.20	0.029	0.020	1.45
E	0.013	0.005	2.60	0.038	0.007	5.43	0.030	0.007	4.29
F	0.016	0.007	2.29	0.039	0.007	5.57	0.051	0.007	7.29
G	0.016	0.005	3.20	0.019	0.007	2.71	0.027	0.005	5.40
H	0.009	0.005	1.80	0.023	0.005	4.60	0.032	0.007	4.57
I	0.009	0.005	1.80	0.033	0.007	4.71	0.026	0.005	5.20
J	0.010	0.005	2.00	0.078	0.078	1.00	0.082	0.078	1.05
Average			2.25			4.70			4.41

1. Peak transient drift ratio = 0.49%
2. Peak transient drift = 1.26% (at peak shear strength)
3. Peak transient drift ratio = 2.23%
4. Monitoring location varies as a function of load step; see Figure 4-49 to Figure 4-51
5. Crack width at peak transient drift ratio
6. Crack width at zero lateral force in the same half cycle of loading (see Figure 4-48)

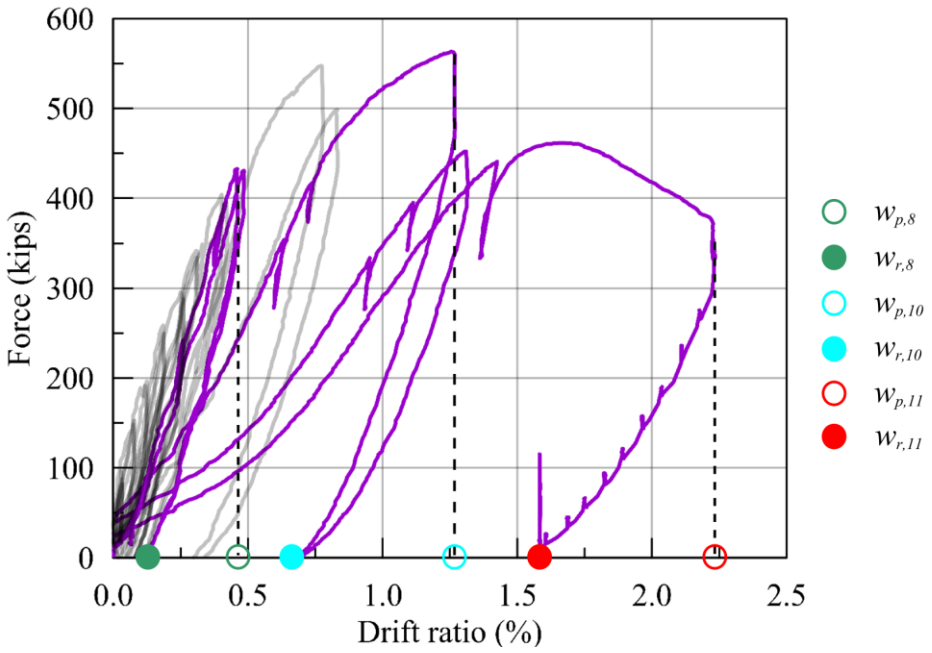

Figure 4-48. First quadrant of the force-drift relationship for SW2

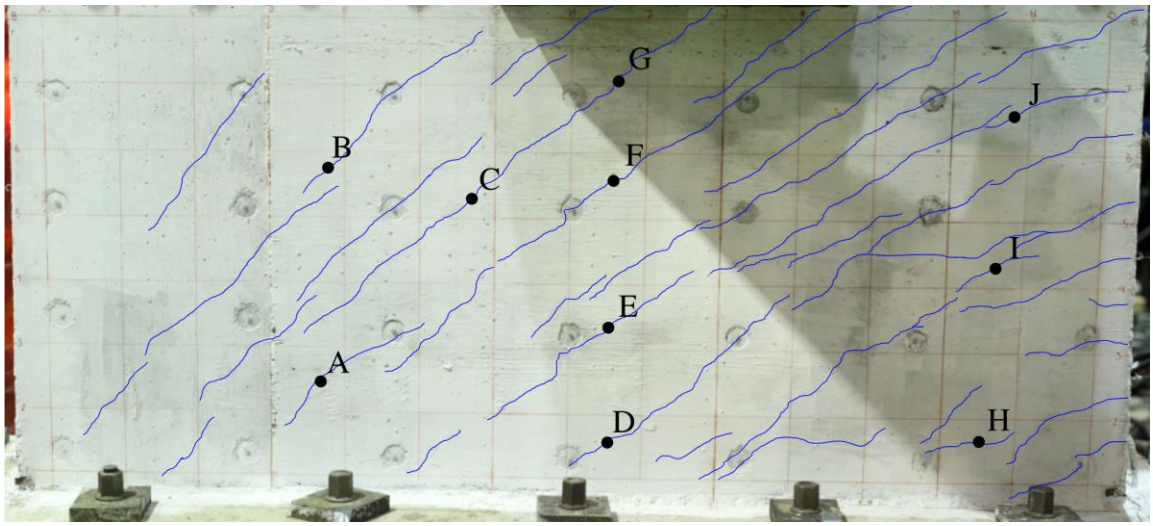

Figure 4-49. Crack width measurement locations for SW2, LS8

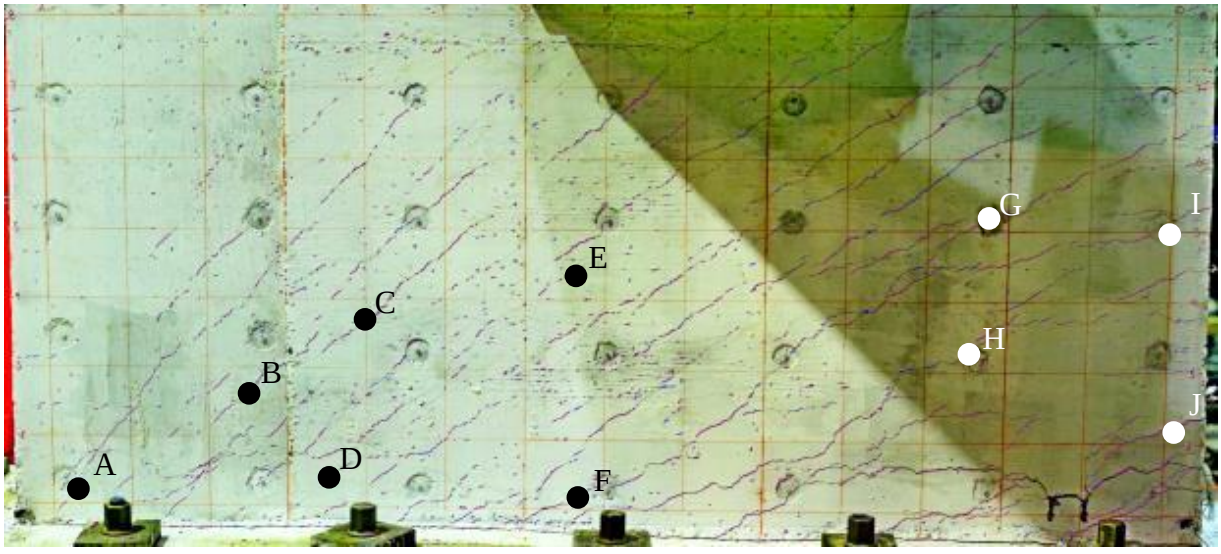

Figure 4-50. Crack width measurement locations for SW2, LS10

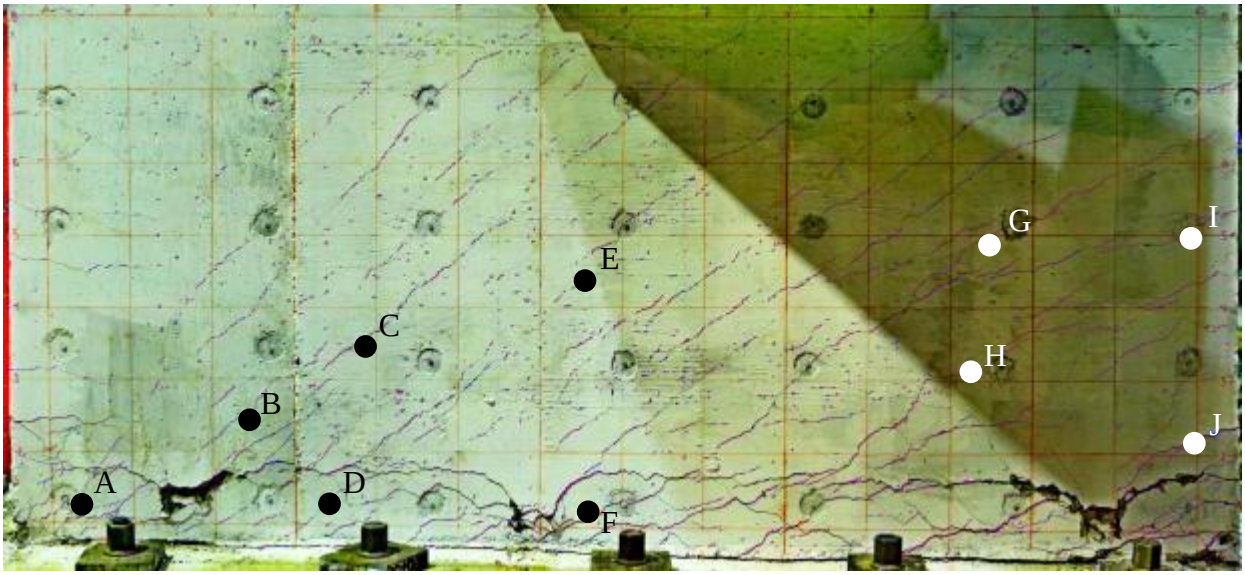

Figure 4-51. Crack width measurement locations for SW2, LS11

Table 4-27. Crack width data, in inch, for SW3

$\left(h_w/l_w = 0.54, \rho_l = 0.67\%, \rho_t = 0.67\%, f_c^{'} = 7800 \text{ psi}, V_{max} = 468 \text{ kips at LS12}\right)$

	LS11[1]			LS12[2]			LS13[3]		
Crack ID[4]	$w_{p,11}$[5]	$w_{r,11}$[6]	$\frac{w_{p,11}}{w_{r,11}}$	$w_{p,12}$[5]	$w_{r,12}$[6]	$\frac{w_{p,12}}{w_{r,12}}$	$w_{p,13}$[5]	$w_{r,13}$[6]	$\frac{w_{p,13}}{w_{r,13}}$
A	0.060	0.016	3.75	0.037	0.020	1.85	0.025	0.035	0.71
B	0.040	0.010	4.00	0.027	0.020	1.35	0.027	0.030	0.90
C	0.016	0.009	1.78	0.037	0.016	2.31	0.032	0.025	1.28
D	0.030	0.009	3.33	0.050	0.025	2.00	0.035	0.020	1.75
E	0.016	0.009	1.78	0.038	0.016	2.38	0.043	0.020	2.15
F	0.030	0.016	1.88	0.039	0.020	1.95	0.031	0.010	3.10
G	0.020	0.016	1.25	0.035	0.016	2.19	0.016	0.010	1.60
H	0.009	0.005	1.80	0.035	0.020	1.75	0.034	0.020	1.70
I	0.030	0.013	2.31	0.030	0.016	1.88	0.029	0.005	5.80
J	0.025	0.010	2.50	0.022	0.005	4.40	0.024	0.005	4.80
Average			2.44			2.21			2.38

1. Peak transient drift ratio = 1.10%
2. Peak transient drift = 2.10% (at peak shear strength)
3. Peak transient drift ratio = 2.90%
4. Monitoring location varies as a function of load step; see Figure 4-53 to Figure 4-55
5. Crack width at peak transient drift ratio
6. Crack width at zero lateral force in the same half cycle of loading (see Figure 4-52)

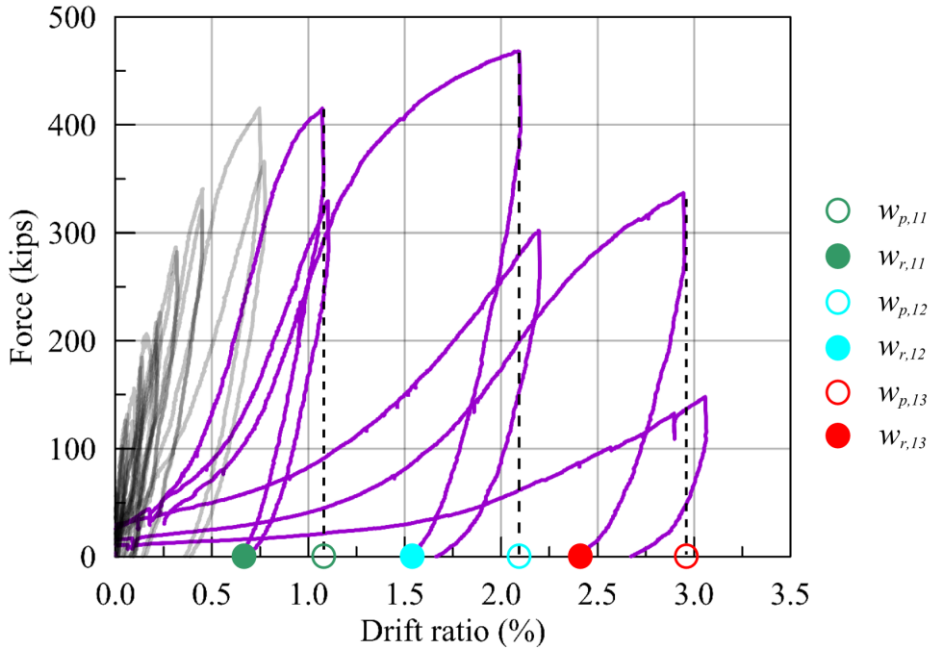

Figure 4-52. First quadrant of the force-drift relationship for SW3

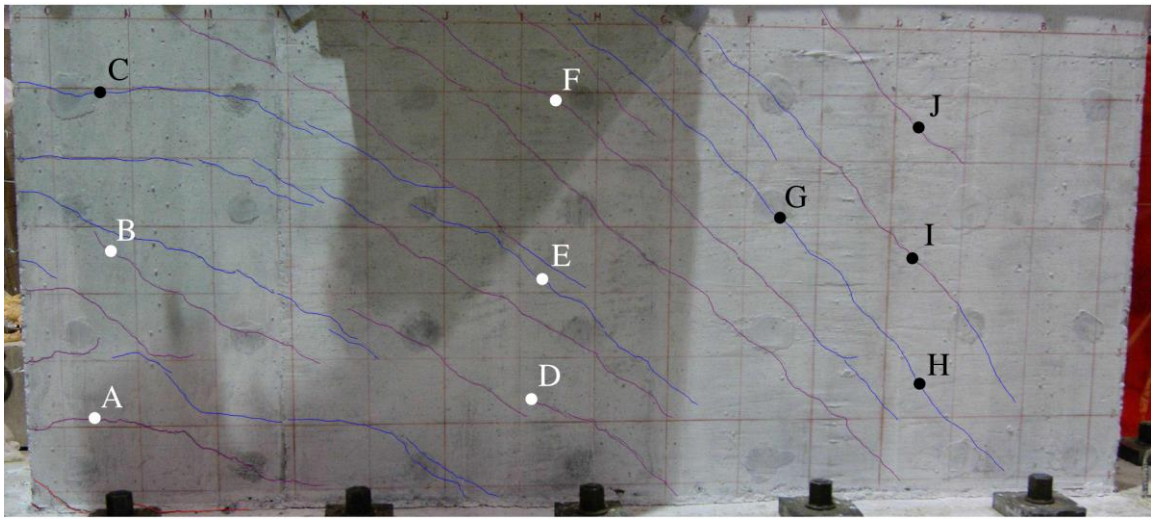

Figure 4-53. Crack width measurement locations for SW3, LS11

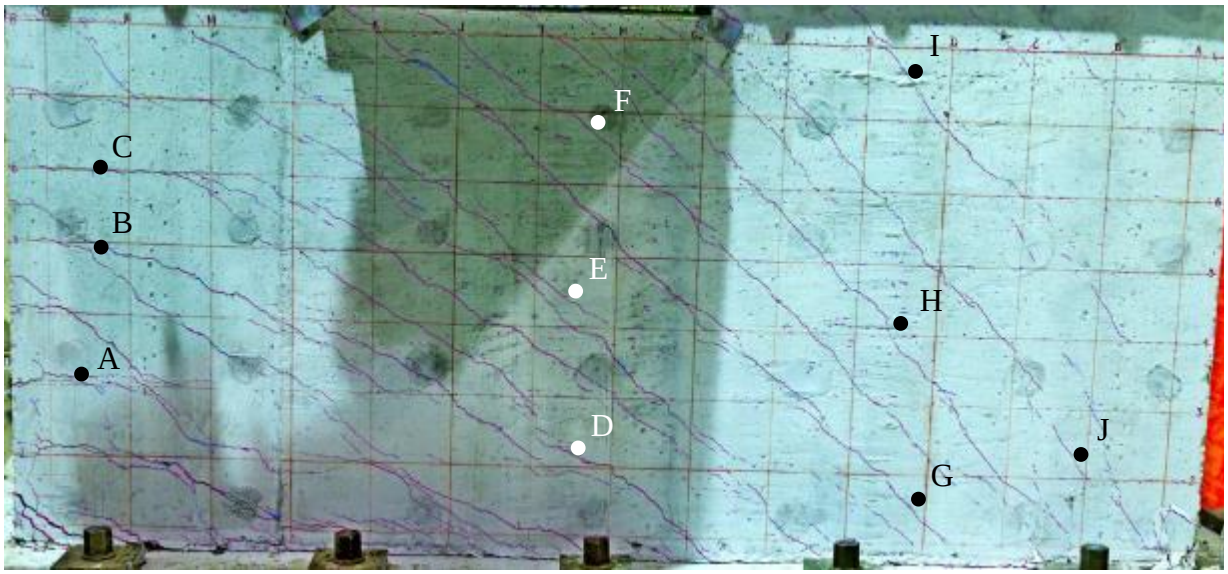

Figure 4-54. Crack width measurement locations for SW3, LS12

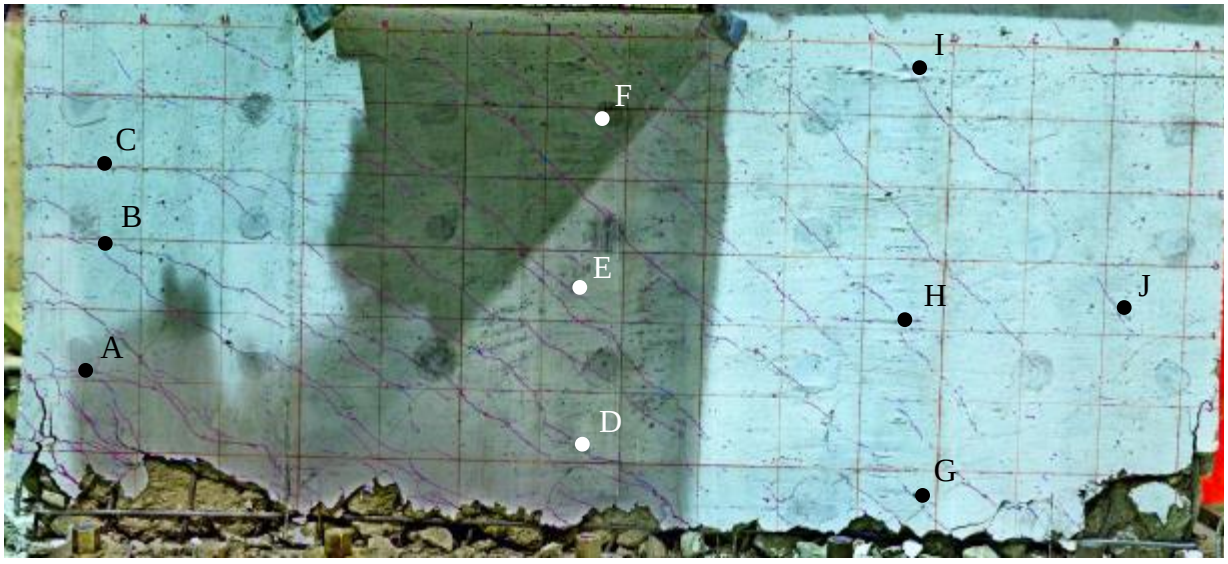

Figure 4-55. Crack width measurement locations for SW3, LS13

Table 4-28. Crack width data, in inch, for SW4

$\left(h_w/l_w = 0.54, \rho_l = 0.33\%, \rho_t = 0.33\%, f_c^{'} = 4200 \text{ psi}, V_{max} = 226 \text{ kips at LS12}\right)$

Crack ID[4]	LS10[1]			LS12[2]			LS14[3]		
	$w_{p,10}$[5]	$w_{r,10}$[6]	$\frac{w_{p,10}}{w_{r,10}}$	$w_{p,12}$[5]	$w_{r,12}$[6]	$\frac{w_{p,12}}{w_{r,12}}$	$w_{p,14}$[5]	$w_{r,14}$[6]	$\frac{w_{p,14}}{w_{r,14}}$
A	0.060	0.030	2.00	0.118	0.050	2.36	0.079	0.016	4.94
B	0.050	0.030	1.67	0.118	0.025	4.72	0.157	0.157	1.00
C	0.020	0.005	4.00	0.035	0.016	2.19	0.035	0.005	7.00
D	0.035	0.013	2.69	0.079	0.013	6.08	0.030	0.020	1.50
E	0.040	0.025	1.60	0.030	0.005	6.00	0.197	0.079	2.49
F	0.060	0.020	3.00	0.079	0.030	2.63	0.197	0.050	3.94
G	0.050	0.020	2.50	0.118	0.035	3.37	0.079	0.050	1.58
H	0.025	0.009	2.78	0.079	0.035	2.26	0.035	0.013	2.69
I	0.025	0.010	2.50	0.030	0.013	2.31	0.035	0.013	2.69
J	0.025	0.009	2.78	0.030	0.016	1.88	0.030	0.010	3.00
Average			2.55			3.38			3.08

1. Peak transient drift ratio = 0.60%
2. Peak transient drift = 1.11% (at peak shear strength)
3. Peak transient drift ratio = 2.29%
4. Monitoring location varies as a function of load step; see Figure 4-57 to Figure 4-59
5. Crack width at peak transient drift ratio
6. Crack width at zero lateral force in the same half cycle of loading (see Figure 4-56)

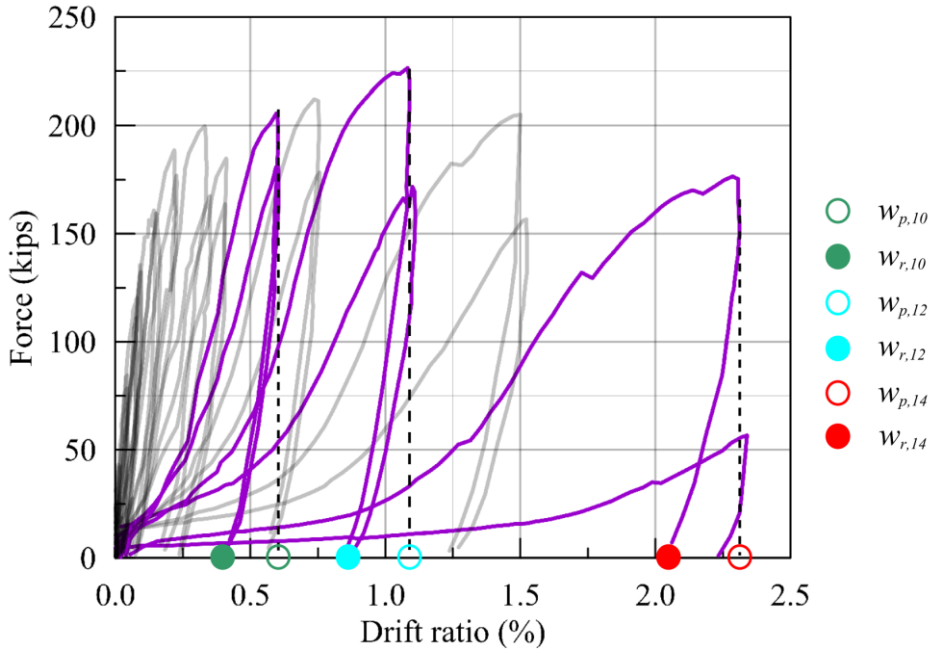

Figure 4-56. First quadrant of the force-drift relationship for SW4

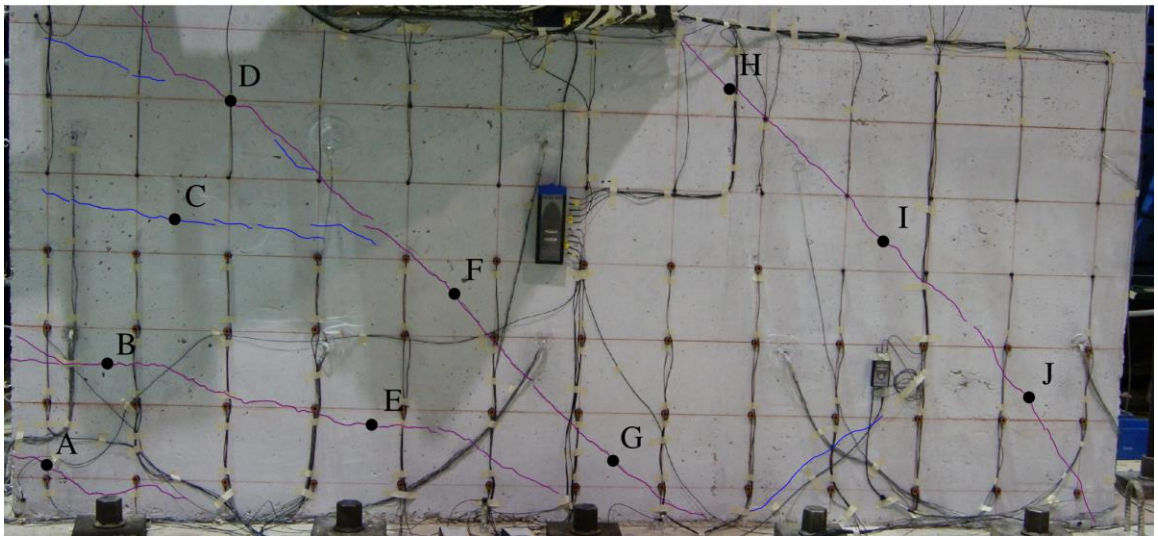

Figure 4-57. Crack width measurement locations for SW4, LS10

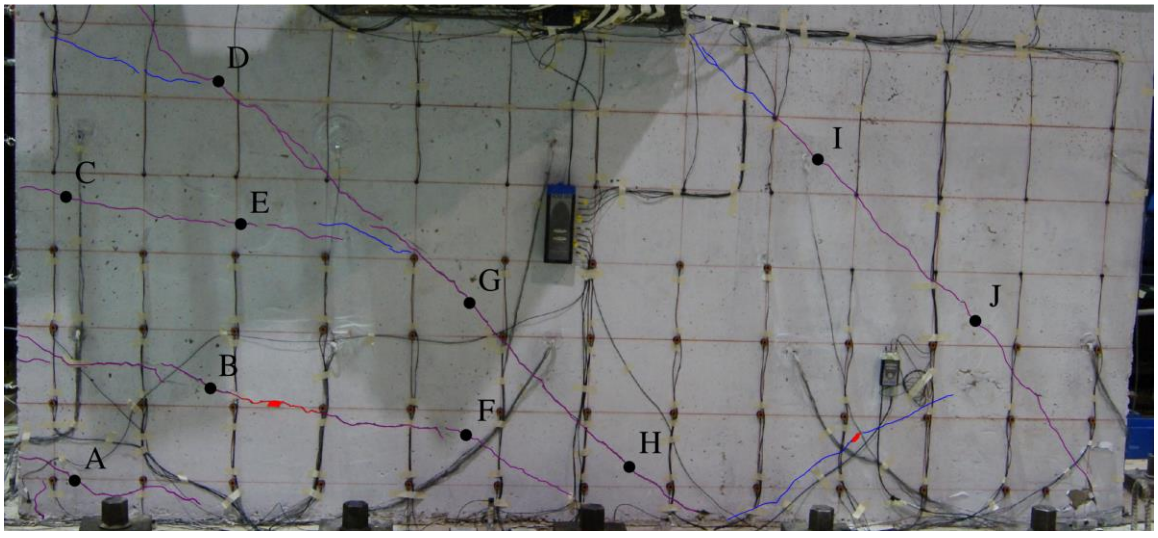

Figure 4-58. Crack width measurement locations for SW4, LS12

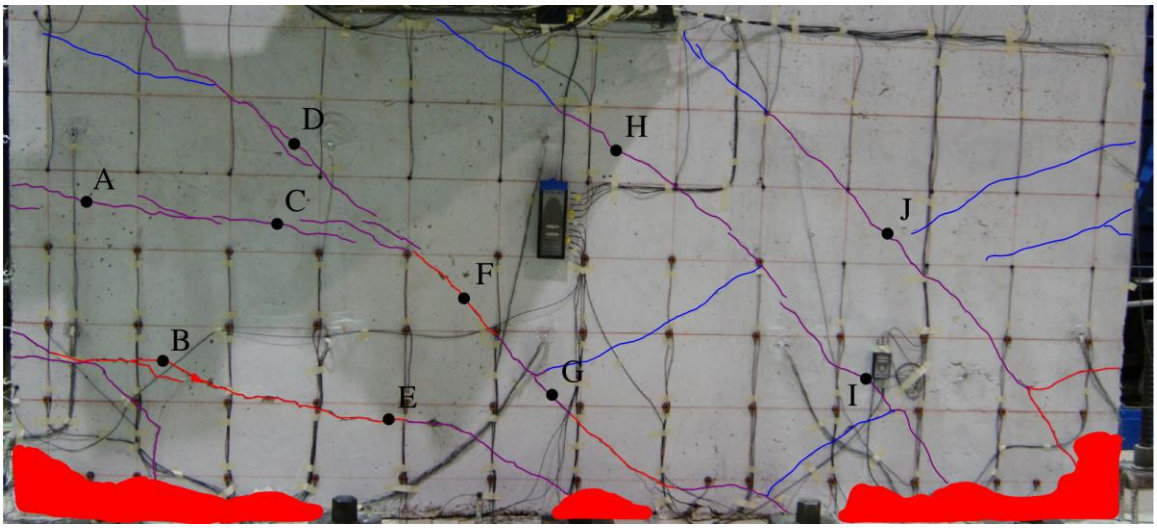

Figure 4-59. Crack width measurement locations for SW4, LS14

Table 4-29. Crack width data, in inch, for SW5

$\left(h_w/l_w = 0.33, \rho_l = 1.00\%, \rho_t = 1.00\%, f_c^{'} = 4300 \text{ psi}, V_{max} = 726 \text{ kips at LS8}\right)$

	LS7[1]			LS8[2]		
Crack ID[3]	$w_{p,7}$[4]	$w_{r,7}$[5]	$\frac{w_{p,7}}{w_{r,7}}$	$w_{p,8}$[4]	$w_{r,8}$[5]	$\frac{w_{p,8}}{w_{r,8}}$
A	0.035	0.013	2.69	0.034	0.030	1.13
B	0.013	0.005	2.60	0.029	0.009	3.22
C	0.020	0.005	4.00	0.026	0.005	5.20
D	0.013	0.005	2.60	0.030	0.016	1.88
E	0.020	0.005	4.00	0.027	0.007	3.86
F	0.016	0.005	3.20	0.032	0.009	3.56
G	0.020	0.005	4.00	0.028	0.009	3.11
H	0.010	0.007	1.43	0.032	0.007	4.57
I	0.020	0.005	4.00	0.026	0.007	3.71
J	0.013	0.007	1.86	0.026	0.005	3.20
Average			3.04			3.54

1. Peak transient drift ratio = 0.72%
2. Peak transient drift = 1.30% (at peak shear strength)
3. Monitoring location varies as a function of load step
4. Crack width at peak transient drift ratio; see Figure 4-61 and Figure 4-62
5. Crack width at zero lateral force in the same half cycle of loading (see Figure 4-60)

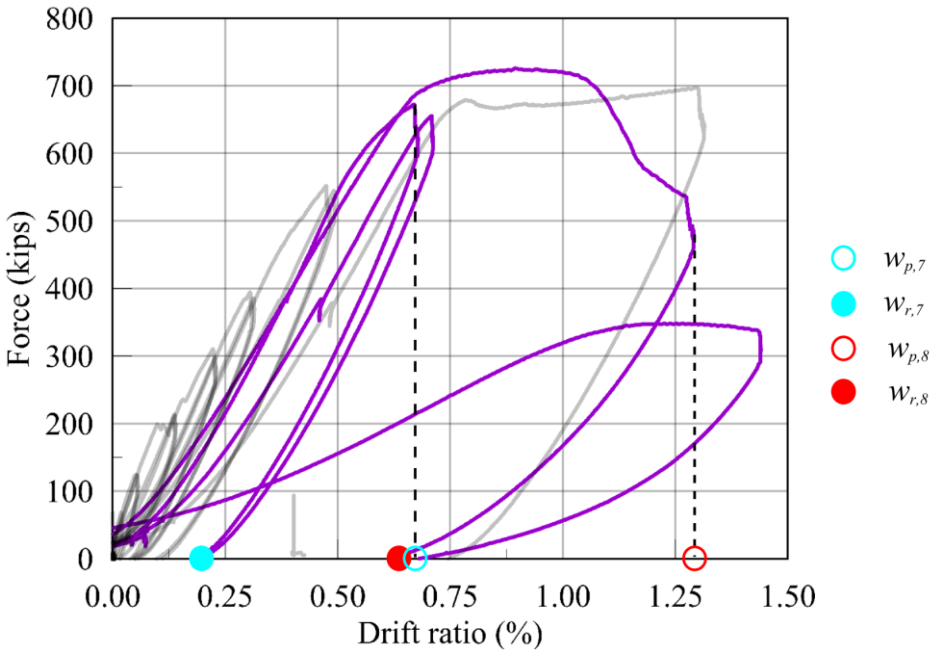

Figure 4-60. First quadrant of the force-drift relationship for SW5

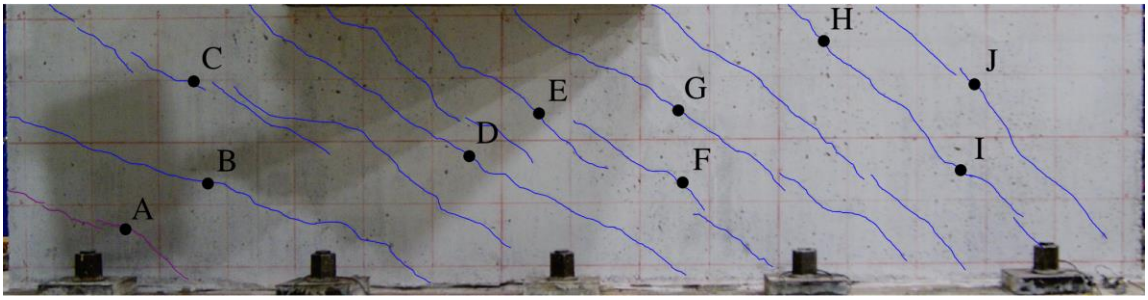

Figure 4-61. Crack width measurement locations for SW5, LS7

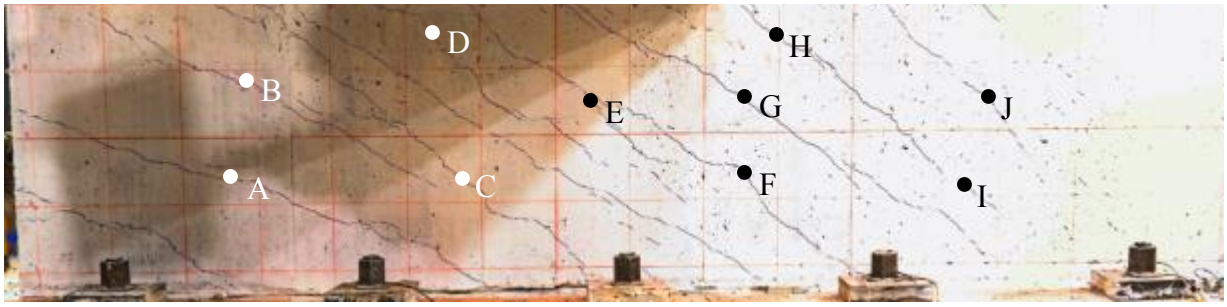

Figure 4-62. Crack width measurement locations for SW5, LS8

Table 4-30. Crack width data, in inch, for SW6

$\left(h_w/l_w = 0.33, \rho_l = 0.63\%, \rho_t = 0.69\%, f_c^{'} = 3800 \text{ psi}, V_{max} = 570 \text{ kips at LS8}\right)$

	LS6[1]			LS8[2]			LS10[3]			LS11[4]		
Crack ID[5]	$w_{p,6}$ [6]	$w_{r,6}$ [7]	$\frac{w_{p,6}}{w_{r,6}}$	$w_{p,8}$ [6]	$w_{r,8}$ [7]	$\frac{w_{p,8}}{w_{r,8}}$	$w_{p,10}$ [6]	$w_{r,10}$ [7]	$\frac{w_{p,10}}{w_{r,10}}$	$w_{p,11}$ [6]	$w_{r,11}$ [7]	$\frac{w_{p,11}}{w_{r,11}}$
A	0.016	0.005	3.20	0.038	0.025	1.52	0.138	0.050	2.76	0.125	0.063	1.98
B	0.020	0.005	4.00	0.033	0.010	3.30	0.048	0.013	3.69	0.125	0.040	3..13
C	0.025	0.005	5.00	0.039	0.010	3.90	0.109	0.013	8.38	0.060	0.007	8.57
D	0.016	0.005	3.20	0.040	0.020	2.00	0.045	0.007	6.43	0.063	0.035	1.80
E	0.020	0.005	4.00	0.030	0.013	2.31	0.044	0.013	3.38	0.030	0.007	4.29
F	0.013	0.005	2.60	0.039	0.010	3.90	0.045	0.025	1.80	0.063	0.009	7.00
G	0.020	0.005	4.00	0.031	0.005	6.20	0.034	0.005	6.80	0.050	0.016	3.13
H	0.016	0.005	3.20	0.026	0.005	5.20	0.028	0.016	1.75	0.050	0.030	1.67
I	0.013	0.005	2.60	0.022	0.007	3.14	0.024	0.005	4.80	0.030	0.005	6.00
J	0.010	0.005	2.00	0.022	0.005	4.40	0.034	0.005	6.80	0.030	0.013	2.31
Average			3.38			3.59			4.66			3.99

1. Peak transient drift ratio = 0.43%
2. Peak transient drift = 0.80% (at peak shear strength)
3. Peak transient drift ratio = 1.70%
4. Peak transient drift ratio = 2.45%
5. Monitoring location varies by load step; see Figure 4-64 to Figure 4-67
6. Crack width at peak transient drift ratio
7. Crack width at zero lateral force in the same half cycle of loading (see Figure 4-63)

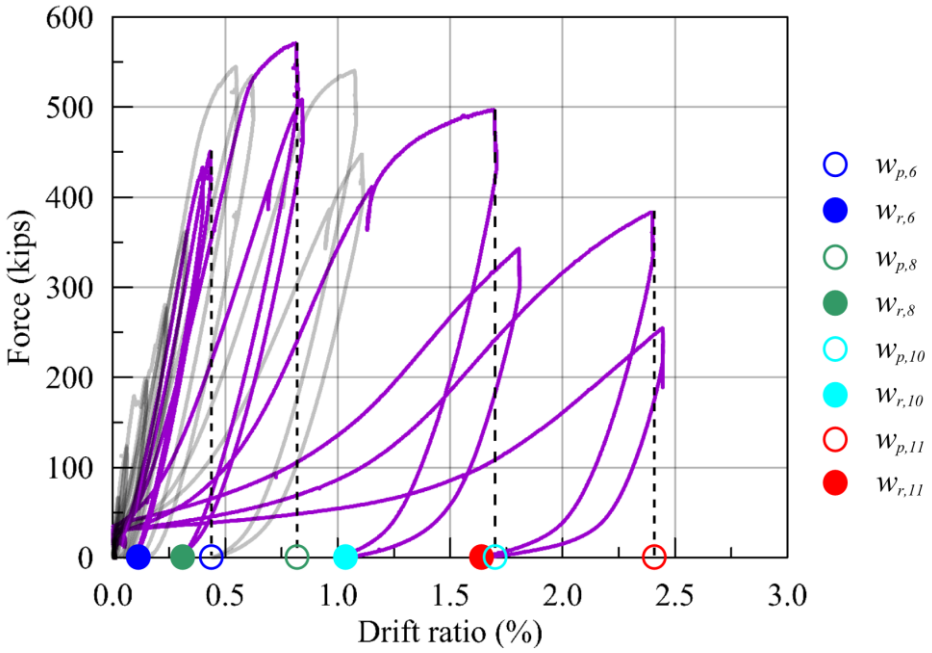

Figure 4-63. First quadrant of the force-drift relationship for SW6

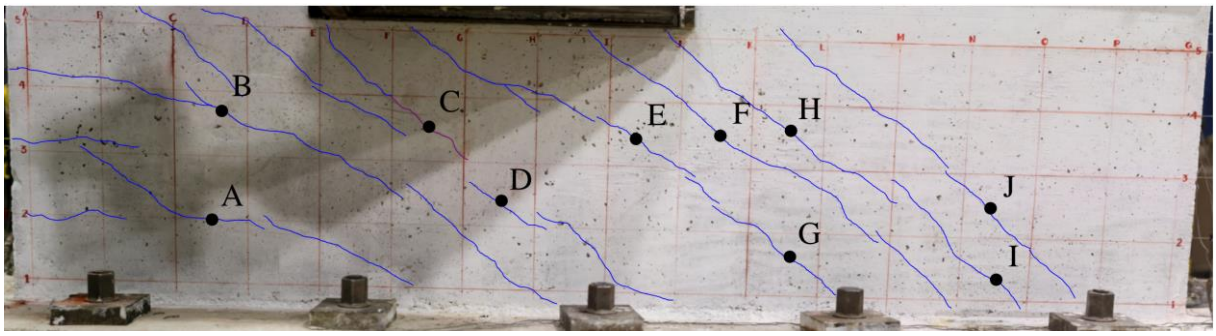

Figure 4-64. Crack width measurement locations for SW6, LS6

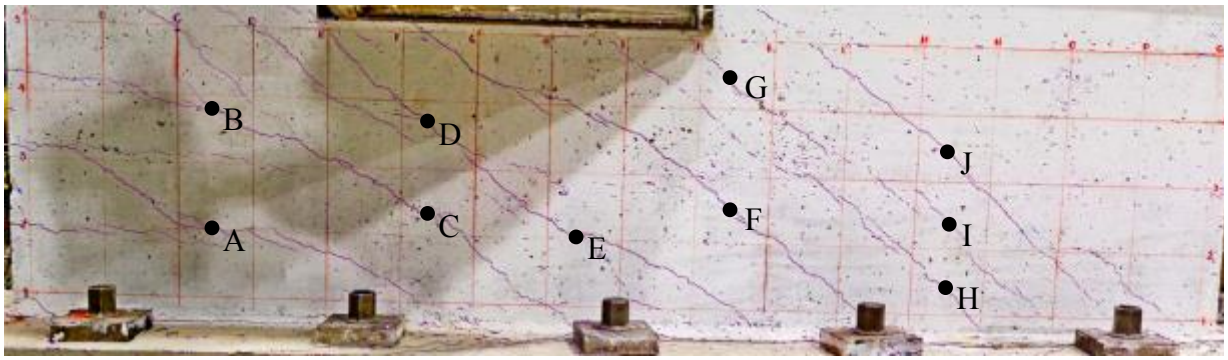

Figure 4-65. Crack width measurement locations for SW6, LS8

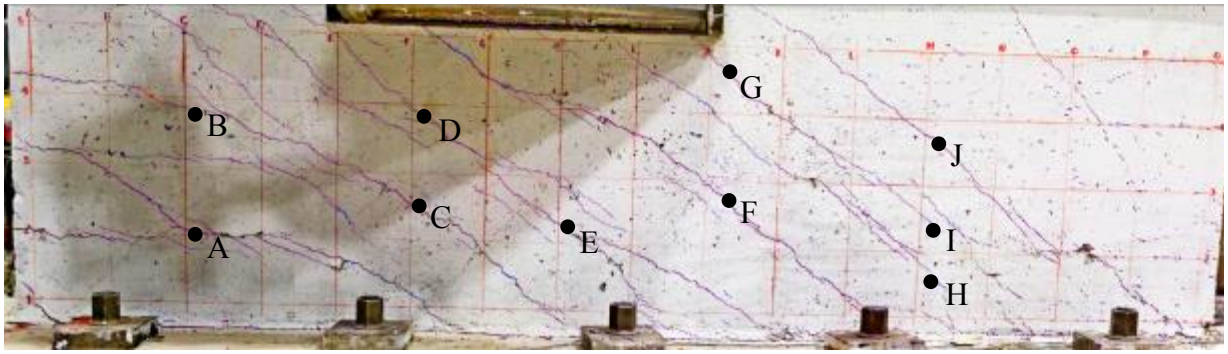

Figure 4-66. Crack width measurement locations for SW6, LS10

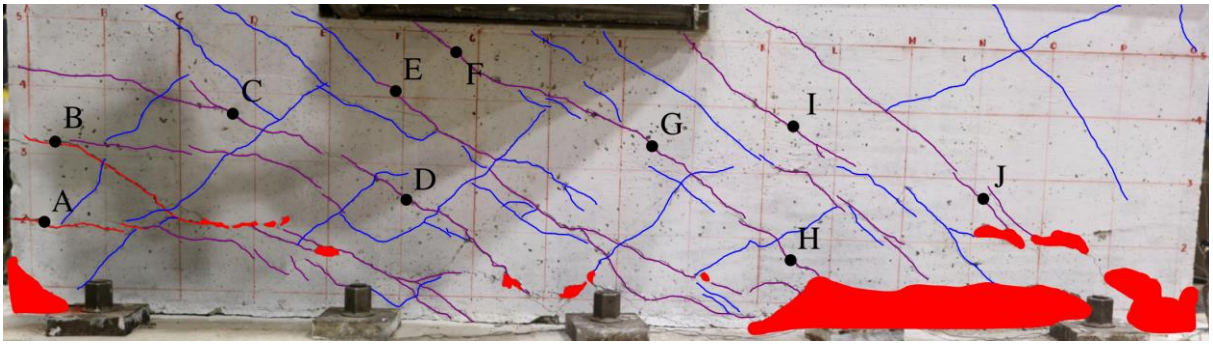

Figure 4-67. Crack width measurement locations for SW6, LS11

Table 4-31. Crack width data, in inch, for SW7

$\left(h_w/l_w = 0.33, \rho_l = 0.34\%, \rho_t = 0.38\%, f_c^{'} = 3800 \text{ psi}, V_{max} = 318 \text{ kips at LS7}\right)$

	LS5[1]			LS7[2]			LS11[3]			LS12[4]		
Crack ID[5]	$w_{p,5}$[6]	$w_{r,5}$[7]	$\frac{w_{p,5}}{w_{r,5}}$	$w_{p,7}$[6]	$w_{r,7}$[7]	$\frac{w_{p,7}}{w_{r,7}}$	$w_{p,11}$[6]	$w_{r,11}$[7]	$\frac{w_{p,11}}{w_{r,11}}$	$w_{p,12}$[6]	$w_{r,12}$[7]	$\frac{w_{p,12}}{w_{r,12}}$
A	0.013	0.005	2.60	0.046	0.005	9.20	0.030	0.009	3.33	0.060	0.020	3.00
B	0.016	0.005	3.20	0.027	0.005	5.40	0.020	0.005	4.00	0.013	0.005	2.60
C	0.009	0.005	1.80	0.043	0.005	8.60	0.030	0.005	6.00	0.025	0.005	5.00
D	0.016	0.005	3.20	0.041	0.005	8.20	0.050	0.016	3.13	0.025	0.005	5.00
E	0.030	0.007	4.29	0.033	0.005	6.60	0.025	0.005	5.00	0.050	0.010	5.00
F	0.030	0.007	4.29	0.043	0.007	6.14	0.050	0.005	10.00	0.050	0.009	5.56
G	0.025	0.007	3.57	0.045	0.007	6.43	0.125	0.016	7.81	0.125	0.010	12.50
H	0.013	0.005	2.60	0.038	0.007	5.43	0.063	0.020	3.15	0.050	0.007	7.14
I	0.013	0.007	1.86	0.043	0.007	6.14	0.030	0.005	6.00	0.025	0.007	3.57
J	0.020	0.007	2.86	0.031	0.007	4.43	0.050	0.007	7.14	0.013	0.005	2.60
Average			3.03			6.66			5.56			5.20

1. Peak transient drift ratio = 0.23%
2. Peak transient drift = 0.48% (at peak shear strength)
3. Peak transient drift ratio = 1.12%
4. Peak transient drift ratio = 1.37%
5. Monitoring location varies by load step; see Figure 4-69 to Figure 4-72
6. Crack width at peak transient drift ratio
7. Crack width at zero lateral force in the same half cycle of loading (see Figure 4-68)

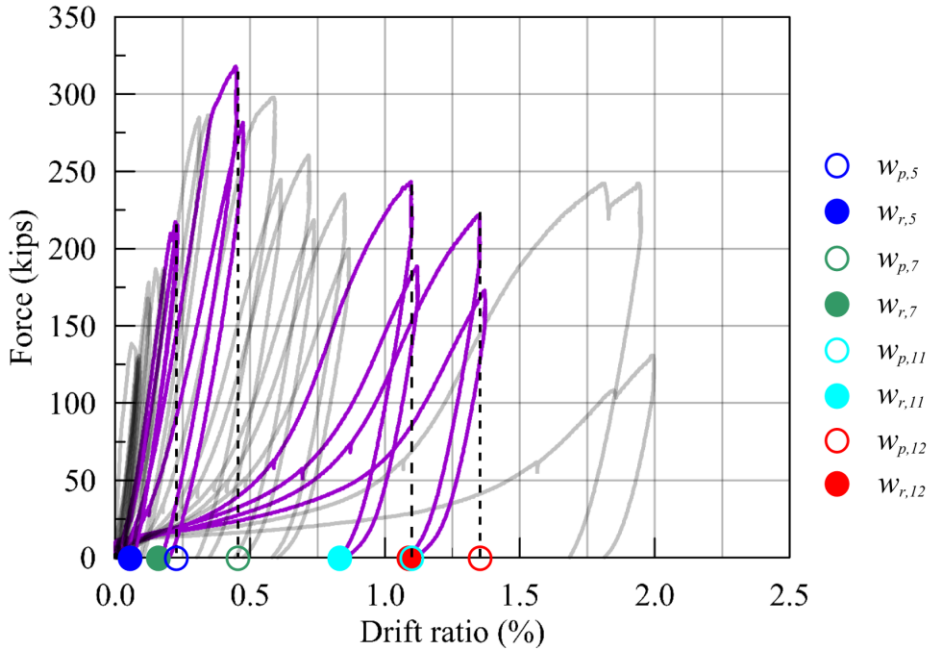

Figure 4-68. First quadrant of the force-drift relationship for SW7

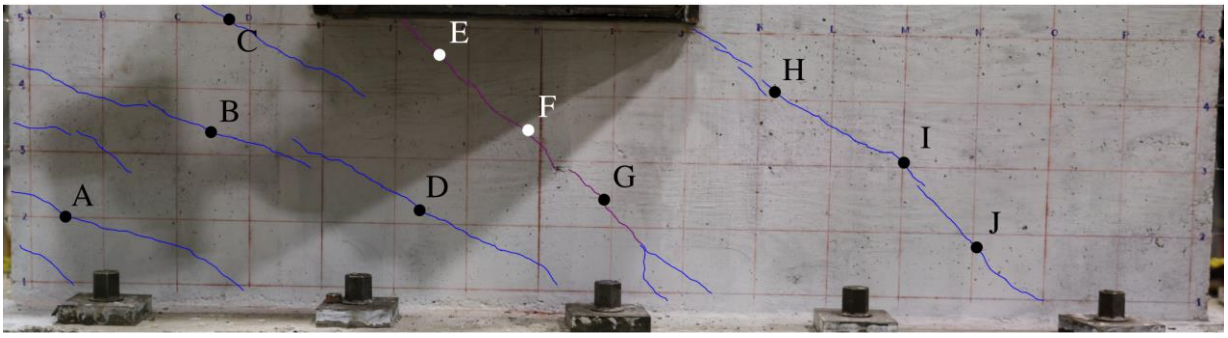

Figure 4-69. Crack width measurement locations for SW7, LS5

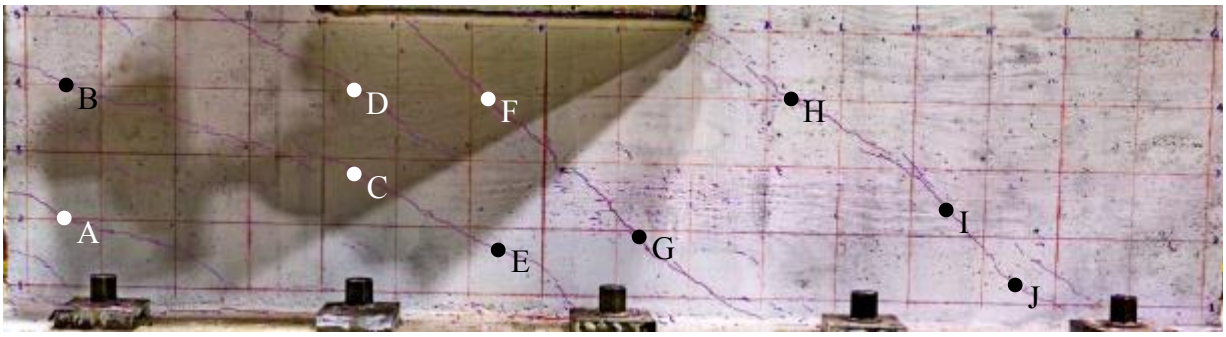

Figure 4-70. Crack width measurement locations for SW6, LS7

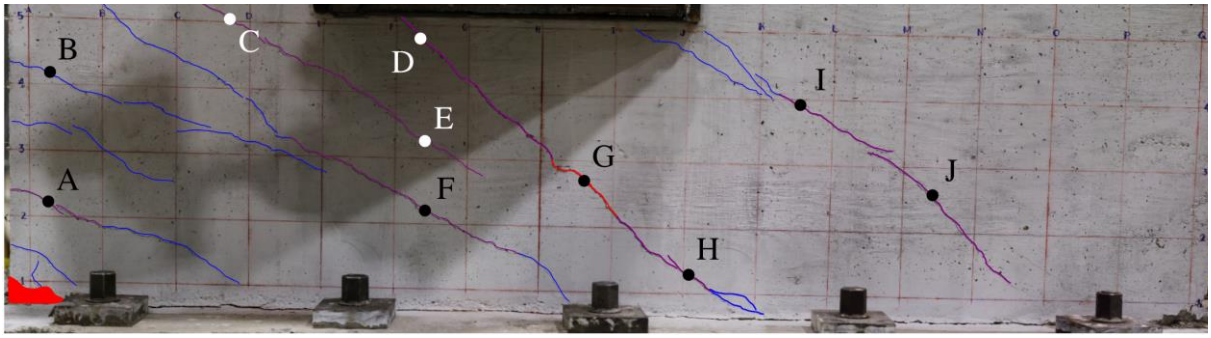

Figure 4-71. Crack width measurement locations for SW7, LS11

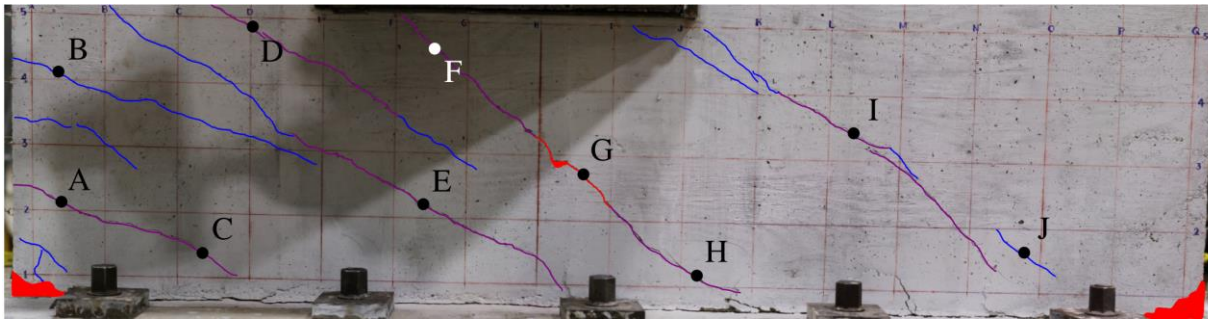

Figure 4-72. Crack width measurement locations for SW7, LS12

Table 4-32. Crack widths data, in inch, for SW8

$\left(h_w/l_w = 0.54, \rho_l = 1.50\%, \rho_t = 1.50\%, f_c^{'} = 3500 \text{ psi}, V_{max} = 623 \text{ kips at LS6}\right)$

	LS4[1]			LS6[2]			LS8[3]		
Crack ID[4]	$w_{p,4}$[5]	$w_{r,4}$[6]	$\frac{w_{p,4}}{w_{r,4}}$	$w_{p,6}$[5]	$w_{r,6}$[6]	$\frac{w_{p,6}}{w_{r,6}}$	$w_{p,8}$[5]	$w_{r,8}$[6]	$\frac{w_{p,8}}{w_{r,8}}$
A	0.010	--[7]	--	0.050	0.009	5.56	0.040	0.009	4.44
B	0.007	--	--	0.009	0.005	1.80	0.009	0.005	1.80
C	0.009	--	--	0.013	0.005	2.60	0.013	0.005	2.60
D	0.009	--	--	0.016	0.005	3.20	0.013	0.005	2.60
E	0.010	--	--	0.020	0.005	4.00	0.020	0.005	4.00
F	0.010	--	--	0.016	0.005	3.20	0.013	0.005	2.60
G	0.013	--	--	0.020	0.005	4.00	0.016	0.005	3.20
H	0.007	--	--	0.020	0.005	4.00	0.016	0.005	3.20
I	0.010	--	--	0.016	0.005	3.20	0.016	0.005	3.20
J	0.013	--	--	0.009	0.005	1.80	0.007	0.005	1.40
Average			--			3.34			2.90

1. Peak transient drift ratio = 0.39%
2. Peak transient drift = 0.74% (at peak shear strength)
3. Peak transient drift ratio = 1.38%
4. Monitoring location varies by load step; see Figure 4-74 and Figure 4-76
5. Crack width at peak transient drift ratio
6. Crack width at zero lateral force in the same half cycle of loading (see Figure 4-73)
7. Crack widths too small to measure

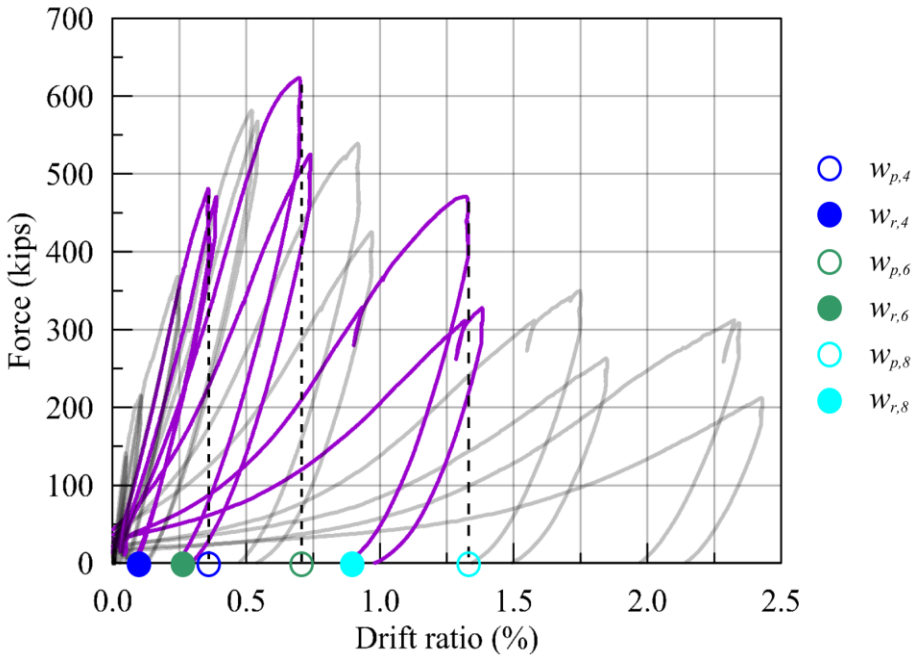

Figure 4-73. First quadrant of the force-drift relationship for SW8

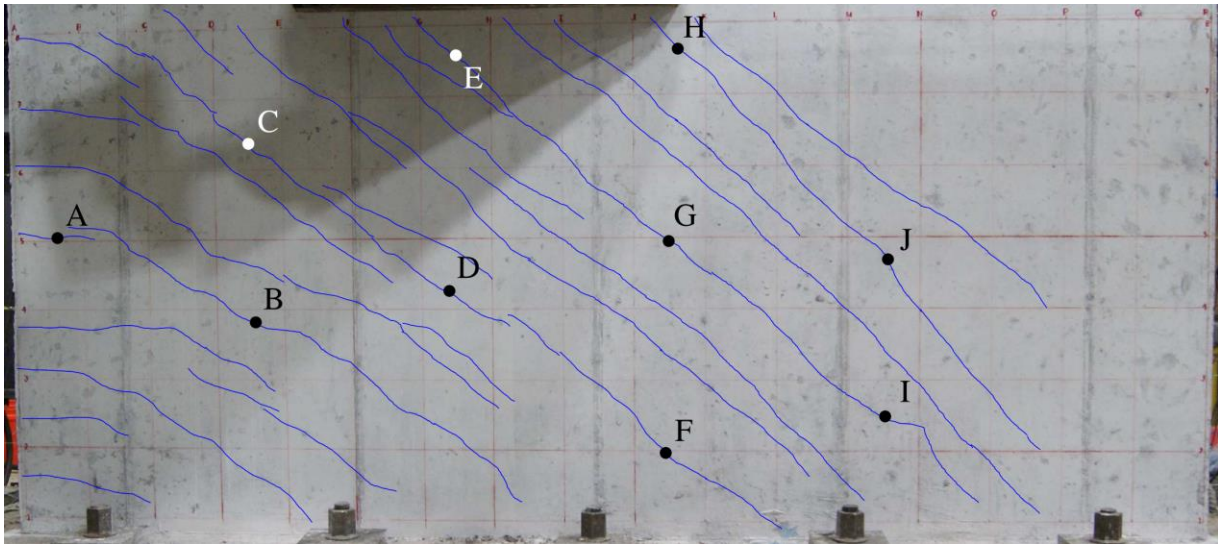

Figure 4-74. Crack width measurement locations for SW8, LS4

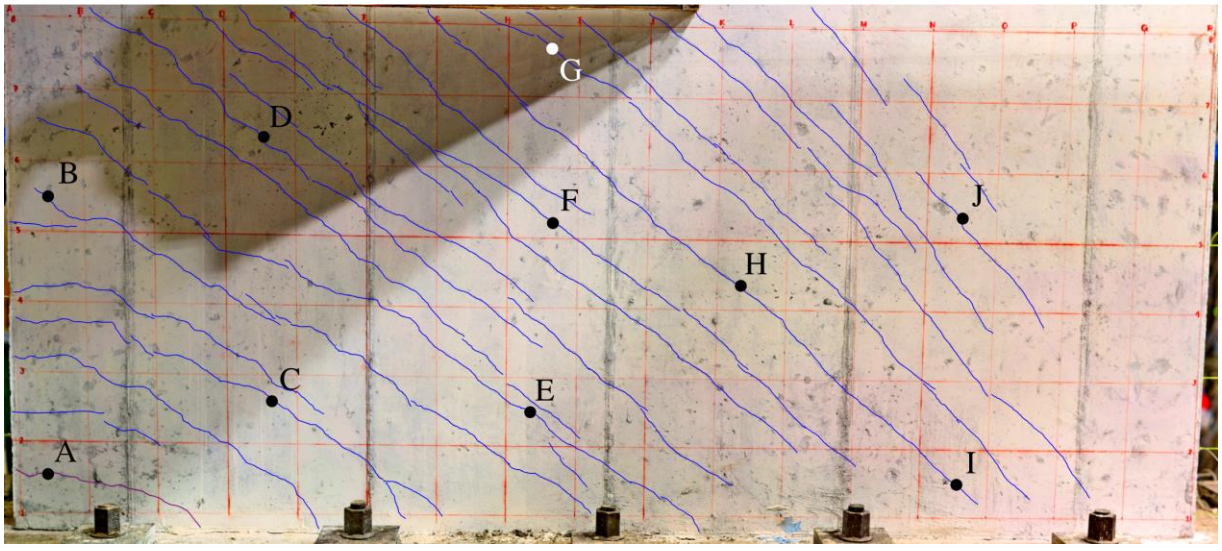

Figure 4-75. Crack width measurement locations for SW8, LS6

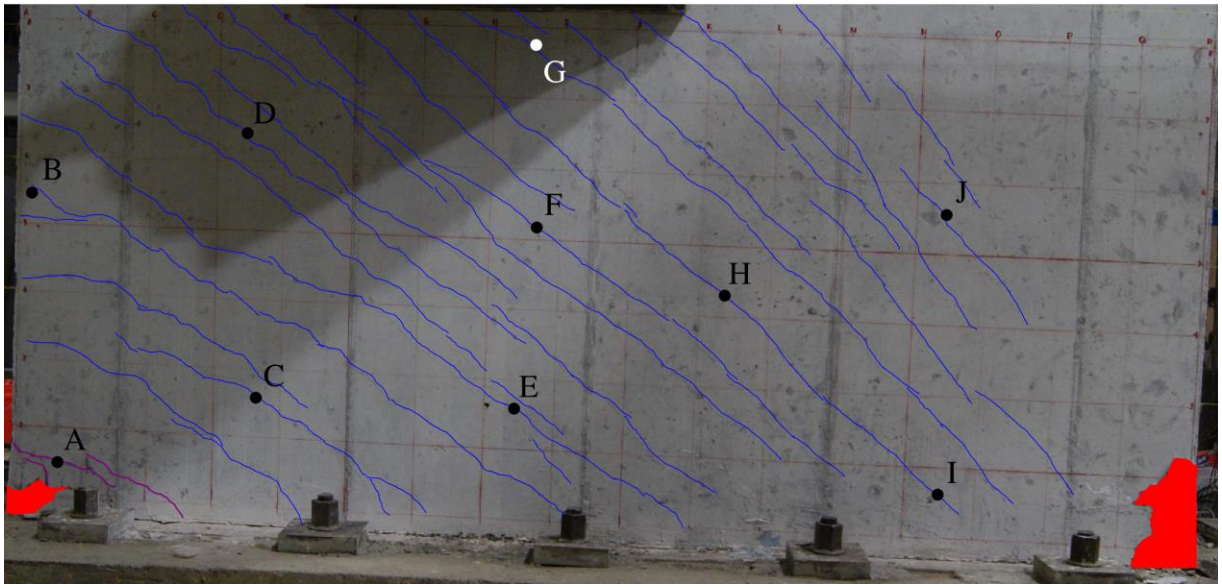

Figure 4-76. Crack width measurement locations for SW8, LS8

Table 4-33. Crack widths data, in inch, for SW9

$\left(h_w/l_w = 0.54, \rho_l = 1.50\%, \rho_t = 0.67\%, f_c^{'} = 4300 \text{ psi}, V_{max} = 633 \text{ kips at LS7}\right)$

	LS5[1]			LS7[2]			LS8[3]		
Crack ID[4]	$w_{p,5}$ [5]	$w_{r,5}$ [6]	$\frac{w_{p,5}}{w_{r,5}}$	$w_{p,7}$ [5]	$w_{r,7}$ [6]	$\frac{w_{p,7}}{w_{r,7}}$	$w_{p,8}$ [5]	$w_{r,8}$ [6]	$\frac{w_{p,8}}{w_{r,8}}$
A	0.016	--	--[7]	0.029	0.005	5.80	0.040	0.013	3.08
B	0.007	--	--	0.026	0.005	5.20	0.007	0.005	1.40
C	0.013	--	--	0.028	0.005	5.60	0.013	0.005	2.60
D	0.020	0.005	4.00	0.019	0.005	3.80	0.013	0.005	2.60
E	0.013	0.005	2.60	0.028	0.005	5.60	0.020	0.005	4.00
F	0.002	0.005	0.40	0.029	0.005	5.80	0.060	0.030	2.00
G	0.016	0.005	3.20	0.025	0.005	5.00	0.035	0.005	7.00
H	0.025	0.005	5.00	0.033	0.005	6.60	0.125	0.035	3.57
I	0.013	0.005	2.60	0.040	0.005	8.00	0.020	0.007	2.86
J	0.013	0.005	2.60	0.032	0.005	6.40	0.250	0.060	4.17
Average			2.91			5.78			3.33

1. Peak transient drift ratio = 0.48%
2. Peak transient drift = 0.83% (at peak shear strength)
3. Peak transient drift ratio = 1.35%
4. Monitoring location varies by load step; see Figure 4-78 to Figure 4-80
5. Crack width at peak transient drift ratio
6. Crack width at zero lateral force in the same half cycle of loading (see Figure 4-77)
7. Crack widths too small to measure

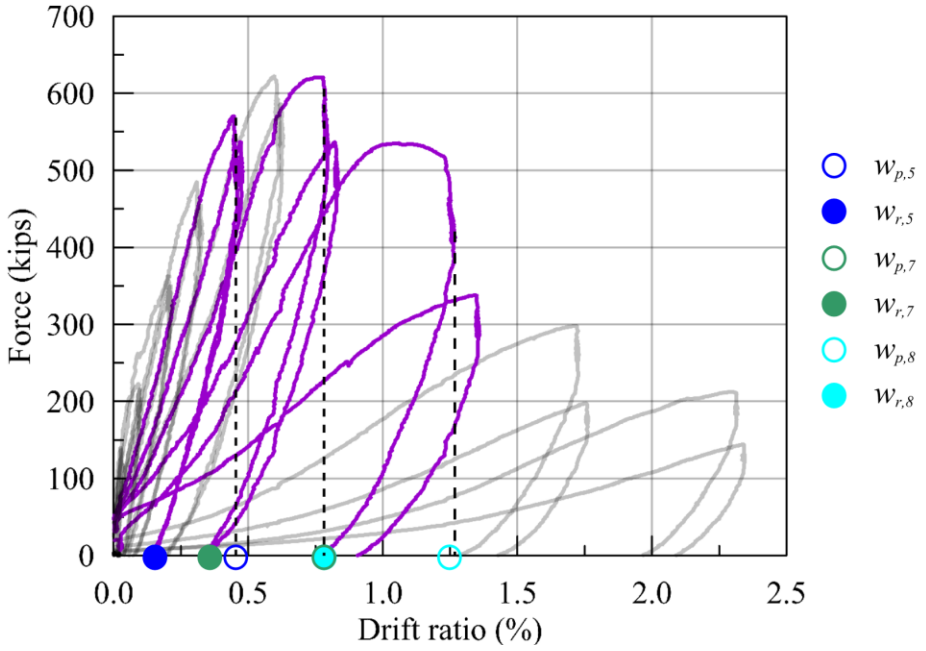

Figure 4-77. First quadrant of the force-drift relationship for SW9

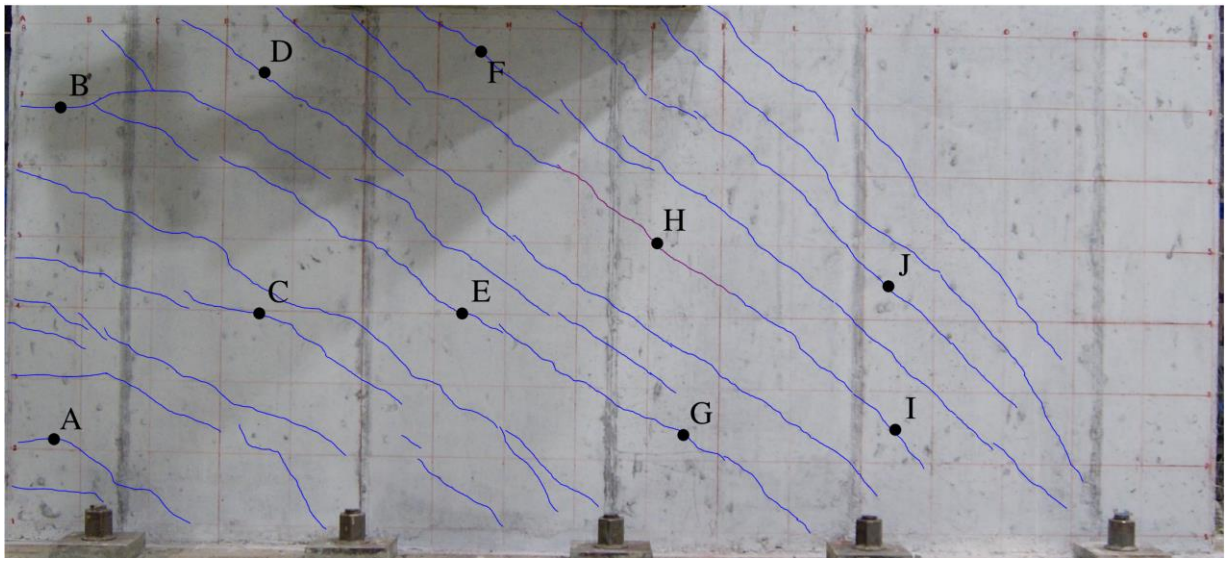

Figure 4-78. Crack width measurement locations for SW9, LS5

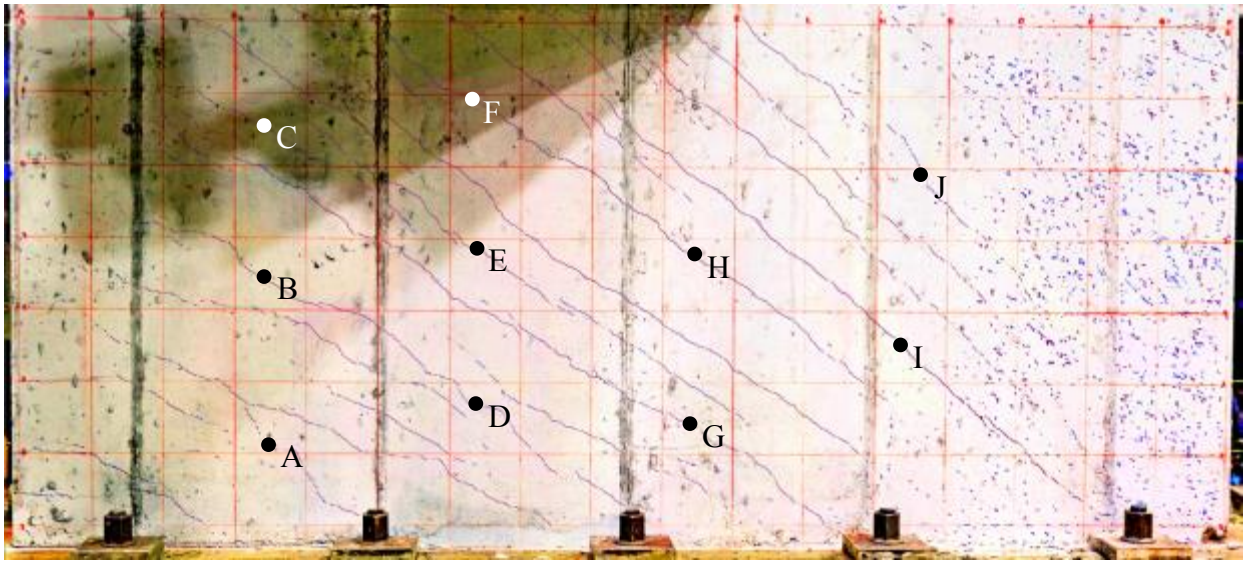

Figure 4-79. Crack width measurement locations for SW9, LS7

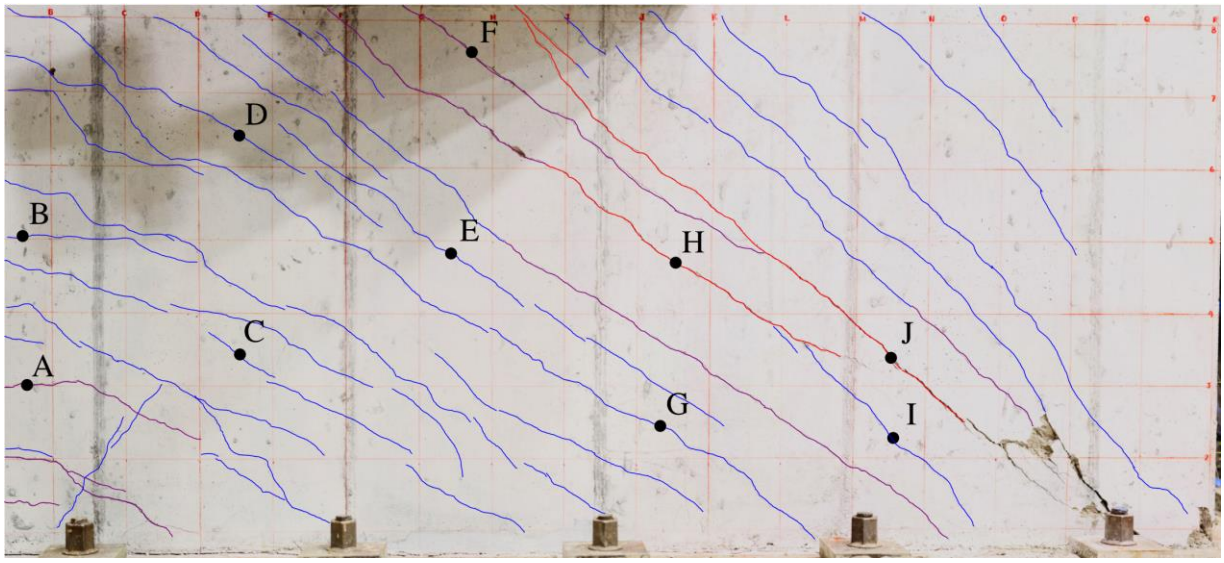

Figure 4-80. Crack width measurement locations for SW9, LS8

Table 4-34. Crack widths data, in inch, for SW10

$\left(h_w/l_w = 0.54, \rho_l = 1.50\%, \rho_t = 0.33\%, f_c^{'} = 4600 \text{ psi}, V_{\max} = 528 \text{ kips at LS6}\right)$

	LS4[1]			LS6[2]			LS8[3]		
Crack ID[4]	$w_{p,4}$ [5]	$w_{r,4}$ [6]	$\frac{w_{p,4}}{w_{r,4}}$	$w_{p,6}$ [5]	$w_{r,6}$ [6]	$\frac{w_{p,6}}{w_{r,6}}$	$w_{p,8}$ [5]	$w_{r,8}$ [6]	$\frac{w_{p,8}}{w_{r,8}}$
A	0.009	--[7]	--	0.009	--	--	0.114	0.125	0.91
B	0.007	--	--	0.009	--	--	0.025	0.007	3.57
C	0.007	--	--	0.016	0.005	3.20	0.050	0.125	0.40
D	0.013	--	--	0.010	0.005	2.00	0.013	0.007	1.86
E	0.013	0.005	2.60	0.013	0.009	1.44	0.030	0.020	1.50
F	0.010	0.005	2.00	0.016	0.007	2.29	0.060	0.030	2.00
G	0.010	0.005	2.00	0.016	0.005	3.20	0.010	0.005	2.00
H	0.016	0.005	3.20	0.007	0.007	1.00	0.183	0.250	0.73
I	0.020	0.007	2.86	0.025	0.030	0.83	0.013	0.010	1.30
J	0.016	0.005	3.20	0.020	0.060	0.33	0.060	0.016	3.75
Average			2.64			1.79			1.80

1. Peak transient drift ratio = 0.38%
2. Peak transient drift = 0.77% (at peak shear strength)
3. Peak transient drift ratio = 1.42%
4. Monitoring location varies by load step; see Figure 4-82 and Figure 4-84
5. Crack width at peak transient drift ratio
6. Crack width at zero lateral force in the same half cycle of loading (see Figure 4-81)
7. Crack widths too small to measure

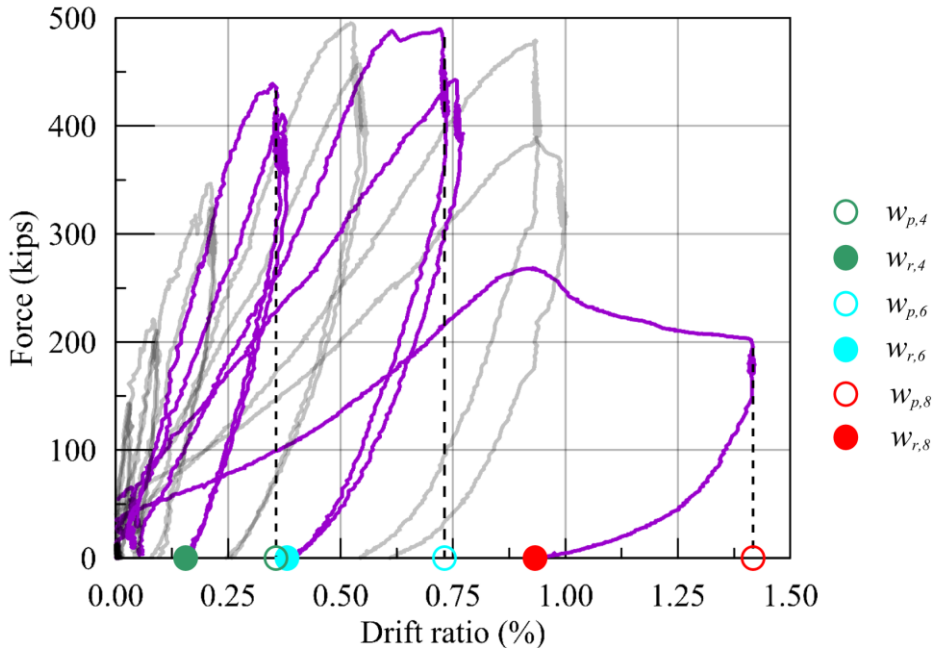

Figure 4-81. First quadrant of the force-drift relationship for SW10

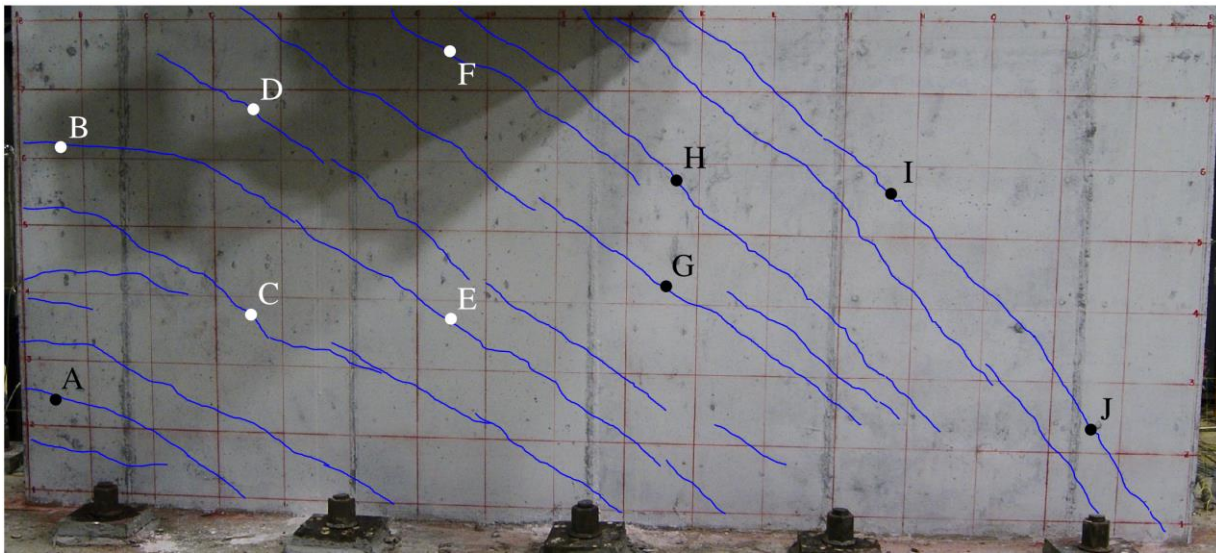

Figure 4-82. Crack width measurement locations for SW10, LS4

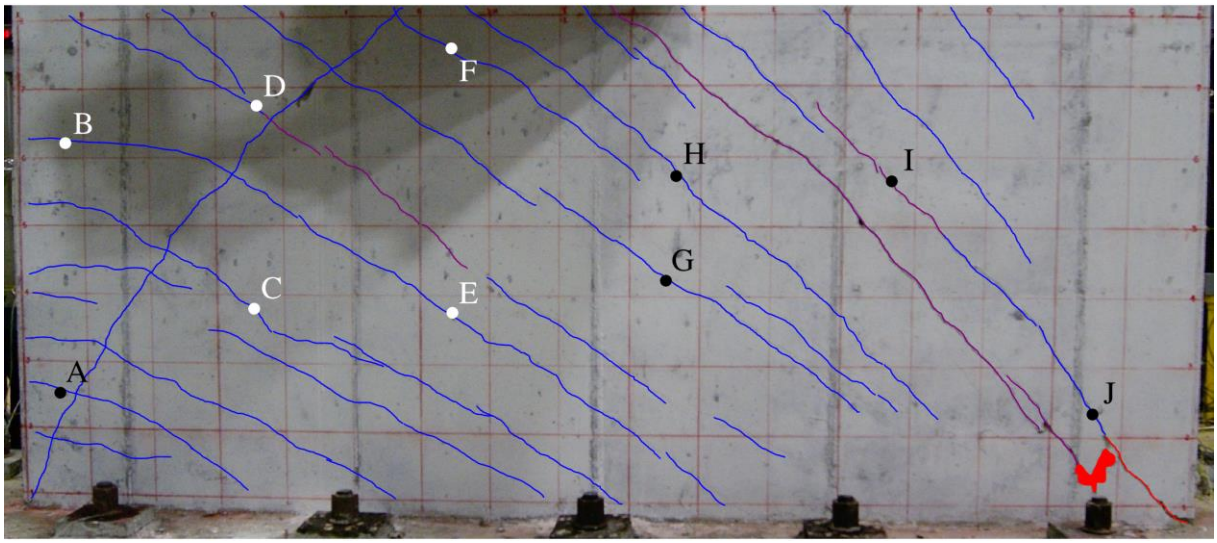

Figure 4-83. Crack width measurement locations for SW10, LS6

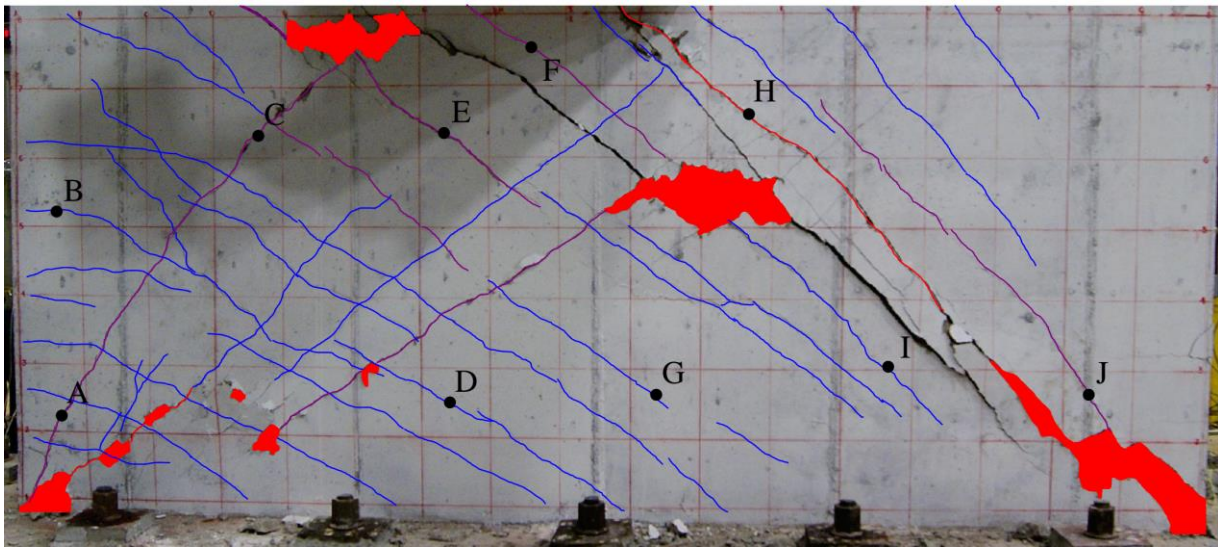

Figure 4-84. Crack width measurement locations for SW10, LS8

Table 4-35. Crack width data, in inch, for SW11

$\left(h_w/l_w = 0.54, \rho_l = 0.67\%, \rho_t = 0.67\%, \rho_{be} = 1.50\%, f_c^{'} = 5000 \text{ psi}, V_{max} = 424 \text{ kips at LS5}\right)$

	LS3[1]			LS5[2]			LS8[3]			LS9[4]		
Crack ID[5]	$w_{p,3}$ [6]	$w_{r,3}$ [7]	$\frac{w_{p,3}}{w_{r,3}}$	$w_{p,5}$ [6]	$w_{r,5}$ [7]	$\frac{w_{p,5}}{w_{r,5}}$	$w_{p,8}$ [6]	$w_{r,8}$ [7]	$\frac{w_{p,8}}{w_{r,8}}$	$w_{p,9}$ [6]	$w_{r,9}$ [7]	$\frac{w_{p,9}}{w_{r,9}}$
A	0.005	0.005	1.00	0.009	0.007	1.29	0.009	0.005	1.80	0.009	0.009	1.00
B	0.009	0.005	1.80	0.060	0.016	3.75	0.125	0.035	3.57	0.125	0.050	2.50
C	0.005	0.005	1.00	0.020	0.007	2.86	0.020	0.007	2.86	0.020	0.007	2.86
D	0.010	0.005	2.00	0.020	0.007	2.86	0.025	0.005	5.00	0.025	0.005	5.00
E	0.013	0.005	2.60	0.020	0.007	2.86	0.035	0.009	3.89	0.025	0.005	5.00
F	0.013	0.005	2.60	0.016	0.007	2.29	0.020	0.007	2.86	0.020	0.007	2.86
G	0.010	0.005	2.00	0.025	0.007	3.57	0.035	0.007	5.00	0.035	0.007	5.00
H	0.016	0.007	2.29	0.016	0.007	2.29	0.025	0.005	5.00	0.025	0.007	3.57
I	0.013	0.005	2.60	0.025	0.007	3.57	0.030	0.009	3.33	0.030	0.013	2.31
J	0.016	0.005	3.20	0.020	0.007	2.86	0.020	0.005	4.00	0.025	0.005	5.00
Average			2.11			2.82			3.73			3.51

1. Peak transient drift ratio = 0.26%
2. Peak transient drift = 0.59% (at peak shear strength)
3. Peak transient drift ratio = 1.34%
4. Peak transient drift ratio = 1.82%
5. Monitoring locations varies by load step; see Figure 4-86 and Figure 4-89
6. Crack width at peak transient drift ratio
7. Crack width at zero lateral force in the same half cycle of loading (see Figure 4-85)

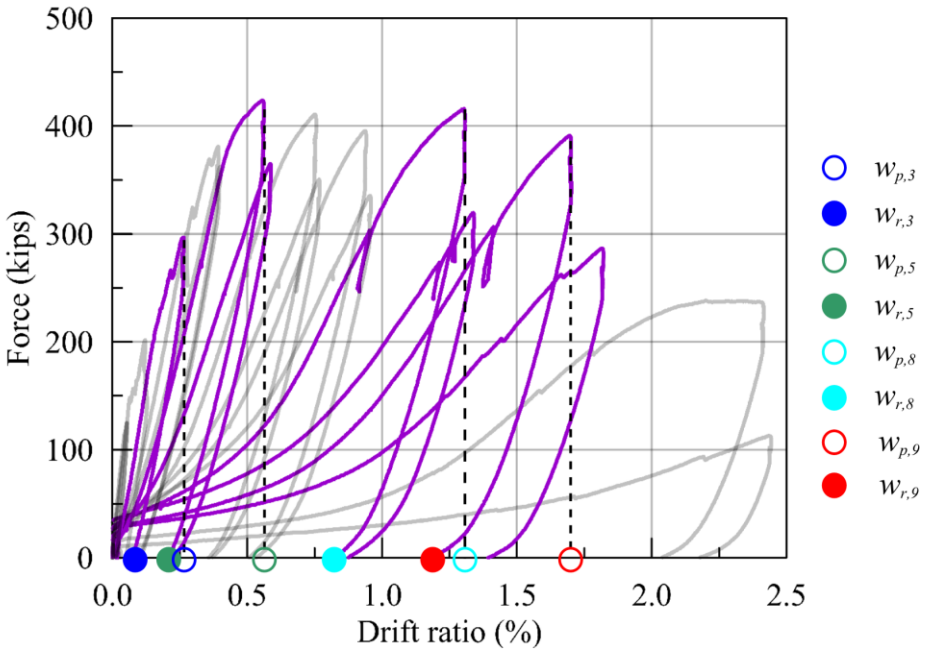

Figure 4-85. First quadrant of the force-drift relationship for SW11

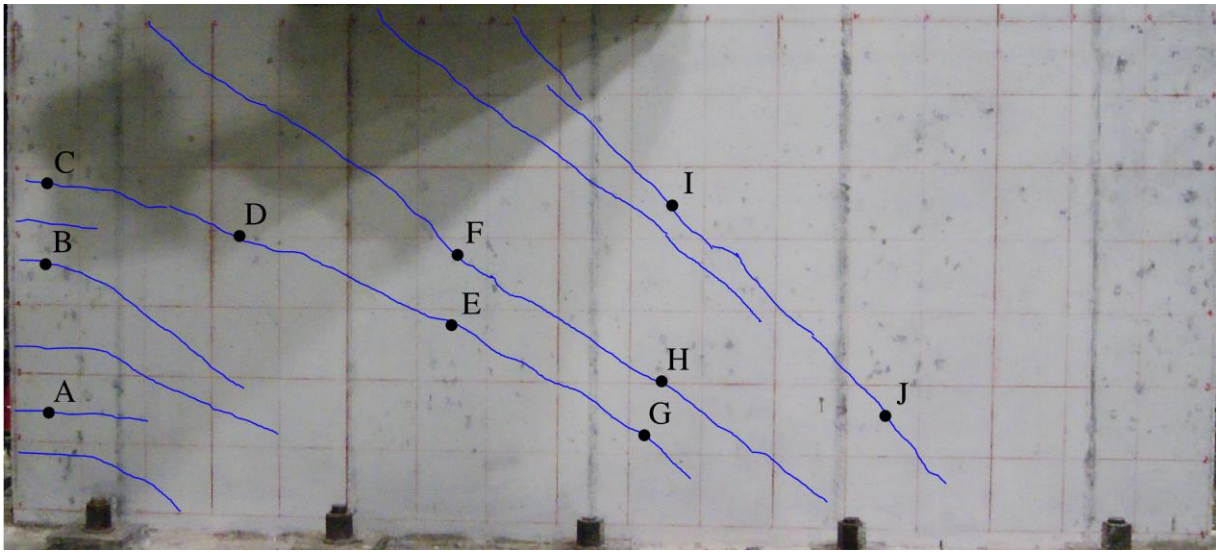

Figure 4-86. Crack width measurement locations for SW11, LS3

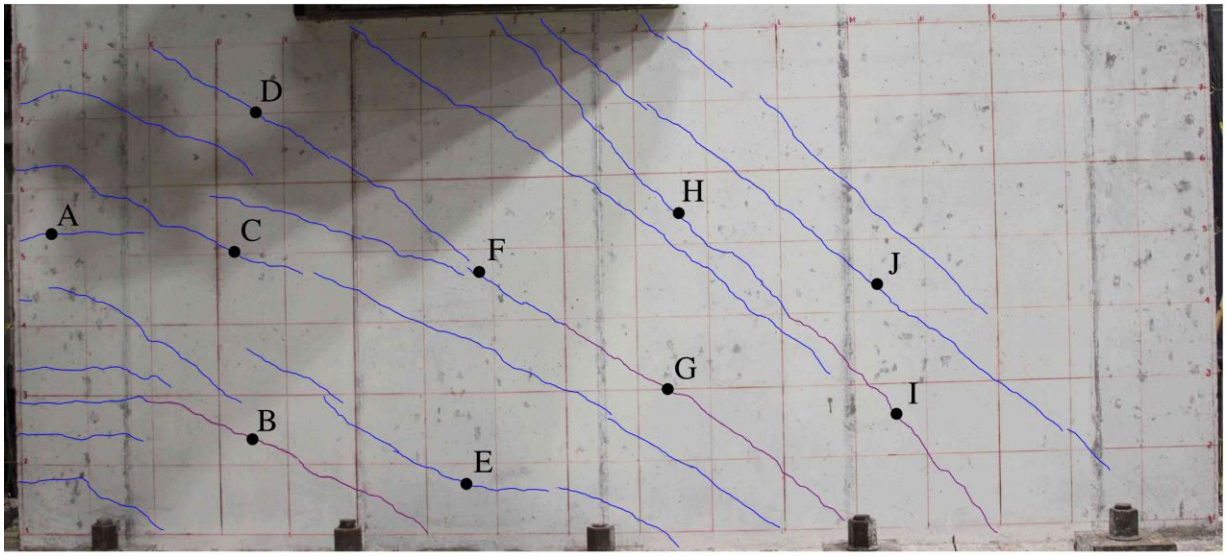

Figure 4-87. Crack width measurement locations for SW11, LS5

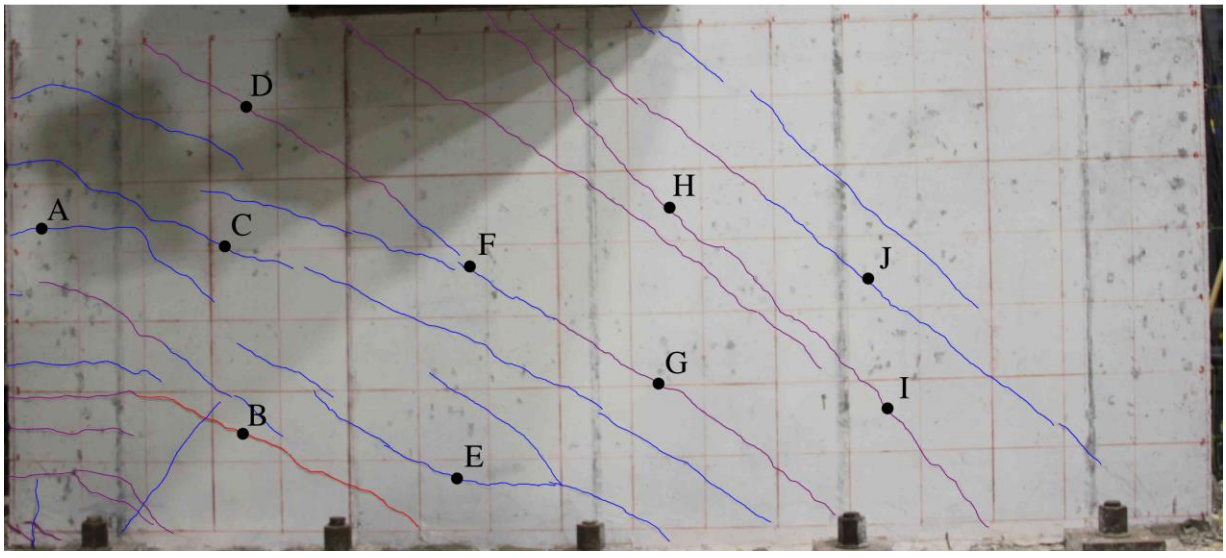

Figure 4-88. Crack width measurement locations for SW11, LS8

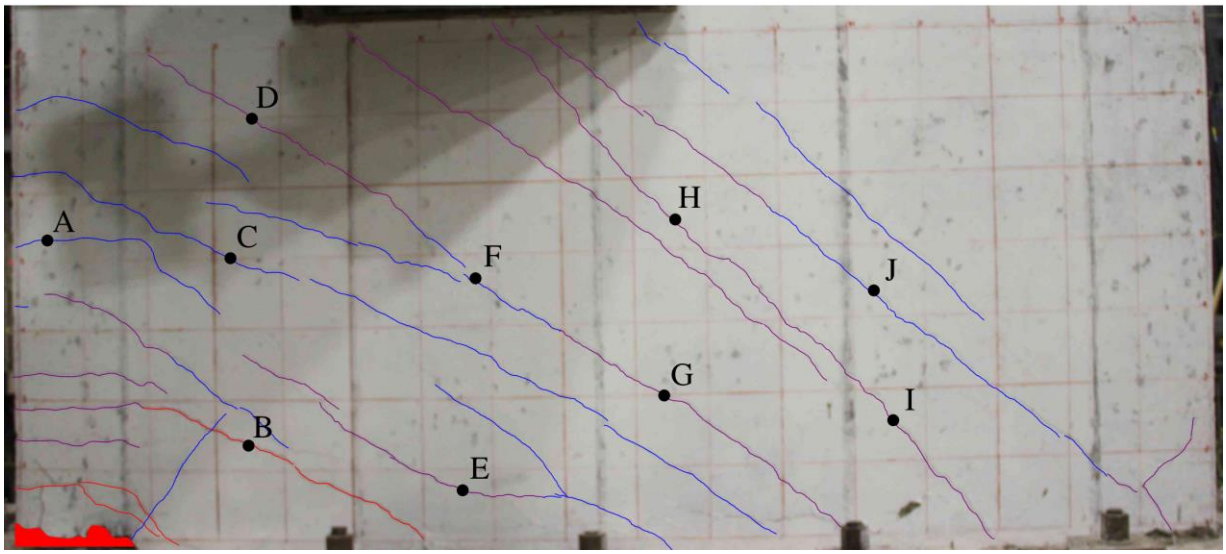

Figure 4-89. Crack width measurement locations for SW11, LS9

Table 4-36. Crack width data, in inch, for SW12

$\left(h_w/l_w = 0.54, \rho_l = 0.33\%, \rho_t = 0.33\%, \rho_{be} = 2.00\%, f_c^{'} = 5000 \text{ psi}, V_{max} = 416 \text{ kips at LS8}\right)$

	LS5[1]			LS8[2]			LS9[3]		
Crack ID[4]	$w_{p,5}$[5]	$w_{r,5}$[6]	$\frac{w_{p,5}}{w_{r,5}}$	$w_{p,8}$[5]	$w_{r,8}$[6]	$\frac{w_{p,8}}{w_{r,8}}$	$w_{p,10}$[5]	$w_{r,10}$[6]	$\frac{w_{p,10}}{w_{r,10}}$
A	0.040	0.010	4.00	0.060	0.035	1.71	0.060	0.060	1.00
B	0.035	0.007	5.00	0.049	0.007	7.00	0.048	0.020	2.40
C	0.025	0.009	2.78	0.047	0.013	3.62	0.044	0.013	3.38
D	0.030	0.010	3.00	0.058	0.009	6.44	0.058	0.016	3.63
E	0.040	0.010	4.00	0.038	0.005	7.60	0.048	0.009	5.33
F	0.030	0.005	6.00	0.042	0.005	8.40	0.045	0.007	6.43
G	0.060	0.013	4.62	0.046	0.005	9.20	0.056	0.016	3.50
H	0.016	0.005	3.20	0.052	0.005	10.40	0.050	0.010	5.00
I	0.016	0.005	3.20	0.054	0.005	10.80	0.049	0.016	3.06
J	0.025	0.005	5.00	0.051	0.005	10.20	0.049	0.005	9.80
Average			4.08			7.54			4.35

1. Peak transient drift ratio = 0.57%
2. Peak transient drift = 1.28% (at peak shear strength)
3. Peak transient drift ratio = 1.60%
4. Monitoring location varies by load step; see Figure 4-91 to Figure 4-93
5. Crack width at peak transient drift ratio
6. Crack width at zero lateral force in the same half cycle of loading (see Figure 4-90)

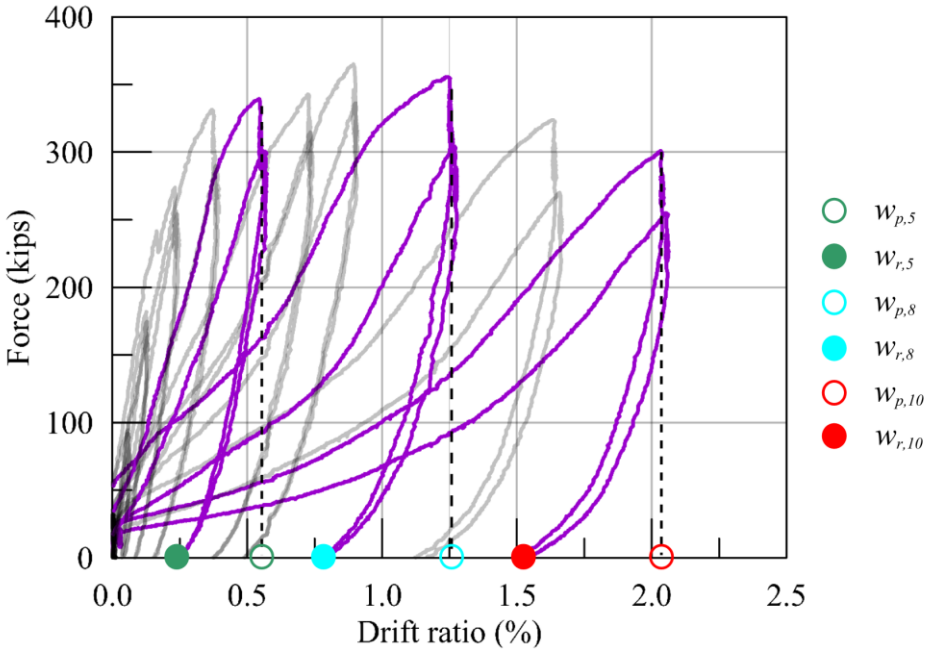

Figure 4-90. First quadrant of the force-drift relationship for SW12

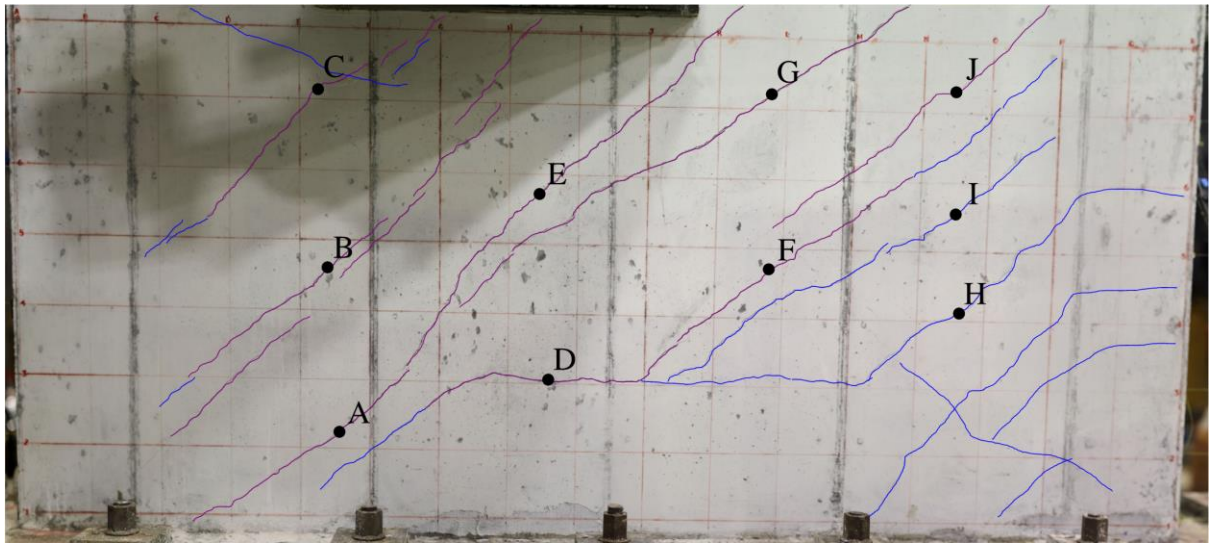

Figure 4-91. Crack width measurement locations for SW12, LS5

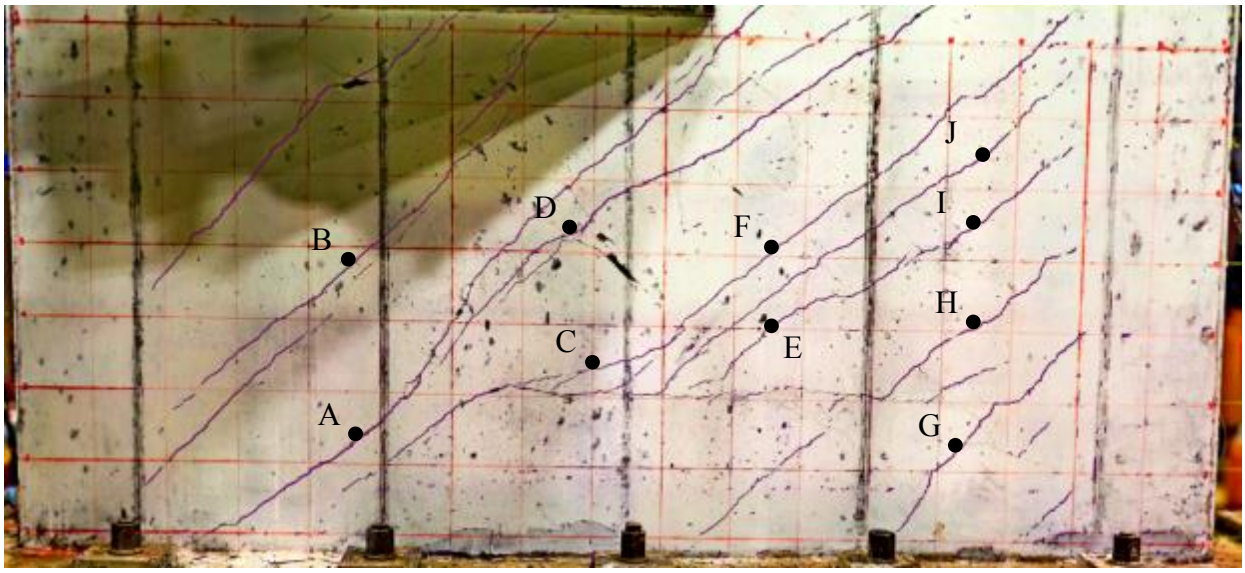

Figure 4-92. Crack width measurement locations for SW12, LS8

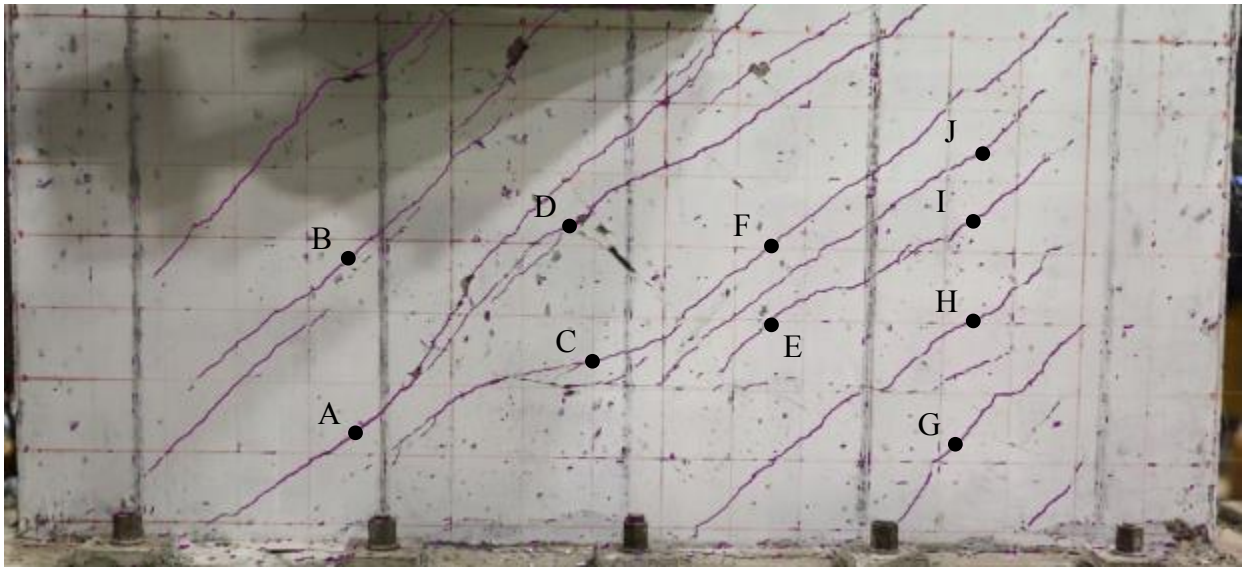

Figure 4-93. Crack width measurement locations for SW12, LS9

The locations at which the widths of cracks were monitored in the 12 walls were not selected scientifically because there was no plan at the time of testing to process crack-width data to determine the relative amplitude of cracks at peak transient displacement and zero lateral load, in the same load step. The chosen locations, which varied between load steps for a given wall, can be considered to be representative. There was no attempt made to compute a maximum crack width in a wall at zero lateral load force in each load step, in part because such information will not drive a method of repair.

The widths of cracks in a reinforced concrete shear wall are a function of many factors, including web reinforcement ratios, web reinforcement diameters, type of loading (i.e., monotonic versus cyclic) and loading stage (pre-peak strength, at peak strength, post-peak strength). Ten of the 12 walls tested had the same web reinforcement ratios in the vertical and horizontal directions, and those walls are the focus of the discussion below: SW1 to SW8, SW11 and SW12. Table 4-37 bins the average values of the crack width ratios reported for walls SW1 to SW8; none of these walls include boundary elements.

Table 4-37. Average crack width ratio[1] for walls SW1 to SW8

Load stage[2]	Web reinforcement ratio		
	$\rho \leq 0.40\%$	$0.40\% < \rho \leq 1.0\%$	$\rho = 1.5\%$
Pre-peak	2.8	2.8	--[3]
Peak	5.0	3.8	3.3
Post-peak	4.6	4.3	2.9

1. Average of mean values of crack width reported in Table 4-25 to Table 4-32
2. Displacements in the pre-peak strength region, displacement at peak strength, and displacement in the post-peak strength region
3. Information not reported because the crack widths at zero lateral load were too small to be measured using a crack width gage

The results of Table 4-37 should be considered indicative and not quantitative. The average crack width ratio is maximized at peak strength or in the post-peak region, which is an expected result. Complicating this interpretation of results are two factors, namely 1) damage in the form of cracking appears to localize at displacements greater than that associated with peak strength, or, not all cracks grow in length and width in proportion to the increasing story drift, and 2) in the post-peak region, some significant fraction of the total story drift is associated with base sliding. However, on the basis of this small dataset, which is the only one of its type to the knowledge of the author, 1) in the pre-peak region of response, the average crack width ratio is on the order of 3 (if the web reinforcement ratio is less than 1%), 2) at displacement consistent with peak strength, the average crack width ratio is greatest for small web reinforcement ratios and smallest for a high web reinforcement ratios, and between 3 and 5 for the reinforcement ratios considered here, and 3) in the post-peak region, the average crack width ratios are similar in magnitude to those at peak strength, namely between 3 and 5.

For SW11 (SW12), which included boundary elements within the web of the wall, the average crack width ratio in the pre-peak, peak and post-peak stages were 2.1 (4.1), 2.8 (7.5) and 3.7 (4.4), respectively. The significant differences in the values for the two walls, at pre-peak (2.1 versus 4.1) and peak (2.8 versus 7.5) stages is attributed to the higher web reinforcement ratios in SW11: 0.67% in SW11 and 0.33% in SW12.

4.5 Summary

The experimental dataset from walls SW1 to SW12 provides important information on

damage to reinforced concrete shear walls. Damage to the walls was binned by a state that mapped to a repair measure: 1) visible cracking, 2) cracks with a maximum width greater than 0.02 inch or 0.04 inch, 3) crushing of concrete in the toe regions, 4) sliding at the base, 5) crack widths greater than 0.125 inch, and 6) widespread crushing of concrete. The experimental dataset was also mined to estimate the ratio of crack width at peak transient displacement to crack width at zero lateral load upon subsequent unloading: information that could prove useful for future post-earthquake reconnaissance reporting.

On the basis of the data presented above, observations can be made regarding earthquake damage to walls, as recorded in the unloaded (post-earthquake) condition:

- Cracking visible to the naked eye will develop at deformations smaller than those associated with peak shear strength.
- Cracks with a width greater than or equal to 0.02 inch will develop at deformations smaller than those associated with peak shear strength.
- Cracks with a width greater than or equal to 0.04 inch will develop at deformations at or near those associated with peak shear strength.
- Cracks with a width greater than 0.125 inch will develop at deformations greater than those associated with peak shear strength.
- Crushing of concrete at the toes (boundaries) of a wall will occur at deformations near or at those associated with peak shear strength.
- Walls will only slide atop a foundation after the peak lateral strength has been attained.

- The scatter evident in Figure 4-39 through Figure 4-43 is due to the wide range of specimens tested: aspect ratios between 0.33 and 0.94, web reinforcement ratios between 0.33% and 1.5%, non-uniform reinforcement layouts, and concrete compressive strengths between 3500 psi and 7800 psi.
- For the walls with equal web reinforcement ratios in the horizontal and vertical directions, and not reinforced with boundary elements, 1) in the pre-peak strength region, the average crack width ratio is on the order of 3 if the web rebar ratio is less than 1%, 2) at displacement consistent with peak strength, the average crack width ratio is a function of web reinforcement ratio and can be taken as 4, and 3) in the post-peak region, the average crack width ratios are similar in magnitude to those at peak strength, namely, approximately 4. The greater the web reinforcement ratio, the smaller the average crack width ratio in the pre-peak strength region and at peak strength.
- For the walls with equal web reinforcements ratios in the horizontal and vertical directions, and reinforced with boundary elements, the greater the web reinforcement ratio, the smaller the average crack width ratio in the pre-peak strength region and at peak strength.

SECTION 5
FRAGILITY FUNCTIONS

5.1 General

The performance of a building or structure during an earthquake can be measured in terms of collapse, casualties incurred, damage sustained (repair cost) and time required to repair or replace damaged structural components. To assess the probable seismic performance of a structure for a user-specified characterization of an earthquake, an earthquake scenario (i.e., combination of moment magnitude and distance), or over a period of time (e.g., one year [annualized], a 50-year life), the Applied Technology Council (ATC) developed the methodology and recommended procedures that was published as FEMA P-58 Seismic Performance Assessment of Buildings (FEMA, 2012). Fragility functions are central to FEMA P-58 and its risk-calculation procedures.

Fragility functions are cumulative distributions that relate the probability a damage threshold (as defined by damage states and methods of repair) is met or exceeded given a value of a demand parameter (e.g. acceleration or story drift ratio). Damage states are physical measures or descriptors that are observed or documented by engineers/inspectors during a post-earthquake evaluation. Gulec and his co-workers documented damage states and the corresponding repair methods for low aspect ratio reinforced concrete shear walls using available data, as discussed in Chapter 4. Fragility functions were then developed, and presented in Gulec and Whittaker (2009) and Gulec et al. (2009, 2010), for such shear walls based on these damage states and methods of repair, where the damage states and methods of repair were subject to review and revision by expert design professionals and contractors.

The data Gulec used to develop fragility functions were based on recorded observations of damage to specimens tested in laboratories. The tests were performed over a number of decades and no metadata were available. In some cases cracks were recorded on drawings of wall elevations, with maximum crack widths identified. In other cases, maximum crack widths were recorded but no drawings were generated. Cracks and their widths (often just maximum value on a given wall) were associated with peak transient displacements: information that is not available to engineers and inspectors after an earthquake because the wall is unloaded at that time. The tests and documentation of SW1 to SW12, with recorded crack length and width (along the length of each crack) at both peak transient and at displacements at zero lateral load make updates to the Gulec fragility functions possible.

Accordingly, the damage states reported in Chapter 4 for walls SW1 to SW12 are used herein to develop a new set of fragility functions for planar (rectangular), low aspect ratio reinforced concrete shear walls. The damage states of Chapter 4 were reported for the unloaded condition, thus mimicking the post-earthquake condition. The reporting of damage as a function of displacement at zero lateral load makes this dataset truly unique.

5.2 Fragility functions developed by Gulec (2009)

Gulec (2009) compiled a database of results from tests of 434 low aspect ratio reinforced concrete shear walls, which included walls with rectangular (planar), barbell and flanged cross sections (referred to as the database). The database was assembled using information from testing programs dating back to 1952. Much of the reported information focused on maximum shear

strength (Gulec and Whittaker, 2009). The data required to develop fragility functions, which are characterized by damage states (e.g., crack lengths and widths, volume of crushed concrete, reinforcement yielding and buckling, and photographs documenting the extent of damage), were rarely reported. Very rarely were photographs (or sketches) provided that enable the reader to understand the extent of damage, and where provided, the photographs (and sketches) depicted damage at the end of the test, when the walls strength have been substantially degraded from the peak values (in push and pull directions).

The lack of detailed information on damage to the walls catalogued in the database led Gulec (2009) to exclude 323 of the 434 walls from the fragility analysis. Of the remaining 111 walls, 51 had rectangular or planar cross sections. The aspect ratio of the walls with rectangular cross sections ranged from 0.25 to 2.00, with web thickness between 1.77 inches and 6.00 inches. The compressive strength of the concrete in the rectangular walls ranged from 2915 psi to 7537 psi. The horizontal and vertical reinforcement ratios in the webs of the rectangular walls ranged between 0.00% and 1.61%, and 0.00% to 2.14%, respectively.

The damage states and corresponding methods of repair defined by Gulec (2009) were chosen based on an analysis of the reported test data, guidelines for repair of reinforced concrete walls such as, FEMA 306 (ATC, 1998) and FEMA 308 (ATC, 1998) and the opinion of the expert design professionals associated with the FEMA P-58 project. Damage states included the onset of visible cracking, width of cracks beyond threshold values, reinforcement yielding or buckling, concrete crushing, and base sliding. Gulec, working indirectly with the design professionals involved in the FEMA P-58 project, assigned a method of repair (MoR) to each damage state.

Methods of repair included cosmetic repair, epoxy-resin injection of cracks, partial replacement of the wall, and full replacement of the wall. Table 5-1 presents the damage states of Gulec (2009) and their corresponding methods of repair. The following sub-sections provide a description of the method of repair used for each damage state, adapted from Gulec (2009), Gulec and Whittaker (2009), Gulec et al. (2009).

5.2.1 MoR-1, Cosmetic repair

Cosmetic repairs are required for visible cracks with a width less than 0.02 inch. These thin cracks do not compromise the shear strength of a wall or materially affect its lateral stiffness. (Restrained shrinkage, associated with cracks not visible to the naked eye, does affect the lateral stiffness of low aspect ratio walls per Luna et al. (2015). Additional thin cracks (widths less than 0.02inch) are assumed not to reduce stiffness further.) Cosmetic repairs (e.g., painting) are used to restore the aesthetic appearance of the wall but not improve its strength or stiffness.

If reinforced concrete shear walls are used to confine gases or fluids, such as containment vessels in nuclear power plants, even thin cracks may need to be repaired. Rizkalla et al. (1984), Greiner and Ramm (1995), Hamilton et al. (2004), and Hutchinson and Soppe (2012) showed that cracks with widths ranging from 0.002 inch to 0.007 inch could increase the permeability of a wall to allow passage of a gas. Hutchinson and Soppe (2012) also noted that "[O]nce cracked,

Table 5-1. Damage states and methods of repair as defined by Gulec and Whittaker (2009)

Damage state ID	Damage state	Method of Repair (MoR)
DS1.1	Initiation of cracking	Cosmetic repair (MoR-1)
DS1.2	Initiation of flexural cracking	
DS1.3	Initiation of shear cracking	
DS1.4	Maximum measured crack widths less than 0.02 inch (0.5 mm)	
DS2.1	Initiation of yielding in horizontal web reinforcement	Epoxy-resin injection (MoR-2)
DS2.2	Initiation of yielding in vertical web reinforcement	
DS2.3	Initiation of yielding in vertical boundary element reinforcement	
DS2.4a	Maximum measured shear crack width greater than 0.02 inch (0.5 mm) but less than 0.12 inch (3 mm)	
DS2.5a	Maximum measured flexural crack width greater than 0.02 inch (0.5 mm) but less than 0.12 inch (3 mm)	
DS2.4b	Maximum measured shear crack width greater than 0.04 inch (1 mm) but less than 0.12 inch (3 mm)	
DS2.5b	Maximum measured flexural crack width greater than 0.04 inch (1 mm) but less than 0.12 inch (3 mm)	
DS3.1	Concrete crushing at the compression toes/initiation of crushing in the wall web	Partial wall replacement (MoR-3)
DS3.2	Vertical cracking in the toe regions of the web	
DS3.3	Buckling of boundary element reinforcement	
DS3.4	Flexural crack widths greater than 0.12 inch (3mm)	
DS4.1	Initiation of base sliding	Full wall replacement (MoR-4)
DS4.2	Wide diagonal cracks	
DS4.3	Widespread crushing of concrete	
DS4.4	Reinforcement fracture	
DS4.5	Shear crack widths greater than 0.12 inch (3 mm)	

the concrete permeability typically increased anywhere from 10 to 50 times the uncracked permeability for the uniaxial specimens, whereas it increased from 10 and 10000 times the uncracked permeability for the biaxial specimens…" Unresolved issues here include a) the relationship between peak transient crack width and residual crack width (upon which permeability calculations should be based), b) the variation of crack width through the thickness of a wall (if the crack does not penetrate completely through a wall, gas cannot pass, regardless of its width at the surface), and c) the dependence of results on the thickness of a wall (the longer and more torturous the path through the wall, the lower the permeability). Accordingly, cosmetic repair may not be sufficient for walls with thin surface cracks that serve as a confinement function.

5.2.2 MoR-2, Epoxy-resin injection

Cracks in walls are injected with epoxy resin to restore strength and stiffness. Damage states DS2.1, DS2.2, and DS2.3 are associated with the yielding of reinforcement and were used in the absence of information regarding crack width. Cracks are assumed to have formed on the surface of a wall if the reinforcement has yielded. Damages states 2.4 and 2.5 are used when crack-width data are available. Damage states 2.4 and 2.5 provide different crack width thresholds for epoxy-resin injection, a) 0.02 inch and b) 0.04 inch. Two values of minimum crack widths were provided by Gulec and Whittaker (2009) because there was no consensus within the design professional community regarding the minimum crack width for epoxy-resin injection, and the same two ranges on crack width are used here.

5.2.3 MoR-3, Partial wall replacement

MoR-3 requires partial removal of reinforcement and concrete in the damaged zones of a reinforced concrete shear wall. The damage states associated with this method of repair include concrete crushing at the toes of a wall, initiation of concrete crushing within the web of a wall, vertical cracking in the toe regions of a wall, and buckling of vertical reinforcement. This method of repair is also used if the width of flexural cracks exceed 0.12 inch. Walls with flexural cracks wider than 0.12 inch cannot be repaired by epoxy-resin injection alone to restore pre-earthquake strength and stiffness (Gulec and Whittaker, 2009) and so partial wall replacement is required.

5.2.4 MoR-4, Full wall panel replacement

Gulec and Whittaker (2009) associated full replacement of a wall panel with damage states including sliding near the base of a wall (see Figure 5-1), wide diagonal cracks, wide spread concrete crushing, fracture of reinforcement, and shear cracks with width greater than 0.12 inch (3 mm). The Gulec proposed repair for a wall that has slid near its base is identical to that recommended in FEMA 306 (ATC, 1998b). Wide diagonal cracks indicate failure by diagonal tension: yielding of tension reinforcement at locations of cracks (see Figure 5-2). If reinforcement of a sufficient amount is provided to prevent diagonal tension failure, the lateral strength of a wall will be dictated by the axial capacity of the compression struts that form within its web (see Figure 5-2). Crushed concrete cannot be repaired by injections of epoxy grout and the wall panel must be replaced. The final damage state Gulec associated with wall replacement was fracture of reinforcement. He noted that fracture of reinforcement (DS4.4) is rarely seen in tests of squat walls:

only 3 of the 111 walls in the reduced database. Because fracture of reinforcement may occur after the damage associated with DS4.1, DS4.2, and DS4.3, it too is associated with replacement of a wall panel.

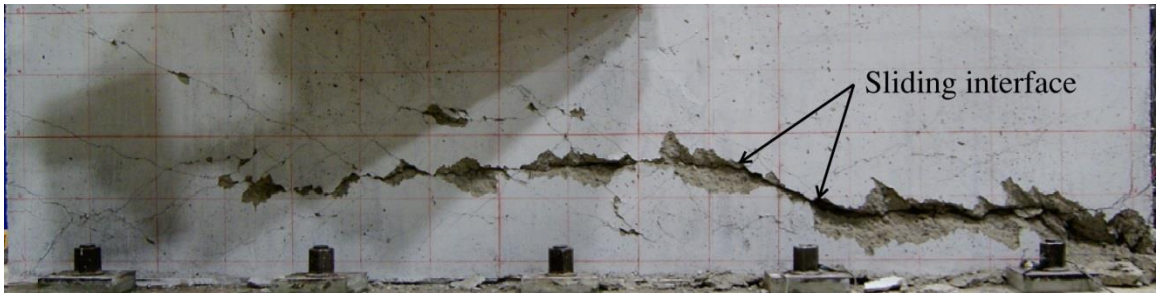

Figure 5-1. Crack in wall SW5 after LS8 (peak transient drift ratio of 0.89%)

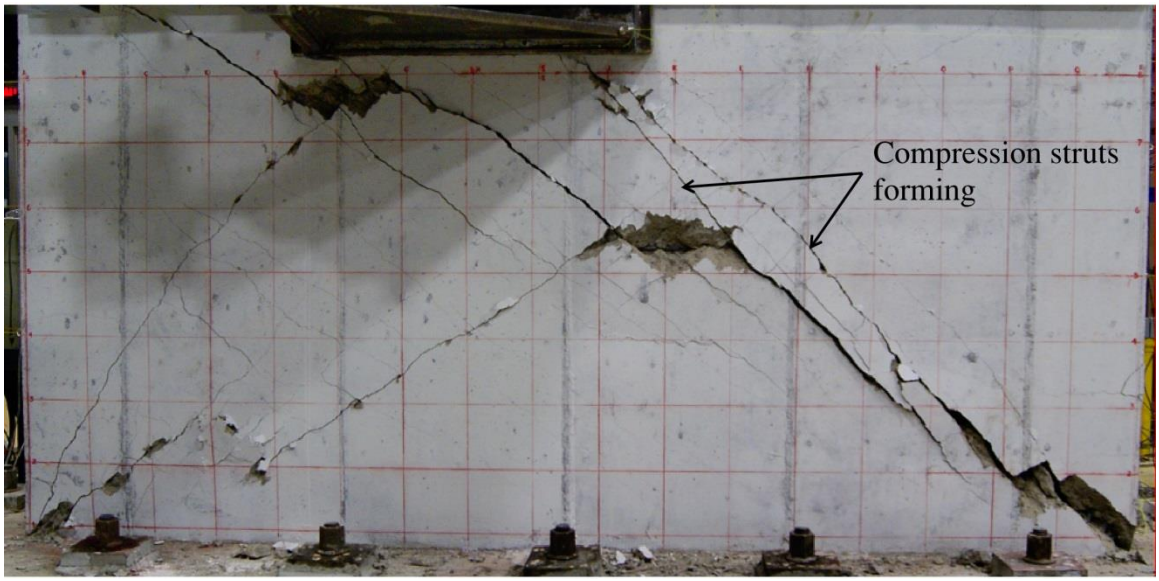

Figure 5-2. Cracking in wall SW10 after LS8 (peak transient drift ratio of 0.95%)

5.2.5 Gulec and Whittaker (2009) fragility functions

Gulec and Whittaker (2009) developed fragility functions for low aspect ratio walls using the damages states and methods of repair of Table 5-1. These fragility functions present the probability that certain method of repair will be required given a story drift ratio. Story drift ratio was chosen as the demand parameter because it was reported in the articles, reports and mined by Gulec. Gulec and Whittaker (2009) noted drift ratio "is the best single story-level demand parameter for most structural elements." They used peak transient displacement (or drift ratio) because data for damage states in the unloaded state were not available in the literature.

To enable risk calculations, fragility functions are generally associated with a continuous cumulative distribution function. Gulec and Whittaker (2009) tested four cumulative distribution functions: 1) lognormal, 2) gamma, 3) Weibull, and 4) beta. Goodness-of-fit tests (i.e., the Kolmogorov-Smirnov test and the Lilliefors test for the lognormal distribution, only) were used to evaluate the cumulative distribution functions as they related to the available test data. Of the four, Gulec determined the lognormal cumulative distribution best described the available test data for low aspect ratio reinforced concrete shear walls.

Table 8-21 of Gulec and Whittaker (2009), which is reproduced as Table 21 in Gulec et al. (2009), is provided here as Table 5-2: recommended values of the median peak transient story drift ratio, D, and logarithmic standard deviation, β, for four methods of repair for rectangular walls. Method of Repair 2b was assumed to best represent MoR-2 on the basis of input from the expert design professionals on the ATC-58 project team (see Gulec and Whittaker, 2009; Gulec et al., 2009). These fragility functions are plotted in Figure 5-3.

Table 5-2. Gulec et al. (2009) fragility function parameters for rectangular, low aspect ratio, reinforced concrete shear walls

MoR	θ	β	H	H_{crit}
1	0.07	0.79	0.082	0.140
2	0.55	0.34	0.181	0.207
3	1.09	0.27	0.122	0.164
4	1.30	0.35	0.202	0.154

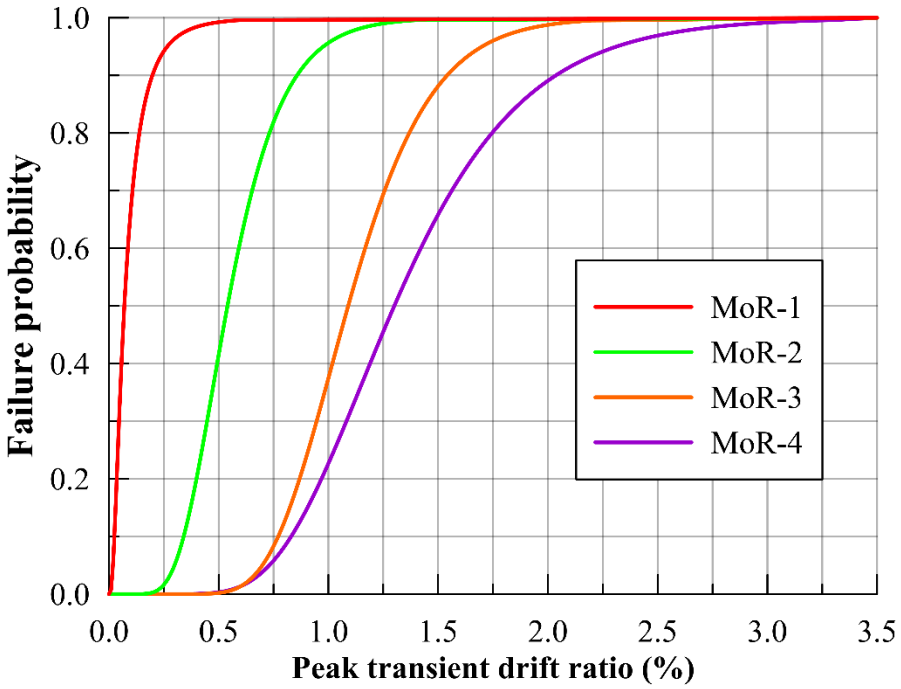

Figure 5-3. Fragility functions of Gulec and Whittaker (2009)

5.3 Proposed fragility functions

The fragility functions developed here utilize the procedures presented in Appendix H of Volume 1 of FEMA P-58 and the damage states reported in Chapter 4. These fragility functions are compared with those developed by Gulec and Whittaker (2009), and Gulec et al. (2009, 2010) using a common basis: a lognormal cumulative distribution function and the damage states and methods of repair introduced previously. The demand parameter used for the functions is peak transient drift ratio because this is a product of analysis. Importantly, and different from prior investigations, the peak transient drift ratio is related to the damage observed at the displacement associated with zero lateral load upon subsequent unloading. For example, in a half loading cycle to a positive peak transient drift ratio of say 1.00% and back to zero lateral load, for with the residual drift ratio is say 0.40%, shear cracks with width greater than 0.02 inch (0.5 mm) but less than 0.12 inch (3 mm), which maps to DS2.4a, are observed at a zero lateral force. Accordingly, DS2.4a is associated with a peak transient drift ratio of 1.00% rather than the damage state associated with wider cracks that existed at the peak transient drift ratio.

For completeness, the mathematical expressions used to describe the lognormal cumulative distribution function in Appendix H in Volume 1 of FEMA P-58 are presented below in Eq. (5-1) to Eq. (5-4):

$$F_i(D) = \Phi\left(\frac{\ln(D/\theta_i)}{\beta_i}\right) \qquad \text{Eq. (5-1)}$$

$$\beta_i = \sqrt{\beta_r^2 + \beta_u^2} \qquad \text{Eq. (5-2)}$$

$$\theta = e^{\left(\frac{1}{M}\sum_{i=1}^{M}\ln d_i\right)} \qquad \text{Eq. (5-3)}$$

$$\beta_r = \sqrt{\frac{1}{M-1}\sum_{i=1}^{M}\left(\ln\left(d_i/\theta\right)\right)^2} \qquad \text{Eq. (5-4)}$$

where $F_i(D)$ is the lognormal cumulative distribution function for the i^{th} method of repair given a peak transient drift ratio, D, Φ is the standard normal (Gaussian) cumulative distribution function, θ_i is the median value of the probability cumulative distribution function, β_i is the logarithmic standard deviation, β_r is the variability observed in the experimental data, β_u is the uncertainty that the experimental data represents actual conditions (described further in FEMA P-58), M is the number of specimens tested, and d_i is the demand in test i at which the damage state was first observed.

All of the fragility functions developed below are assessed using the Lilliefors goodness-of-fit-test presented in Section H.3.3 in Volume 1 of FEMA P-58:

$$H = \max_x \left|F_i(d) - S_M(d)\right| \qquad \text{Eq. (5-5)}$$

where H is the test parameter, $F_i(d)$ is the lognormal cumulative distribution function for the i^{th} method of repair as defined in Eq. (5-1), and $S_M(d)$ is the sample cumulative distribution function. The test parameter, H, is the maximum difference between the fragility function developed from the experimental data and the sample cumulative distribution function. It is compared with a critical test parameter, H_{crit}, to determine if the differences between the two functions are

statistically significant, that is, the relationship between drift ratio and damage observed is more than just random chance. The fragility function passes the goodness-of-fit test if $H < H_{crit}$.

The fragility functions are tested using a critical test parameter based on a 5% significance level per FEMA P-58. The mathematical expression governing H_{crit} at a 5% significance level (from Table H-4 in Volume 1 of FEMA P-58) is presented in Eq. (5-6), where M is the number of samples.

$$H_{crit} = 0.895 \Big/ \left(M^{0.5} - 0.01 + 0.85 M^{-0.5} \right) \qquad \text{Eq. (5-6)}$$

5.3.1 Damage states of SW1 to SW12

Chapter 4 documented damage states for walls SW1 to SW12 using the displacement associated with zero lateral load as the demand parameter. These damage states included a) onset of visible cracking, b) residual crack width between specified limits, c) onset of concrete crushing, d) the formation of wide diagonal cracks, e) vertical cracking in the toe regions and f) residual sliding at the base of the wall. As noted in Chapter 4, the term residual denotes damage observed at displacements associated with zero lateral force, which is, mimicking the damage observed by an engineer/inspector after an earthquake. All of these damage states correspond to method of repairs shown in Table 5-1, as defined previously by Gulec and Whittaker (2009). Buckling of reinforcement and fracture of reinforcement (see Table 5-1) were not observed in the testing of walls SW1 to SW12 and so are not addressed in the fragility functions developed later in this

chapter. Similarly, yielding of reinforcement is not used as a surrogate for crack width because locations, lengths and widths of cracks were logged.

Table 4-1 through Table 4-23 present the damage states observed in walls SW1 to SW12 using the descriptors of Table 5-1 and the corresponding methods of repair (MoR). The aspect ratio, h_w/l_w, vertical reinforcement ratio, ρ_l, horizontal reinforcement ratio, ρ_t, and compressive strength of concrete, f'_c, for each wall are identified in each table; the vertical reinforcement ratio in the boundary members of walls SW11 and SW12 is presented in Table 5-13 and Table 4-23. The peak transient drift ratio reported in the tables is the drift ratio prior to the unloaded condition for which the damage state is reported.

Table 5-3. Damage states observed in SW1[1]

$\left(h_w/l_w = 0.94, \rho_l = 0.67\%, \rho_t = 0.67\%, f'_c = 3600 \text{ psi}\right)$

Damage at zero lateral load[2]	Load step (LS)	Drift ratio (%)	Damage state as defined in Table 5-1	Method of repair (MoR)
Visible cracking	1	0.06	DS1.1	MoR-1
0.02 in $\leq w <$ 0.04 in	7	0.61	DS2.4a	MoR-2a
0.04 in $\leq w \leq$ 0.125 in	8	0.84	DS2.5b	MoR-2b
Concrete crushing in toe regions	10	1.68	DS3.1	MoR-3
$w >$ 0.125 in	10	1.68	DS4.2	MoR-4
Sliding at the base	10	2.60	DS4.1	

1. Peak transient drift ratio prior to damage measured in the unloaded condition
2. Damage states not observed during testing of this wall: vertical cracking in the toe regions and widespread crushing of concrete

Table 5-4. Damage states observed in SW2[1]

$\left(h_w/l_w = 0.54, \rho_l = 1.00\%, \rho_t = 1.00\%, f_c' = 7000 \text{ psi}\right)$

Damage at zero lateral load[2]	Load step (LS)	Drift ratio (%)	Damage state as defined in Table 5-1	Method of repair (MoR)
Visible cracking	2	0.08	DS1.1	MoR-1
0.02 in $\leq w <$ 0.04 in	9	0.78	DS2.4a	MoR-2a
0.04 in $\leq w \leq$ 0.125 in	10	1.26	DS2.4b	MoR-2b
Concrete crushing in toe regions	11	1.68	DS3.1	MoR-3

1. Peak transient drift ratio prior to damage measured in the unloaded condition
2. The following damage states were not observed during testing: cracks with widths greater than 0.125 inch, vertical cracks in the toe regions, widespread crushing of concrete and sliding at the base

Table 5-5. Damage states observed in SW3[1]

$\left(h_w/l_w = 0.54, \rho_l = 0.67\%, \rho_t = 0.67\%, f_c' = 7800 \text{ psi}\right)$

Damage at zero lateral load[2]	Load step (LS)	Drift ratio (%)	Damage state as defined in Table 5-1	Method of repair (MoR)
Visible cracking	3	0.06	DS1.1	MoR-1
0.02 in $\leq w <$ 0.04 in	10	0.75	DS2.4a	MoR-2a
0.04 in $\leq w \leq$ 0.125 in	12	1.82	DS2.5b	MoR-2b
Concrete crushing in toe regions	12	2.09	DS3.1	MoR-3
Sliding at the base	12	2.09	DS4.1	MoR-4

1. Peak transient drift ratio prior to damage measured in the unloaded condition
2. The following damage states were not observed during testing: cracks with widths greater than 0.125 inch, vertical cracks in the toe regions and widespread crushing of concrete

Table 5-6. Damage states observed in SW4[1]

$\left(h_w/l_w = 0.54, \rho_l = 0.33\%, \rho_t = 0.33\%, f_c' = 4200 \text{ psi}\right)$

Damage at zero lateral load[2]	Load step (LS)	Drift ratio[1] (%)	Damage state as defined in Table 5-1	Method of repair (MoR)
Visible cracking	3	0.04	DS1.1	MoR-1
0.02 in $\leq w <$ 0.04 in	9	0.41	DS2.4a	MoR-2a
Vertical cracks in the toe regions	10	0.60	DS3.2	MoR-3
0.04 in $\leq w \leq$ 0.125 in	11	0.75	DS2.4b	MoR-2b
Concrete crushing in toe regions	12	1.08	DS3.1	MoR-3
Sliding at the base	13	1.50	DS4.1	MoR-4

1. Peak transient drift ratio prior to damage measured in the unloaded condition
2. The following damage states were not observed during testing: cracks with widths greater than 0.125 inch and widespread crushing of concrete

Table 5-7. Damage states observed in SW5[1]

$\left(h_w/l_w = 0.33, \rho_l = 1.00\%, \rho_t = 1.00\%, f_c' = 4300 \text{ psi}\right)$

Damage at zero lateral load[2]	Load step (LS)	Drift ratio (%)	Damage state as defined in Table 5-1	Method of repair (MoR)
Visible cracking	1	0.02	DS1.1	MoR-1
0.02 in $\leq w <$ 0.04 in	7	0.67	DS2.4a	MoR2.4a
0.04 in $\leq w \leq$ 0.125 in	8	0.89	DS2.4b	MoR2.4b
Concrete crushing in the toe regions	8	0.89	DS3.1	MoR-3
Sliding near the base[3]	8	0.89	DS4.1	MoR-4
$w >$ 0.125 in	8	0.89	DS4.2	
Widespread crushing of concrete	8	0.89	DS4.3	

1. Peak transient drift ratio prior to damage measured in the unloaded condition
2. The following damage states were not observed during testing: vertical cracks in the toe region
3. Sliding along a plane approximately seven inches above the base of the wall

Table 5-8. Damage states observed in SW6[1]

$\left(h_w/l_w = 0.33, \rho_l = 0.63\%, \rho_t = 0.69\%, f_c' = 3800 \text{ psi}\right)$

Damage at zero lateral load[2]	Load step (LS)	Drift ratio[1] (%)	Damage state as defined in Table 5-1	Method of repair (MoR)
Visible cracking	2	0.04	DS1.1	0.21
0.02 in $\leq w <$ 0.04 in	8	0.81	DS2.4a	0.86
0.04 in $\leq w \leq$ 0.125 in	9	1.07	DS2.4b	0.83
Concrete crushing in toe regions	9	1.07	DS3.1	0.83
$w >$ 0.125 in	10	1.69	DS4.2	0.79
Sliding at the base	10	1.81	DS4.1	0.58

1. Peak transient drift ratio prior to damage measured in the unloaded condition
2. The following damage states were not observed during testing: vertical cracks in the toe region and widespread crushing of concrete

Table 5-9. Damage states observed in SW7[1]

$\left(h_w/l_w = 0.33, \rho_l = 0.34\%, \rho_t = 0.38\%, f_c' = 3800 \text{ psi}\right)$

Damage at zero lateral load[2]	Load step (LS)	Drift ratio[1] (%)	Damage state as defined in Table 5-1	Method of repair (MoR)
Visible cracking	2	0.08	DS1.1	MoR-1
0.02 in $\leq w <$ 0.04 in	7	0.45	DS2.4a	MoR-2a
Vertical cracks in toe regions	9	0.70	DS3.2	MoR-3
Sliding at the base	9	0.70	DS4.1	MoR-4
Concrete crushing in toe regions	10	0.85	DS3.1	MoR-3
0.04 in $\leq w \leq$ 0.125 in	13	1.94	DS2.4b	MoR-2b

1. Peak transient drift ratio prior to damage measured in the unloaded condition
2. The following damage states were not observed during testing: cracks with widths greater than 0.125 inch and widespread crushing of concrete

Table 5-10. Damage states observed in SW8[1]

$\left(h_w/l_w = 0.54, \rho_l = 1.50\%, \rho_t = 1.50\%, f_c' = 3500 \text{ psi}\right)$

Damage at zero lateral load[2]	Load step (LS)	Drift ratio[1] (%)	Damage state as defined in Table 5-1	Method of repair (MoR)
Visible cracking	4	0.34	DS1.1	MoR-1
0.02 in $\leq w <$ 0.04 in	7	0.88	DS2.4a	MoR-2a
Concrete crushing in toe regions	7	0.88	DS3.1	MoR-3
Vertical cracks in toe regions	7	0.88	DS3.2	
Sliding at the base	8	1.33	DS4.1	MoR-4
Widespread crushing of concrete	10	2.34	DS4.3	

1. Peak transient drift ratio prior to damage measured in the unloaded condition
2. The following damage states were not observed during testing: cracks with widths greater than 0.04 inch

Table 5-11. Damage states observed in SW9[1]

$\left(h_w/l_w = 0.54, \rho_l = 1.50\%, \rho_t = 0.67\%, f_c' = 4300 \text{ psi}\right)$

Damage at zero lateral load[2]	Load step (LS)	Drift ratio[1] (%)	Damage state as defined in Table 5-1	Method of repair (MoR)
Visible cracking	2	0.07	DS1.1	MoR-1
0.02 in $\leq w <$ 0.04 in	7	0.76	DS2.4a	MoR-2a
0.04 in $\leq w \leq$ 0.125 in	8	1.23	DS2.4b	MoR-2b
Concrete crushing in toe regions	8	1.23	DS3.1	MoR-3
Sliding at the base	8	1.35	DS4.1	MoR-4

1. Peak transient drift ratio prior to damage measured in the unloaded condition
2. The following damage states were not observed during testing: cracks with widths greater than 0.125 inch, vertical cracks in the toe region and widespread crushing of concrete

Table 5-12. Damage states observed in SW10[1]

$\left(h_w/l_w = 0.54, \rho_l = 1.50\%, \rho_t = 0.33\%, f_c' = 4600 \text{ psi}\right)$

Damage at zero lateral load[2]	Load step (LS)	Drift ratio[1] (%)	Damage state as defined in Table 5-1	Method of repair (MoR)
Visible cracking	2	0.09	DS1.1	MoR-1
0.02 in $\leq w <$ 0.04 in	5	0.42	DS2.4a	MoR-2a
0.04 in $\leq w \leq$ 0.125 in	5	0.42	DS2.4b	MoR-2b
$w >$ 0.125 in	6	0.59	DS4.2	MoR-4
Concrete crushing in toe regions	7	0.75	DS3.1	MoR-3
Widespread crushing of concrete	7	0.75	DS4.3	MoR-4
Sliding at the base	8	0.95	DS4.1	

1. Peak transient drift ratio prior to damage measured in the unloaded condition
2. The following damage states were not observed during testing: vertical cracks in the toe region

Table 5-13. Damage states observed in SW11[1]

$\left(h_w/l_w = 0.54, \rho_l = 0.67\%, \rho_t = 0.67\%, \rho_{be} = 1.50\%, f_c' = 5000 \text{ psi}\right)$

Damage at zero lateral load[2]	Load Step (LS)	Drift ratio[1] (%)	Damage state as defined in Table 5-1	Method of repair (MoR)
Visible cracking	2	0.09	DS1.1	MoR-1
0.02 in $\leq w <$ 0.04 in	5	0.57	DS2.4a	MoR-2a
0.04 in $\leq w \leq$ 0.125 in	6	0.75	DS2.4b	MoR-2b
Vertical cracks in toe regions	7	0.93	DS3.2	MoR-3
Concrete crushing in toe regions	8	1.30	DS3.1	
Sliding at the base	9	1.82	DS4.1	MoR-4

1. Peak transient drift ratio prior to damage measured in the unloaded condition
2. The following damage states were not observed during testing: cracks with widths greater than 0.125 inch and widespread crushing of concrete

Table 5-14. Damage states observed in SW12[1]

$\left(h_w/l_w = 0.54, \rho_l = 0.33\%, \rho_t = 0.33\%, \rho_{be} = 2.00\%, f_c' = 5000 \text{ psi}\right)$

Damage at zero lateral load[2]	Load Step (LS)	Drift ratio[1] (%)	Damage state as defined in Table 5-1	Method of repair (MoR)
Visible cracking	1	0.03	DS1.1	MoR-1
0.02 in $\leq w <$ 0.04 in	5	0.54	DS2.4a	MoR-2.4a
0.04 in $\leq w \leq$ 0.125 in	7	0.90	DS2.4b	MoR-2.4b
Concrete crushing in toe regions	8	1.27	DS3.1	MoR-3
Sliding at the base	9	1.64	DS4.1	MoR-4
$w >$ 0.125 in	9	1.64	DS4.2	

1. Peak transient drift ratio prior to damage measured in the unloaded condition
2. The following damage states were not observed during testing: vertical cracks in toe regions and widespread crushing of concrete

5.3.2 Development of fragility functions for walls SW1 to SW12

The fragility functions developed in this section use the characterizations of damage presented in Table 4-1 through Table 4-23. Two sets of fragility functions are developed, compared and discussed. The first set uses the drift ratio which first triggers a particular MoR to be used: Method 1. For example, if a wall has two damage states associated with MoR-3, one damage state being DS3.2 which occurs at a drift ratio of 0.80% and the second damage state being DS3.1 which occurs at a drift ratio of 1.20%, then the drift ratio of 0.80% will be used for that wall for MoR-3. The fragility functions of Method 1 will have one data point per wall per repair method. The second set is developed using all available damage states for all walls: Method 2. Each fragility function is tested using the goodness-of-fit test discussed in Section 5.3.

Table 5-15 and Table 5-16 present the distribution parameters for Method 1 and Method 2, respectively. Column 1 identifies the method of repair (MoR) of interest. Column 2 and Column

3 of the tables present the median peak transient drift ratio, θ, and logarithmic standard deviation, β, for each MoR. (More than 30 samples are needed to calculate a reliable value of logarithmic standard deviation but Luna and the author tested only 12 walls, and so the values reported for β in the tables below are approximate.) The test parameter, H, and the critical test parameter, H_{crit}, for each MoR are presented in columns 4 and 5 of the tables. Figure 5-4 and Figure 5-5 plot the empirical (from test data) and theoretical fragility functions for Method 1 and Method 2, respectively. The empirical and fitted fragility functions are in good agreement given the small number of data points.

Table 5-15. Method 1 fragility function distribution parameters

MoR	θ	β	H	H_{crit}
1	0.06	0.72	0.229	0.242
2a	0.62	0.29	0.117	0.242
2b	0.99	0.44	0.134	0.251
3	1.07	0.40	0.138	0.242
4	1.30	0.42	0.215	0.251

The Method 1 and Method 2 median peak transient drift ratio and logarithmic standard deviations for MoR-1, MoR-2a and MoR-2b are the same (see Table 5-15 and Table 5-16) because one damage state was recorded in each of the walls for each MoR: onset of visible cracking for MoR-1, cracks with widths greater than 0.02 inch for MoR-2a, and cracks with widths greater than 0.04 inch for MoR2-b. Multiple damage states were observed on some of the walls for MoR-3 and MoR-4. All five of the distributions for Method 1 and Method 2 (see Table 5-15 and Table 5-16, respectively) passed the goodness-of-fit test.

FEMA P-58 considers a fragility function to be of high quality based on two criteria: 1) passing the Lilliefors goodness-of-fit test at a 5% significance level and 2) having a logarithmic

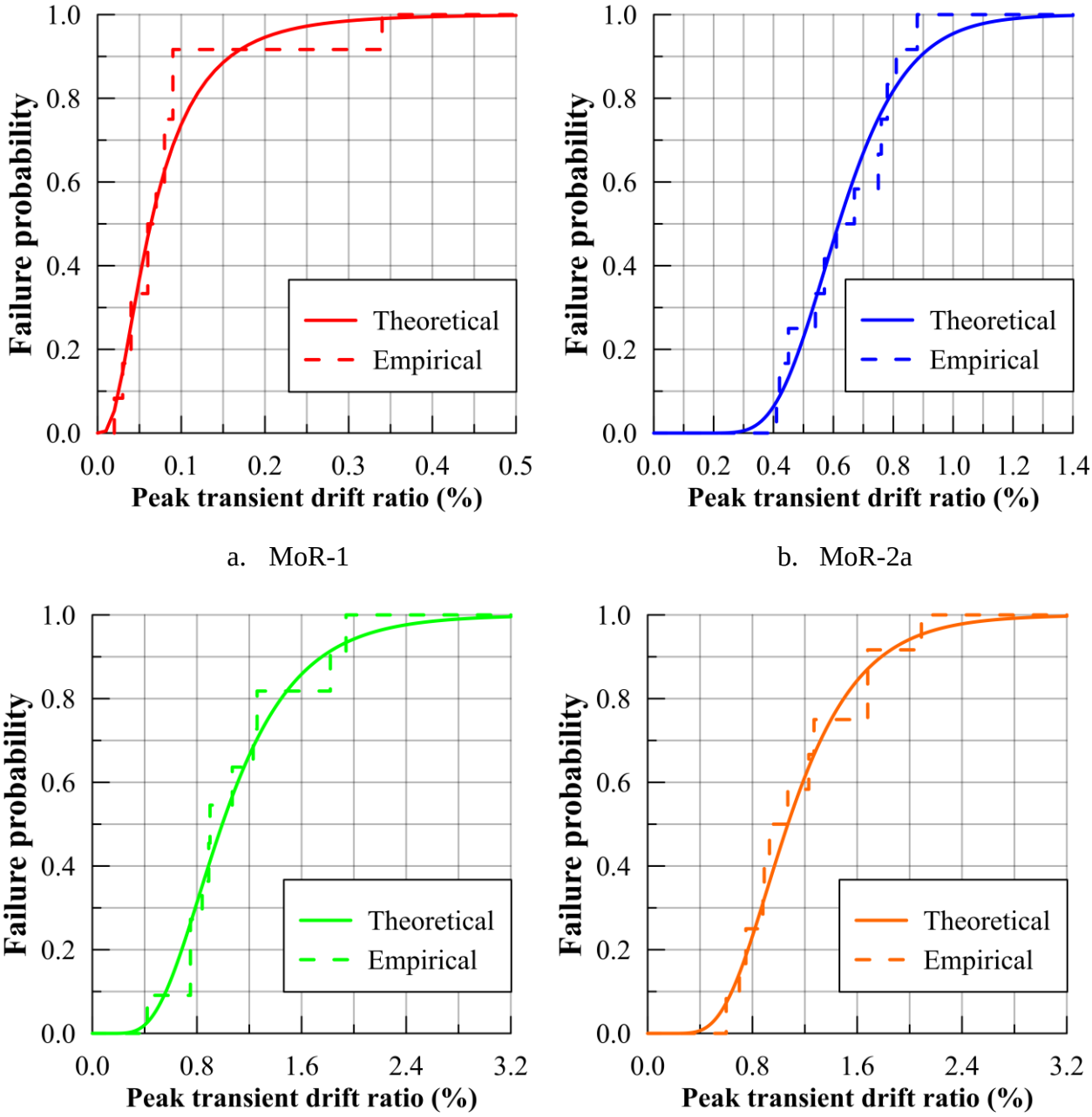

a. MoR-1

b. MoR-2a

c. MoR-2b

d. MoR-3

Figure 5-4. Proposed fragility functions developed with Method 1

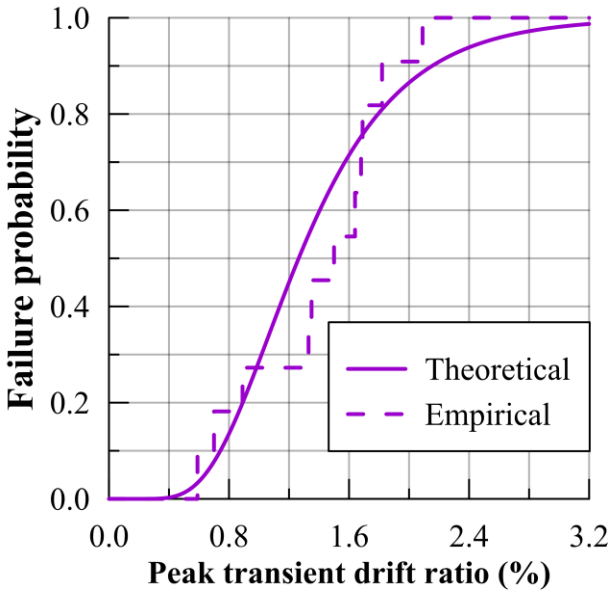

a. MoR-4

Figure 5-4. Proposed fragility functions developed with Method 1 (cont.)

Table 5-16. Method 2 fragility function distribution parameters

MoR	θ	β	H	H_{crit}
1	0.06	0.72	0.229	0.242
2a	0.62	0.29	0.117	0.242
2b	0.99	0.44	0.134	0.251
3	1.07	0.37	0.115	0.219
4	1.36	0.46	0.105	0.213

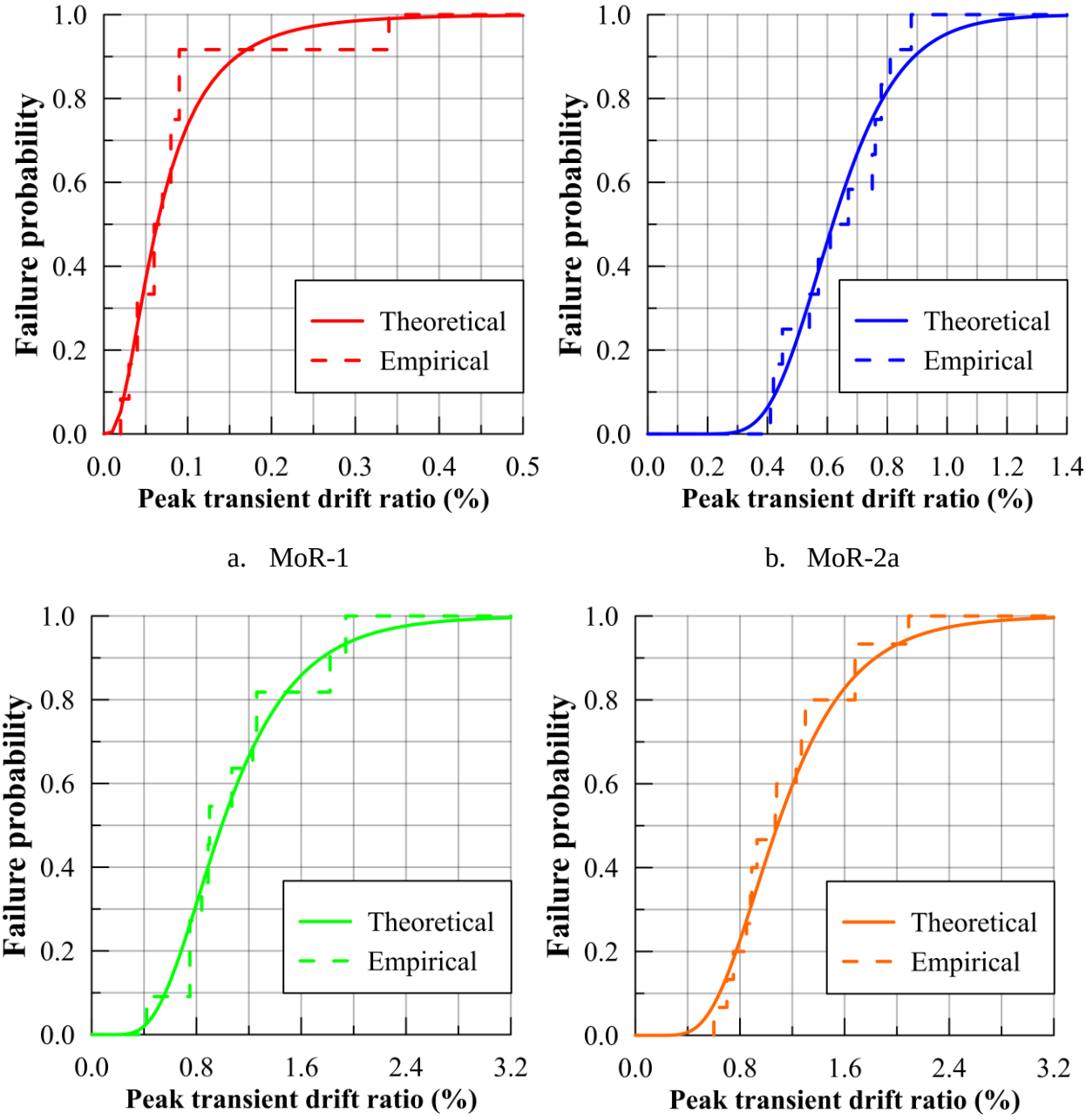

Figure 5-5. Proposed fragility functions developed with Method 2

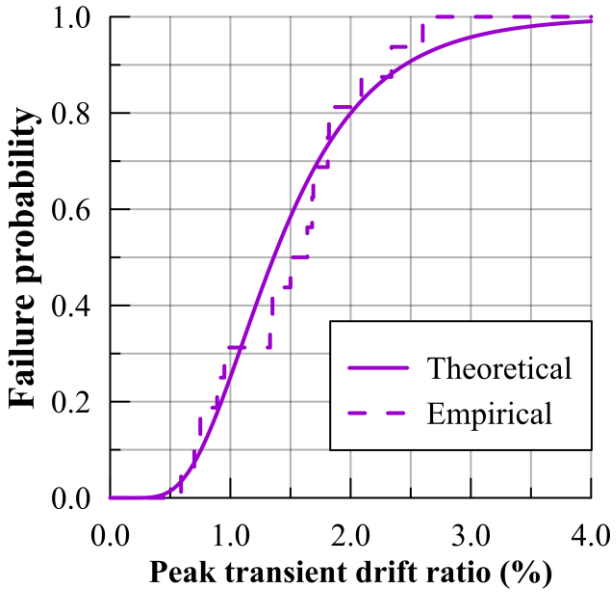

a. MoR-4

Figure 5-5. Proposed fragility functions developed with Method 2 (cont.)

standard deviation less than 0.6. MoR-2a, MoR-2b, MoR-3 and MoR-4 of Method 1 meet these conditions. MoR-1 does not meet these conditions but this is due to the presence of an outlier in the dataset, namely, SW8 has a drift ratio of 0.34% associated with MoR-1 whereas the corresponding drift ratios in all other walls were less than 0.09%. (The vertical and horizontal reinforcement ratios in SW8 were both 1.5%, which resulted in very fine cracks forming across the face of the wall). MoR-2a, MoR-2b, MoR-3 and MoR-4 of Method 2 are high quality.

It is challenging to develop fragility functions using a) a small sample size, and b) data from tests of walls with different aspect ratios (= 0.94, 0.54, and 0.33), different concrete compressive strengths, and widely varying reinforcement ratios. Many more tests would have to

be performed to develop high quality fragility functions for low aspect ratio walls considering aspect ratio, concrete compressive strength, and web and boundary element reinforcement ratios.

5.3.3 Comparison of proposed fragility functions with Gulec and Whittaker (2009)

Table 5-17 presents the median peak transient drift ratio and logarithmic standard deviation for the Method 1 fragility functions proposed above and the fragility functions proposed in Table 8-21 of Gulec and Whittaker (and Table 21 of Gulec et al., 2009). Table 21 of Gulec et al. (2009) is reproduced in Volume 3 of FEMA P-58. Identical to Gulec and Whittaker (2009) and Gulec et al. (2009) MoR-2b is assumed to best represent MoR-2.

Table 5-17. Current and proposed parameters for fragility functions

MoR	Gulec and Whittaker (2009)		Proposed here	
	θ	β	θ	β
1	0.07	0.79	0.06	0.71
2[1]	0.55	0.34	0.99	0.44
3	1.09	0.27	1.07	0.40
4	1.30	0.35	1.30	0.42

1. MoR-2b is assumed to best represent MoR-2

Interestingly, the proposed values of θ and β for MoR-1, MoR-3 and MoR-4 are virtually identical to those recommended in FEMA P-58 because different datasets, and different levels of reporting detail were available to Gulec and the author. However, a) hairline cracks (MoR-1) do not close completely upon unloading (i.e., they are visible at both peak transient displacement and zero lateral force), and damage associated with either partial (MoR-3) or full (MoR-4) wall replacement (see Table 5-1) will not be substantially different at peak transient displacement and zero lateral load. The large values of β for MoR-1 are attributed to a) the challenge associated

with identifying hairline cracks, and b) the relationship between web reinforcement ratio and rebar spacing, and crack width, noting that the fragility functions are assumed to be independent of reinforcement ratio, concrete compressive strength and wall aspect ratio, which they are not.

The major difference between the current and proposed parameters in Table 5-17 is for MoR-2: epoxy resin injection of cracks. The median value recommended by Gulec and Whittaker was based on analysis of reported crack-width data, which was likely based exclusively on widths measured at peak transient drift, which close (in most instances) as the lateral load is reduced to zero. Crack width was measured and reported at zero lateral load in the dataset used by the author.

5.4 Summary

The data collected and reduced from the Luna and Rivera dataset provided an opportunity to re-assess the fragility functions proposed by Gulec et al. (2009) for low aspect ratio, rectangular, reinforced concrete shear walls. The significant change proposed here is to increase the median drift ratio for MoR-2 from 0.55% to 1.0%, which has a technical basis, as described above. Recommended values are provided in Table 5-18 and the functions are plotted in Figure 5-6. A user of these fragility functions must recognize that the functions apply to a very broad family of reinforced concrete shear walls, namely, aspect ratio between 0.33 and 1.00, concrete compressive strength between 3500 psi and 7000 psi, web reinforcement ratio between 0.3% and 1.5% and shear walls with and without vertical boundary reinforcement. For a wall with properties falling within these bounds, the median value for a given MoR may be significantly different from that

reported in the table, but the logarithmic standard deviation is likely smaller than that reported in the table.

Table 5-18. Recommended parameters for fragility functions: low aspect ratio shear walls

MoR	θ	β
1	0.06	0.7
2	1.0	0.4
3	1.1	0.4
4	1.3	0.4

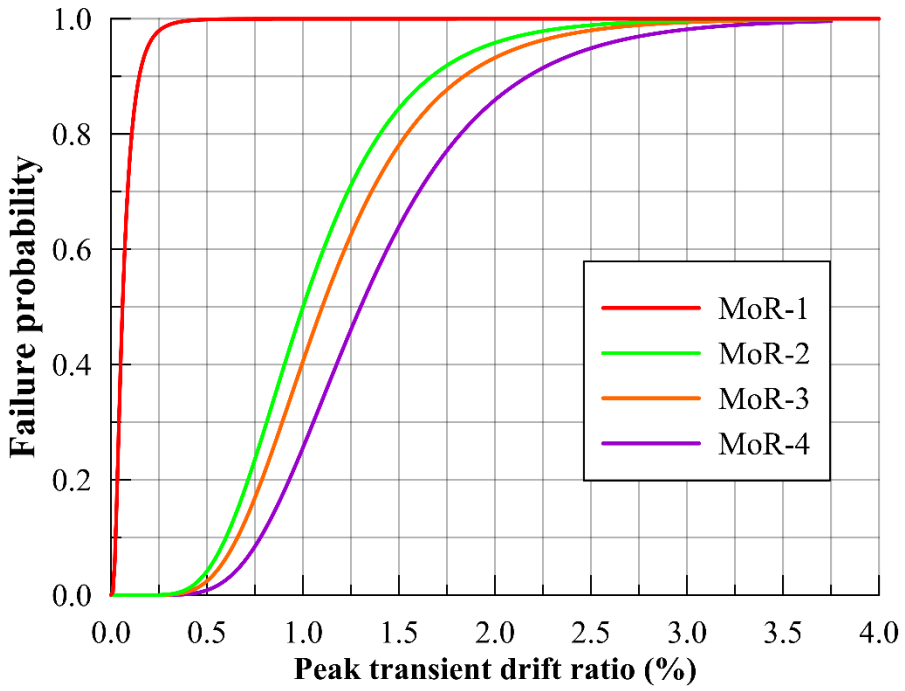

Figure 5-6. Recommended fragility functions: low aspect ratio shear walls

SECTION 6
SUMMARY AND CONCLUSIONS

6.1 Summary

Many low- and medium-rise buildings, and most safety-related nuclear structures, are constructed with low aspect ratio reinforced concrete shear walls to resist the lateral forces generated by windstorms and earthquakes. Under extreme earthquake loadings, low aspect ratio shear walls will likely be damaged so it is imperative to develop robust procedures for post-earthquake evaluation and repair. Repair strategies are routinely based on damage observed and documented by post-earthquake visual inspections. Types of damage (or damage states) include, but are not limited to, the onset of visible cracking, crack widths exceeding threshold values, concrete crushing in the toe regions of walls, vertical cracking in the toe regions of walls, sliding at the base of a wall, wide diagonal cracks, widespread crushing of concrete, buckling of reinforcement and fracture of reinforcement. Collection and documentation of such damage states is laborious and approximate due to the methods currently employed by engineers/inspectors. Importantly, crack width is measured at discrete locations on a wall, and the areal density of cracking (aggregate product of length and width, divided by wall are) which should be used to assess damage, is not calculated accurately.

A primary goal of documenting earthquake damage is to identify repair methods that could restore an earthquake-damaged wall to its pre-earthquake condition. One decision point, in terms of chosen repair, is whether the peak shear strength of a wall has been reached. If the peak shear strength of the wall has not been reached, and this can be proven, a structural repair is likely not required. However, the archival literature and consensus standards do not provide guidance for

inspectors/engineers to correlate damage recorded during a post-earthquake evaluation and whether the peak shear strength of a wall has been reached.

The probable performance of a shear wall during an earthquake can be estimated using fragility functions that plot the probability of exceeding a user-specified damage state (e.g., cracks requiring injection of epoxy resin to restore the pre-earthquake stiffness and strength of a wall) as a function of a demand parameter that is predicted by analysis (e.g., peak story drift). Currently available fragility functions are built from data recorded at instants of peak transient displacement, which is information that is not available to an engineer/inspector during a post-earthquake inspection. Rather, information on damage is collected at zero lateral loading during a post-earthquake inspection, which means that some available fragility functions, such as those reported in Volume 3 of FEMA P-58 (FEMA, 2012), are likely inaccurate. Such data were collected by the author during the tests of twelve, large-scale, low aspect ratio reinforced concrete shear walls at the University at Buffalo (e.g., Luna, 2015 and Luna et al., 2015). These had varying aspect ratios (0.33, 0.54 and 0.94), concrete compressive strength (3500 psi to 7800 psi), vertical reinforcement ratio (0.33% to 1.5%) and horizontal reinforcement ratio (0.33% to 1.5%). Two walls included in-plane boundary elements. Damage states were documented at peak transient displacements and at zero lateral loading (i.e., the post-earthquake condition). The methods used to document damage included hand sketches, low-resolution photographs and high-resolution photographs. This data set is unique.

An automated, non-contact imaging tool (I-Crack) was developed in MATLAB (Mathworks, 2013) using digital data mined from very high-resolution photographs. Image

processing techniques and algorithms were developed using data collected from a single wall. The tool was validated by comparing results for eight walls with numerous manual measurements of crack width along the length of each crack, using traditional gages, for each wall. Importantly, a) I-Crack can calculate the areal density of cracking, which is impractical by manual methods, and b) the input to I-Crack can be collected quickly (i.e., high-resolution photographs), which improves safety in both the field and laboratory.

6.2 Conclusions and Observations

The key objectives of this report were to 1) develop a non-contact imaging tool for recording damage to reinforced concrete walls (i.e., I-Crack), 2) correlate observed damage to whether the peak shear strength of a wall had been reached, and 3) review and update the fragility functions developed by Gulec and Whittaker (2009) using the dataset developed by the author and Luna. These objectives were achieved. The key conclusions of the report are provided below, together with some related observations.

6.2.1 Automated detection and measurement of cracks (I-Crack)

1. The automated algorithm I-Crack can effectively and efficiently replace traditional methods of documenting earthquake damage to reinforced concrete shear walls (and other components).
2. Five edge detection algorithms, all of which are available within MATLAB, were evaluated for use in I-Crack: Roberts, Sobel, Prewitt, Canny and Laplacian of Gaussian.

The Prewitt edge detection algorithm proved best and is recommended for use with I-Crack.

3. Image segmentation is used to separate cracks from surface defects present on all reinforced concrete walls. Orientation angle and the major-minor axes length ratio can be used to differentiate cracks from surface defects.
4. Crack widths and lengths are measured using sub-routines available in MATLAB.
5. The crack widths calculated by I-Crack match closely with values measured manually, providing high confidence the algorithm is robust.

The algorithm for I-Crack was written in MATLAB and the source code is available in Appendix A for the interested user. Information on I-Crack is available in the archival literature (Rivera et al., 2015).

6.2.2 Correlating damage with the attainment of peak shear strength of a wall

1. Onset of visible cracking will occur in the unloaded condition at displacements less than that associated with peak shear strength.
2. Cracks with a width at zero lateral load of greater than 0.02 inch will develop prior to a rectangular wall attaining its peak shear strength.
3. Cracks with a width at zero lateral load of greater than 0.04 inch will develop as a rectangular wall attains its peak shear strength.
4. Cracks with a width at zero lateral load of greater than 0.125 inch will develop after a rectangular wall has achieved its peak shear strength.

5. Concrete in the toe regions of a rectangular wall will crush when the wall has achieved its peak shear strength or has attained a displacement greater than that associated with peak shear strength.
6. Widespread crushing of concrete in the web of a rectangular wall will occur at displacements similar to or at the displacement associated with peak shear strength.
7. Sliding at the base of a rectangular wall occurs after peak shear strength has been achieved and does not limit peak resistance.
8. The average crack width ratio for walls with equal horizontal and vertical web reinforcement ratios, and do not include boundary elements, is on the order of 3 in the pre-peak strength region, 4 at peak strength and approximately 4 in the post-peak strength region. The average crack width ratio decreases for the pre-peak strength region and peak strength region as the web vertical and horizontal reinforcement ratios increase.
9. For walls with in-plane boundary elements and equal horizontal and vertical reinforcement ratios, the average crack width ratio decreases in the pre-peak strength region and peak strength region as the web reinforcement ratio increases.

6.2.3 Updated fragility functions

1. Data collected by the author and Luna (2015) enabled a detailed re-assessment of the fragility functions developed by Gulec (2009) and presented in Gulec and Whittaker (2009) and Gulec et al. (2009, 2010), for low aspect ratio, rectangular, reinforced concrete shear walls.

2. The major update to the fragility functions presented in Gulec and Whittaker (2009) and Gulec et al. (2009, 2010) is to increase the median drift ratio of MoR-2, namely, epoxy resin injection of cracks to restore pre-earthquake strength and stiffness, from 0.55% to 1.0%. This substantial increase in median drift ratio addresses the relationship between cracks widths at zero lateral loading (i.e., mimicking post-earthquake conditions) and the peak transient displacement that produced the cracks, which subsequently partially close upon unloading.
3. The median peak transient drift ratios and logarithmic standard deviations for MoR-1, MoR-3 and MoR-4 reported by Gulec were by-and-large confirmed by the analysis of the experimental data collected by the author and Luna.
4. Users of the proposed fragility functions must recognize that the values of the parameters of the lognormal distributions proposed here (and previously by Gulec) were developed using data from tests of low aspect ratio shear walls with widely varying aspect ratios, concrete compressive strengths, and reinforcement ratios. Values of the parameters for a wall with given mechanical and geometric properties may vary significantly from those proposed in this report.

SECTION 7
REFERENCES

Abdel-Qader, I., Abudayyeh, O., and Kelly, M. (2003). "Analysis of edge-detection techniques for crack identification in bridges." Journal of Computing in Civil Engineering, 17(4), 255-263.

Adobe Systems Inc. (2010). Adobe Photoshop Elements version 9.0.3, www.adobe.com.

American Concrete Institute (ACI). (2004). "Concrete repair guide (ACI 546R-04)." Farmington Hills, MI.

American Concrete Institute (ACI). (2014). "Building code requirements for structural concrete (ACI 318-14) and commentary." Farmington Hills, MI

American Society of Civil Engineers (ASCE). (2005). "Seismic design criteria for structures, systems and components in nuclear facilities." ASCE/SEI Standard 43-05, Reston, VA

American Society of Civil Engineers (ASCE). (2010). "Minimum design loads for buildings and other structures." ASCE/SEI Standard 7-10, Reston, VA

American Society of Civil Engineers (ASCE). (2016). "Seismic analysis of safety-related nuclear structures and commentary." ASCE/SEI Standard 4-16, Reston, VA

American Society for Testing and Materials (ASTM) (2009). "Standard specification for deformed and plain low-alloy steel bars for concrete reinforcement (ASTM A706/A706M-09b)." West Conshohocken, PA.

American Society for Testing and Materials (ASTM) (2011). "Standard specification for concrete aggregates (ASTM C33/C33M-11a)." West Conshohocken, PA.

American Society for Testing and Materials (ASTM) (2012). "Standard specification for coal fly ash and raw or calcined natural pozzolan for use in concrete (ASTM C618-12a)." West Conshohocken, PA.

American Society for Testing and Materials (ASTM) (2012). "Standard specification for deformed and plain carbon-steel bars for concrete reinforcement (ASTM A615/A615M-12)." West Conshohocken, PA.

American Society for Testing and Materials (ASTM) (2012). "Standard specification for Portland cement (ASTM C150/C150M-12)." West Conshohocken, PA.

American Society for Testing and Materials (ASTM) (2012). "Standard test method for compressive strength of cylindrical concrete specimens (ASTM C39/C39M-12)." West Conshohocken, PA.

American Society for Testing and Materials (ASTM) (2012). "Standard test methods and definitions for mechanical testing of steel products (ASTM A370-12a)." West Conshohocken, PA.

Applied Technology Council (ATC). (1998). "Evaluation of earthquake damaged concrete and masonry wall buildings – basic procedures manual (ATC-43, FEMA 306)." Federal Emergency Management Agency, Washington D.C.

Applied Technology Council (ATC). (1998). "Repair of earthquake damaged concrete and masonry wall buildings (FEMA 308)." Federal Emergency Management Agency, Washington D.C.

Applied Technology Council (ATC). (2012). "Seismic performance assessment of buildings, volume 1 – methodology (FEMA P-58-1)." Federal Emergency Management Agency, Washington, D.C.

Applied Technology Council (ATC). (2012). "Seismic performance assessment of buildings, volume 3 – supporting electronic material and background documentation (FEMA P-58-3)." Federal Emergency Management Agency, Washington, D.C.

Bluebeam Software, Inc. (2016). Bluebeam Revu x64 CAD, Pasadena, CA.

Choudhary, G. K. and Dey, S. (2012). "Crack detection in concrete surfaces using image processing, fuzzy logic, and neural networks." Proceedings, 5th International Conference on Advanced Computational Intelligence (ICACI), Nanjing, Jiangsu, China, 404-411.

CTL Group. (2017). http://www.ctlgroup.com/home/. Accessed July 16, 2017.

Epackachi, S. and A. S. Whittaker. (2017). "Shear-controlled reinforced concrete walls," Chapter 8 and Appendices C and D, in NIST GCR-17-917-45, Recommended Modeling Parameters and Acceptance Criteria for Nonlinear Analysis in Support of Seismic Evaluation, Retrofit and Design, National Institute of Standards and Technology, Gaithersburg, MD.

Fast Stone Soft. (2013). Fast Stone Image Viewer for Windows version 4.7., ww.FastStone.org.

Fujita, Y., Mitani, Y., and Hamamoto, Y. (2006). "A method for crack detection on a concrete structure." Proceedings, 18th International Conference on Pattern Recognition, Hong Kong, China, 901-904.

GigaPan Systems. (2013). http://www.gigapansystems.com/. Accessed August 1, 2013.

Greiner, U. and Ramm, W. (1995). "Air leakage characteristics in cracked concrete." Nuclear Engineering and Design, 156(1-2), 167-172.

Gulec, C. K. (2009). “Performance-based assessment and design of squat reinforced concrete shear walls.” PhD Dissertation, University at Buffalo, Buffalo, NY.

Gulec, C. K., and Whittaker, A. S. (2009). “Performance-based assessment and design of squat reinforced concrete shear walls.” Technical Report MCEER-09-0010, University at Buffalo, Buffalo, NY.

Gulec, C. K., Whittaker, A. S., and Hooper, J. D. (2009). “Damage states and fragility curves for low aspect ratio reinforced concrete walls (FEMA P-58/BD-3.8.8).” Federal Emergency Management Agency, Washington, D.C.

Gulec, C. K., Whittaker, A. S., and Hooper, J. D. (2010). “Fragility functions for low aspect ratio reinforced concrete walls.” Engineering Structures, 32, 2894-2901.

Hamilton, C. H., Hutchinson, T. C., Pardoen, G. C., Salmon, M. W., and Wang, T. (2004). “Gas and aerosol leakage rate through reinforced concrete shear walls: experimental study.” Proceedings, 13th World Conference on Earthquake Engineering, Vancouver, Canada.

Luna, B. N. (2015). “Seismic response of low aspect ratio reinforced concrete walls for buildings and safety-related nuclear applications.” PhD Dissertation, University at Buffalo, Buffalo, NY.

Luna, B. N., Rivera, J. P., and Whittaker, A. S. (2015). “Seismic behavior of low aspect ratio reinforced concrete shear walls.” ACI Structural Journal, 112(5), 593-603.

Luna, B. N., Rivera, J. P., Epackachi, S and Whittaker, A. S. (2018). “Seismic response of low aspect ratio reinforced concrete walls.” Technical Report MCEER-18-0002, University at Buffalo, Buffalo, NY.

MathWorks, Inc (2013). MATLAB R2013a, Natick, MA.

Miyamoto, A., Konno, M. A., and Brüwiler, E. (2007). “Automatic crack recognition system for concrete structures using image processing approach.” Asian Journal of Information Technology, 6(5), 553-561.

Rivera, J. P., Josipovic, G., Lejeune, E., Luna, B. N., and Whittaker, A. S., (2015). “Automated detection and measurement of cracks in reinforced concrete components.” ACI Structural Journal, 112(3), 397-405.

Rizkalla, S. H., Lau, B. L., and Simmonds, S. H. (1984). “Air leakage characteristics in reinforced concrete.” Journal of Structural Engineering, 110(5), 1149-1162.

Rock, J. F. (2012). “Large scale testing of low aspect ratio reinforced concrete walls.” MS Thesis, University at Buffalo, Buffalo, NY.

Soppe, T. E., and Hutchinson, T. C. (2012). “Assessment of gas leakage rates through damaged reinforced-concrete walls.” Journal of Materials in Civil Engineering, 24(5), 560-567.

Yamaguchi, T., Nakamura, S., Saegusa, R., and Hashimoto, S. (2008). “Image-based crack detection for real concrete surfaces.” Transactions on, Electrical and Electronic Engineering, Institute of Electrical Engineers of Japan, 3(1), 128-135.

APPENDIX A
MATLAB CODE FOR I-CRACK

A.1 Introduction

I-Crack was created using MATLAB R2013a (ver. 8.1.0.064), Image Processing Toolbox and the Parallel Processing Toolbox. Appendix A provides the MATLAB code written specifically for I-Crack. The names and a brief description of each code and sub-script are shown in Table A-1. Each MATLAB code and sub-scripts are given in the subsequent sections with detailed comments. If alterations are required to the code, the comments will provide guidance to where these alterations can be made and the possible affects to the results.

Table A-1. MATLAB code and sub-scripts used in I-Crack

Name	Description
Calibrate	Calculates a length per pixel based on the number of pixels in the length of the wall. This code will be unique depending on the object used that has a known parameter (e.g., length or area).
ColorCode	Color codes each feature detected based on the width predicted by I-Crack. Three colors are used to specify the width (blue, purple and red). Features color coded blue have a width less than 0.020 inch. Features color coded purple have a width ranging from 0.020 inch to 0.125 inch. Features color coded red have a width greater than 0.125 inch.
CrackData	Calculates the minimum, maximum, average, 16^{th} percentile, 84^{th} percentile of the detected cracks. CrackData will also calculate the total length, total area of all of the detected cracks and count the number of cracks detected.
crackDetect	Uses an edge detection algorithm supplied by the Image Toolbox in MATLAB to determine where the edges are on the surface defects and cracks.
CrackFill	Uses morphological operations to fill in the space between the edges detected for cracks and surface defects. The morphological operations include bwmorph, bwareaopen, imfill and imclose.
CrackLabel	Applies image segmentation based on the ratio of the major-axis length to the minor-axis length. Each crack and remaining surface defect is then measured after a second image segmentation criterion has been applied. All of the measurements are stored in a numerical array and saved as a comma-separated file for later use.

Table A-1. MATLAB code and sub-scripts used in I-Crack (cont.)

CrackWidthSearch	A post-processing script used to extract the crack widths from the array storing the crack properties. In addition to the array of stored crack properties, a MATLAB figure file (.fig) of the labelled cracks is also required. The .fig file was created using the sub-script CrackLabel.
ICrack	Main computer algorithm used to analyze high-resolution panoramas of reinforced concrete components.
ImageOverlay	One of the final steps in I-Crack that generates a JPEG image that has all of the detected cracks highlighted and color coded based on predicted widths.
orientationFilter	Applies the first criterion used for image segmentation. This sub-script separates the cracks and surface defects based on their angle of inclination. During the development of I-Crack it was observed that many of the surface defects were either horizontal or vertical, while many of the cracks were inclined at an angle.
removeGrid	Used to split the image to decrease processing time and applies the sub-script removeGrid2 to remove the chalk lines present on the face of the specimen
removeGrid2	A sub-script used to remove red chalk lines present on the surface of all the specimens based on the amount of red in each pixel.

A.2 Calibrate

```
%%%%%%%%%%%%%%%%%%%%%%%%%%%%%%%%%%%%%%%%%%%%%%%%%%%%%%%%%%%%%%%%%%%%%%%%%%%%%%%
% Calibrate
% MATLAB code used during pre-processing to determine a length per unit
% pixel. This will allow for a measurement in inches for crack width,
% length, and area. This specific sub-routine will be unique
% for each type of specimen analyzed or for each unique object within the
% panorama used for calibration. At the University at Buffalo, SUNY,
% rectangular walls with equal length were tested. Since the length of each
% specimen remained unchanged, this parameter was used to calculate a
% length per unit pixel. The following sub-routine is written specifically
% for the walls tested at the University at Buffalo.
%
% Written for use in I-Crack
% Written by: Jonathan Rivera and Goran Jospovic
% Contact information: jprivera@buffalo.edu
%%%%%%%%%%%%%%%%%%%%%%%%%%%%%%%%%%%%%%%%%%%%%%%%%%%%%%%%%%%%%%%%%%%%%%%%%%%%%%%

% Load a specific image into MALAB. The file name is inserted between the
% two apostrophes and can be file extensions .jpg or .png
A = imread('SW8_LS6_C1_PEAK1_c.jpg');

% Changes the image to black and white based on a threshold value between
% 0.0 and 1.0. Additionally, the shadows cast by the loading apparatus are
% changed from white to black.
BW = im2bw(A,0.5);
BW1 = imfill(BW,'holes');
```

```
se = strel('square',100);
BW2 = imopen(BW1,se);

for i = 1:7000          % Row position of shadow cast by loading bracket
    for j = 500:18000   % Column position of shadow cast by loading bracket
       BW2(i,j,:)=1;    % Sets pixels to white in the designated rows and
    end                 % columns
end

% Counts the number of white pixels in a specified row by summing along a
% specified row.
numofpixels = sum(BW2,2);

[v, d] = size(numofpixels);
x = round(v/5);
y = round(2*v/5);
z = round(3*v/5);

pix1 = numofpixels(x,1);
pix2 = numofpixels(y,1);
pix3 = numofpixels(z,1);

pix = [pix1, pix2, pix3];
pix = mean(pix);

% Calculates a length per pixel
PixelCal = 120/pix
```

A.3 ColorCode

```
%%%%%%%%%%%%%%%%%%%%%%%%%%%%%%%%%%%%%%%%%%%%%%%%%%%%%%%%%%%%%%%%%%%%%%%%%%%%%%%
% ColorCode
% MATLAB sub-script used to color code the features based on their
% predicted widths. Inputs required for this sub-script include the image
% segmented (IMG_A) and the information regarding the crack widths
% (CrackInfo). Using these two inputs the cracks are categorized and color
% coded based on three width ranges. The first range corresponds to MoR-1,
% crack widths less than 0.020 inch, and is color coded blue. The second
% range corresponds to MoR-2, crack widths ranging from 0.020 inch to 0.125
% inch, and are color coded purple. The third range corresponds to MoR-3
% and MoR-4, crack widths greater than 0.125 inch, and are color coded red.
%
% Input: Black and white image of cracks and remaining surface defects
% after image segmentation and an array with information on the cracks
% Output: Image of cracks and remaining surface defects color coded
%
% Written for use in I-Crack
% Written by: Jonathan Rivera and Goran Jospovic
% Contact information: jprivera@buffalo.edu
%%%%%%%%%%%%%%%%%%%%%%%%%%%%%%%%%%%%%%%%%%%%%%%%%%%%%%%%%%%%%%%%%%%%%%%%%%%%%%%

function [RGB] = ColorCode(IMG_A,CrackInfo)

% Increases the cracks widths artificially to make them more visible after
```

```
% they have been superimposed on a colored image. After the cracks have
% been thickened, MATLAB then labels each crack going from top to bottom,
% left to right.
% IF cracks are required to be thicker in the final image, increase the
% number in "bwmorph"
IMG1 = bwmorph(IMG_A,'thicken',5);
LabelMatrix1 = bwlabel(IMG1,8);

% Creates three matrices full of zeroes the size of the original input image.
% Each matrix defines the contribution of red, green and blue to each
% pixel. The three matrices are then combined to form a single MxMx3
% matrix; where MxM is the size of the input image and the 3 is the number
% of matrices combined.
R = zeros(size(IMG1));
G = zeros(size(IMG1));
B = zeros(size(IMG1));

RGB = cat(3,R,G,B);
RGB = uint8(RGB);

% Color code the cracks by first obtaining the pixels of the current crack
% or remaining surface defect. Then obtain the predicted width from
% CrackInfo and assign a color based on the width.
nCracks = size(CrackInfo);
for lbl = 1:nCracks
    currentLabel = LabelMatrix1 == lbl; % find pixels associated with IMG_A
    width = CrackInfo(lbl,9);

    if width <= 0.02
        rgb = label2rgb(currentLabel,[0 0 1],'k');     % Blue, MoR-1
    elseif width > 0.02 && width <= 0.125
        rgb = label2rgb(currentLabel,[0.5 0 0.5],'k'); % Purple, MoR-2
    elseif width > 0.125
        rgb = label2rgb(currentLabel,[1 0 0],'k');     % Red, MoR-3/4
    end
    RGB = imadd(RGB,rgb);

end

% imshow(RGB)
```

A.4 CrackData

```
%%%%%%%%%%%%%%%%%%%%%%%%%%%%%%%%%%%%%%%%%%%%%%%%%%%%%%%%%%%%%%%%%%%%%%%%%%%%
% CrackData
% This code can be ran separately from I-Crack or as a post-processing
% step. CrackData will go through the CrackInfo array and calculate the
% minimum, maximum, mean, 16th percentile and 84th percentile widths of the
% cracks detected. In addition, the total lengths and total area of cracks
% are calculated.
%
% Input: Array containing all of the crack information calculated and the
% calibration pixel
% Output: Minimum, maximum, mean, 16th percentile, 84th percentile crack
```

```
% width, total crack length and total crack area.
%
% Written as a final step in I-Crack analysis or for post-processing.
% Written by: Jonathan Rivera and Goran Jospovic
% Contact information: jprivera@buffalo.ed
%%%%%%%%%%%%%%%%%%%%%%%%%%%%%%%%%%%%%%%%%%%%%%%%%%%%%%%%%%%%%%%%%%%%%%%%%%%%

function CrackData(CrackInfo,PixelCal)

% Load the array containing all of the information the cracks detected and
% use the min, max, mean, and prctile commands to calculate statistics. If
% other percentiles are required then change the 16 or 84 to the desired
% percentile. The total area and total length are calculated by summing the
% columns in the array associated with length and area.
Crack = CrackInfo(:,9);
MinCrack = min(Crack);
MaxCrack = max(Crack);
AverageCrack = mean(Crack);
Crack16 = prctile(Crack,16);
Crack84 = prctile(Crack,84);
numberofCracks = size(CrackInfo,1);
totalLength = sum(CrackInfo(2:numberofCracks-1,3))*PixelCal;
totalArea = sum(CrackInfo(2:numberofCracks-1,2))*PixelCal*PixelCal;

% Displays in the MATLAB command window the statistics calculated by this
% sub-routine.
disp(['Number of cracks measured: ' num2str(numberofCracks)]);
disp(['Minimum crack width: ' num2str(MinCrack) ' in']);
disp(['Maximum crack width: ' num2str(MaxCrack) ' in']);
disp(['Average crack width: ' num2str(AverageCrack) ' in']);
disp(['16th percentile crack width: ' num2str(Crack16) ' in']);
disp(['84th percentile crack width: ' num2str(Crack84) ' in']);
disp(['Total crack length: ' num2str(totalLength) ' in']);
disp(['Total crack width area: ' num2str(totalArea) ' sq. in']);
```

A.5 crackDetect

```
%%%%%%%%%%%%%%%%%%%%%%%%%%%%%%%%%%%%%%%%%%%%%%%%%%%%%%%%%%%%%%%%%%%%%%%%%%%%
% crackDetect
% The sub-routine used by I-Crack to employ one of the several
% edge-detection algorithms supplied by the Image Toolbox. This sub-routine
% first splits the image into smaller block to decrease the threshold used
% to determine if an edge was detected. Then each sub-image is analyzed by
% an edge-detection algorithm. The edge-detection algorithms are Roberts,
% Sobel, Prewitt, Canny and Laplacian of Gaussian. It is recommended
% that all threshold values be calculated automatically by MATLAB because
% the required threshold value will change with each sub-image.
%
% Input: Grayscale image of the high-resolution panorama
% Output: Black and white image with all of the edges highlighted
%
% Written for use within I-Crack
% Written by: Jonathan Rivera and Goran Jospovic
% Contact information: jprivera@buffalo.edu
```

```
%%%%%%%%%%%%%%%%%%%%%%%%%%%%%%%%%%%%%%%%%%%%%%%%%%%%%%%%%%%%%%%%%%%%%%%%%%%%

function [IBD_F] = crackDetect(IBIG1)
[rows, cols, ~] = size(IBIG1);

% Split the image into smaller sub-images; rsplit and csplit determine the
% number of sub-images per row and column, respectively. These numbers can
% be changed, by increasing the number additional sub-images are created
% and an improved threshold value can be calculated by MATLAB; however the
% required processing time may increase. If rsplit and csplit are decreased
% then the number of sub-images are decreased but the thresholds calculated
% by MATLAB will be more approximate; however processing time maybe
% decreased. For the purpose of analyzing the walls tested at UB an rsplit
% and csplit of 10 worked well after numerous trials.

rsplit = 10;
csplit = 10;

rs = floor(rows/rsplit);
cs = floor(cols/csplit);

IBIG1div = cell(rsplit,csplit);

for r = 1:rsplit
    for c = 1:csplit

        kr = 1*r + rs*(r-1);
        kc = 1*c + cs*(c-1);

        if r == rsplit && c == csplit
            IBIG1div(r,c) = {IBIG1(kr:(rows),kc:(cols),:)};
        elseif c == csplit
            IBIG1div(r,c) = {IBIG1(kr:(kr+rs),kc:(cols),:)};
        elseif r == rsplit
            IBIG1div(r,c) = {IBIG1(kr:(rows),kc:(kc+cs),:)};
        else
            IBIG1div(r,c) = {IBIG1(kr:(kr+rs),kc:(kc+cs),:)};
        end
    end
end

IBIG_crack = cell(rsplit,csplit);  % Allocate memory

% After the image has been split into smaller sub-images, each sub-image is
% then analyzed by an edge-detection algorithms. The edge-detection
% algorithms included in the Image Toolbox can be used. After several
% trials the Prewitt algorithm was selected for use. If one of the other
% algorithms are desired then "prewitt" should be replaced with the correct
% command associated with that edge detection algorithm. The commands
% include:
% 'roberts' for the Robert's algorithm
% 'sobel' for the Sobel algorithm
% 'prewitt' for the Prewitt algorithm
% 'canny' for the Canny algorithm
% 'log' for the Laplacian of Gaussian algorithm
```

```
for r = 1:rsplit
    for c = 1:rsplit
        IBIG_crack(r,c) = {edge(IBIG1div{r,c},'prewitt')};
    end
end

IBD_F = cell2mat(IBIG_crack);
```

A.6 CrackFill

```
%%%%%%%%%%%%%%%%%%%%%%%%%%%%%%%%%%%%%%%%%%%%%%%%%%%%%%%%%%%%%%%%%%%%%%%%%%%%%%%
% CrackFill
% After the edges have been detected, the cracks and surface defects must
% be filled in for image segmentation. To fill in the space between the
% edges detected, several morphological operations are used. These
% morphological operations include bwmorph, bwareaopen, imfill and imclose.
% This code must fill in cracks that are both large and small. During the
% development of this code, thicker cracks were not being filled in
% properly (approximately 0.040 inch and larger) as a result a second part
% was added to fill in these larger cracks.
%
% The parameters that can be changed are associated with bwareaopen and
% imclose. The function bwareaopen removes features that have fewer pixels
% than the threshold value specified. The function imclose morphologically
% closes a region based on the structural element specified.
%
% Input: Black and white image with the edges detected by crackDetect and
% if there are large cracks (approximately 0.040 inch and larger) on the
% surface of the specimen.
% Output: Black and white image with all of the cracks and surface defects
% filled
%
% Written for use in I-Crack
% Written by: Jonathan Rivera and Goran Jospovic
% Contact information: jprivera@buffalo.edu
%%%%%%%%%%%%%%%%%%%%%%%%%%%%%%%%%%%%%%%%%%%%%%%%%%%%%%%%%%%%%%%%%%%%%%%%%%%%%%%

function [Cracksfilled] = CrackFill(IBD_F,CrackLarge)

% Section of the code that is used to fill in the area for smaller cracks
% (approximately 0.040 inch and less).
if strcmp(CrackLarge,'Y') == 1
BW1 = bwmorph(IBD_F,'bridge',Inf); % Bridges unconnected pixels
BW2 = bwmorph(BW1,'fill',Inf);     % Fills isolated interior pixels
BW3 = bwmorph(BW2,'close',Inf);    % Fills the space between the two edges
BW4 = bwmorph(BW3,'bridge',Inf);
BW5 = bwmorph(BW4,'fill',Inf);
BW6 = bwmorph(BW5,'close',Inf);
BW7 = bwareaopen(BW6,75);          % Changing the 2nd number removes spots
BW8 = imfill(BW7,'holes');
BW9 = imclose(BW8,ones(10,10));
BW10 = bwareaopen(BW9,500);
Cracksfilled = BW10;
```

```
elseif strcmp(CrackLarge,'Y') == 0
BW1 = bwmorph(IBD_F,'bridge',Inf);
BW2 = bwmorph(BW1,'fill',Inf);
BW3 = bwmorph(BW2,'close',Inf);
BW4 = bwmorph(BW3,'bridge',Inf);
BW5 = bwmorph(BW4,'fill',Inf);
BW6 = bwmorph(BW5,'close',Inf);
BW7 = bwareaopen(BW6,75);
BW8 = imfill(BW7,'holes');
BW9 = imclose(BW8,ones(10,10));
BW10 = bwareaopen(BW9,500);

SmallCracks = BW10;

BW11 = bwmorph(IBD_F,'bridge',Inf);
BW12 = bwmorph(BW11,'fill',Inf);
BW13 = bwmorph(BW12,'close',Inf);
BW14 = bwmorph(BW13,'bridge',Inf);
BW15 = bwmorph(BW14,'fill',Inf);
BW16 = bwmorph(BW15,'close',Inf);
BW17 = bwareaopen(BW16,75);
BW18 = imfill(BW17,'holes');
BW19 = imclose(BW18,ones(30,30));
BW20 = bwareaopen(BW19,3000);

LargeCracks = BW20;

Cracksfilled = imadd(SmallCracks,LargeCracks);

end
```

A.7 CrackLabel

```
%%%%%%%%%%%%%%%%%%%%%%%%%%%%%%%%%%%%%%%%%%%%%%%%%%%%%%%%%%%%%%%%%%%%%%%%%%%%
% CrackLabel
% This MATLAB sub-routine is used to apply the second criterion used for
% image segmentation and predict the crack widths detected in the
% high-resolution panorama. The second criterion used for image
% segmentation is based on the ratio of the major-axis length to the
% minor-axis length. Once the cracks and surface defects have been
% segmented the widths of the remaining objects are predicted. These
% predicted widths are stored in an array along with other information and
% saved to a comma-separated value file for future use. The comma-value
% separated value file can be opened in Microsoft Excel or reloaded into
% MATLAB as an array.
%
% Input: The black and white image that has been segmented after the
% orientationFilter has been applied, the calibration factor (length per
% pixel), the number of the specimen (SW), load step (LS) and peak (P).
% Output: An image with all of the remaining features labeled by a number,
% an array containing information on the features and a comma-separated
% value file of the array.
%
```

```
% Written for use in I-Crack
% Written by: Jonathan Rivera and Goran Jospovic
% Contact information: jprivera@buffalo.edu
%%%%%%%%%%%%%%%%%%%%%%%%%%%%%%%%%%%%%%%%%%%%%%%%%%%%%%%%%%%%%%%%%%%%%%%%%%%%%%%

function [CrackImage,CrackInfo] = CrackLabel(Cracksfilled,PixelCal,SW,LS,P)
% Cracksfilled is the panorama after orientationFilter has been applied.
% PixelCal is the length per pixel
% SW is the shear wall number tested
% LS is the load stage being analyzed
% P is the peak displacement being analyzed

% First, the black and white image is loaded into the script and closely
% spaced cracks are joined. Afterwards each crack and surface defect are
% labeled left to right, top to bottom. Then using regionprops the
% properties of each surface defect and crack is measured.
IMG1 = Cracksfilled;                % Loads the image into the sub-routine
IMG1 = imclose(IMG1,ones(5,5));     % Merges cracks that are close together
Label = bwlabel(IMG1,8);            % Labels each crack
Measure = regionprops(Label,'all'); % Obtain all properties
Perimeter = [Measure.Perimeter];    % Obtain the perimeter

% Image segmentation based on perimeter is applied and considered secondary
% because the perimeter is used to remove extremely small surface defects.
% The threshold value used for perimeter can be altered based on the needs
% of the user.
allowablePerimeter = Perimeter > 10;
keepCracksIndex = find(allowablePerimeter);

% Create a mask that contains only the features that have a perimeter
% greater than the threshold value.
CrackImage1 = ismember(Label,keepCracksIndex);
Label = bwlabel(CrackImage1,8);     % Labels all of the cracks

% The second image segmentation criterion is applied. Using regionprops
% all of the properties are measured and stored. Then the major and
% minor-axes length are called and stored in an array. The threshold value
% used for the Ratio can be altered to remove more surface defects.
Measure = regionprops(Label,'all'); % Calculates properties of the cracks
Major = [Measure.MajorAxisLength];  % Major-axis length
Minor = [Measure.MinorAxisLength];  % Minor-axis length
Ratio = Major ./ Minor;
allowableRatio = Ratio > 2;         % Threshold value for the ratio
keepCracksIndex = find(allowableRatio);
CrackImage = ismember(Label,keepCracksIndex);

%% Measurement of crack area and length to determine crack width
% The fully segmented image is relabeled using bwlabel and all of the
% properties are measured using regionprops. Area is then stored in an
% array for future use.
AreaIMG = CrackImage;
AreaLabel = bwlabel(AreaIMG,8);
AreaMeas = regionprops(AreaLabel,'all');
numofAreaCracks = size(AreaMeas,1);
CrackInfo = zeros(numofAreaCracks,9); % Initiate array to store properties
AreaColor = label2rgb(AreaLabel,'hsv','k','shuffle');
```

```
for i =1:numofAreaCracks
    CrackInfo(i,1) = i;
    CrackInfo(i,2) = AreaMeas(i).Area;
end

% Using the morphological operations, skel, the panorama is altered to
% reduce the width of the cracks to a single unit. Then calling regionprops
% and measuring area again, the length of each crack can be determined.
LengthIMG = CrackImage;
LengthIMG1 = bwmorph(LengthIMG,'skel',Inf);
LengthLabel = bwlabel(LengthIMG1,8);
LengthMeas = regionprops(LengthLabel,'all');
numberofLengthCracks = size(LengthMeas,1);

for j = 1:numberofLengthCracks
    crackLength = LengthMeas(j).Area;
    CrackInfo(j,3) = crackLength;
end

for i = 1:numofAreaCracks
    CrackInfo(i,4) = (CrackInfo(i,2)/CrackInfo(i,3));
    CrackInfo(i,5:6) = LengthMeas(i).Centroid;
    CrackInfo(i,7:8) = AreaMeas(i).Centroid;
    CrackInfo(i,9) = CrackInfo(i,4)*PixelCal; % Apply calibration factor
end

% Output of the array has nine columns and a number of rows equivalent to
% the number of cracks detected.
% Column 1: Label for each crack detected
% Column 2: The area measured
% Column 3: The length measured
% Column 4: The width measured in pixels
% Column 5 and 6: The x and y coordinates of the centroid for the panorama
% that was altered using 'skel'
% Column 7 and 8: The x and y coordinates of the centroids for the
% unaltered panorama
% Column 9: The width of each crack after the calibration factor has been
% applied to change the unit of measurement to inches.

%% Generates a figure to with the labels of each crack on them
imshow(AreaColor);
for h = 1:numofAreaCracks
   CrackCentroid = AreaMeas(h).Centroid; % Get centroid
   text(CrackCentroid(1), CrackCentroid(2), num2str(h), 'FontSize',12,...
       'FontWeight','Bold','Color','white');
end
saveas(gcf,['CrackMap for SW' int2str(SW) ' LS' int2str(LS) ' Peak '...
           int2str(P) ],'fig');

csvwrite(['CrackInfo for SW' int2str(SW) ' LS' int2str(LS) ' Peak '...
           int2str(P) '.csv'],CrackInfo);
```

A.8 CrackWidthSearch

```
%%%%%%%%%%%%%%%%%%%%%%%%%%%%%%%%%%%%%%%%%%%%%%%%%%%%%%%%%%%%%%%%%%%%%%%%%%%%
% CrackWidthSearch
% A post-processing script used to extract the predicted width of a labeled
% crack or surface defect from a stored array. The labeled cracks are
% stored as a MATLAB figure file (.fig) with the name beginning with
% CrackMap for ... The crack properties are stored in a comma-separated
% value file generated by another MATLAB sub-script called CrackLabel. The
% comma-separated value file can be loaded into MATLAB with csvread and
% stored as an array.
%
% Input: An array with all of the crack properties and .fig file with all
% of the cracks labelled
% Output: Crack width
%
% Written for post-processing after I-Crack has processed a panorama
% Written by: Jonathan Rivera and Goran Jospovic
% Contact information: jprivera@buffalo.edu
%
% MATLAB command window prompts
% CrackInfo = csvread('CrackInfo for ...');
% CrackWidthSearch(CrackInfo)
% Determine crack width?
% [Y/N]
% Number of crack IDs?
% [Enter the number of crack measurements that should be used]
% CrackID number
% [Enter the crack label]
% Average crack width is ...
% Would you like to measure another crack?
% [Y/N]
%%%%%%%%%%%%%%%%%%%%%%%%%%%%%%%%%%%%%%%%%%%%%%%%%%%%%%%%%%%%%%%%%%%%%%%%%%%%

function CrackWidthSearch(CrackInfo)

quest1 = input('Determine crack width? Y/N\n','s');

if strcmp(quest1,'Y')
   quest2 = input('Number of crack IDs?\n');
   CrackID = zeros(quest2,1);              % Initiate search matrix

   for i = 1:quest2
       quest3 = input('CrackID number\n');
       CrackID(i,1) = quest3;
   end

   CrackWidths = zeros(quest2,1);          % Initiate crack width matrix
   for j = 1:quest2
       CrackWidths(j,1) = CrackInfo(CrackID(j,1),9);
   end

   Crackwidth = mean(CrackWidths,1);
   disp(['Average crack width is ' num2str(Crackwidth)]);
   goAgain = input('Would you like to measure another crack? Y/N\n','s');
```

```
    if strcmp(goAgain,'Y')                    % Runs this script again
        CrackWidthSearch(CrackInfo);

    elseif strcmp(goAgain,'N')
    end

elseif strcmp(quest1,'N')

end
```

A.9 ICrack

```
%%%%%%%%%%%%%%%%%%%%%%%%%%%%%%%%%%%%%%%%%%%%%%%%%%%%%%%%%%%%%%%%%%%%%%%%%%%%%%%
% ICrack
% The main MATLAB algorithm used to analyze high-resolution panoramas of
% reinforced concrete components. This algorithm was developed with MATLAB
% 2013a (ver. 8.1.0.064) and requires the Image Processing Toolbox and the
% Parallel Computing Toolbox. I-Crack uses several sub-scripts including
% ColorCode, crackDetect, CrackFill, CrackLabel, ImageOverlay,
% orientationFilter, removeGrid and removeGrid2. Additional sub-scripts
% used with I-Crack are Calibrate, CrackData and CrackWidthSearch.
% Calibrate is a pre-processing script required to determine a calibration
% factor required for input. CrackData and CrackWidthSearch are two
% post-processing scripts used to determine statistics for predicted
% crack widths and to extract specific predicted crack widths.
%
% Input: Number of the shear wall specimen, load stage and peak number,
% calibration factor and if large cracks are present.
% Output: MATLAB figure file (.fig), Comma-separated value (.csv) file with
% crack properties, composite image (.jpg) of the cracks overlaid on the
% high-resolution panorama.
%
% Output file names:
% Comma-separated value file - 'CrackInfo for... .csv'
% MATLAB figure file - 'CrackMap for... .fig'
% JPEG image file - '..._CracksTraced.jpg'
%
% Written for use of analyzing crack patterns and crack widths on
% reinforced concrete components.
% Written by: Jonathan Rivera and Goran Jospovic
% Contact information: jprivera@buffalo.edu
%%%%%%%%%%%%%%%%%%%%%%%%%%%%%%%%%%%%%%%%%%%%%%%%%%%%%%%%%%%%%%%%%%%%%%%%%%%%%%%

clc; close all; clear all;

%% User input
% This user input was designed for the naming convention used for the shear
% walls specimens tested at the University at Buffalo. All that is required
% is the name of the high-resolution panorama, calibration factor and
% determining if large cracks are present.
SW = 8;  % Shear wall number
LS = 6;  % Load stage number
P = 3;   % Peak number
PixelCal = 0.0048;  % Calibrate pixel length
```

```
CracksLarge = 'Y';  % Are cracks present large or small [Y/N]
cd(['C:\Users\STUDENT\Desktop\Validation\SW' int2str(SW)]);
name = ['SW' int2str(SW) '_LS' int2str(LS) '_C1_PEAK' int2str(P) '.jpg'];

%% Load image into MATLAB
fprintf('Reading Image:')
fprintf('\n');
tic
RAW_IMG = imread(name);
toc

%% Apply a filter to remove red grid lines and blemishes
matlabpool open 4         % Engage a multicore processor
fprintf('\n');
fprintf('Removing red gridlines:');
fprintf('\n');
tic
fun1 = @(block_struct)removeGrid(block_struct.data);
IMG1 = blockproc(RAW_IMG,[500 500],fun1,'BorderSize',[25 25],...
       'UseParallel',true);
toc
fprintf('\n');

%% Run edge detection to determine with the cracks and surface defects are
fprintf('Detecting cracks that are present:');
fprintf('\n');
tic
fun2 = @(block_struct)crackDetect(block_struct.data);
IMG2 = blockproc(IMG1,[500 500],fun2,'BorderSize',[25 25],...
       'UseParallel',true);
toc
fprintf('\n');
clearvars IMG1;

%% Apply the fill in area between edge detection
fprintf('Filling in cracks from edge detection:')
fprintf('\n');
tic
fun3 = @(block_struct)CrackFill(block_struct.data,CracksLarge);
IMG3 = blockproc(IMG2,[250 250],fun3,'BorderSize',[25 25],...
       'UseParallel',true);
toc
fprintf('\n');
clearvars IMG2;

%% Apply secondary filter based on crack orientation
fprintf('Filtering based on angles:');
fprintf('\n');
tic
fun4 = @(block_struct)orientationFilter(block_struct.data);
IMG4 = blockproc(IMG3,[500 500],fun4,'BorderSize',[25 25],...
       'UseParallel',true);
toc
fprintf('\n');
clearvars IMG3;
```

```
%% Label the cracks
fprintf('Applying secondary filter to remove surface imperfections\n')
fprintf('and labeling cracks:')
tic
[IMG5, CrackInfo] = CrackLabel(IMG4,PixelCal,SW,LS,P);
toc
fprintf('\n');
clearvars IMG4;

% matlabpool close; % Disengages multicore processing

%% Colorcode the cracks based on width
fprintf('Colorcoding cracks based on width:\n');
tic
fun6 = @(block_struct)ColorCode(block_struct.data);
IMG6 = blockproc(IMG5,[2000 2000],fun6,'BorderSize',[25 25],...
       'UseParallel',true);
toc
fprintf('\n');

%% Overlay colorcoded crack image on RAW_IMG
fprintf('Overlaying color coded cracks on GigaPan\n');
tic
IMG7 = ImageOverlay(RAW_IMG,IMG6,IMG5,SW,LS,P);
toc
imwrite(IMG7,['SW' int2str(SW) '_LS' int2str(LS) '_C1_PEAK' int2str(P)
'_CracksTraced.jpg'],'jpg');

%% Determine the average crack width per crack
% CrackWidthSearch(CrackInfo);

%% Determine relevant data for the entire wall
% This portion of the code will determine the minimum, maximum, average,
% 16th, 84th percentile crack width.  It will also display the number of
% cracks as well as a distribution of the crack widths in a histogram.
% CrackData(CrackInfo,PixelCal);
```

A.10 ImageOverlay

```
%%%%%%%%%%%%%%%%%%%%%%%%%%%%%%%%%%%%%%%%%%%%%%%%%%%%%%%%%%%%%%%%%%%%%%%%%%%%%%%
% ImageOverlay
% This sub-script is one of the final steps in the I-Crack analysis and
% allows the user to visualize the crack widths. Using the pre-processed
% panorama, black and white image of all the cracks detected and
% color-coded, the cracks are superimposed on the pre-processed panorama.
% The final image is then saved by I-Crack.
%
% If it is desired that the cracks be thicker in the final image, they can
% be thickened by increasing the number in Line 29.
%
% Input: Pre-processed panorama, image after the panorama has been
% processed by morphological operations, image with all of the cracks color
% coded without the shear wall specimen present.
% Output: Composite image with cracks highlighted
```

```
%
% Written to create a JPEG image with all of the detected cracks
% highlighted and color coded based on their width.
% Written by: Jonathan Rivera and Goran Jospovic
% Contact information: jprivera@buffalo.edu
%%%%%%%%%%%%%%%%%%%%%%%%%%%%%%%%%%%%%%%%%%%%%%%%%%%%%%%%%%%%%%%%%%%%%%%%%%%%

function[IMG4] = ImageOverlay(IMG1,IMG2,IMG3,SW,LS,P)
% Extract the individual red, green, and blue color channels.
redChannel = IMG1(:, :, 1);
greenChannel = IMG1(:, :, 2);
blueChannel = IMG1(:, :, 3);

% Same, but this time for the second image.
redChannel2 = IMG2(:, :, 1);
greenChannel2 = IMG2(:, :, 2);
blueChannel2 = IMG2(:, :, 3);

mask = bwmorph(IMG3,'thicken',5);
% imwrite(mask,['SW' num2str(SW) '_LS' num2str(LS) '_PEAK' num2str(P)...
% '_mask.jpg'],'jpg');

% Create a blank image the size of the original image. Then the image with
% the detected cracks are inserted into this blank image.
bigMask = false(size(redChannel));
bigMask(:,:) = mask;

% Create a composite image with the cracks highlighted on the pre-processed
% panorama.
redChannel(bigMask) = redChannel2(mask);
greenChannel(bigMask) = greenChannel2(mask);
blueChannel(bigMask) = blueChannel2(mask);
IMG4 = cat(3, redChannel, greenChannel, blueChannel);
```

A.11 orientationFilter

```
%%%%%%%%%%%%%%%%%%%%%%%%%%%%%%%%%%%%%%%%%%%%%%%%%%%%%%%%%%%%%%%%%%%%%%%%%%%%
% orientationFilter
% A sub-script used to apply image segmentation based on the angle of
% inclination of either the crack or surface defect. During the development
% of I-Crack it was observed that many of the surface defects were
% horizontal or vertical while many of the cracks were inclined at an
% angle.
%
% Input: Black and white image after morphological operations have been
% applied and direction of the cracks
% Output: Black and white image with many surface defects removed
%
% Written to segment the image based on angles
% Written by: Jonathan Rivera and Goran Jospovic
% Contact information: jprivera@buffalo.edu
%%%%%%%%%%%%%%%%%%%%%%%%%%%%%%%%%%%%%%%%%%%%%%%%%%%%%%%%%%%%%%%%%%%%%%%%%%%%

function [IBD_F] = orientationFilter(IBIG1,CrackDir)
```

```
% To increase the speed of processing the image is split into smaller
% sub-images. The number of sub-images in controlled by rsplit and csplit.

[rows, cols, ~] = size(IBIG1);

rsplit = 10;
csplit = 10;

rs = floor(rows/rsplit);
cs = floor(cols/csplit);

IBIG1div = cell(rsplit,csplit);

for r = 1:rsplit
    for c = 1:csplit
        kr = 1*r + rs*(r-1);
        kc = 1*c + cs*(c-1);
        if r == rsplit && c == csplit
            IBIG1div(r,c) = {IBIG1(kr:(rows),kc:(cols),:)};
        elseif c == csplit
            IBIG1div(r,c) = {IBIG1(kr:(kr+rs),kc:(cols),:)};
        elseif r == rsplit
            IBIG1div(r,c) = {IBIG1(kr:(rows),kc:(kc+cs),:)};
        else
            IBIG1div(r,c) = {IBIG1(kr:(kr+rs),kc:(kc+cs),:)};
        end
    end
end

IBIG_orientation = cell(rsplit,csplit);  % Allocate memory
Measure = cell(rsplit,csplit);

% Segment the image based on the angle of inclination
for r = 1:rsplit
    for c = 1:csplit
        Measure(r,c) = {regionprops(IBIG1div{r,c},'all')};
        Orientation = [Measure{r,c}.Orientation];
        if strcmp(CrackDir,'L') == 1
            allowableOrientation = Orientation > -75 & Orientation < -5;
        elseif strcmp(CrackDir,'L') == 0
            allowableOrientation = Orientation > 5 & Orientation < 75 ;
        end
        keepCrackIndex = find(allowableOrientation);
        IBIG_orientation(r,c) = {ismember(IBIG1div{r,c},keepCrackIndex)};
    end
end

IBD_F = cell2mat(IBIG_orientation);
```

A.12 removeGrid

```
%%%%%%%%%%%%%%%%%%%%%%%%%%%%%%%%%%%%%%%%%%%%%%%%%%%%%%%%%%%%%%%%%%%%%%%%%%%%
% removeGrid
% During the development of I-Crack it was observed that the red chalk
% lines must be removed to reduce the number of unnecessary edges recorded.
% This sub-script will split the high-resolution panorama into smaller
% sub-images and apply a filter (removeGrid2) to remove the chalk lines.
% The number of sub-images are controlled by rsplit and csplit.
%
% Input: High-resolution panorama with an RGB color scheme
% Output: Grayscale image with the red chalk lines removed
%
% Written to reduce the number of unnecessary edges recorded
% Written by: Jonathan Rivera and Goran Jospovic
% Contact information: jprivera@buffalo.edu
%%%%%%%%%%%%%%%%%%%%%%%%%%%%%%%%%%%%%%%%%%%%%%%%%%%%%%%%%%%%%%%%%%%%%%%%%%%%

function[IBD_S] = removeGrid(IBIG)
 [rows, cols, ~] = size(IBIG);
 rsplit = 10; csplit = 10;
 rs = floor(rows/rsplit)-1;
 cs = floor(cols/csplit)-1;
 IBIGdiv = cell(rsplit,csplit);

for r = 1:rsplit
    for c = 1:csplit
        kr = 1*r + rs*(r-1);
        kc = 1*c + cs*(c-1);
        if r == rsplit && c == csplit
            IBIGdiv(r,c) = {IBIG(kr:(rows),kc:(cols),:)};
        elseif c == csplit
            IBIGdiv(r,c) = {IBIG(kr:(kr+rs),kc:(cols),:)};
        elseif r == rsplit
            IBIGdiv(r,c) = {IBIG(kr:(rows),kc:(kc+cs),:)};
        else
            IBIGdiv(r,c) = {IBIG(kr:(kr+rs),kc:(kc+cs),:)};
        end
    end
end

% Apply the filter removeGrid2 to the smaller sub-images to remove the red
% chalk lines on the surface of the shear walls
IBIGdiv_G = cell(rsplit,csplit);
IBIGdiv_NoGrid = cell(rsplit,csplit);

for r = 1:rsplit
    for c = 1:csplit
        IBIGdiv_NoGrid(r,c) = {removeGrid2(IBIGdiv{r,c},false)};
        IBIGdiv_NoGrid(r,c) = {removeGrid2(IBIGdiv_NoGrid{r,c},false)};
        IBIGdiv_NoGrid(r,c) = {removeGrid2(IBIGdiv_NoGrid{r,c},false)};
        IBIGdiv_NoGrid(r,c) = {removeGrid2(IBIGdiv_NoGrid{r,c},false)};
        IBIGdiv_G(r,c) = {rgb2gray(IBIGdiv_NoGrid{r,c})};
    end
end
```

```
IBD_S = cell2mat(IBIGdiv_G);

end
```

A.13 removeGrid2

```
%%%%%%%%%%%%%%%%%%%%%%%%%%%%%%%%%%%%%%%%%%%%%%%%%%%%%%%%%%%%%%%%%%%%%%%%%%%%
% removeGrid2
% This sub-script in conjunction with removeGrid are used to remove the red
% chalk lines present on all of the specimens tested at the University at
% Buffalo. To remove the gridlines a threshold value is selected based on
% the amount of red present in each pixel. Thesholding was used because the
% amount of red present in the pixels containing chalk lines will out
% weigh all of the other colors. For pixels containing enough red, that
% pixel is replaced with and "averaged" pixel.
%
% A threshold value of 10 is initially set based on numerous trials during
% the development of this sub-script. By increasing the value to a higher
% number more pixels associated with the gridlines may not be replaced.
%
% Input: An RGB colored image
% Output: An image with the chalk lines replaced with an averaged pixel
%
% Written for removal of the red grid present on all of the specimens
% Written by: Jonathan Rivera and Goran Jospovic
% Contact information: jprivera@buffalo.edu
%%%%%%%%%%%%%%%%%%%%%%%%%%%%%%%%%%%%%%%%%%%%%%%%%%%%%%%%%%%%%%%%%%%%%%%%%%%%

function [ image ] = removeGrid2(I)
[row,col,~] = size(I);
np = row*col;
th =10; % Threshold value used for gridline removal

% To find an average pixel to replace the pixels associated with the
% gridlines, the value of each color (red, green and blue) are summed and
% divided by the number of pixels present.

ravg = sum(sum(I(:,:,1)))/np;
gavg = sum(sum(I(:,:,2)))/np;
bavg = sum(sum(I(:,:,3)))/np;

% Creating a logical matrix (full of 0s and 1s) based on the presence of
% red in each pixel. If that pixel exceeds the threshold a 1 is placed in
% the logical matrix, if not then a 0 returned.

grid = zeros(row,col);
for r = 1:row
    for c = 1:col
        if (I(r,c,2)<(gavg-th)) && (I(r,c,3)<(bavg-th)) && (I(r,c,1) > ...
           (ravg-2*th))
            grid(r,c) = 1;
        end
```

```
    end
end

% Invert the previous logical matrix and insert reinsert the image to
% obtain a better approximation of the averaged pixel.
grid2 = abs(grid -1);
pts = sum(sum(grid2));
Iback(:,:,1) = uint8(grid2).*I(:,:,1);
Iback(:,:,2) = uint8(grid2).*I(:,:,2);
Iback(:,:,3) = uint8(grid2).*I(:,:,3);
ravg = sum(sum(Iback(:,:,1)))/pts;
gavg = sum(sum(Iback(:,:,2)))/pts;
bavg = sum(sum(Iback(:,:,3)))/pts;

I1 = I;

% Insert the averaged pixel where the red grid lines were detected.
for j = 1:row
    for k = 1:col
        if (grid(j,k)==1)
            I1(j,k,1) = ravg;
            I1(j,k,2) = gavg;
            I1(j,k,3) = bavg;
        end
    end
end
image = I1;
```

APPENDIX B
I-CRACK TUTORIAL

Appendix B provides a tutorial on how to apply pre-processing techniques, analyze a high-resolution panorama with I-Crack and extract crack widths from the analysis. The software used for this tutorial includes FastStone Image Viewer version 4.7 and MATLAB R2013a (ver. 8.1.0.064) with Image Toolbox and Parallel Processing Toolbox. The FastStone Image Viewer is free software that is available for download at http://www.faststone.org/FSViewerDetail.htm. The computer that was used to develop and validate I-Crack had a Windows 7 (64-bit) operating system with an Intel core i5 processor with speeds up to 3.10 GHz and 8.00 GB of RAM.

The specimen used for this tutorial is SW6 at a displacement of 0.32 inch (story drift angle of 0.8%); the peak displacement for LS8 and corresponding to peak shear strength. SW6 had a length of 10 feet, a height of 41 inches from the top of the foundation to the line of loading and a thickness of eight inches. This specimen had a vertical and horizontal reinforcement ratio of 0.67% and a compressive strength of 3800 psi. An unprocessed high-resolution panorama of SW6 is shown in Figure B-1.

Figure B-1. Unprocessed GigaPan of SW6 at LS8

B.1 Getting started and pre-processing

Before any pre-processing can begin, it is necessary to place all of the MATLAB codes and the panorama into a single folder. The codes are Calibrate.m, ColorCode.m, CrackData.m, CrackDetect.m, CrackFill.m, CrackLabel.m, CrackWidthSearch.m, ICrack.m, ImageOverlay.m, oreintationFilter.m, removeGrid.m, and removeGrid2.m. Once everything is in a single folder open FastStone Image Viewer and navigate to the folder where everything is saved, shown in Figure B-2. Then double click on the panorama that needs to be pre-processed and open it to full screen. Once the panorama is full screen, move the mouse to the left of the screen and open the File and Slideshow Menu, shown in Figure B-3. Select the Auto-Adjust Colors option to process the panorama for overexposure; enclosed in the red box. The results are shown in Figure B-4. Then select the Adjust Lighting option (enclosed in the blue box) to process the panorama for shadows; the options for Adjust Lighting are shown at the bottom of the screen and reproduced in Figure B-5. To adjust the lightning in the panorama, simply move the sliders left or right until the shadows are reduced and the cracks are more defined. Then save the new panorama in the same folder as the original panorama. A fully processed panorama is shown in Figure B-6.

Once the panorama has been pre-processed for overexposure and shadows, a calibration factor must be determined. The calibration factor should be based on a unique object in the panorama that has a known width, length or area. Additionally, the code required to determine the calibration factor will be based on the unique object. For SW6, the calibration factor is based on the length of the wall. Open Calibrate.m in MATLAB, change the image name in Line 23 to the panorama that is being analyzed (e.g. SW6_LS1_C1_PEAK1.png) and hit Run. The wall is changed to white while the background is changed to black; shown in Figure B-7. The calibration factor is displayed in the Command Window as PixelCal, in this case 0.0041.

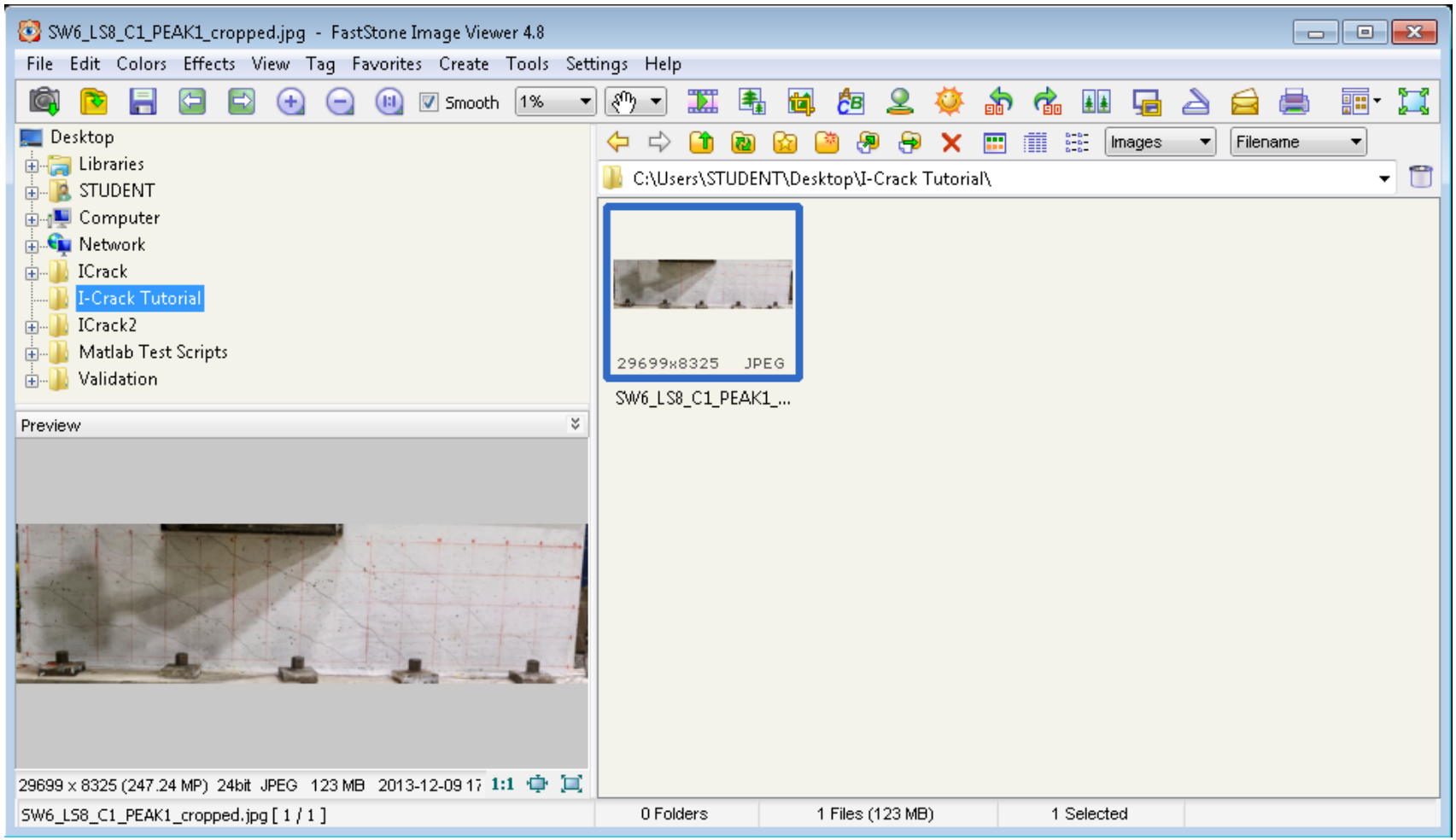

Figure B-2. FastStone Image Viewer

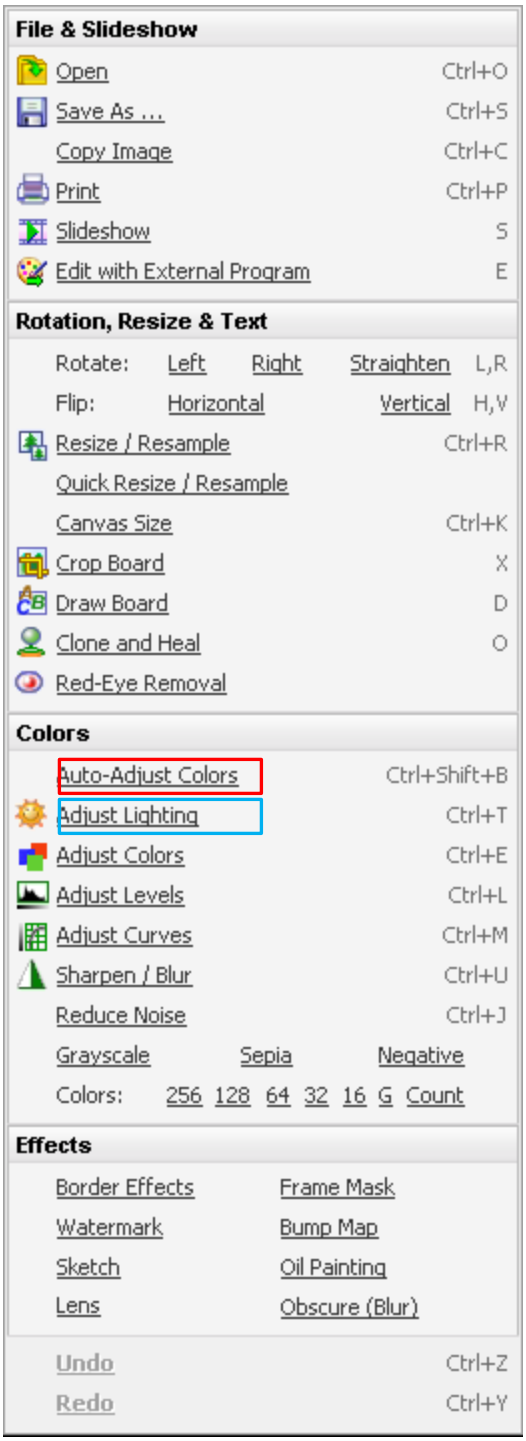

Figure B-3. File and Slideshow Menu

Figure B-4. Panorama process for overexposure

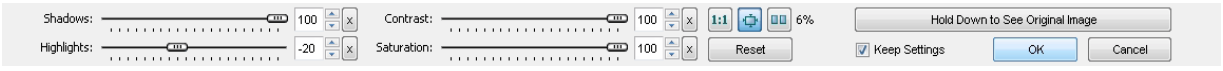

Figure B-5. Adjust Lighting options

Figure B-6. Processed panorama

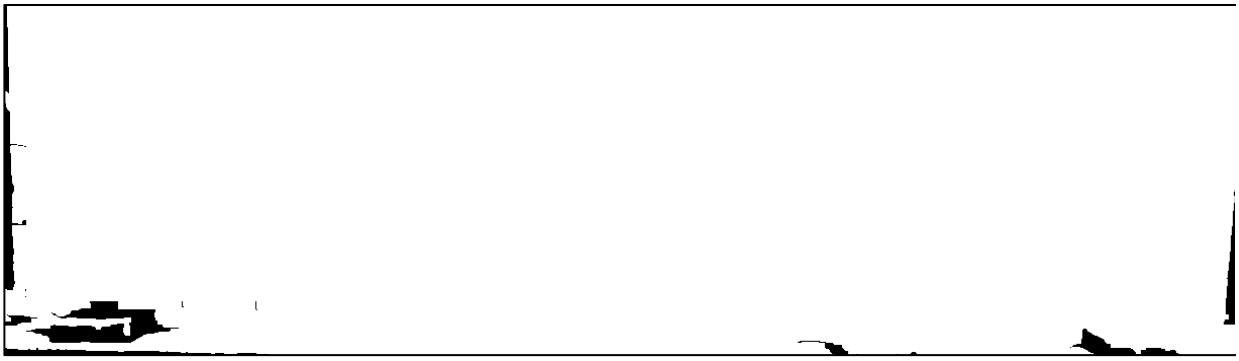

Figure B-7. Panorama used to determine the calibration factor

B.2 I-Crack analysis

Once the panorama has been pre-processed and a calibration factor determined, open ICrack.m in MATLAB. If default settings are to be used, only PixelCal, CracksLarge, CrackDir¸ and name should be changed; Lines 42, 43, 44 and 48, respectively. If other settings need to be changed see the comments in the sub-scripts. PixelCal is the calibration factor that was calculated based on a unique object. CracksLarge controls the sub-script CrackFill.m and tells that sub-script if cracks wider than 0.030 inch are present. CrackDir controls the sub-script orientationFilter.m, which applies image segmentation to remove surface defects from the panorama. The final variable that should be changed is name and is referring to the name of the panorama that will be analyzed. The code used for this tutorial is reproduced below.

```
%% User input
% This user input was designed for the naming convention used for the shear
% walls specimens tested at the University at Buffalo. All that is required
% is the name of the high-resolution panorama, calibration factor and
% determining if larger cracks are present.
SW = 6;  % Shear wall number
LS = 8;  % Load stage number
P = 1;   % Peak number
PixelCal = 0.0041;  % Calibrate pixel length
CracksLarge = 'Y';  % Are cracks present larger than 0.030 inch [Y/N]
CrackDir = 'L';     % Angle of cracks present during image capture
                    % If crack angles range from 5 to 75 degrees use 'R'
                    % If crack angles range from -5 to -75 degrees use 'L'
% cd(['C:\Users\STUDENT\Desktop\Validation\SW' int2str(SW)]);
% name = ['SW' int2str(SW) '_LS' int2str(LS) '_C1_PEAK' int2str(P) '.png'];
```

```
name = 'SW6_LS8_C1_PEAK1.png';
```

After Lines 42, 43, 44 and 48 have been changed to fit the specific specimen, press the Run button to execute I-Crack; enclosed in the red box of Figure B-8. The runtime for I-Crack will depend on the number of cracks detected and the size of the image. The final composite image for this tutorial is shown in Figure B-9. For further discussion on the intermediate steps and post-processing, the area of interest will be narrowed to the area enclosed in the red box of Figure B-6 and enlarged in Figure B-10.

Figure B-8. MATLAB Editor tab

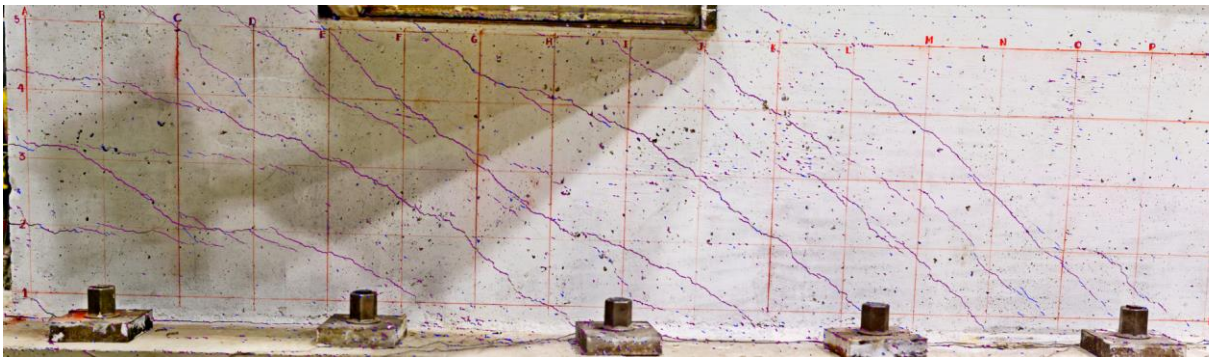

Figure B-9. Composite image of SW6

I-Crack processes the high-resolution panorama using several sub-scripts. Each sub-script generates a new image that is passed to the next sub-script for processing. I-Crack follows the following steps in processing a high-resolution panorama:

1. Load the panorama into MATLAB using imread; shown in Figure B-10.
2. Replace the red chalk lines using removeGrid2 and change the image to grayscale using removeGrid; shown in Figure B-11 and Figure B-12, respectively.
3. Use the edge detection algorithm to detect the edges of the cracks and surface defects; shown in Figure B-13.
4. Then I-Crack fills in the void between the edges that are detected using morphological operations; shown in Figure B-14.
5. With the cracks filled, image segmentation is applied based on angle of inclination and the major-minor axes ratio; shown in Figure B-15 and Figure B-16, respectively.
6. Once the image has been segmented, all of the remaining cracks are measured and labelled for post-processing; shown in Figure B-17. The measurements are saved in a comma-separated value file for further use.
7. Then I-Crack color codes the cracks based on their predicted widths and overlays the color coded cracks on the original image; shown in Figure B-18.

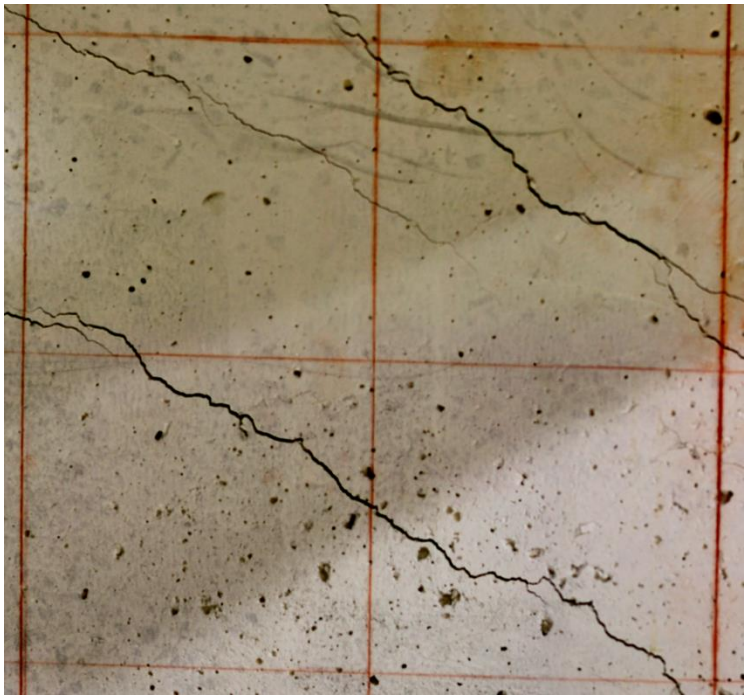

Figure B-10. Area enclosed in the red box of Figure B-6

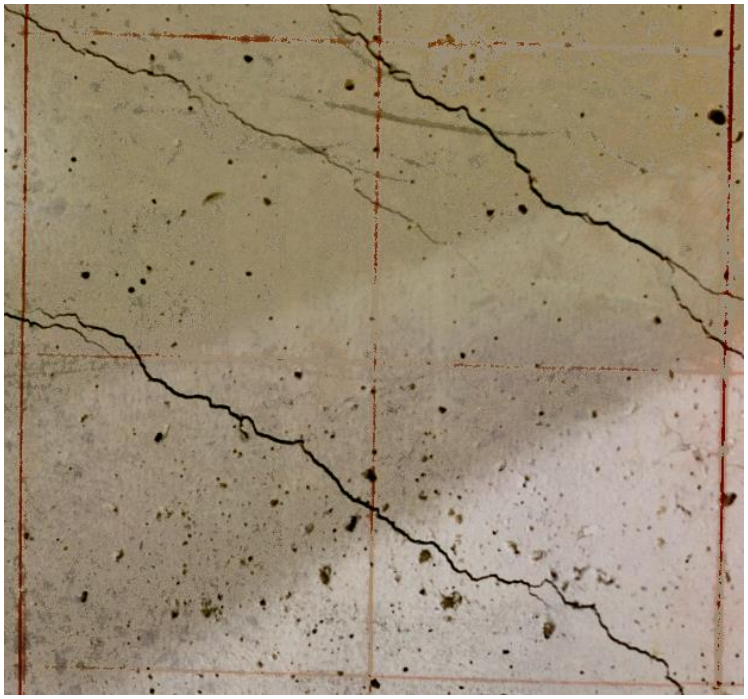

Figure B-11. Red chalk lines replaced using removeGrid2

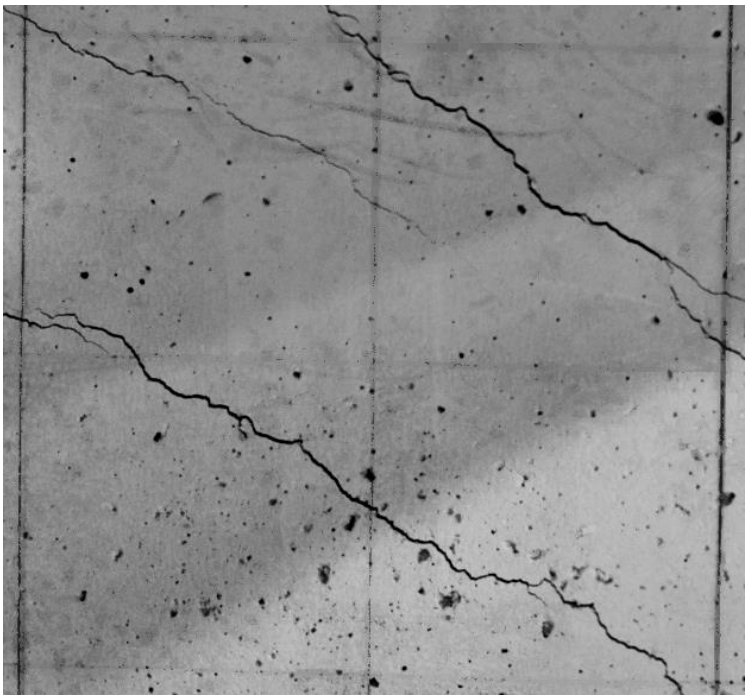

Figure B-12. Grayscale image of the area enclosed in the red box

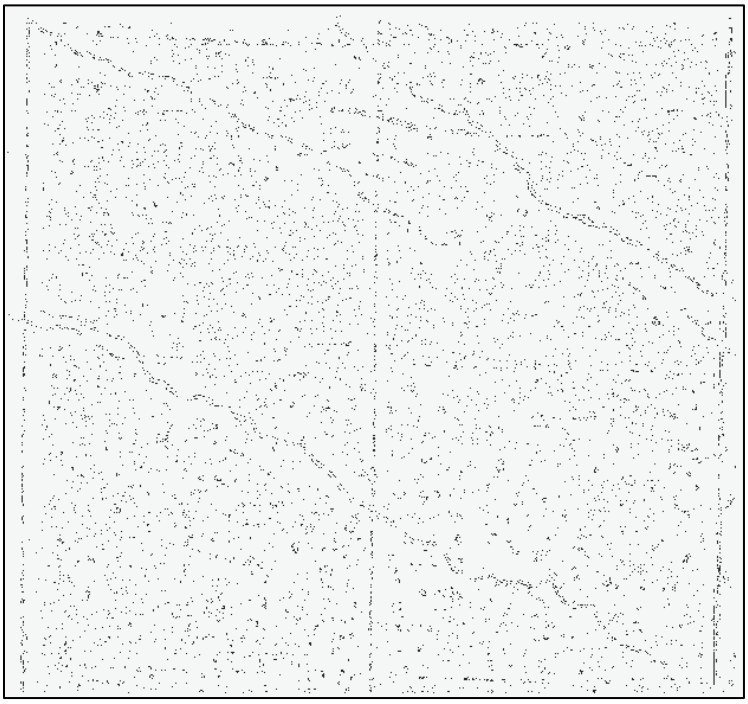

Figure B-13. Results from the Prewitt edge detection algorithm

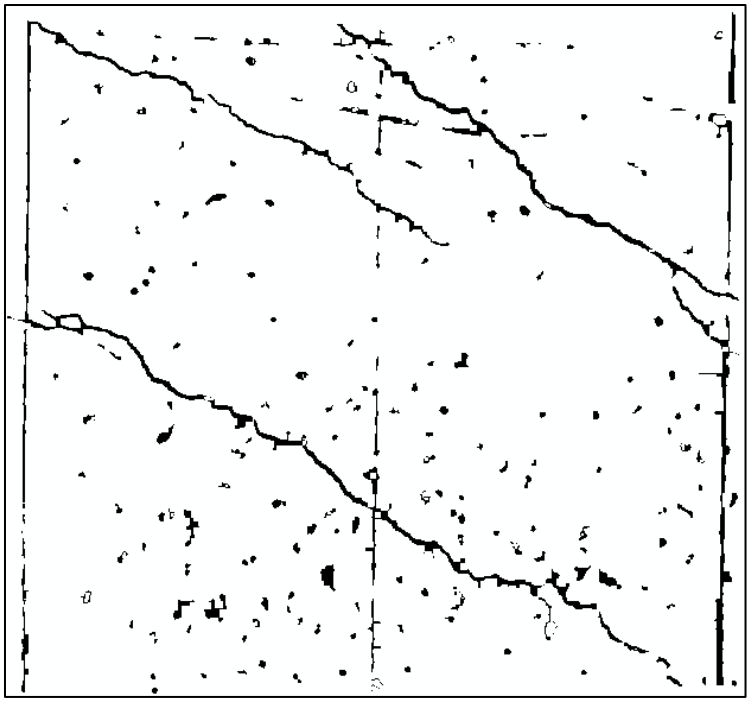

Figure B-14. Application of the morphological operations

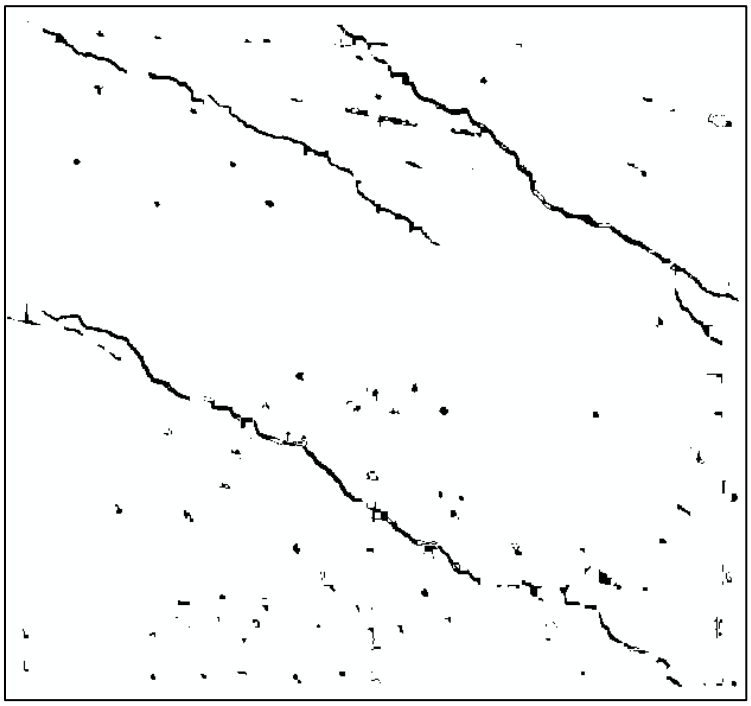

Figure B-15. Image segmentation based on angle of inclination

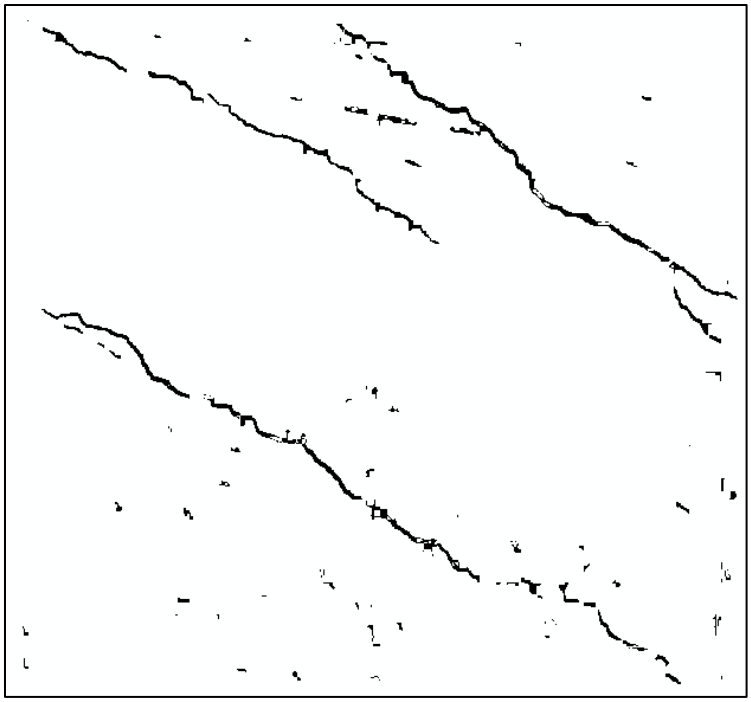

Figure B-16. Image segmentation major-minor axes length ratio

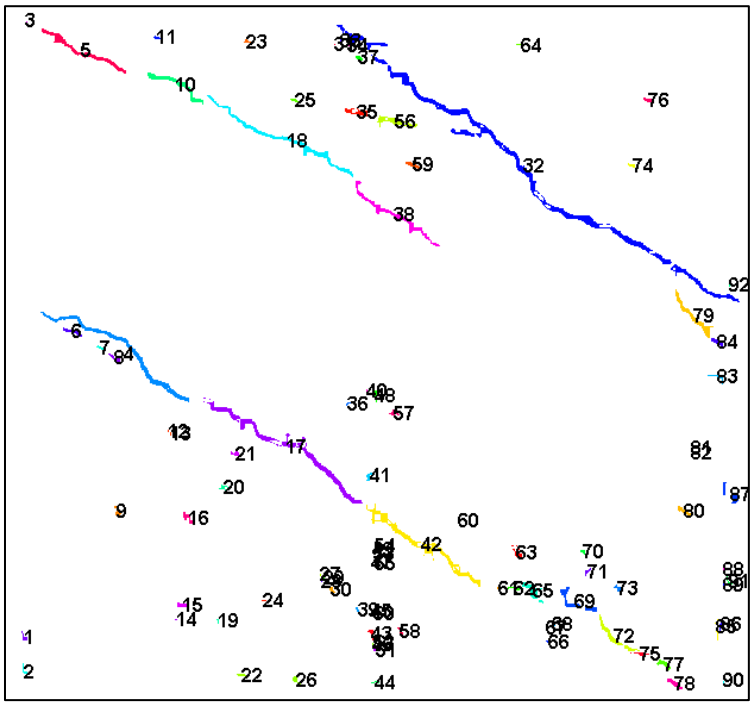

Figure B-17. Labelling of the cracks for post-processing

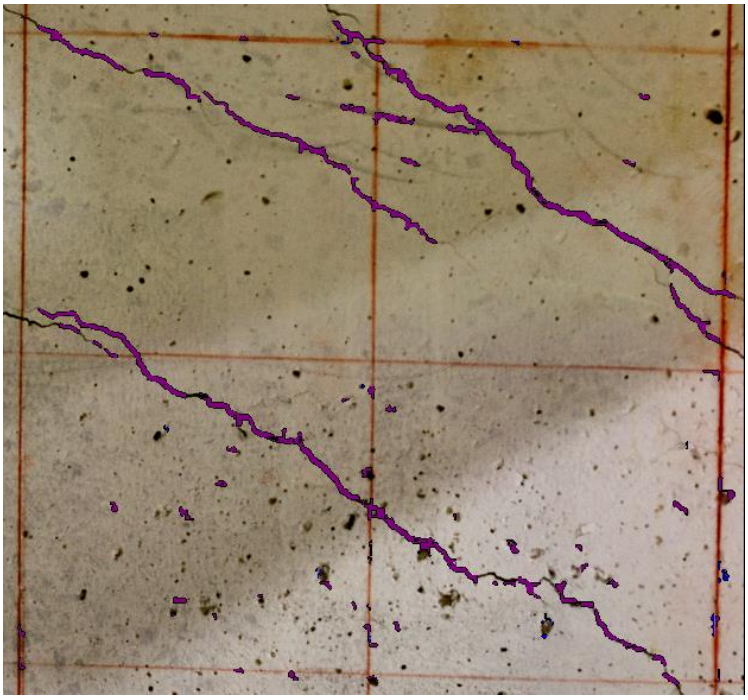

Figure B-18. Composite image

B.3 Post-processing

Post-processing is required to extract the predicted crack width for a specified crack after I-Crack has completed its analysis. The requirements for post-processing include the comma-separated value file that has every crack width saved, a figure similar to Figure B-17 and the MATLAB code CrackWidthSearch.m. The steps for post-processing include:

1. Opening a figure similar to Figure B-17 by double clicking the MATLAB figure file (.fig) that was generated by I-Crack in the Current Folder menu.
2. Then load the comma-separated value file into MATLAB using csvread:

   CrackInfo = csvread('CrackInfo for SW6 LS8 C1 Peak2.csv);
3. Once the crack widths have been loaded use the following code in the Command Window to extract the required crack widths:

   CrackWidthSearch(CrackInfo)

4. When CrackWidthSearch is called, a series of prompts will appear as follows:

   Determine crack width? Y/N

   Number of crack IDs?

   CrackID number

   Would you like to measure another crack? Y/N

The “Number of crack IDs?” is asking the user to input the number of measurements that will be used to determine an average crack width. The CrackID number is the label assigned to the crack and shown in the MATLAB figure file. After inputting the CrackID number, an averaged crack width is shown in the Command Window. If more measurements are required enter Y for Would you like to measure another crack? and the script will begin again.

MCEER Technical Reports

MCEER publishes technical reports on a variety of subjects written by authors funded through MCEER. These reports can be downloaded from the MCEER website at http://www.buffalo.edu/mceer. They can also be requested through NTIS, P.O. Box 1425, Springfield, Virginia 22151. NTIS accession numbers are shown in parenthesis, if available.

NCEER-87-0001 "First-Year Program in Research, Education and Technology Transfer," 3/5/87, (PB88-134275, A04, MF-A01).

NCEER-87-0002 "Experimental Evaluation of Instantaneous Optimal Algorithms for Structural Control," by R.C. Lin, T.T. Soong and A.M. Reinhorn, 4/20/87, (PB88-134341, A04, MF-A01).

NCEER-87-0003 "Experimentation Using the Earthquake Simulation Facilities at University at Buffalo," by A.M. Reinhorn and R.L. Ketter, not available.

NCEER-87-0004 "The System Characteristics and Performance of a Shaking Table," by J.S. Hwang, K.C. Chang and G.C. Lee, 6/1/87, (PB88-134259, A03, MF-A01). This report is available only through NTIS (see address given above).

NCEER-87-0005 "A Finite Element Formulation for Nonlinear Viscoplastic Material Using a Q Model," by O. Gyebi and G. Dasgupta, 11/2/87, (PB88-213764, A08, MF-A01).

NCEER-87-0006 "Symbolic Manipulation Program (SMP) - Algebraic Codes for Two and Three Dimensional Finite Element Formulations," by X. Lee and G. Dasgupta, 11/9/87, (PB88-218522, A05, MF-A01).

NCEER-87-0007 "Instantaneous Optimal Control Laws for Tall Buildings Under Seismic Excitations," by J.N. Yang, A. Akbarpour and P. Ghaemmaghami, 6/10/87, (PB88-134333, A06, MF-A01). This report is only available through NTIS (see address given above).

NCEER-87-0008 "IDARC: Inelastic Damage Analysis of Reinforced Concrete Frame - Shear-Wall Structures," by Y.J. Park, A.M. Reinhorn and S.K. Kunnath, 7/20/87, (PB88-134325, A09, MF-A01). This report is only available through NTIS (see address given above).

NCEER-87-0009 "Liquefaction Potential for New York State: A Preliminary Report on Sites in Manhattan and Buffalo," by M. Budhu, V. Vijayakumar, R.F. Giese and L. Baumgras, 8/31/87, (PB88-163704, A03, MF-A01). This report is available only through NTIS (see address given above).

NCEER-87-0010 "Vertical and Torsional Vibration of Foundations in Inhomogeneous Media," by A.S. Veletsos and K.W. Dotson, 6/1/87, (PB88-134291, A03, MF-A01). This report is only available through NTIS (see address given above).

NCEER-87-0011 "Seismic Probabilistic Risk Assessment and Seismic Margins Studies for Nuclear Power Plants," by Howard H.M. Hwang, 6/15/87, (PB88-134267, A03, MF-A01). This report is only available through NTIS (see address given above).

NCEER-87-0012 "Parametric Studies of Frequency Response of Secondary Systems Under Ground-Acceleration Excitations," by Y. Yong and Y.K. Lin, 6/10/87, (PB88-134309, A03, MF-A01). This report is only available through NTIS (see address given above).

NCEER-87-0013 "Frequency Response of Secondary Systems Under Seismic Excitation," by J.A. HoLung, J. Cai and Y.K. Lin, 7/31/87, (PB88-134317, A05, MF-A01). This report is only available through NTIS (see address given above).

NCEER-87-0014 "Modelling Earthquake Ground Motions in Seismically Active Regions Using Parametric Time Series Methods," by G.W. Ellis and A.S. Cakmak, 8/25/87, (PB88-134283, A08, MF-A01). This report is only available through NTIS (see address given above).

NCEER-87-0015 "Detection and Assessment of Seismic Structural Damage," by E. DiPasquale and A.S. Cakmak, 8/25/87, (PB88-163712, A05, MF-A01). This report is only available through NTIS (see address given above).

NCEER-87-0016 "Pipeline Experiment at Parkfield, California," by J. Isenberg and E. Richardson, 9/15/87, (PB88-163720, A03, MF-A01). This report is available only through NTIS (see address given above).

NCEER-87-0017 "Digital Simulation of Seismic Ground Motion," by M. Shinozuka, G. Deodatis and T. Harada, 8/31/87, (PB88-155197, A04, MF-A01). This report is available only through NTIS (see address given above).

NCEER-87-0018 "Practical Considerations for Structural Control: System Uncertainty, System Time Delay and Truncation of Small Control Forces," J.N. Yang and A. Akbarpour, 8/10/87, (PB88-163738, A08, MF-A01). This report is only available through NTIS (see address given above).

NCEER-87-0019 "Modal Analysis of Nonclassically Damped Structural Systems Using Canonical Transformation," by J.N. Yang, S. Sarkani and F.X. Long, 9/27/87, (PB88-187851, A04, MF-A01).

NCEER-87-0020 "A Nonstationary Solution in Random Vibration Theory," by J.R. Red-Horse and P.D. Spanos, 11/3/87, (PB88-163746, A03, MF-A01).

NCEER-87-0021 "Horizontal Impedances for Radially Inhomogeneous Viscoelastic Soil Layers," by A.S. Veletsos and K.W. Dotson, 10/15/87, (PB88-150859, A04, MF-A01).

NCEER-87-0022 "Seismic Damage Assessment of Reinforced Concrete Members," by Y.S. Chung, C. Meyer and M. Shinozuka, 10/9/87, (PB88-150867, A05, MF-A01). This report is available only through NTIS (see address given above).

NCEER-87-0023 "Active Structural Control in Civil Engineering," by T.T. Soong, 11/11/87, (PB88-187778, A03, MF-A01).

NCEER-87-0024 "Vertical and Torsional Impedances for Radially Inhomogeneous Viscoelastic Soil Layers," by K.W. Dotson and A.S. Veletsos, 12/87, (PB88-187786, A03, MF-A01).

NCEER-87-0025 "Proceedings from the Symposium on Seismic Hazards, Ground Motions, Soil-Liquefaction and Engineering Practice in Eastern North America," October 20-22, 1987, edited by K.H. Jacob, 12/87, (PB88-188115, A23, MF-A01). This report is available only through NTIS (see address given above).

NCEER-87-0026 "Report on the Whittier-Narrows, California, Earthquake of October 1, 1987," by J. Pantelic and A. Reinhorn, 11/87, (PB88-187752, A03, MF-A01). This report is available only through NTIS (see address given above).

NCEER-87-0027 "Design of a Modular Program for Transient Nonlinear Analysis of Large 3-D Building Structures," by S. Srivastav and J.F. Abel, 12/30/87, (PB88-187950, A05, MF-A01). This report is only available through NTIS (see address given above).

NCEER-87-0028 "Second-Year Program in Research, Education and Technology Transfer," 3/8/88, (PB88-219480, A04, MF-A01).

NCEER-88-0001 "Workshop on Seismic Computer Analysis and Design of Buildings With Interactive Graphics," by W. McGuire, J.F. Abel and C.H. Conley, 1/18/88, (PB88-187760, A03, MF-A01). This report is only available through NTIS (see address given above).

NCEER-88-0002 "Optimal Control of Nonlinear Flexible Structures," by J.N. Yang, F.X. Long and D. Wong, 1/22/88, (PB88-213772, A06, MF-A01).

NCEER-88-0003 "Substructuring Techniques in the Time Domain for Primary-Secondary Structural Systems," by G.D. Manolis and G. Juhn, 2/10/88, (PB88-213780, A04, MF-A01).

NCEER-88-0004 "Iterative Seismic Analysis of Primary-Secondary Systems," by A. Singhal, L.D. Lutes and P.D. Spanos, 2/23/88, (PB88-213798, A04, MF-A01).

NCEER-88-0005 "Stochastic Finite Element Expansion for Random Media," by P.D. Spanos and R. Ghanem, 3/14/88, (PB88-213806, A03, MF-A01).

NCEER-88-0006 "Combining Structural Optimization and Structural Control," by F.Y. Cheng and C.P. Pantelides, 1/10/88, (PB88-213814, A05, MF-A01).

NCEER-88-0007 "Seismic Performance Assessment of Code-Designed Structures," by H.H-M. Hwang, J-W. Jaw and H-J. Shau, 3/20/88, (PB88-219423, A04, MF-A01). This report is only available through NTIS (see address given above).

NCEER-88-0008 "Reliability Analysis of Code-Designed Structures Under Natural Hazards," by H.H-M. Hwang, H. Ushiba and M. Shinozuka, 2/29/88, (PB88-229471, A07, MF-A01). This report is only available through NTIS (see address given above).

NCEER-88-0009 "Seismic Fragility Analysis of Shear Wall Structures," by J-W Jaw and H.H-M. Hwang, 4/30/88, (PB89-102867, A04, MF-A01).

NCEER-88-0010 "Base Isolation of a Multi-Story Building Under a Harmonic Ground Motion - A Comparison of Performances of Various Systems," by F-G Fan, G. Ahmadi and I.G. Tadjbakhsh, 5/18/88, (PB89-122238, A06, MF-A01). This report is only available through NTIS (see address given above).

NCEER-88-0011 "Seismic Floor Response Spectra for a Combined System by Green's Functions," by F.M. Lavelle, L.A. Bergman and P.D. Spanos, 5/1/88, (PB89-102875, A03, MF-A01).

NCEER-88-0012 "A New Solution Technique for Randomly Excited Hysteretic Structures," by G.Q. Cai and Y.K. Lin, 5/16/88, (PB89-102883, A03, MF-A01).

NCEER-88-0013 "A Study of Radiation Damping and Soil-Structure Interaction Effects in the Centrifuge," by K. Weissman, supervised by J.H. Prevost, 5/24/88, (PB89-144703, A06, MF-A01).

NCEER-88-0014 "Parameter Identification and Implementation of a Kinematic Plasticity Model for Frictional Soils," by J.H. Prevost and D.V. Griffiths, not available.

NCEER-88-0015 "Two- and Three- Dimensional Dynamic Finite Element Analyses of the Long Valley Dam," by D.V. Griffiths and J.H. Prevost, 6/17/88, (PB89-144711, A04, MF-A01).

NCEER-88-0016 "Damage Assessment of Reinforced Concrete Structures in Eastern United States," by A.M. Reinhorn, M.J. Seidel, S.K. Kunnath and Y.J. Park, 6/15/88, (PB89-122220, A04, MF-A01). This report is only available through NTIS (see address given above).

NCEER-88-0017 "Dynamic Compliance of Vertically Loaded Strip Foundations in Multilayered Viscoelastic Soils," by S. Ahmad and A.S.M. Israil, 6/17/88, (PB89-102891, A04, MF-A01).

NCEER-88-0018 "An Experimental Study of Seismic Structural Response With Added Viscoelastic Dampers," by R.C. Lin, Z. Liang, T.T. Soong and R.H. Zhang, 6/30/88, (PB89-122212, A05, MF-A01). This report is available only through NTIS (see address given above).

NCEER-88-0019 "Experimental Investigation of Primary - Secondary System Interaction," by G.D. Manolis, G. Juhn and A.M. Reinhorn, 5/27/88, (PB89-122204, A04, MF-A01).

NCEER-88-0020 "A Response Spectrum Approach For Analysis of Nonclassically Damped Structures," by J.N. Yang, S. Sarkani and F.X. Long, 4/22/88, (PB89-102909, A04, MF-A01).

NCEER-88-0021 "Seismic Interaction of Structures and Soils: Stochastic Approach," by A.S. Veletsos and A.M. Prasad, 7/21/88, (PB89-122196, A04, MF-A01). This report is only available through NTIS (see address given above).

NCEER-88-0022 "Identification of the Serviceability Limit State and Detection of Seismic Structural Damage," by E. DiPasquale and A.S. Cakmak, 6/15/88, (PB89-122188, A05, MF-A01). This report is available only through NTIS (see address given above).

NCEER-88-0023 "Multi-Hazard Risk Analysis: Case of a Simple Offshore Structure," by B.K. Bhartia and E.H. Vanmarcke, 7/21/88, (PB89-145213, A05, MF-A01).

NCEER-88-0024 "Automated Seismic Design of Reinforced Concrete Buildings," by Y.S. Chung, C. Meyer and M. Shinozuka, 7/5/88, (PB89-122170, A06, MF-A01). This report is available only through NTIS (see address given above).

NCEER-88-0025 "Experimental Study of Active Control of MDOF Structures Under Seismic Excitations," by L.L. Chung, R.C. Lin, T.T. Soong and A.M. Reinhorn, 7/10/88, (PB89-122600, A04, MF-A01).

NCEER-88-0026 "Earthquake Simulation Tests of a Low-Rise Metal Structure," by J.S. Hwang, K.C. Chang, G.C. Lee and R.L. Ketter, 8/1/88, (PB89-102917, A04, MF-A01).

NCEER-88-0027 "Systems Study of Urban Response and Reconstruction Due to Catastrophic Earthquakes," by F. Kozin and H.K. Zhou, 9/22/88, (PB90-162348, A04, MF-A01).

NCEER-88-0028 "Seismic Fragility Analysis of Plane Frame Structures," by H.H-M. Hwang and Y.K. Low, 7/31/88, (PB89-131445, A06, MF-A01).

NCEER-88-0029 "Response Analysis of Stochastic Structures," by A. Kardara, C. Bucher and M. Shinozuka, 9/22/88, (PB89-174429, A04, MF-A01).

NCEER-88-0030 "Nonnormal Accelerations Due to Yielding in a Primary Structure," by D.C.K. Chen and L.D. Lutes, 9/19/88, (PB89-131437, A04, MF-A01).

NCEER-88-0031 "Design Approaches for Soil-Structure Interaction," by A.S. Veletsos, A.M. Prasad and Y. Tang, 12/30/88, (PB89-174437, A03, MF-A01). This report is available only through NTIS (see address given above).

NCEER-88-0032 "A Re-evaluation of Design Spectra for Seismic Damage Control," by C.J. Turkstra and A.G. Tallin, 11/7/88, (PB89-145221, A05, MF-A01).

NCEER-88-0033 "The Behavior and Design of Noncontact Lap Splices Subjected to Repeated Inelastic Tensile Loading," by V.E. Sagan, P. Gergely and R.N. White, 12/8/88, (PB89-163737, A08, MF-A01).

NCEER-88-0034 "Seismic Response of Pile Foundations," by S.M. Mamoon, P.K. Banerjee and S. Ahmad, 11/1/88, (PB89-145239, A04, MF-A01).

NCEER-88-0035 "Modeling of R/C Building Structures With Flexible Floor Diaphragms (IDARC2)," by A.M. Reinhorn, S.K. Kunnath and N. Panahshahi, 9/7/88, (PB89-207153, A07, MF-A01).

NCEER-88-0036 "Solution of the Dam-Reservoir Interaction Problem Using a Combination of FEM, BEM with Particular Integrals, Modal Analysis, and Substructuring," by C-S. Tsai, G.C. Lee and R.L. Ketter, 12/31/88, (PB89-207146, A04, MF-A01).

NCEER-88-0037 "Optimal Placement of Actuators for Structural Control," by F.Y. Cheng and C.P. Pantelides, 8/15/88, (PB89-162846, A05, MF-A01).

NCEER-88-0038 "Teflon Bearings in Aseismic Base Isolation: Experimental Studies and Mathematical Modeling," by A. Mokha, M.C. Constantinou and A.M. Reinhorn, 12/5/88, (PB89-218457, A10, MF-A01). This report is available only through NTIS (see address given above).

NCEER-88-0039 "Seismic Behavior of Flat Slab High-Rise Buildings in the New York City Area," by P. Weidlinger and M. Ettouney, 10/15/88, (PB90-145681, A04, MF-A01).

NCEER-88-0040 "Evaluation of the Earthquake Resistance of Existing Buildings in New York City," by P. Weidlinger and M. Ettouney, 10/15/88, not available.

NCEER-88-0041 "Small-Scale Modeling Techniques for Reinforced Concrete Structures Subjected to Seismic Loads," by W. Kim, A. El-Attar and R.N. White, 11/22/88, (PB89-189625, A05, MF-A01).

NCEER-88-0042 "Modeling Strong Ground Motion from Multiple Event Earthquakes," by G.W. Ellis and A.S. Cakmak, 10/15/88, (PB89-174445, A03, MF-A01).

NCEER-88-0043 "Nonstationary Models of Seismic Ground Acceleration," by M. Grigoriu, S.E. Ruiz and E. Rosenblueth, 7/15/88, (PB89-189617, A04, MF-A01).

NCEER-88-0044 "SARCF User's Guide: Seismic Analysis of Reinforced Concrete Frames," by Y.S. Chung, C. Meyer and M. Shinozuka, 11/9/88, (PB89-174452, A08, MF-A01).

NCEER-88-0045 "First Expert Panel Meeting on Disaster Research and Planning," edited by J. Pantelic and J. Stoyle, 9/15/88, (PB89-174460, A05, MF-A01).

NCEER-88-0046 "Preliminary Studies of the Effect of Degrading Infill Walls on the Nonlinear Seismic Response of Steel Frames," by C.Z. Chrysostomou, P. Gergely and J.F. Abel, 12/19/88, (PB89-208383, A05, MF-A01).

NCEER-88-0047 "Reinforced Concrete Frame Component Testing Facility - Design, Construction, Instrumentation and Operation," by S.P. Pessiki, C. Conley, T. Bond, P. Gergely and R.N. White, 12/16/88, (PB89-174478, A04, MF-A01).

NCEER-89-0001 "Effects of Protective Cushion and Soil Compliancy on the Response of Equipment Within a Seismically Excited Building," by J.A. HoLung, 2/16/89, (PB89-207179, A04, MF-A01).

NCEER-89-0002 "Statistical Evaluation of Response Modification Factors for Reinforced Concrete Structures," by H.H-M. Hwang and J-W. Jaw, 2/17/89, (PB89-207187, A05, MF-A01).

NCEER-89-0003 "Hysteretic Columns Under Random Excitation," by G-Q. Cai and Y.K. Lin, 1/9/89, (PB89-196513, A03, MF-A01).

NCEER-89-0004 "Experimental Study of `Elephant Foot Bulge' Instability of Thin-Walled Metal Tanks," by Z-H. Jia and R.L. Ketter, 2/22/89, (PB89-207195, A03, MF-A01).

NCEER-89-0005 "Experiment on Performance of Buried Pipelines Across San Andreas Fault," by J. Isenberg, E. Richardson and T.D. O'Rourke, 3/10/89, (PB89-218440, A04, MF-A01). This report is available only through NTIS (see address given above).

NCEER-89-0006 "A Knowledge-Based Approach to Structural Design of Earthquake-Resistant Buildings," by M. Subramani, P. Gergely, C.H. Conley, J.F. Abel and A.H. Zaghw, 1/15/89, (PB89-218465, A06, MF-A01).

NCEER-89-0007 "Liquefaction Hazards and Their Effects on Buried Pipelines," by T.D. O'Rourke and P.A. Lane, 2/1/89, (PB89-218481, A09, MF-A01).

NCEER-89-0008 "Fundamentals of System Identification in Structural Dynamics," by H. Imai, C-B. Yun, O. Maruyama and M. Shinozuka, 1/26/89, (PB89-207211, A04, MF-A01).

NCEER-89-0009 "Effects of the 1985 Michoacan Earthquake on Water Systems and Other Buried Lifelines in Mexico," by A.G. Ayala and M.J. O'Rourke, 3/8/89, (PB89-207229, A06, MF-A01).

NCEER-89-R010 "NCEER Bibliography of Earthquake Education Materials," by K.E.K. Ross, Second Revision, 9/1/89, (PB90-125352, A05, MF-A01). This report is replaced by NCEER-92-0018.

NCEER-89-0011 "Inelastic Three-Dimensional Response Analysis of Reinforced Concrete Building Structures (IDARC-3D), Part I - Modeling," by S.K. Kunnath and A.M. Reinhorn, 4/17/89, (PB90-114612, A07, MF-A01). This report is available only through NTIS (see address given above).

NCEER-89-0012 "Recommended Modifications to ATC-14," by C.D. Poland and J.O. Malley, 4/12/89, (PB90-108648, A15, MF-A01).

NCEER-89-0013 "Repair and Strengthening of Beam-to-Column Connections Subjected to Earthquake Loading," by M. Corazao and A.J. Durrani, 2/28/89, (PB90-109885, A06, MF-A01).

NCEER-89-0014 "Program EXKAL2 for Identification of Structural Dynamic Systems," by O. Maruyama, C-B. Yun, M. Hoshiya and M. Shinozuka, 5/19/89, (PB90-109877, A09, MF-A01).

NCEER-89-0015 "Response of Frames With Bolted Semi-Rigid Connections, Part I - Experimental Study and Analytical Predictions," by P.J. DiCorso, A.M. Reinhorn, J.R. Dickerson, J.B. Radziminski and W.L. Harper, 6/1/89, not available.

NCEER-89-0016 "ARMA Monte Carlo Simulation in Probabilistic Structural Analysis," by P.D. Spanos and M.P. Mignolet, 7/10/89, (PB90-109893, A03, MF-A01).

NCEER-89-P017 "Preliminary Proceedings from the Conference on Disaster Preparedness - The Place of Earthquake Education in Our Schools," Edited by K.E.K. Ross, 6/23/89, (PB90-108606, A03, MF-A01).

NCEER-89-0017 "Proceedings from the Conference on Disaster Preparedness - The Place of Earthquake Education in Our Schools," Edited by K.E.K. Ross, 12/31/89, (PB90-207895, A012, MF-A02). This report is available only through NTIS (see address given above).

NCEER-89-0018 "Multidimensional Models of Hysteretic Material Behavior for Vibration Analysis of Shape Memory Energy Absorbing Devices, by E.J. Graesser and F.A. Cozzarelli, 6/7/89, (PB90-164146, A04, MF-A01).

NCEER-89-0019 "Nonlinear Dynamic Analysis of Three-Dimensional Base Isolated Structures (3D-BASIS)," by S. Nagarajaiah, A.M. Reinhorn and M.C. Constantinou, 8/3/89, (PB90-161936, A06, MF-A01). This report has been replaced by NCEER-93-0011.

NCEER-89-0020 "Structural Control Considering Time-Rate of Control Forces and Control Rate Constraints," by F.Y. Cheng and C.P. Pantelides, 8/3/89, (PB90-120445, A04, MF-A01).

NCEER-89-0021 "Subsurface Conditions of Memphis and Shelby County," by K.W. Ng, T-S. Chang and H-H.M. Hwang, 7/26/89, (PB90-120437, A03, MF-A01).

NCEER-89-0022 "Seismic Wave Propagation Effects on Straight Jointed Buried Pipelines," by K. Elhmadi and M.J. O'Rourke, 8/24/89, (PB90-162322, A10, MF-A02).

NCEER-89-0023 "Workshop on Serviceability Analysis of Water Delivery Systems," edited by M. Grigoriu, 3/6/89, (PB90-127424, A03, MF-A01).

NCEER-89-0024 "Shaking Table Study of a 1/5 Scale Steel Frame Composed of Tapered Members," by K.C. Chang, J.S. Hwang and G.C. Lee, 9/18/89, (PB90-160169, A04, MF-A01).

NCEER-89-0025 "DYNA1D: A Computer Program for Nonlinear Seismic Site Response Analysis - Technical Documentation," by Jean H. Prevost, 9/14/89, (PB90-161944, A07, MF-A01). This report is available only through NTIS (see address given above).

NCEER-89-0026 "1:4 Scale Model Studies of Active Tendon Systems and Active Mass Dampers for Aseismic Protection," by A.M. Reinhorn, T.T. Soong, R.C. Lin, Y.P. Yang, Y. Fukao, H. Abe and M. Nakai, 9/15/89, (PB90-173246, A10, MF-A02). This report is available only through NTIS (see address given above).

NCEER-89-0027 "Scattering of Waves by Inclusions in a Nonhomogeneous Elastic Half Space Solved by Boundary Element Methods," by P.K. Hadley, A. Askar and A.S. Cakmak, 6/15/89, (PB90-145699, A07, MF-A01).

NCEER-89-0028 "Statistical Evaluation of Deflection Amplification Factors for Reinforced Concrete Structures," by H.H.M. Hwang, J-W. Jaw and A.L. Ch'ng, 8/31/89, (PB90-164633, A05, MF-A01).

NCEER-89-0029 "Bedrock Accelerations in Memphis Area Due to Large New Madrid Earthquakes," by H.H.M. Hwang, C.H.S. Chen and G. Yu, 11/7/89, (PB90-162330, A04, MF-A01).

NCEER-89-0030 "Seismic Behavior and Response Sensitivity of Secondary Structural Systems," by Y.Q. Chen and T.T. Soong, 10/23/89, (PB90-164658, A08, MF-A01).

NCEER-89-0031 "Random Vibration and Reliability Analysis of Primary-Secondary Structural Systems," by Y. Ibrahim, M. Grigoriu and T.T. Soong, 11/10/89, (PB90-161951, A04, MF-A01).

NCEER-89-0032 "Proceedings from the Second U.S. - Japan Workshop on Liquefaction, Large Ground Deformation and Their Effects on Lifelines, September 26-29, 1989," Edited by T.D. O'Rourke and M. Hamada, 12/1/89, (PB90-209388, A22, MF-A03).

NCEER-89-0033 "Deterministic Model for Seismic Damage Evaluation of Reinforced Concrete Structures," by J.M. Bracci, A.M. Reinhorn, J.B. Mander and S.K. Kunnath, 9/27/89, (PB91-108803, A06, MF-A01).

NCEER-89-0034 "On the Relation Between Local and Global Damage Indices," by E. DiPasquale and A.S. Cakmak, 8/15/89, (PB90-173865, A05, MF-A01).

NCEER-89-0035 "Cyclic Undrained Behavior of Nonplastic and Low Plasticity Silts," by A.J. Walker and H.E. Stewart, 7/26/89, (PB90-183518, A10, MF-A01).

NCEER-89-0036 "Liquefaction Potential of Surficial Deposits in the City of Buffalo, New York," by M. Budhu, R. Giese and L. Baumgrass, 1/17/89, (PB90-208455, A04, MF-A01).

NCEER-89-0037 "A Deterministic Assessment of Effects of Ground Motion Incoherence," by A.S. Veletsos and Y. Tang, 7/15/89, (PB90-164294, A03, MF-A01).

NCEER-89-0038 "Workshop on Ground Motion Parameters for Seismic Hazard Mapping," July 17-18, 1989, edited by R.V. Whitman, 12/1/89, (PB90-173923, A04, MF-A01).

NCEER-89-0039 "Seismic Effects on Elevated Transit Lines of the New York City Transit Authority," by C.J. Costantino, C.A. Miller and E. Heymsfield, 12/26/89, (PB90-207887, A06, MF-A01).

NCEER-89-0040 "Centrifugal Modeling of Dynamic Soil-Structure Interaction," by K. Weissman, Supervised by J.H. Prevost, 5/10/89, (PB90-207879, A07, MF-A01).

NCEER-89-0041 "Linearized Identification of Buildings With Cores for Seismic Vulnerability Assessment," by I-K. Ho and A.E. Aktan, 11/1/89, (PB90-251943, A07, MF-A01).

NCEER-90-0001 "Geotechnical and Lifeline Aspects of the October 17, 1989 Loma Prieta Earthquake in San Francisco," by T.D. O'Rourke, H.E. Stewart, F.T. Blackburn and T.S. Dickerman, 1/90, (PB90-208596, A05, MF-A01).

NCEER-90-0002 "Nonnormal Secondary Response Due to Yielding in a Primary Structure," by D.C.K. Chen and L.D. Lutes, 2/28/90, (PB90-251976, A07, MF-A01).

NCEER-90-0003 "Earthquake Education Materials for Grades K-12," by K.E.K. Ross, 4/16/90, (PB91-251984, A05, MF-A05). This report has been replaced by NCEER-92-0018.

NCEER-90-0004 "Catalog of Strong Motion Stations in Eastern North America," by R.W. Busby, 4/3/90, (PB90-251984, A05, MF-A01).

NCEER-90-0005 "NCEER Strong-Motion Data Base: A User Manual for the GeoBase Release (Version 1.0 for the Sun3)," by P. Friberg and K. Jacob, 3/31/90 (PB90-258062, A04, MF-A01).

NCEER-90-0006 "Seismic Hazard Along a Crude Oil Pipeline in the Event of an 1811-1812 Type New Madrid Earthquake," by H.H.M. Hwang and C-H.S. Chen, 4/16/90, (PB90-258054, A04, MF-A01).

NCEER-90-0007 "Site-Specific Response Spectra for Memphis Sheahan Pumping Station," by H.H.M. Hwang and C.S. Lee, 5/15/90, (PB91-108811, A05, MF-A01).

NCEER-90-0008 "Pilot Study on Seismic Vulnerability of Crude Oil Transmission Systems," by T. Ariman, R. Dobry, M. Grigoriu, F. Kozin, M. O'Rourke, T. O'Rourke and M. Shinozuka, 5/25/90, (PB91-108837, A06, MF-A01).

NCEER-90-0009 "A Program to Generate Site Dependent Time Histories: EQGEN," by G.W. Ellis, M. Srinivasan and A.S. Cakmak, 1/30/90, (PB91-108829, A04, MF-A01).

NCEER-90-0010 "Active Isolation for Seismic Protection of Operating Rooms," by M.E. Talbott, Supervised by M. Shinozuka, 6/8/9, (PB91-110205, A05, MF-A01).

NCEER-90-0011 "Program LINEARID for Identification of Linear Structural Dynamic Systems," by C-B. Yun and M. Shinozuka, 6/25/90, (PB91-110312, A08, MF-A01).

NCEER-90-0012 "Two-Dimensional Two-Phase Elasto-Plastic Seismic Response of Earth Dams," by A.N. Yiagos, Supervised by J.H. Prevost, 6/20/90, (PB91-110197, A13, MF-A02).

NCEER-90-0013 "Secondary Systems in Base-Isolated Structures: Experimental Investigation, Stochastic Response and Stochastic Sensitivity," by G.D. Manolis, G. Juhn, M.C. Constantinou and A.M. Reinhorn, 7/1/90, (PB91-110320, A08, MF-A01).

NCEER-90-0014 "Seismic Behavior of Lightly-Reinforced Concrete Column and Beam-Column Joint Details," by S.P. Pessiki, C.H. Conley, P. Gergely and R.N. White, 8/22/90, (PB91-108795, A11, MF-A02).

NCEER-90-0015 "Two Hybrid Control Systems for Building Structures Under Strong Earthquakes," by J.N. Yang and A. Danielians, 6/29/90, (PB91-125393, A04, MF-A01).

NCEER-90-0016 "Instantaneous Optimal Control with Acceleration and Velocity Feedback," by J.N. Yang and Z. Li, 6/29/90, (PB91-125401, A03, MF-A01).

NCEER-90-0017 "Reconnaissance Report on the Northern Iran Earthquake of June 21, 1990," by M. Mehrain, 10/4/90, (PB91-125377, A03, MF-A01).

NCEER-90-0018 "Evaluation of Liquefaction Potential in Memphis and Shelby County," by T.S. Chang, P.S. Tang, C.S. Lee and H. Hwang, 8/10/90, (PB91-125427, A09, MF-A01).

NCEER-90-0019 "Experimental and Analytical Study of a Combined Sliding Disc Bearing and Helical Steel Spring Isolation System," by M.C. Constantinou, A.S. Mokha and A.M. Reinhorn, 10/4/90, (PB91-125385, A06, MF-A01). This report is available only through NTIS (see address given above).

NCEER-90-0020 "Experimental Study and Analytical Prediction of Earthquake Response of a Sliding Isolation System with a Spherical Surface," by A.S. Mokha, M.C. Constantinou and A.M. Reinhorn, 10/11/90, (PB91-125419, A05, MF-A01).

NCEER-90-0021 "Dynamic Interaction Factors for Floating Pile Groups," by G. Gazetas, K. Fan, A. Kaynia and E. Kausel, 9/10/90, (PB91-170381, A05, MF-A01).

NCEER-90-0022 "Evaluation of Seismic Damage Indices for Reinforced Concrete Structures," by S. Rodriguez-Gomez and A.S. Cakmak, 9/30/90, PB91-171322, A06, MF-A01).

NCEER-90-0023 "Study of Site Response at a Selected Memphis Site," by H. Desai, S. Ahmad, E.S. Gazetas and M.R. Oh, 10/11/90, (PB91-196857, A03, MF-A01).

NCEER-90-0024 "A User's Guide to Strongmo: Version 1.0 of NCEER's Strong-Motion Data Access Tool for PCs and Terminals," by P.A. Friberg and C.A.T. Susch, 11/15/90, (PB91-171272, A03, MF-A01).

NCEER-90-0025 "A Three-Dimensional Analytical Study of Spatial Variability of Seismic Ground Motions," by L-L. Hong and A.H.-S. Ang, 10/30/90, (PB91-170399, A09, MF-A01).

NCEER-90-0026 "MUMOID User's Guide - A Program for the Identification of Modal Parameters," by S. Rodriguez-Gomez and E. DiPasquale, 9/30/90, (PB91-171298, A04, MF-A01).

NCEER-90-0027 "SARCF-II User's Guide - Seismic Analysis of Reinforced Concrete Frames," by S. Rodriguez-Gomez, Y.S. Chung and C. Meyer, 9/30/90, (PB91-171280, A05, MF-A01).

NCEER-90-0028 "Viscous Dampers: Testing, Modeling and Application in Vibration and Seismic Isolation," by N. Makris and M.C. Constantinou, 12/20/90 (PB91-190561, A06, MF-A01).

NCEER-90-0029 "Soil Effects on Earthquake Ground Motions in the Memphis Area," by H. Hwang, C.S. Lee, K.W. Ng and T.S. Chang, 8/2/90, (PB91-190751, A05, MF-A01).

NCEER-91-0001 "Proceedings from the Third Japan-U.S. Workshop on Earthquake Resistant Design of Lifeline Facilities and Countermeasures for Soil Liquefaction, December 17-19, 1990," edited by T.D. O'Rourke and M. Hamada, 2/1/91, (PB91-179259, A99, MF-A04).

NCEER-91-0002 "Physical Space Solutions of Non-Proportionally Damped Systems," by M. Tong, Z. Liang and G.C. Lee, 1/15/91, (PB91-179242, A04, MF-A01).

NCEER-91-0003 "Seismic Response of Single Piles and Pile Groups," by K. Fan and G. Gazetas, 1/10/91, (PB92-174994, A04, MF-A01).

NCEER-91-0004 "Damping of Structures: Part 1 - Theory of Complex Damping," by Z. Liang and G. Lee, 10/10/91, (PB92-197235, A12, MF-A03).

NCEER-91-0005 "3D-BASIS - Nonlinear Dynamic Analysis of Three Dimensional Base Isolated Structures: Part II," by S. Nagarajaiah, A.M. Reinhorn and M.C. Constantinou, 2/28/91, (PB91-190553, A07, MF-A01). This report has been replaced by NCEER-93-0011.

NCEER-91-0006 "A Multidimensional Hysteretic Model for Plasticity Deforming Metals in Energy Absorbing Devices," by E.J. Graesser and F.A. Cozzarelli, 4/9/91, (PB92-108364, A04, MF-A01).

NCEER-91-0007 "A Framework for Customizable Knowledge-Based Expert Systems with an Application to a KBES for Evaluating the Seismic Resistance of Existing Buildings," by E.G. Ibarra-Anaya and S.J. Fenves, 4/9/91, (PB91-210930, A08, MF-A01).

NCEER-91-0008 "Nonlinear Analysis of Steel Frames with Semi-Rigid Connections Using the Capacity Spectrum Method," by G.G. Deierlein, S-H. Hsieh, Y-J. Shen and J.F. Abel, 7/2/91, (PB92-113828, A05, MF-A01).

NCEER-91-0009 "Earthquake Education Materials for Grades K-12," by K.E.K. Ross, 4/30/91, (PB91-212142, A06, MF-A01). This report has been replaced by NCEER-92-0018.

NCEER-91-0010 "Phase Wave Velocities and Displacement Phase Differences in a Harmonically Oscillating Pile," by N. Makris and G. Gazetas, 7/8/91, (PB92-108356, A04, MF-A01).

NCEER-91-0011 "Dynamic Characteristics of a Full-Size Five-Story Steel Structure and a 2/5 Scale Model," by K.C. Chang, G.C. Yao, G.C. Lee, D.S. Hao and Y.C. Yeh," 7/2/91, (PB93-116648, A06, MF-A02).

NCEER-91-0012 "Seismic Response of a 2/5 Scale Steel Structure with Added Viscoelastic Dampers," by K.C. Chang, T.T. Soong, S-T. Oh and M.L. Lai, 5/17/91, (PB92-110816, A05, MF-A01).

NCEER-91-0013 "Earthquake Response of Retaining Walls; Full-Scale Testing and Computational Modeling," by S. Alampalli and A-W.M. Elgamal, 6/20/91, not available.

NCEER-91-0014 "3D-BASIS-M: Nonlinear Dynamic Analysis of Multiple Building Base Isolated Structures," by P.C. Tsopelas, S. Nagarajaiah, M.C. Constantinou and A.M. Reinhorn, 5/28/91, (PB92-113885, A09, MF-A02).

NCEER-91-0015 "Evaluation of SEAOC Design Requirements for Sliding Isolated Structures," by D. Theodossiou and M.C. Constantinou, 6/10/91, (PB92-114602, A11, MF-A03).

NCEER-91-0016 "Closed-Loop Modal Testing of a 27-Story Reinforced Concrete Flat Plate-Core Building," by H.R. Somaprasad, T. Toksoy, H. Yoshiyuki and A.E. Aktan, 7/15/91, (PB92-129980, A07, MF-A02).

NCEER-91-0017 "Shake Table Test of a 1/6 Scale Two-Story Lightly Reinforced Concrete Building," by A.G. El-Attar, R.N. White and P. Gergely, 2/28/91, (PB92-222447, A06, MF-A02).

NCEER-91-0018 "Shake Table Test of a 1/8 Scale Three-Story Lightly Reinforced Concrete Building," by A.G. El-Attar, R.N. White and P. Gergely, 2/28/91, (PB93-116630, A08, MF-A02).

NCEER-91-0019 "Transfer Functions for Rigid Rectangular Foundations," by A.S. Veletsos, A.M. Prasad and W.H. Wu, 7/31/91, not available.

NCEER-91-0020 "Hybrid Control of Seismic-Excited Nonlinear and Inelastic Structural Systems," by J.N. Yang, Z. Li and A. Danielians, 8/1/91, (PB92-143171, A06, MF-A02).

NCEER-91-0021 "The NCEER-91 Earthquake Catalog: Improved Intensity-Based Magnitudes and Recurrence Relations for U.S. Earthquakes East of New Madrid," by L. Seeber and J.G. Armbruster, 8/28/91, (PB92-176742, A06, MF-A02).

NCEER-91-0022 "Proceedings from the Implementation of Earthquake Planning and Education in Schools: The Need for Change - The Roles of the Changemakers," by K.E.K. Ross and F. Winslow, 7/23/91, (PB92-129998, A12, MF-A03).

NCEER-91-0023 "A Study of Reliability-Based Criteria for Seismic Design of Reinforced Concrete Frame Buildings," by H.H.M. Hwang and H-M. Hsu, 8/10/91, (PB92-140235, A09, MF-A02).

NCEER-91-0024 "Experimental Verification of a Number of Structural System Identification Algorithms," by R.G. Ghanem, H. Gavin and M. Shinozuka, 9/18/91, (PB92-176577, A18, MF-A04).

NCEER-91-0025 "Probabilistic Evaluation of Liquefaction Potential," by H.H.M. Hwang and C.S. Lee," 11/25/91, (PB92-143429, A05, MF-A01).

NCEER-91-0026 "Instantaneous Optimal Control for Linear, Nonlinear and Hysteretic Structures - Stable Controllers," by J.N. Yang and Z. Li, 11/15/91, (PB92-163807, A04, MF-A01).

NCEER-91-0027 "Experimental and Theoretical Study of a Sliding Isolation System for Bridges," by M.C. Constantinou, A. Kartoum, A.M. Reinhorn and P. Bradford, 11/15/91, (PB92-176973, A10, MF-A03).

NCEER-92-0001 "Case Studies of Liquefaction and Lifeline Performance During Past Earthquakes, Volume 1: Japanese Case Studies," Edited by M. Hamada and T. O'Rourke, 2/17/92, (PB92-197243, A18, MF-A04).

NCEER-92-0002 "Case Studies of Liquefaction and Lifeline Performance During Past Earthquakes, Volume 2: United States Case Studies," Edited by T. O'Rourke and M. Hamada, 2/17/92, (PB92-197250, A20, MF-A04).

NCEER-92-0003 "Issues in Earthquake Education," Edited by K. Ross, 2/3/92, (PB92-222389, A07, MF-A02).

NCEER-92-0004 "Proceedings from the First U.S. - Japan Workshop on Earthquake Protective Systems for Bridges," Edited by I.G. Buckle, 2/4/92, (PB94-142239, A99, MF-A06).

NCEER-92-0005 "Seismic Ground Motion from a Haskell-Type Source in a Multiple-Layered Half-Space," A.P. Theoharis, G. Deodatis and M. Shinozuka, 1/2/92, not available.

NCEER-92-0006 "Proceedings from the Site Effects Workshop," Edited by R. Whitman, 2/29/92, (PB92-197201, A04, MF-A01).

NCEER-92-0007 "Engineering Evaluation of Permanent Ground Deformations Due to Seismically-Induced Liquefaction," by M.H. Baziar, R. Dobry and A-W.M. Elgamal, 3/24/92, (PB92-222421, A13, MF-A03).

NCEER-92-0008 "A Procedure for the Seismic Evaluation of Buildings in the Central and Eastern United States," by C.D. Poland and J.O. Malley, 4/2/92, (PB92-222439, A20, MF-A04).

NCEER-92-0009 "Experimental and Analytical Study of a Hybrid Isolation System Using Friction Controllable Sliding Bearings," by M.Q. Feng, S. Fujii and M. Shinozuka, 5/15/92, (PB93-150282, A06, MF-A02).

NCEER-92-0010 "Seismic Resistance of Slab-Column Connections in Existing Non-Ductile Flat-Plate Buildings," by A.J. Durrani and Y. Du, 5/18/92, (PB93-116812, A06, MF-A02).

NCEER-92-0011 "The Hysteretic and Dynamic Behavior of Brick Masonry Walls Upgraded by Ferrocement Coatings Under Cyclic Loading and Strong Simulated Ground Motion," by H. Lee and S.P. Prawel, 5/11/92, not available.

NCEER-92-0012 "Study of Wire Rope Systems for Seismic Protection of Equipment in Buildings," by G.F. Demetriades, M.C. Constantinou and A.M. Reinhorn, 5/20/92, (PB93-116655, A08, MF-A02).

NCEER-92-0013 "Shape Memory Structural Dampers: Material Properties, Design and Seismic Testing," by P.R. Witting and F.A. Cozzarelli, 5/26/92, (PB93-116663, A05, MF-A01).

NCEER-92-0014 "Longitudinal Permanent Ground Deformation Effects on Buried Continuous Pipelines," by M.J. O'Rourke, and C. Nordberg, 6/15/92, (PB93-116671, A08, MF-A02).

NCEER-92-0015 "A Simulation Method for Stationary Gaussian Random Functions Based on the Sampling Theorem," by M. Grigoriu and S. Balopoulou, 6/11/92, (PB93-127496, A05, MF-A01).

NCEER-92-0016 "Gravity-Load-Designed Reinforced Concrete Buildings: Seismic Evaluation of Existing Construction and Detailing Strategies for Improved Seismic Resistance," by G.W. Hoffmann, S.K. Kunnath, A.M. Reinhorn and J.B. Mander, 7/15/92, (PB94-142007, A08, MF-A02).

NCEER-92-0017 "Observations on Water System and Pipeline Performance in the Limón Area of Costa Rica Due to the April 22, 1991 Earthquake," by M. O'Rourke and D. Ballantyne, 6/30/92, (PB93-126811, A06, MF-A02).

NCEER-92-0018 "Fourth Edition of Earthquake Education Materials for Grades K-12," Edited by K.E.K. Ross, 8/10/92, (PB93-114023, A07, MF-A02).

NCEER-92-0019 "Proceedings from the Fourth Japan-U.S. Workshop on Earthquake Resistant Design of Lifeline Facilities and Countermeasures for Soil Liquefaction," Edited by M. Hamada and T.D. O'Rourke, 8/12/92, (PB93-163939, A99, MF-E11).

NCEER-92-0020 "Active Bracing System: A Full Scale Implementation of Active Control," by A.M. Reinhorn, T.T. Soong, R.C. Lin, M.A. Riley, Y.P. Wang, S. Aizawa and M. Higashino, 8/14/92, (PB93-127512, A06, MF-A02).

NCEER-92-0021 "Empirical Analysis of Horizontal Ground Displacement Generated by Liquefaction-Induced Lateral Spreads," by S.F. Bartlett and T.L. Youd, 8/17/92, (PB93-188241, A06, MF-A02).

NCEER-92-0022 "IDARC Version 3.0: Inelastic Damage Analysis of Reinforced Concrete Structures," by S.K. Kunnath, A.M. Reinhorn and R.F. Lobo, 8/31/92, (PB93-227502, A07, MF-A02).

NCEER-92-0023 "A Semi-Empirical Analysis of Strong-Motion Peaks in Terms of Seismic Source, Propagation Path and Local Site Conditions, by M. Kamiyama, M.J. O'Rourke and R. Flores-Berrones, 9/9/92, (PB93-150266, A08, MF-A02).

NCEER-92-0024 "Seismic Behavior of Reinforced Concrete Frame Structures with Nonductile Details, Part I: Summary of Experimental Findings of Full Scale Beam-Column Joint Tests," by A. Beres, R.N. White and P. Gergely, 9/30/92, (PB93-227783, A05, MF-A01).

NCEER-92-0025 "Experimental Results of Repaired and Retrofitted Beam-Column Joint Tests in Lightly Reinforced Concrete Frame Buildings," by A. Beres, S. El-Borgi, R.N. White and P. Gergely, 10/29/92, (PB93-227791, A05, MF-A01).

NCEER-92-0026 "A Generalization of Optimal Control Theory: Linear and Nonlinear Structures," by J.N. Yang, Z. Li and S. Vongchavalitkul, 11/2/92, (PB93-188621, A05, MF-A01).

NCEER-92-0027 "Seismic Resistance of Reinforced Concrete Frame Structures Designed Only for Gravity Loads: Part I - Design and Properties of a One-Third Scale Model Structure," by J.M. Bracci, A.M. Reinhorn and J.B. Mander, 12/1/92, (PB94-104502, A08, MF-A02).

NCEER-92-0028 "Seismic Resistance of Reinforced Concrete Frame Structures Designed Only for Gravity Loads: Part II - Experimental Performance of Subassemblages," by L.E. Aycardi, J.B. Mander and A.M. Reinhorn, 12/1/92, (PB94-104510, A08, MF-A02).

NCEER-92-0029 "Seismic Resistance of Reinforced Concrete Frame Structures Designed Only for Gravity Loads: Part III - Experimental Performance and Analytical Study of a Structural Model," by J.M. Bracci, A.M. Reinhorn and J.B. Mander, 12/1/92, (PB93-227528, A09, MF-A01).

NCEER-92-0030 "Evaluation of Seismic Retrofit of Reinforced Concrete Frame Structures: Part I - Experimental Performance of Retrofitted Subassemblages," by D. Choudhuri, J.B. Mander and A.M. Reinhorn, 12/8/92, (PB93-198307, A07, MF-A02).

NCEER-92-0031 "Evaluation of Seismic Retrofit of Reinforced Concrete Frame Structures: Part II - Experimental Performance and Analytical Study of a Retrofitted Structural Model," by J.M. Bracci, A.M. Reinhorn and J.B. Mander, 12/8/92, (PB93-198315, A09, MF-A03).

NCEER-92-0032 "Experimental and Analytical Investigation of Seismic Response of Structures with Supplemental Fluid Viscous Dampers," by M.C. Constantinou and M.D. Symans, 12/21/92, (PB93-191435, A10, MF-A03). This report is available only through NTIS (see address given above).

NCEER-92-0033 "Reconnaissance Report on the Cairo, Egypt Earthquake of October 12, 1992," by M. Khater, 12/23/92, (PB93-188621, A03, MF-A01).

NCEER-92-0034 "Low-Level Dynamic Characteristics of Four Tall Flat-Plate Buildings in New York City," by H. Gavin, S. Yuan, J. Grossman, E. Pekelis and K. Jacob, 12/28/92, (PB93-188217, A07, MF-A02).

NCEER-93-0001 "An Experimental Study on the Seismic Performance of Brick-Infilled Steel Frames With and Without Retrofit," by J.B. Mander, B. Nair, K. Wojtkowski and J. Ma, 1/29/93, (PB93-227510, A07, MF-A02).

NCEER-93-0002 "Social Accounting for Disaster Preparedness and Recovery Planning," by S. Cole, E. Pantoja and V. Razak, 2/22/93, (PB94-142114, A12, MF-A03).

NCEER-93-0003 "Assessment of 1991 NEHRP Provisions for Nonstructural Components and Recommended Revisions," by T.T. Soong, G. Chen, Z. Wu, R-H. Zhang and M. Grigoriu, 3/1/93, (PB93-188639, A06, MF-A02).

NCEER-93-0004 "Evaluation of Static and Response Spectrum Analysis Procedures of SEAOC/UBC for Seismic Isolated Structures," by C.W. Winters and M.C. Constantinou, 3/23/93, (PB93-198299, A10, MF-A03).

NCEER-93-0005 "Earthquakes in the Northeast - Are We Ignoring the Hazard? A Workshop on Earthquake Science and Safety for Educators," edited by K.E.K. Ross, 4/2/93, (PB94-103066, A09, MF-A02).

NCEER-93-0006 "Inelastic Response of Reinforced Concrete Structures with Viscoelastic Braces," by R.F. Lobo, J.M. Bracci, K.L. Shen, A.M. Reinhorn and T.T. Soong, 4/5/93, (PB93-227486, A05, MF-A02).

NCEER-93-0007 "Seismic Testing of Installation Methods for Computers and Data Processing Equipment," by K. Kosar, T.T. Soong, K.L. Shen, J.A. HoLung and Y.K. Lin, 4/12/93, (PB93-198299, A07, MF-A02).

NCEER-93-0008 "Retrofit of Reinforced Concrete Frames Using Added Dampers," by A. Reinhorn, M. Constantinou and C. Li, not available.

NCEER-93-0009 "Seismic Behavior and Design Guidelines for Steel Frame Structures with Added Viscoelastic Dampers," by K.C. Chang, M.L. Lai, T.T. Soong, D.S. Hao and Y.C. Yeh, 5/1/93, (PB94-141959, A07, MF-A02).

NCEER-93-0010 "Seismic Performance of Shear-Critical Reinforced Concrete Bridge Piers," by J.B. Mander, S.M. Waheed, M.T.A. Chaudhary and S.S. Chen, 5/12/93, (PB93-227494, A08, MF-A02).

NCEER-93-0011 "3D-BASIS-TABS: Computer Program for Nonlinear Dynamic Analysis of Three Dimensional Base Isolated Structures," by S. Nagarajaiah, C. Li, A.M. Reinhorn and M.C. Constantinou, 8/2/93, (PB94-141819, A09, MF-A02).

NCEER-93-0012 "Effects of Hydrocarbon Spills from an Oil Pipeline Break on Ground Water," by O.J. Helweg and H.H.M. Hwang, 8/3/93, (PB94-141942, A06, MF-A02).

NCEER-93-0013 "Simplified Procedures for Seismic Design of Nonstructural Components and Assessment of Current Code Provisions," by M.P. Singh, L.E. Suarez, E.E. Matheu and G.O. Maldonado, 8/4/93, (PB94-141827, A09, MF-A02).

NCEER-93-0014 "An Energy Approach to Seismic Analysis and Design of Secondary Systems," by G. Chen and T.T. Soong, 8/6/93, (PB94-142767, A11, MF-A03).

NCEER-93-0015 "Proceedings from School Sites: Becoming Prepared for Earthquakes - Commemorating the Third Anniversary of the Loma Prieta Earthquake," Edited by F.E. Winslow and K.E.K. Ross, 8/16/93, (PB94-154275, A16, MF-A02).

NCEER-93-0016 "Reconnaissance Report of Damage to Historic Monuments in Cairo, Egypt Following the October 12, 1992 Dahshur Earthquake," by D. Sykora, D. Look, G. Croci, E. Karaesmen and E. Karaesmen, 8/19/93, (PB94-142221, A08, MF-A02).

NCEER-93-0017 "The Island of Guam Earthquake of August 8, 1993," by S.W. Swan and S.K. Harris, 9/30/93, (PB94-141843, A04, MF-A01).

NCEER-93-0018 "Engineering Aspects of the October 12, 1992 Egyptian Earthquake," by A.W. Elgamal, M. Amer, K. Adalier and A. Abul-Fadl, 10/7/93, (PB94-141983, A05, MF-A01).

NCEER-93-0019 "Development of an Earthquake Motion Simulator and its Application in Dynamic Centrifuge Testing," by I. Krstelj, Supervised by J.H. Prevost, 10/23/93, (PB94-181773, A-10, MF-A03).

NCEER-93-0020 "NCEER-Taisei Corporation Research Program on Sliding Seismic Isolation Systems for Bridges: Experimental and Analytical Study of a Friction Pendulum System (FPS)," by M.C. Constantinou, P. Tsopelas, Y-S. Kim and S. Okamoto, 11/1/93, (PB94-142775, A08, MF-A02).

NCEER-93-0021 "Finite Element Modeling of Elastomeric Seismic Isolation Bearings," by L.J. Billings, Supervised by R. Shepherd, 11/8/93, not available.

NCEER-93-0022 "Seismic Vulnerability of Equipment in Critical Facilities: Life-Safety and Operational Consequences," by K. Porter, G.S. Johnson, M.M. Zadeh, C. Scawthorn and S. Eder, 11/24/93, (PB94-181765, A16, MF-A03).

NCEER-93-0023 "Hokkaido Nansei-oki, Japan Earthquake of July 12, 1993, by P.I. Yanev and C.R. Scawthorn, 12/23/93, (PB94-181500, A07, MF-A01).

NCEER-94-0001 "An Evaluation of Seismic Serviceability of Water Supply Networks with Application to the San Francisco Auxiliary Water Supply System," by I. Markov, Supervised by M. Grigoriu and T. O'Rourke, 1/21/94, (PB94-204013, A07, MF-A02).

NCEER-94-0002 "NCEER-Taisei Corporation Research Program on Sliding Seismic Isolation Systems for Bridges: Experimental and Analytical Study of Systems Consisting of Sliding Bearings, Rubber Restoring Force Devices and Fluid Dampers," Volumes I and II, by P. Tsopelas, S. Okamoto, M.C. Constantinou, D. Ozaki and S. Fujii, 2/4/94, (PB94-181740, A09, MF-A02 and PB94-181757, A12, MF-A03).

NCEER-94-0003 "A Markov Model for Local and Global Damage Indices in Seismic Analysis," by S. Rahman and M. Grigoriu, 2/18/94, (PB94-206000, A12, MF-A03).

NCEER-94-0004 "Proceedings from the NCEER Workshop on Seismic Response of Masonry Infills," edited by D.P. Abrams, 3/1/94, (PB94-180783, A07, MF-A02).

NCEER-94-0005 "The Northridge, California Earthquake of January 17, 1994: General Reconnaissance Report," edited by J.D. Goltz, 3/11/94, (PB94-193943, A10, MF-A03).

NCEER-94-0006 "Seismic Energy Based Fatigue Damage Analysis of Bridge Columns: Part I - Evaluation of Seismic Capacity," by G.A. Chang and J.B. Mander, 3/14/94, (PB94-219185, A11, MF-A03).

NCEER-94-0007 "Seismic Isolation of Multi-Story Frame Structures Using Spherical Sliding Isolation Systems," by T.M. Al-Hussaini, V.A. Zayas and M.C. Constantinou, 3/17/94, (PB94-193745, A09, MF-A02).

NCEER-94-0008 "The Northridge, California Earthquake of January 17, 1994: Performance of Highway Bridges," edited by I.G. Buckle, 3/24/94, (PB94-193851, A06, MF-A02).

NCEER-94-0009 "Proceedings of the Third U.S.-Japan Workshop on Earthquake Protective Systems for Bridges," edited by I.G. Buckle and I. Friedland, 3/31/94, (PB94-195815, A99, MF-A06).

NCEER-94-0010 "3D-BASIS-ME: Computer Program for Nonlinear Dynamic Analysis of Seismically Isolated Single and Multiple Structures and Liquid Storage Tanks," by P.C. Tsopelas, M.C. Constantinou and A.M. Reinhorn, 4/12/94, (PB94-204922, A09, MF-A02).

NCEER-94-0011 "The Northridge, California Earthquake of January 17, 1994: Performance of Gas Transmission Pipelines," by T.D. O'Rourke and M.C. Palmer, 5/16/94, (PB94-204989, A05, MF-A01).

NCEER-94-0012 "Feasibility Study of Replacement Procedures and Earthquake Performance Related to Gas Transmission Pipelines," by T.D. O'Rourke and M.C. Palmer, 5/25/94, (PB94-206638, A09, MF-A02).

NCEER-94-0013 "Seismic Energy Based Fatigue Damage Analysis of Bridge Columns: Part II - Evaluation of Seismic Demand," by G.A. Chang and J.B. Mander, 6/1/94, (PB95-18106, A08, MF-A02).

NCEER-94-0014 "NCEER-Taisei Corporation Research Program on Sliding Seismic Isolation Systems for Bridges: Experimental and Analytical Study of a System Consisting of Sliding Bearings and Fluid Restoring Force/Damping Devices," by P. Tsopelas and M.C. Constantinou, 6/13/94, (PB94-219144, A10, MF-A03).

NCEER-94-0015 "Generation of Hazard-Consistent Fragility Curves for Seismic Loss Estimation Studies," by H. Hwang and J-R. Huo, 6/14/94, (PB95-181996, A09, MF-A02).

NCEER-94-0016 "Seismic Study of Building Frames with Added Energy-Absorbing Devices," by W.S. Pong, C.S. Tsai and G.C. Lee, 6/20/94, (PB94-219136, A10, A03).

NCEER-94-0017 "Sliding Mode Control for Seismic-Excited Linear and Nonlinear Civil Engineering Structures," by J. Yang, J. Wu, A. Agrawal and Z. Li, 6/21/94, (PB95-138483, A06, MF-A02).

NCEER-94-0018 "3D-BASIS-TABS Version 2.0: Computer Program for Nonlinear Dynamic Analysis of Three Dimensional Base Isolated Structures," by A.M. Reinhorn, S. Nagarajaiah, M.C. Constantinou, P. Tsopelas and R. Li, 6/22/94, (PB95-182176, A08, MF-A02).

NCEER-94-0019 "Proceedings of the International Workshop on Civil Infrastructure Systems: Application of Intelligent Systems and Advanced Materials on Bridge Systems," Edited by G.C. Lee and K.C. Chang, 7/18/94, (PB95-252474, A20, MF-A04).

NCEER-94-0020 "Study of Seismic Isolation Systems for Computer Floors," by V. Lambrou and M.C. Constantinou, 7/19/94, (PB95-138533, A10, MF-A03).

NCEER-94-0021 "Proceedings of the U.S.-Italian Workshop on Guidelines for Seismic Evaluation and Rehabilitation of Unreinforced Masonry Buildings," Edited by D.P. Abrams and G.M. Calvi, 7/20/94, (PB95-138749, A13, MF-A03).

NCEER-94-0022 "NCEER-Taisei Corporation Research Program on Sliding Seismic Isolation Systems for Bridges: Experimental and Analytical Study of a System Consisting of Lubricated PTFE Sliding Bearings and Mild Steel Dampers," by P. Tsopelas and M.C. Constantinou, 7/22/94, (PB95-182184, A08, MF-A02).

NCEER-94-0023 “Development of Reliability-Based Design Criteria for Buildings Under Seismic Load,” by Y.K. Wen, H. Hwang and M. Shinozuka, 8/1/94, (PB95-211934, A08, MF-A02).

NCEER-94-0024 “Experimental Verification of Acceleration Feedback Control Strategies for an Active Tendon System,” by S.J. Dyke, B.F. Spencer, Jr., P. Quast, M.K. Sain, D.C. Kaspari, Jr. and T.T. Soong, 8/29/94, (PB95-212320, A05, MF-A01).

NCEER-94-0025 “Seismic Retrofitting Manual for Highway Bridges,” Edited by I.G. Buckle and I.F. Friedland, published by the Federal Highway Administration (PB95-212676, A15, MF-A03).

NCEER-94-0026 “Proceedings from the Fifth U.S.-Japan Workshop on Earthquake Resistant Design of Lifeline Facilities and Countermeasures Against Soil Liquefaction,” Edited by T.D. O’Rourke and M. Hamada, 11/7/94, (PB95-220802, A99, MF-E08).

NCEER-95-0001 "Experimental and Analytical Investigation of Seismic Retrofit of Structures with Supplemental Damping: Part 1 - Fluid Viscous Damping Devices," by A.M. Reinhorn, C. Li and M.C. Constantinou, 1/3/95, (PB95-266599, A09, MF-A02).

NCEER-95-0002 "Experimental and Analytical Study of Low-Cycle Fatigue Behavior of Semi-Rigid Top-And-Seat Angle Connections," by G. Pekcan, J.B. Mander and S.S. Chen, 1/5/95, (PB95-220042, A07, MF-A02).

NCEER-95-0003 "NCEER-ATC Joint Study on Fragility of Buildings," by T. Anagnos, C. Rojahn and A.S. Kiremidjian, 1/20/95, (PB95-220026, A06, MF-A02).

NCEER-95-0004 "Nonlinear Control Algorithms for Peak Response Reduction," by Z. Wu, T.T. Soong, V. Gattulli and R.C. Lin, 2/16/95, (PB95-220349, A05, MF-A01).

NCEER-95-0005 "Pipeline Replacement Feasibility Study: A Methodology for Minimizing Seismic and Corrosion Risks to Underground Natural Gas Pipelines," by R.T. Eguchi, H.A. Seligson and D.G. Honegger, 3/2/95, (PB95-252326, A06, MF-A02).

NCEER-95-0006 "Evaluation of Seismic Performance of an 11-Story Frame Building During the 1994 Northridge Earthquake," by F. Naeim, R. DiSulio, K. Benuska, A. Reinhorn and C. Li, not available.

NCEER-95-0007 "Prioritization of Bridges for Seismic Retrofitting," by N. Basöz and A.S. Kiremidjian, 4/24/95, (PB95-252300, A08, MF-A02).

NCEER-95-0008 "Method for Developing Motion Damage Relationships for Reinforced Concrete Frames," by A. Singhal and A.S. Kiremidjian, 5/11/95, (PB95-266607, A06, MF-A02).

NCEER-95-0009 "Experimental and Analytical Investigation of Seismic Retrofit of Structures with Supplemental Damping: Part II - Friction Devices," by C. Li and A.M. Reinhorn, 7/6/95, (PB96-128087, A11, MF-A03).

NCEER-95-0010 "Experimental Performance and Analytical Study of a Non-Ductile Reinforced Concrete Frame Structure Retrofitted with Elastomeric Spring Dampers," by G. Pekcan, J.B. Mander and S.S. Chen, 7/14/95, (PB96-137161, A08, MF-A02).

NCEER-95-0011 "Development and Experimental Study of Semi-Active Fluid Damping Devices for Seismic Protection of Structures," by M.D. Symans and M.C. Constantinou, 8/3/95, (PB96-136940, A23, MF-A04).

NCEER-95-0012 "Real-Time Structural Parameter Modification (RSPM): Development of Innervated Structures," by Z. Liang, M. Tong and G.C. Lee, 4/11/95, (PB96-137153, A06, MF-A01).

NCEER-95-0013 "Experimental and Analytical Investigation of Seismic Retrofit of Structures with Supplemental Damping: Part III - Viscous Damping Walls," by A.M. Reinhorn and C. Li, 10/1/95, (PB96-176409, A11, MF-A03).

NCEER-95-0014 "Seismic Fragility Analysis of Equipment and Structures in a Memphis Electric Substation," by J-R. Huo and H.H.M. Hwang, 8/10/95, (PB96-128087, A09, MF-A02).

NCEER-95-0015 "The Hanshin-Awaji Earthquake of January 17, 1995: Performance of Lifelines," Edited by M. Shinozuka, 11/3/95, (PB96-176383, A15, MF-A03).

NCEER-95-0016 "Highway Culvert Performance During Earthquakes," by T.L. Youd and C.J. Beckman, available as NCEER-96-0015.

NCEER-95-0017 "The Hanshin-Awaji Earthquake of January 17, 1995: Performance of Highway Bridges," Edited by I.G. Buckle, 12/1/95, not available.

NCEER-95-0018 "Modeling of Masonry Infill Panels for Structural Analysis," by A.M. Reinhorn, A. Madan, R.E. Valles, Y. Reichmann and J.B. Mander, 12/8/95, (PB97-110886, MF-A01, A06).

NCEER-95-0019 "Optimal Polynomial Control for Linear and Nonlinear Structures," by A.K. Agrawal and J.N. Yang, 12/11/95, (PB96-168737, A07, MF-A02).

NCEER-95-0020 "Retrofit of Non-Ductile Reinforced Concrete Frames Using Friction Dampers," by R.S. Rao, P. Gergely and R.N. White, 12/22/95, (PB97-133508, A10, MF-A02).

NCEER-95-0021 "Parametric Results for Seismic Response of Pile-Supported Bridge Bents," by G. Mylonakis, A. Nikolaou and G. Gazetas, 12/22/95, (PB97-100242, A12, MF-A03).

NCEER-95-0022 "Kinematic Bending Moments in Seismically Stressed Piles," by A. Nikolaou, G. Mylonakis and G. Gazetas, 12/23/95, (PB97-113914, MF-A03, A13).

NCEER-96-0001 "Dynamic Response of Unreinforced Masonry Buildings with Flexible Diaphragms," by A.C. Costley and D.P. Abrams," 10/10/96, (PB97-133573, MF-A03, A15).

NCEER-96-0002 "State of the Art Review: Foundations and Retaining Structures," by I. Po Lam, not available.

NCEER-96-0003 "Ductility of Rectangular Reinforced Concrete Bridge Columns with Moderate Confinement," by N. Wehbe, M. Saiidi, D. Sanders and B. Douglas, 11/7/96, (PB97-133557, A06, MF-A02).

NCEER-96-0004 "Proceedings of the Long-Span Bridge Seismic Research Workshop," edited by I.G. Buckle and I.M. Friedland, not available.

NCEER-96-0005 "Establish Representative Pier Types for Comprehensive Study: Eastern United States," by J. Kulicki and Z. Prucz, 5/28/96, (PB98-119217, A07, MF-A02).

NCEER-96-0006 "Establish Representative Pier Types for Comprehensive Study: Western United States," by R. Imbsen, R.A. Schamber and T.A. Osterkamp, 5/28/96, (PB98-118607, A07, MF-A02).

NCEER-96-0007 "Nonlinear Control Techniques for Dynamical Systems with Uncertain Parameters," by R.G. Ghanem and M.I. Bujakov, 5/27/96, (PB97-100259, A17, MF-A03).

NCEER-96-0008 "Seismic Evaluation of a 30-Year Old Non-Ductile Highway Bridge Pier and Its Retrofit," by J.B. Mander, B. Mahmoodzadegan, S. Bhadra and S.S. Chen, 5/31/96, (PB97-110902, MF-A03, A10).

NCEER-96-0009 "Seismic Performance of a Model Reinforced Concrete Bridge Pier Before and After Retrofit," by J.B. Mander, J.H. Kim and C.A. Ligozio, 5/31/96, (PB97-110910, MF-A02, A10).

NCEER-96-0010 "IDARC2D Version 4.0: A Computer Program for the Inelastic Damage Analysis of Buildings," by R.E. Valles, A.M. Reinhorn, S.K. Kunnath, C. Li and A. Madan, 6/3/96, (PB97-100234, A17, MF-A03).

NCEER-96-0011 "Estimation of the Economic Impact of Multiple Lifeline Disruption: Memphis Light, Gas and Water Division Case Study," by S.E. Chang, H.A. Seligson and R.T. Eguchi, 8/16/96, (PB97-133490, A11, MF-A03).

NCEER-96-0012 "Proceedings from the Sixth Japan-U.S. Workshop on Earthquake Resistant Design of Lifeline Facilities and Countermeasures Against Soil Liquefaction, Edited by M. Hamada and T. O'Rourke, 9/11/96, (PB97-133581, A99, MF-A06).

NCEER-96-0013 "Chemical Hazards, Mitigation and Preparedness in Areas of High Seismic Risk: A Methodology for Estimating the Risk of Post-Earthquake Hazardous Materials Release," by H.A. Seligson, R.T. Eguchi, K.J. Tierney and K. Richmond, 11/7/96, (PB97-133565, MF-A02, A08).

NCEER-96-0014 "Response of Steel Bridge Bearings to Reversed Cyclic Loading," by J.B. Mander, D-K. Kim, S.S. Chen and G.J. Premus, 11/13/96, (PB97-140735, A12, MF-A03).

NCEER-96-0015 "Highway Culvert Performance During Past Earthquakes," by T.L. Youd and C.J. Beckman, 11/25/96, (PB97-133532, A06, MF-A01).

NCEER-97-0001 "Evaluation, Prevention and Mitigation of Pounding Effects in Building Structures," by R.E. Valles and A.M. Reinhorn, 2/20/97, (PB97-159552, A14, MF-A03).

NCEER-97-0002 "Seismic Design Criteria for Bridges and Other Highway Structures," by C. Rojahn, R. Mayes, D.G. Anderson, J. Clark, J.H. Hom, R.V. Nutt and M.J. O'Rourke, 4/30/97, (PB97-194658, A06, MF-A03).

NCEER-97-0003 “Proceedings of the U.S.-Italian Workshop on Seismic Evaluation and Retrofit,” Edited by D.P. Abrams and G.M. Calvi, 3/19/97, (PB97-194666, A13, MF-A03).

NCEER-97-0004 "Investigation of Seismic Response of Buildings with Linear and Nonlinear Fluid Viscous Dampers," by A.A. Seleemah and M.C. Constantinou, 5/21/97, (PB98-109002, A15, MF-A03).

NCEER-97-0005 "Proceedings of the Workshop on Earthquake Engineering Frontiers in Transportation Facilities," edited by G.C. Lee and I.M. Friedland, 8/29/97, (PB98-128911, A25, MR-A04).

NCEER-97-0006 "Cumulative Seismic Damage of Reinforced Concrete Bridge Piers," by S.K. Kunnath, A. El-Bahy, A. Taylor and W. Stone, 9/2/97, (PB98-108814, A11, MF-A03).

NCEER-97-0007 "Structural Details to Accommodate Seismic Movements of Highway Bridges and Retaining Walls," by R.A. Imbsen, R.A. Schamber, E. Thorkildsen, A. Kartoum, B.T. Martin, T.N. Rosser and J.M. Kulicki, 9/3/97, (PB98-108996, A09, MF-A02).

NCEER-97-0008 "A Method for Earthquake Motion-Damage Relationships with Application to Reinforced Concrete Frames," by A. Singhal and A.S. Kiremidjian, 9/10/97, (PB98-108988, A13, MF-A03).

NCEER-97-0009 "Seismic Analysis and Design of Bridge Abutments Considering Sliding and Rotation," by K. Fishman and R. Richards, Jr., 9/15/97, (PB98-108897, A06, MF-A02).

NCEER-97-0010 "Proceedings of the FHWA/NCEER Workshop on the National Representation of Seismic Ground Motion for New and Existing Highway Facilities," edited by I.M. Friedland, M.S. Power and R.L. Mayes, 9/22/97, (PB98-128903, A21, MF-A04).

NCEER-97-0011 "Seismic Analysis for Design or Retrofit of Gravity Bridge Abutments," by K.L. Fishman, R. Richards, Jr. and R.C. Divito, 10/2/97, (PB98-128937, A08, MF-A02).

NCEER-97-0012 "Evaluation of Simplified Methods of Analysis for Yielding Structures," by P. Tsopelas, M.C. Constantinou, C.A. Kircher and A.S. Whittaker, 10/31/97, (PB98-128929, A10, MF-A03).

NCEER-97-0013 "Seismic Design of Bridge Columns Based on Control and Repairability of Damage," by C-T. Cheng and J.B. Mander, 12/8/97, (PB98-144249, A11, MF-A03).

NCEER-97-0014 "Seismic Resistance of Bridge Piers Based on Damage Avoidance Design," by J.B. Mander and C-T. Cheng, 12/10/97, (PB98-144223, A09, MF-A02).

NCEER-97-0015 “Seismic Response of Nominally Symmetric Systems with Strength Uncertainty,” by S. Balopoulou and M. Grigoriu, 12/23/97, (PB98-153422, A11, MF-A03).

NCEER-97-0016 “Evaluation of Seismic Retrofit Methods for Reinforced Concrete Bridge Columns,” by T.J. Wipf, F.W. Klaiber and F.M. Russo, 12/28/97, (PB98-144215, A12, MF-A03).

NCEER-97-0017 “Seismic Fragility of Existing Conventional Reinforced Concrete Highway Bridges,” by C.L. Mullen and A.S. Cakmak, 12/30/97, (PB98-153406, A08, MF-A02).

NCEER-97-0018 “Loss Asssessment of Memphis Buildings,” edited by D.P. Abrams and M. Shinozuka, 12/31/97, (PB98-144231, A13, MF-A03).

NCEER-97-0019 “Seismic Evaluation of Frames with Infill Walls Using Quasi-static Experiments,” by K.M. Mosalam, R.N. White and P. Gergely, 12/31/97, (PB98-153455, A07, MF-A02).

NCEER-97-0020 “Seismic Evaluation of Frames with Infill Walls Using Pseudo-dynamic Experiments,” by K.M. Mosalam, R.N. White and P. Gergely, 12/31/97, (PB98-153430, A07, MF-A02).

NCEER-97-0021 “Computational Strategies for Frames with Infill Walls: Discrete and Smeared Crack Analyses and Seismic Fragility,” by K.M. Mosalam, R.N. White and P. Gergely, 12/31/97, (PB98-153414, A10, MF-A02).

NCEER-97-0022 "Proceedings of the NCEER Workshop on Evaluation of Liquefaction Resistance of Soils," edited by T.L. Youd and I.M. Idriss, 12/31/97, (PB98-155617, A15, MF-A03).

MCEER-98-0001 "Extraction of Nonlinear Hysteretic Properties of Seismically Isolated Bridges from Quick-Release Field Tests," by Q. Chen, B.M. Douglas, E.M. Maragakis and I.G. Buckle, 5/26/98, (PB99-118838, A06, MF-A01).

MCEER-98-0002 "Methodologies for Evaluating the Importance of Highway Bridges," by A. Thomas, S. Eshenaur and J. Kulicki, 5/29/98, (PB99-118846, A10, MF-A02).

MCEER-98-0003 "Capacity Design of Bridge Piers and the Analysis of Overstrength," by J.B. Mander, A. Dutta and P. Goel, 6/1/98, (PB99-118853, A09, MF-A02).

MCEER-98-0004 "Evaluation of Bridge Damage Data from the Loma Prieta and Northridge, California Earthquakes," by N. Basoz and A. Kiremidjian, 6/2/98, (PB99-118861, A15, MF-A03).

MCEER-98-0005 "Screening Guide for Rapid Assessment of Liquefaction Hazard at Highway Bridge Sites," by T. L. Youd, 6/16/98, (PB99-118879, A06, not available on microfiche).

MCEER-98-0006 "Structural Steel and Steel/Concrete Interface Details for Bridges," by P. Ritchie, N. Kauhl and J. Kulicki, 7/13/98, (PB99-118945, A06, MF-A01).

MCEER-98-0007 "Capacity Design and Fatigue Analysis of Confined Concrete Columns," by A. Dutta and J.B. Mander, 7/14/98, (PB99-118960, A14, MF-A03).

MCEER-98-0008 "Proceedings of the Workshop on Performance Criteria for Telecommunication Services Under Earthquake Conditions," edited by A.J. Schiff, 7/15/98, (PB99-118952, A08, MF-A02).

MCEER-98-0009 "Fatigue Analysis of Unconfined Concrete Columns," by J.B. Mander, A. Dutta and J.H. Kim, 9/12/98, (PB99-123655, A10, MF-A02).

MCEER-98-0010 "Centrifuge Modeling of Cyclic Lateral Response of Pile-Cap Systems and Seat-Type Abutments in Dry Sands," by A.D. Gadre and R. Dobry, 10/2/98, (PB99-123606, A13, MF-A03).

MCEER-98-0011 "IDARC-BRIDGE: A Computational Platform for Seismic Damage Assessment of Bridge Structures," by A.M. Reinhorn, V. Simeonov, G. Mylonakis and Y. Reichman, 10/2/98, (PB99-162919, A15, MF-A03).

MCEER-98-0012 "Experimental Investigation of the Dynamic Response of Two Bridges Before and After Retrofitting with Elastomeric Bearings," by D.A. Wendichansky, S.S. Chen and J.B. Mander, 10/2/98, (PB99-162927, A15, MF-A03).

MCEER-98-0013 "Design Procedures for Hinge Restrainers and Hinge Sear Width for Multiple-Frame Bridges," by R. Des Roches and G.L. Fenves, 11/3/98, (PB99-140477, A13, MF-A03).

MCEER-98-0014 "Response Modification Factors for Seismically Isolated Bridges," by M.C. Constantinou and J.K. Quarshie, 11/3/98, (PB99-140485, A14, MF-A03).

MCEER-98-0015 "Proceedings of the U.S.-Italy Workshop on Seismic Protective Systems for Bridges," edited by I.M. Friedland and M.C. Constantinou, 11/3/98, (PB2000-101711, A22, MF-A04).

MCEER-98-0016 "Appropriate Seismic Reliability for Critical Equipment Systems: Recommendations Based on Regional Analysis of Financial and Life Loss," by K. Porter, C. Scawthorn, C. Taylor and N. Blais, 11/10/98, (PB99-157265, A08, MF-A02).

MCEER-98-0017 "Proceedings of the U.S. Japan Joint Seminar on Civil Infrastructure Systems Research," edited by M. Shinozuka and A. Rose, 11/12/98, (PB99-156713, A16, MF-A03).

MCEER-98-0018 "Modeling of Pile Footings and Drilled Shafts for Seismic Design," by I. PoLam, M. Kapuskar and D. Chaudhuri, 12/21/98, (PB99-157257, A09, MF-A02).

MCEER-99-0001 "Seismic Evaluation of a Masonry Infilled Reinforced Concrete Frame by Pseudodynamic Testing," by S.G. Buonopane and R.N. White, 2/16/99, (PB99-162851, A09, MF-A02).

MCEER-99-0002 "Response History Analysis of Structures with Seismic Isolation and Energy Dissipation Systems: Verification Examples for Program SAP2000," by J. Scheller and M.C. Constantinou, 2/22/99, (PB99-162869, A08, MF-A02).

MCEER-99-0003 "Experimental Study on the Seismic Design and Retrofit of Bridge Columns Including Axial Load Effects," by A. Dutta, T. Kokorina and J.B. Mander, 2/22/99, (PB99-162877, A09, MF-A02).

MCEER-99-0004 "Experimental Study of Bridge Elastomeric and Other Isolation and Energy Dissipation Systems with Emphasis on Uplift Prevention and High Velocity Near-source Seismic Excitation," by A. Kasalanati and M. C. Constantinou, 2/26/99, (PB99-162885, A12, MF-A03).

MCEER-99-0005 "Truss Modeling of Reinforced Concrete Shear-flexure Behavior," by J.H. Kim and J.B. Mander, 3/8/99, (PB99-163693, A12, MF-A03).

MCEER-99-0006 "Experimental Investigation and Computational Modeling of Seismic Response of a 1:4 Scale Model Steel Structure with a Load Balancing Supplemental Damping System," by G. Pekcan, J.B. Mander and S.S. Chen, 4/2/99, (PB99-162893, A11, MF-A03).

MCEER-99-0007 "Effect of Vertical Ground Motions on the Structural Response of Highway Bridges," by M.R. Button, C.J. Cronin and R.L. Mayes, 4/10/99, (PB2000-101411, A10, MF-A03).

MCEER-99-0008 "Seismic Reliability Assessment of Critical Facilities: A Handbook, Supporting Documentation, and Model Code Provisions," by G.S. Johnson, R.E. Sheppard, M.D. Quilici, S.J. Eder and C.R. Scawthorn, 4/12/99, (PB2000-101701, A18, MF-A04).

MCEER-99-0009 "Impact Assessment of Selected MCEER Highway Project Research on the Seismic Design of Highway Structures," by C. Rojahn, R. Mayes, D.G. Anderson, J.H. Clark, D'Appolonia Engineering, S. Gloyd and R.V. Nutt, 4/14/99, (PB99-162901, A10, MF-A02).

MCEER-99-0010 "Site Factors and Site Categories in Seismic Codes," by R. Dobry, R. Ramos and M.S. Power, 7/19/99, (PB2000-101705, A08, MF-A02).

MCEER-99-0011 "Restrainer Design Procedures for Multi-Span Simply-Supported Bridges," by M.J. Randall, M. Saiidi, E. Maragakis and T. Isakovic, 7/20/99, (PB2000-101702, A10, MF-A02).

MCEER-99-0012 "Property Modification Factors for Seismic Isolation Bearings," by M.C. Constantinou, P. Tsopelas, A. Kasalanati and E. Wolff, 7/20/99, (PB2000-103387, A11, MF-A03).

MCEER-99-0013 "Critical Seismic Issues for Existing Steel Bridges," by P. Ritchie, N. Kauhl and J. Kulicki, 7/20/99, (PB2000-101697, A09, MF-A02).

MCEER-99-0014 "Nonstructural Damage Database," by A. Kao, T.T. Soong and A. Vender, 7/24/99, (PB2000-101407, A06, MF-A01).

MCEER-99-0015 "Guide to Remedial Measures for Liquefaction Mitigation at Existing Highway Bridge Sites," by H.G. Cooke and J. K. Mitchell, 7/26/99, (PB2000-101703, A11, MF-A03).

MCEER-99-0016 "Proceedings of the MCEER Workshop on Ground Motion Methodologies for the Eastern United States," edited by N. Abrahamson and A. Becker, 8/11/99, (PB2000-103385, A07, MF-A02).

MCEER-99-0017 "Quindío, Colombia Earthquake of January 25, 1999: Reconnaissance Report," by A.P. Asfura and P.J. Flores, 10/4/99, (PB2000-106893, A06, MF-A01).

MCEER-99-0018 "Hysteretic Models for Cyclic Behavior of Deteriorating Inelastic Structures," by M.V. Sivaselvan and A.M. Reinhorn, 11/5/99, (PB2000-103386, A08, MF-A02).

MCEER-99-0019 "Proceedings of the 7th U.S.- Japan Workshop on Earthquake Resistant Design of Lifeline Facilities and Countermeasures Against Soil Liquefaction," edited by T.D. O'Rourke, J.P. Bardet and M. Hamada, 11/19/99, (PB2000-103354, A99, MF-A06).

MCEER-99-0020 "Development of Measurement Capability for Micro-Vibration Evaluations with Application to Chip Fabrication Facilities," by G.C. Lee, Z. Liang, J.W. Song, J.D. Shen and W.C. Liu, 12/1/99, (PB2000-105993, A08, MF-A02).

MCEER-99-0021 "Design and Retrofit Methodology for Building Structures with Supplemental Energy Dissipating Systems," by G. Pekcan, J.B. Mander and S.S. Chen, 12/31/99, (PB2000-105994, A11, MF-A03).

MCEER-00-0001 "The Marmara, Turkey Earthquake of August 17, 1999: Reconnaissance Report," edited by C. Scawthorn; with major contributions by M. Bruneau, R. Eguchi, T. Holzer, G. Johnson, J. Mander, J. Mitchell, W. Mitchell, A. Papageorgiou, C. Scaethorn, and G. Webb, 3/23/00, (PB2000-106200, A11, MF-A03).

MCEER-00-0002 "Proceedings of the MCEER Workshop for Seismic Hazard Mitigation of Health Care Facilities," edited by G.C. Lee, M. Ettouney, M. Grigoriu, J. Hauer and J. Nigg, 3/29/00, (PB2000-106892, A08, MF-A02).

MCEER-00-0003 "The Chi-Chi, Taiwan Earthquake of September 21, 1999: Reconnaissance Report," edited by G.C. Lee and C.H. Loh, with major contributions by G.C. Lee, M. Bruneau, I.G. Buckle, S.E. Chang, P.J. Flores, T.D. O'Rourke, M. Shinozuka, T.T. Soong, C-H. Loh, K-C. Chang, Z-J. Chen, J-S. Hwang, M-L. Lin, G-Y. Liu, K-C. Tsai, G.C. Yao and C-L. Yen, 4/30/00, (PB2001-100980, A10, MF-A02).

MCEER-00-0004 "Seismic Retrofit of End-Sway Frames of Steel Deck-Truss Bridges with a Supplemental Tendon System: Experimental and Analytical Investigation," by G. Pekcan, J.B. Mander and S.S. Chen, 7/1/00, (PB2001-100982, A10, MF-A02).

MCEER-00-0005 "Sliding Fragility of Unrestrained Equipment in Critical Facilities," by W.H. Chong and T.T. Soong, 7/5/00, (PB2001-100983, A08, MF-A02).

MCEER-00-0006 "Seismic Response of Reinforced Concrete Bridge Pier Walls in the Weak Direction," by N. Abo-Shadi, M. Saiidi and D. Sanders, 7/17/00, (PB2001-100981, A17, MF-A03).

MCEER-00-0007 "Low-Cycle Fatigue Behavior of Longitudinal Reinforcement in Reinforced Concrete Bridge Columns," by J. Brown and S.K. Kunnath, 7/23/00, (PB2001-104392, A08, MF-A02).

MCEER-00-0008 "Soil Structure Interaction of Bridges for Seismic Analysis," I. PoLam and H. Law, 9/25/00, (PB2001-105397, A08, MF-A02).

MCEER-00-0009 "Proceedings of the First MCEER Workshop on Mitigation of Earthquake Disaster by Advanced Technologies (MEDAT-1), edited by M. Shinozuka, D.J. Inman and T.D. O'Rourke, 11/10/00, (PB2001-105399, A14, MF-A03).

MCEER-00-0010 "Development and Evaluation of Simplified Procedures for Analysis and Design of Buildings with Passive Energy Dissipation Systems, Revision 01," by O.M. Ramirez, M.C. Constantinou, C.A. Kircher, A.S. Whittaker, M.W. Johnson, J.D. Gomez and C. Chrysostomou, 11/16/01, (PB2001-105523, A23, MF-A04).

MCEER-00-0011 "Dynamic Soil-Foundation-Structure Interaction Analyses of Large Caissons," by C-Y. Chang, C-M. Mok, Z-L. Wang, R. Settgast, F. Waggoner, M.A. Ketchum, H.M. Gonnermann and C-C. Chin, 12/30/00, (PB2001-104373, A07, MF-A02).

MCEER-00-0012 "Experimental Evaluation of Seismic Performance of Bridge Restrainers," by A.G. Vlassis, E.M. Maragakis and M. Saiid Saiidi, 12/30/00, (PB2001-104354, A09, MF-A02).

MCEER-00-0013 "Effect of Spatial Variation of Ground Motion on Highway Structures," by M. Shinozuka, V. Saxena and G. Deodatis, 12/31/00, (PB2001-108755, A13, MF-A03).

MCEER-00-0014 "A Risk-Based Methodology for Assessing the Seismic Performance of Highway Systems," by S.D. Werner, C.E. Taylor, J.E. Moore, II, J.S. Walton and S. Cho, 12/31/00, (PB2001-108756, A14, MF-A03).

MCEER-01-0001 "Experimental Investigation of P-Delta Effects to Collapse During Earthquakes," by D. Vian and M. Bruneau, 6/25/01, (PB2002-100534, A17, MF-A03).

MCEER-01-0002 "Proceedings of the Second MCEER Workshop on Mitigation of Earthquake Disaster by Advanced Technologies (MEDAT-2)," edited by M. Bruneau and D.J. Inman, 7/23/01, (PB2002-100434, A16, MF-A03).

MCEER-01-0003 "Sensitivity Analysis of Dynamic Systems Subjected to Seismic Loads," by C. Roth and M. Grigoriu, 9/18/01, (PB2003-100884, A12, MF-A03).

MCEER-01-0004 "Overcoming Obstacles to Implementing Earthquake Hazard Mitigation Policies: Stage 1 Report," by D.J. Alesch and W.J. Petak, 12/17/01, (PB2002-107949, A07, MF-A02).

MCEER-01-0005 "Updating Real-Time Earthquake Loss Estimates: Methods, Problems and Insights," by C.E. Taylor, S.E. Chang and R.T. Eguchi, 12/17/01, (PB2002-107948, A05, MF-A01).

MCEER-01-0006 "Experimental Investigation and Retrofit of Steel Pile Foundations and Pile Bents Under Cyclic Lateral Loadings," by A. Shama, J. Mander, B. Blabac and S. Chen, 12/31/01, (PB2002-107950, A13, MF-A03).

MCEER-02-0001 "Assessment of Performance of Bolu Viaduct in the 1999 Duzce Earthquake in Turkey" by P.C. Roussis, M.C. Constantinou, M. Erdik, E. Durukal and M. Dicleli, 5/8/02, (PB2003-100883, A08, MF-A02).

MCEER-02-0002 "Seismic Behavior of Rail Counterweight Systems of Elevators in Buildings," by M.P. Singh, Rildova and L.E. Suarez, 5/27/02. (PB2003-100882, A11, MF-A03).

MCEER-02-0003 "Development of Analysis and Design Procedures for Spread Footings," by G. Mylonakis, G. Gazetas, S. Nikolaou and A. Chauncey, 10/02/02, (PB2004-101636, A13, MF-A03, CD-A13).

MCEER-02-0004 "Bare-Earth Algorithms for Use with SAR and LIDAR Digital Elevation Models," by C.K. Huyck, R.T. Eguchi and B. Houshmand, 10/16/02, (PB2004-101637, A07, CD-A07).

MCEER-02-0005 "Review of Energy Dissipation of Compression Members in Concentrically Braced Frames," by K.Lee and M. Bruneau, 10/18/02, (PB2004-101638, A10, CD-A10).

MCEER-03-0001 "Experimental Investigation of Light-Gauge Steel Plate Shear Walls for the Seismic Retrofit of Buildings" by J. Berman and M. Bruneau, 5/2/03, (PB2004-101622, A10, MF-A03, CD-A10).

MCEER-03-0002 "Statistical Analysis of Fragility Curves," by M. Shinozuka, M.Q. Feng, H. Kim, T. Uzawa and T. Ueda, 6/16/03, (PB2004-101849, A09, CD-A09).

MCEER-03-0003 "Proceedings of the Eighth U.S.-Japan Workshop on Earthquake Resistant Design f Lifeline Facilities and Countermeasures Against Liquefaction," edited by M. Hamada, J.P. Bardet and T.D. O'Rourke, 6/30/03, (PB2004-104386, A99, CD-A99).

MCEER-03-0004 "Proceedings of the PRC-US Workshop on Seismic Analysis and Design of Special Bridges," edited by L.C. Fan and G.C. Lee, 7/15/03, (PB2004-104387, A14, CD-A14).

MCEER-03-0005 "Urban Disaster Recovery: A Framework and Simulation Model," by S.B. Miles and S.E. Chang, 7/25/03, (PB2004-104388, A07, CD-A07).

MCEER-03-0006 "Behavior of Underground Piping Joints Due to Static and Dynamic Loading," by R.D. Meis, M. Maragakis and R. Siddharthan, 11/17/03, (PB2005-102194, A13, MF-A03, CD-A00).

MCEER-04-0001 "Experimental Study of Seismic Isolation Systems with Emphasis on Secondary System Response and Verification of Accuracy of Dynamic Response History Analysis Methods," by E. Wolff and M. Constantinou, 1/16/04 (PB2005-102195, A99, MF-E08, CD-A00).

MCEER-04-0002 "Tension, Compression and Cyclic Testing of Engineered Cementitious Composite Materials," by K. Kesner and S.L. Billington, 3/1/04, (PB2005-102196, A08, CD-A08).

MCEER-04-0003 "Cyclic Testing of Braces Laterally Restrained by Steel Studs to Enhance Performance During Earthquakes," by O.C. Celik, J.W. Berman and M. Bruneau, 3/16/04, (PB2005-102197, A13, MF-A03, CD-A00).

MCEER-04-0004 "Methodologies for Post Earthquake Building Damage Detection Using SAR and Optical Remote Sensing: Application to the August 17, 1999 Marmara, Turkey Earthquake," by C.K. Huyck, B.J. Adams, S. Cho, R.T. Eguchi, B. Mansouri and B. Houshmand, 6/15/04, (PB2005-104888, A10, CD-A00).

MCEER-04-0005 "Nonlinear Structural Analysis Towards Collapse Simulation: A Dynamical Systems Approach," by M.V. Sivaselvan and A.M. Reinhorn, 6/16/04, (PB2005-104889, A11, MF-A03, CD-A00).

MCEER-04-0006 "Proceedings of the Second PRC-US Workshop on Seismic Analysis and Design of Special Bridges," edited by G.C. Lee and L.C. Fan, 6/25/04, (PB2005-104890, A16, CD-A00).

MCEER-04-0007 "Seismic Vulnerability Evaluation of Axially Loaded Steel Built-up Laced Members," by K. Lee and M. Bruneau, 6/30/04, (PB2005-104891, A16, CD-A00).

MCEER-04-0008 "Evaluation of Accuracy of Simplified Methods of Analysis and Design of Buildings with Damping Systems for Near-Fault and for Soft-Soil Seismic Motions," by E.A. Pavlou and M.C. Constantinou, 8/16/04, (PB2005-104892, A08, MF-A02, CD-A00).

MCEER-04-0009 "Assessment of Geotechnical Issues in Acute Care Facilities in California," by M. Lew, T.D. O'Rourke, R. Dobry and M. Koch, 9/15/04, (PB2005-104893, A08, CD-A00).

MCEER-04-0010 "Scissor-Jack-Damper Energy Dissipation System," by A.N. Sigaher-Boyle and M.C. Constantinou, 12/1/04 (PB2005-108221).

MCEER-04-0011 "Seismic Retrofit of Bridge Steel Truss Piers Using a Controlled Rocking Approach," by M. Pollino and M. Bruneau, 12/20/04 (PB2006-105795).

MCEER-05-0001 "Experimental and Analytical Studies of Structures Seismically Isolated with an Uplift-Restraint Isolation System," by P.C. Roussis and M.C. Constantinou, 1/10/05 (PB2005-108222).

MCEER-05-0002 "A Versatile Experimentation Model for Study of Structures Near Collapse Applied to Seismic Evaluation of Irregular Structures," by D. Kusumastuti, A.M. Reinhorn and A. Rutenberg, 3/31/05 (PB2006-101523).

MCEER-05-0003 "Proceedings of the Third PRC-US Workshop on Seismic Analysis and Design of Special Bridges," edited by L.C. Fan and G.C. Lee, 4/20/05, (PB2006-105796).

MCEER-05-0004 "Approaches for the Seismic Retrofit of Braced Steel Bridge Piers and Proof-of-Concept Testing of an Eccentrically Braced Frame with Tubular Link," by J.W. Berman and M. Bruneau, 4/21/05 (PB2006-101524).

MCEER-05-0005 "Simulation of Strong Ground Motions for Seismic Fragility Evaluation of Nonstructural Components in Hospitals," by A. Wanitkorkul and A. Filiatrault, 5/26/05 (PB2006-500027).

MCEER-05-0006 "Seismic Safety in California Hospitals: Assessing an Attempt to Accelerate the Replacement or Seismic Retrofit of Older Hospital Facilities," by D.J. Alesch, L.A. Arendt and W.J. Petak, 6/6/05 (PB2006-105794).

MCEER-05-0007 "Development of Seismic Strengthening and Retrofit Strategies for Critical Facilities Using Engineered Cementitious Composite Materials," by K. Kesner and S.L. Billington, 8/29/05 (PB2006-111701).

MCEER-05-0008 "Experimental and Analytical Studies of Base Isolation Systems for Seismic Protection of Power Transformers," by N. Murota, M.Q. Feng and G-Y. Liu, 9/30/05 (PB2006-111702).

MCEER-05-0009 "3D-BASIS-ME-MB: Computer Program for Nonlinear Dynamic Analysis of Seismically Isolated Structures," by P.C. Tsopelas, P.C. Roussis, M.C. Constantinou, R. Buchanan and A.M. Reinhorn, 10/3/05 (PB2006-111703).

MCEER-05-0010 "Steel Plate Shear Walls for Seismic Design and Retrofit of Building Structures," by D. Vian and M. Bruneau, 12/15/05 (PB2006-111704).

MCEER-05-0011 "The Performance-Based Design Paradigm," by M.J. Astrella and A. Whittaker, 12/15/05 (PB2006-111705).

MCEER-06-0001 "Seismic Fragility of Suspended Ceiling Systems," H. Badillo-Almaraz, A.S. Whittaker, A.M. Reinhorn and G.P. Cimellaro, 2/4/06 (PB2006-111706).

MCEER-06-0002 "Multi-Dimensional Fragility of Structures," by G.P. Cimellaro, A.M. Reinhorn and M. Bruneau, 3/1/06 (PB2007-106974, A09, MF-A02, CD A00).

MCEER-06-0003 "Built-Up Shear Links as Energy Dissipators for Seismic Protection of Bridges," by P. Dusicka, A.M. Itani and I.G. Buckle, 3/15/06 (PB2006-111708).

MCEER-06-0004 "Analytical Investigation of the Structural Fuse Concept," by R.E. Vargas and M. Bruneau, 3/16/06 (PB2006-111709).

MCEER-06-0005 "Experimental Investigation of the Structural Fuse Concept," by R.E. Vargas and M. Bruneau, 3/17/06 (PB2006-111710).

MCEER-06-0006 "Further Development of Tubular Eccentrically Braced Frame Links for the Seismic Retrofit of Braced Steel Truss Bridge Piers," by J.W. Berman and M. Bruneau, 3/27/06 (PB2007-105147).

MCEER-06-0007 "REDARS Validation Report," by S. Cho, C.K. Huyck, S. Ghosh and R.T. Eguchi, 8/8/06 (PB2007-106983).

MCEER-06-0008 "Review of Current NDE Technologies for Post-Earthquake Assessment of Retrofitted Bridge Columns," by J.W. Song, Z. Liang and G.C. Lee, 8/21/06 (PB2007-106984).

MCEER-06-0009 "Liquefaction Remediation in Silty Soils Using Dynamic Compaction and Stone Columns," by S. Thevanayagam, G.R. Martin, R. Nashed, T. Shenthan, T. Kanagalingam and N. Ecemis, 8/28/06 (PB2007-106985).

MCEER-06-0010 "Conceptual Design and Experimental Investigation of Polymer Matrix Composite Infill Panels for Seismic Retrofitting," by W. Jung, M. Chiewanichakorn and A.J. Aref, 9/21/06 (PB2007-106986).

MCEER-06-0011 "A Study of the Coupled Horizontal-Vertical Behavior of Elastomeric and Lead-Rubber Seismic Isolation Bearings," by G.P. Warn and A.S. Whittaker, 9/22/06 (PB2007-108679).

MCEER-06-0012 "Proceedings of the Fourth PRC-US Workshop on Seismic Analysis and Design of Special Bridges: Advancing Bridge Technologies in Research, Design, Construction and Preservation," Edited by L.C. Fan, G.C. Lee and L. Ziang, 10/12/06 (PB2007-109042).

MCEER-06-0013 "Cyclic Response and Low Cycle Fatigue Characteristics of Plate Steels," by P. Dusicka, A.M. Itani and I.G. Buckle, 11/1/06 06 (PB2007-106987).

MCEER-06-0014 "Proceedings of the Second US-Taiwan Bridge Engineering Workshop," edited by W.P. Yen, J. Shen, J-Y. Chen and M. Wang, 11/15/06 (PB2008-500041).

MCEER-06-0015 "User Manual and Technical Documentation for the REDARS^{TM} Import Wizard," by S. Cho, S. Ghosh, C.K. Huyck and S.D. Werner, 11/30/06 (PB2007-114766).

MCEER-06-0016 "Hazard Mitigation Strategy and Monitoring Technologies for Urban and Infrastructure Public Buildings: Proceedings of the China-US Workshops," edited by X.Y. Zhou, A.L. Zhang, G.C. Lee and M. Tong, 12/12/06 (PB2008-500018).

MCEER-07-0001 "Static and Kinetic Coefficients of Friction for Rigid Blocks," by C. Kafali, S. Fathali, M. Grigoriu and A.S. Whittaker, 3/20/07 (PB2007-114767).

MCEER-07-0002 "Hazard Mitigation Investment Decision Making: Organizational Response to Legislative Mandate," by L.A. Arendt, D.J. Alesch and W.J. Petak, 4/9/07 (PB2007-114768).

MCEER-07-0003 "Seismic Behavior of Bidirectional-Resistant Ductile End Diaphragms with Unbonded Braces in Straight or Skewed Steel Bridges," by O. Celik and M. Bruneau, 4/11/07 (PB2008-105141).

MCEER-07-0004 "Modeling Pile Behavior in Large Pile Groups Under Lateral Loading," by A.M. Dodds and G.R. Martin, 4/16/07(PB2008-105142).

MCEER-07-0005 "Experimental Investigation of Blast Performance of Seismically Resistant Concrete-Filled Steel Tube Bridge Piers," by S. Fujikura, M. Bruneau and D. Lopez-Garcia, 4/20/07 (PB2008-105143).

MCEER-07-0006 "Seismic Analysis of Conventional and Isolated Liquefied Natural Gas Tanks Using Mechanical Analogs," by I.P. Christovasilis and A.S. Whittaker, 5/1/07, not available.

MCEER-07-0007 "Experimental Seismic Performance Evaluation of Isolation/Restraint Systems for Mechanical Equipment – Part 1: Heavy Equipment Study," by S. Fathali and A. Filiatrault, 6/6/07 (PB2008-105144).

MCEER-07-0008 "Seismic Vulnerability of Timber Bridges and Timber Substructures," by A.A. Sharma, J.B. Mander, I.M. Friedland and D.R. Allicock, 6/7/07 (PB2008-105145).

MCEER-07-0009 "Experimental and Analytical Study of the XY-Friction Pendulum (XY-FP) Bearing for Bridge Applications," by C.C. Marin-Artieda, A.S. Whittaker and M.C. Constantinou, 6/7/07 (PB2008-105191).

MCEER-07-0010 "Proceedings of the PRC-US Earthquake Engineering Forum for Young Researchers," Edited by G.C. Lee and X.Z. Qi, 6/8/07 (PB2008-500058).

MCEER-07-0011 "Design Recommendations for Perforated Steel Plate Shear Walls," by R. Purba and M. Bruneau, 6/18/07, (PB2008-105192).

MCEER-07-0012 "Performance of Seismic Isolation Hardware Under Service and Seismic Loading," by M.C. Constantinou, A.S. Whittaker, Y. Kalpakidis, D.M. Fenz and G.P. Warn, 8/27/07, (PB2008-105193).

MCEER-07-0013 "Experimental Evaluation of the Seismic Performance of Hospital Piping Subassemblies," by E.R. Goodwin, E. Maragakis and A.M. Itani, 9/4/07, (PB2008-105194).

MCEER-07-0014 "A Simulation Model of Urban Disaster Recovery and Resilience: Implementation for the 1994 Northridge Earthquake," by S. Miles and S.E. Chang, 9/7/07, (PB2008-106426).

MCEER-07-0015 "Statistical and Mechanistic Fragility Analysis of Concrete Bridges," by M. Shinozuka, S. Banerjee and S-H. Kim, 9/10/07, (PB2008-106427).

MCEER-07-0016 "Three-Dimensional Modeling of Inelastic Buckling in Frame Structures," by M. Schachter and AM. Reinhorn, 9/13/07, (PB2008-108125).

MCEER-07-0017 "Modeling of Seismic Wave Scattering on Pile Groups and Caissons," by I. Po Lam, H. Law and C.T. Yang, 9/17/07 (PB2008-108150).

MCEER-07-0018 "Bridge Foundations: Modeling Large Pile Groups and Caissons for Seismic Design," by I. Po Lam, H. Law and G.R. Martin (Coordinating Author), 12/1/07 (PB2008-111190).

MCEER-07-0019 "Principles and Performance of Roller Seismic Isolation Bearings for Highway Bridges," by G.C. Lee, Y.C. Ou, Z. Liang, T.C. Niu and J. Song, 12/10/07 (PB2009-110466).

MCEER-07-0020 "Centrifuge Modeling of Permeability and Pinning Reinforcement Effects on Pile Response to Lateral Spreading," by L.L Gonzalez-Lagos, T. Abdoun and R. Dobry, 12/10/07 (PB2008-111191).

MCEER-07-0021 "Damage to the Highway System from the Pisco, Perú Earthquake of August 15, 2007," by J.S. O'Connor, L. Mesa and M. Nykamp, 12/10/07, (PB2008-108126).

MCEER-07-0022 "Experimental Seismic Performance Evaluation of Isolation/Restraint Systems for Mechanical Equipment – Part 2: Light Equipment Study," by S. Fathali and A. Filiatrault, 12/13/07 (PB2008-111192).

MCEER-07-0023 "Fragility Considerations in Highway Bridge Design," by M. Shinozuka, S. Banerjee and S.H. Kim, 12/14/07 (PB2008-111193).

MCEER-07-0024 "Performance Estimates for Seismically Isolated Bridges," by G.P. Warn and A.S. Whittaker, 12/30/07 (PB2008-112230).

MCEER-08-0001 "Seismic Performance of Steel Girder Bridge Superstructures with Conventional Cross Frames," by L.P. Carden, A.M. Itani and I.G. Buckle, 1/7/08, (PB2008-112231).

MCEER-08-0002 "Seismic Performance of Steel Girder Bridge Superstructures with Ductile End Cross Frames with Seismic Isolators," by L.P. Carden, A.M. Itani and I.G. Buckle, 1/7/08 (PB2008-112232).

MCEER-08-0003 "Analytical and Experimental Investigation of a Controlled Rocking Approach for Seismic Protection of Bridge Steel Truss Piers," by M. Pollino and M. Bruneau, 1/21/08 (PB2008-112233).

MCEER-08-0004 "Linking Lifeline Infrastructure Performance and Community Disaster Resilience: Models and Multi-Stakeholder Processes," by S.E. Chang, C. Pasion, K. Tatebe and R. Ahmad, 3/3/08 (PB2008-112234).

MCEER-08-0005 "Modal Analysis of Generally Damped Linear Structures Subjected to Seismic Excitations," by J. Song, Y-L. Chu, Z. Liang and G.C. Lee, 3/4/08 (PB2009-102311).

MCEER-08-0006 "System Performance Under Multi-Hazard Environments," by C. Kafali and M. Grigoriu, 3/4/08 (PB2008-112235).

MCEER-08-0007 "Mechanical Behavior of Multi-Spherical Sliding Bearings," by D.M. Fenz and M.C. Constantinou, 3/6/08 (PB2008-112236).

MCEER-08-0008 "Post-Earthquake Restoration of the Los Angeles Water Supply System," by T.H.P. Tabucchi and R.A. Davidson, 3/7/08 (PB2008-112237).

MCEER-08-0009 "Fragility Analysis of Water Supply Systems," by A. Jacobson and M. Grigoriu, 3/10/08 (PB2009-105545).

MCEER-08-0010 "Experimental Investigation of Full-Scale Two-Story Steel Plate Shear Walls with Reduced Beam Section Connections," by B. Qu, M. Bruneau, C-H. Lin and K-C. Tsai, 3/17/08 (PB2009-106368).

MCEER-08-0011 "Seismic Evaluation and Rehabilitation of Critical Components of Electrical Power Systems," S. Ersoy, B. Feizi, A. Ashrafi and M. Ala Saadeghvaziri, 3/17/08 (PB2009-105546).

MCEER-08-0012 "Seismic Behavior and Design of Boundary Frame Members of Steel Plate Shear Walls," by B. Qu and M. Bruneau, 4/26/08 . (PB2009-106744).

MCEER-08-0013 "Development and Appraisal of a Numerical Cyclic Loading Protocol for Quantifying Building System Performance," by A. Filiatrault, A. Wanitkorkul and M. Constantinou, 4/27/08 (PB2009-107906).

MCEER-08-0014 "Structural and Nonstructural Earthquake Design: The Challenge of Integrating Specialty Areas in Designing Complex, Critical Facilities," by W.J. Petak and D.J. Alesch, 4/30/08 (PB2009-107907).

MCEER-08-0015 "Seismic Performance Evaluation of Water Systems," by Y. Wang and T.D. O'Rourke, 5/5/08 (PB2009-107908).

MCEER-08-0016 "Seismic Response Modeling of Water Supply Systems," by P. Shi and T.D. O'Rourke, 5/5/08 (PB2009-107910).

MCEER-08-0017 "Numerical and Experimental Studies of Self-Centering Post-Tensioned Steel Frames," by D. Wang and A. Filiatrault, 5/12/08 (PB2009-110479).

MCEER-08-0018 "Development, Implementation and Verification of Dynamic Analysis Models for Multi-Spherical Sliding Bearings," by D.M. Fenz and M.C. Constantinou, 8/15/08 (PB2009-107911).

MCEER-08-0019 "Performance Assessment of Conventional and Base Isolated Nuclear Power Plants for Earthquake Blast Loadings," by Y.N. Huang, A.S. Whittaker and N. Luco, 10/28/08 (PB2009-107912).

MCEER-08-0020 "Remote Sensing for Resilient Multi-Hazard Disaster Response – Volume I: Introduction to Damage Assessment Methodologies," by B.J. Adams and R.T. Eguchi, 11/17/08 (PB2010-102695).

MCEER-08-0021 "Remote Sensing for Resilient Multi-Hazard Disaster Response – Volume II: Counting the Number of Collapsed Buildings Using an Object-Oriented Analysis: Case Study of the 2003 Bam Earthquake," by L. Gusella, C.K. Huyck and B.J. Adams, 11/17/08 (PB2010-100925).

MCEER-08-0022 "Remote Sensing for Resilient Multi-Hazard Disaster Response – Volume III: Multi-Sensor Image Fusion Techniques for Robust Neighborhood-Scale Urban Damage Assessment," by B.J. Adams and A. McMillan, 11/17/08 (PB2010-100926).

MCEER-08-0023 "Remote Sensing for Resilient Multi-Hazard Disaster Response – Volume IV: A Study of Multi-Temporal and Multi-Resolution SAR Imagery for Post-Katrina Flood Monitoring in New Orleans," by A. McMillan, J.G. Morley, B.J. Adams and S. Chesworth, 11/17/08 (PB2010-100927).

MCEER-08-0024 "Remote Sensing for Resilient Multi-Hazard Disaster Response – Volume V: Integration of Remote Sensing Imagery and VIEWS^{TM} Field Data for Post-Hurricane Charley Building Damage Assessment," by J.A. Womble, K. Mehta and B.J. Adams, 11/17/08 (PB2009-115532).

MCEER-08-0025 "Building Inventory Compilation for Disaster Management: Application of Remote Sensing and Statistical Modeling," by P. Sarabandi, A.S. Kiremidjian, R.T. Eguchi and B. J. Adams, 11/20/08 (PB2009-110484).

MCEER-08-0026 "New Experimental Capabilities and Loading Protocols for Seismic Qualification and Fragility Assessment of Nonstructural Systems," by R. Retamales, G. Mosqueda, A. Filiatrault and A. Reinhorn, 11/24/08 (PB2009-110485).

MCEER-08-0027 "Effects of Heating and Load History on the Behavior of Lead-Rubber Bearings," by I.V. Kalpakidis and M.C. Constantinou, 12/1/08 (PB2009-115533).

MCEER-08-0028 "Experimental and Analytical Investigation of Blast Performance of Seismically Resistant Bridge Piers," by S.Fujikura and M. Bruneau, 12/8/08 (PB2009-115534).

MCEER-08-0029 "Evolutionary Methodology for Aseismic Decision Support," by Y. Hu and G. Dargush, 12/15/08.

MCEER-08-0030 "Development of a Steel Plate Shear Wall Bridge Pier System Conceived from a Multi-Hazard Perspective," by D. Keller and M. Bruneau, 12/19/08 (PB2010-102696).

MCEER-09-0001 "Modal Analysis of Arbitrarily Damped Three-Dimensional Linear Structures Subjected to Seismic Excitations," by Y.L. Chu, J. Song and G.C. Lee, 1/31/09 (PB2010-100922).

MCEER-09-0002 "Air-Blast Effects on Structural Shapes," by G. Ballantyne, A.S. Whittaker, A.J. Aref and G.F. Dargush, 2/2/09 (PB2010-102697).

MCEER-09-0003 "Water Supply Performance During Earthquakes and Extreme Events," by A.L. Bonneau and T.D. O'Rourke, 2/16/09 (PB2010-100923).

MCEER-09-0004 "Generalized Linear (Mixed) Models of Post-Earthquake Ignitions," by R.A. Davidson, 7/20/09 (PB2010-102698).

MCEER-09-0005 "Seismic Testing of a Full-Scale Two-Story Light-Frame Wood Building: NEESWood Benchmark Test," by I.P. Christovasilis, A. Filiatrault and A. Wanitkorkul, 7/22/09 (PB2012-102401).

MCEER-09-0006 "IDARC2D Version 7.0: A Program for the Inelastic Damage Analysis of Structures," by A.M. Reinhorn, H. Roh, M. Sivaselvan, S.K. Kunnath, R.E. Valles, A. Madan, C. Li, R. Lobo and Y.J. Park, 7/28/09 (PB2010-103199).

MCEER-09-0007 "Enhancements to Hospital Resiliency: Improving Emergency Planning for and Response to Hurricanes," by D.B. Hess and L.A. Arendt, 7/30/09 (PB2010-100924).

MCEER-09-0008 "Assessment of Base-Isolated Nuclear Structures for Design and Beyond-Design Basis Earthquake Shaking," by Y.N. Huang, A.S. Whittaker, R.P. Kennedy and R.L. Mayes, 8/20/09 (PB2010-102699).

MCEER-09-0009 "Quantification of Disaster Resilience of Health Care Facilities," by G.P. Cimellaro, C. Fumo, A.M Reinhorn and M. Bruneau, 9/14/09 (PB2010-105384).

MCEER-09-0010 "Performance-Based Assessment and Design of Squat Reinforced Concrete Shear Walls," by C.K. Gulec and A.S. Whittaker, 9/15/09 (PB2010-102700).

MCEER-09-0011 "Proceedings of the Fourth US-Taiwan Bridge Engineering Workshop," edited by W.P. Yen, J.J. Shen, T.M. Lee and R.B. Zheng, 10/27/09 (PB2010-500009).

MCEER-09-0012 "Proceedings of the Special International Workshop on Seismic Connection Details for Segmental Bridge Construction," edited by W. Phillip Yen and George C. Lee, 12/21/09 (PB2012-102402).

MCEER-10-0001 "Direct Displacement Procedure for Performance-Based Seismic Design of Multistory Woodframe Structures," by W. Pang and D. Rosowsky, 4/26/10 (PB2012-102403).

MCEER-10-0002 "Simplified Direct Displacement Design of Six-Story NEESWood Capstone Building and Pre-Test Seismic Performance Assessment," by W. Pang, D. Rosowsky, J. van de Lindt and S. Pei, 5/28/10 (PB2012-102404).

MCEER-10-0003 "Integration of Seismic Protection Systems in Performance-Based Seismic Design of Woodframed Structures," by J.K. Shinde and M.D. Symans, 6/18/10 (PB2012-102405).

MCEER-10-0004 "Modeling and Seismic Evaluation of Nonstructural Components: Testing Frame for Experimental Evaluation of Suspended Ceiling Systems," by A.M. Reinhorn, K.P. Ryu and G. Maddaloni, 6/30/10 (PB2012-102406).

MCEER-10-0005 "Analytical Development and Experimental Validation of a Structural-Fuse Bridge Pier Concept," by S. El-Bahey and M. Bruneau, 10/1/10 (PB2012-102407).

MCEER-10-0006 "A Framework for Defining and Measuring Resilience at the Community Scale: The PEOPLES Resilience Framework," by C.S. Renschler, A.E. Frazier, L.A. Arendt, G.P. Cimellaro, A.M. Reinhorn and M. Bruneau, 10/8/10 (PB2012-102408).

MCEER-10-0007 "Impact of Horizontal Boundary Elements Design on Seismic Behavior of Steel Plate Shear Walls," by R. Purba and M. Bruneau, 11/14/10 (PB2012-102409).

MCEER-10-0008 "Seismic Testing of a Full-Scale Mid-Rise Building: The NEESWood Capstone Test," by S. Pei, J.W. van de Lindt, S.E. Pryor, H. Shimizu, H. Isoda and D.R. Rammer, 12/1/10 (PB2012-102410).

MCEER-10-0009 "Modeling the Effects of Detonations of High Explosives to Inform Blast-Resistant Design," by P. Sherkar, A.S. Whittaker and A.J. Aref, 12/1/10 (PB2012-102411).

MCEER-10-0010 "L'Aquila Earthquake of April 6, 2009 in Italy: Rebuilding a Resilient City to Withstand Multiple Hazards," by G.P. Cimellaro, I.P. Christovasilis, A.M. Reinhorn, A. De Stefano and T. Kirova, 12/29/10.

MCEER-11-0001 "Numerical and Experimental Investigation of the Seismic Response of Light-Frame Wood Structures," by I.P. Christovasilis and A. Filiatrault, 8/8/11 (PB2012-102412).

MCEER-11-0002 "Seismic Design and Analysis of a Precast Segmental Concrete Bridge Model," by M. Anagnostopoulou, A. Filiatrault and A. Aref, 9/15/11.

MCEER-11-0003 'Proceedings of the Workshop on Improving Earthquake Response of Substation Equipment," Edited by A.M. Reinhorn, 9/19/11 (PB2012-102413).

MCEER-11-0004 "LRFD-Based Analysis and Design Procedures for Bridge Bearings and Seismic Isolators," by M.C. Constantinou, I. Kalpakidis, A. Filiatrault and R.A. Ecker Lay, 9/26/11.

MCEER-11-0005 "Experimental Seismic Evaluation, Model Parameterization, and Effects of Cold-Formed Steel-Framed Gypsum Partition Walls on the Seismic Performance of an Essential Facility," by R. Davies, R. Retamales, G. Mosqueda and A. Filiatrault, 10/12/11.

MCEER-11-0006 "Modeling and Seismic Performance Evaluation of High Voltage Transformers and Bushings," by A.M. Reinhorn, K. Oikonomou, H. Roh, A. Schiff and L. Kempner, Jr., 10/3/11.

MCEER-11-0007 "Extreme Load Combinations: A Survey of State Bridge Engineers," by G.C. Lee, Z. Liang, J.J. Shen and J.S. O'Connor, 10/14/11.

MCEER-12-0001 "Simplified Analysis Procedures in Support of Performance Based Seismic Design," by Y.N. Huang and A.S. Whittaker.

MCEER-12-0002 "Seismic Protection of Electrical Transformer Bushing Systems by Stiffening Techniques," by M. Koliou, A. Filiatrault, A.M. Reinhorn and N. Oliveto, 6/1/12.

MCEER-12-0003 "Post-Earthquake Bridge Inspection Guidelines," by J.S. O'Connor and S. Alampalli, 6/8/12.

MCEER-12-0004 "Integrated Design Methodology for Isolated Floor Systems in Single-Degree-of-Freedom Structural Fuse Systems," by S. Cui, M. Bruneau and M.C. Constantinou, 6/13/12.

MCEER-12-0005 "Characterizing the Rotational Components of Earthquake Ground Motion," by D. Basu, A.S. Whittaker and M.C. Constantinou, 6/15/12.

MCEER-12-0006 "Bayesian Fragility for Nonstructural Systems," by C.H. Lee and M.D. Grigoriu, 9/12/12.

MCEER-12-0007 "A Numerical Model for Capturing the In-Plane Seismic Response of Interior Metal Stud Partition Walls," by R.L. Wood and T.C. Hutchinson, 9/12/12.

MCEER-12-0008 "Assessment of Floor Accelerations in Yielding Buildings," by J.D. Wieser, G. Pekcan, A.E. Zaghi, A.M. Itani and E. Maragakis, 10/5/12.

MCEER-13-0001 "Experimental Seismic Study of Pressurized Fire Sprinkler Piping Systems," by Y. Tian, A. Filiatrault and G. Mosqueda, 4/8/13.

MCEER-13-0002 "Enhancing Resource Coordination for Multi-Modal Evacuation Planning," by D.B. Hess, B.W. Conley and C.M. Farrell, 2/8/13.

MCEER-13-0003 "Seismic Response of Base Isolated Buildings Considering Pounding to Moat Walls," by A. Masroor and G. Mosqueda, 2/26/13.

MCEER-13-0004 "Seismic Response Control of Structures Using a Novel Adaptive Passive Negative Stiffness Device," by D.T.R. Pasala, A.A. Sarlis, S. Nagarajaiah, A.M. Reinhorn, M.C. Constantinou and D.P. Taylor, 6/10/13.

MCEER-13-0005 "Negative Stiffness Device for Seismic Protection of Structures," by A.A. Sarlis, D.T.R. Pasala, M.C. Constantinou, A.M. Reinhorn, S. Nagarajaiah and D.P. Taylor, 6/12/13.

MCEER-13-0006 "Emilia Earthquake of May 20, 2012 in Northern Italy: Rebuilding a Resilient Community to Withstand Multiple Hazards," by G.P. Cimellaro, M. Chiriatti, A.M. Reinhorn and L. Tirca, June 30, 2013.

MCEER-13-0007 "Precast Concrete Segmental Components and Systems for Accelerated Bridge Construction in Seismic Regions," by A.J. Aref, G.C. Lee, Y.C. Ou and P. Sideris, with contributions from K.C. Chang, S. Chen, A. Filiatrault and Y. Zhou, June 13, 2013.

MCEER-13-0008 "A Study of U.S. Bridge Failures (1980-2012)," by G.C. Lee, S.B. Mohan, C. Huang and B.N. Fard, June 15, 2013.

MCEER-13-0009 "Development of a Database Framework for Modeling Damaged Bridges," by G.C. Lee, J.C. Qi and C. Huang, June 16, 2013.

MCEER-13-0010 "Model of Triple Friction Pendulum Bearing for General Geometric and Frictional Parameters and for Uplift Conditions," by A.A. Sarlis and M.C. Constantinou, July 1, 2013.

MCEER-13-0011 "Shake Table Testing of Triple Friction Pendulum Isolators under Extreme Conditions," by A.A. Sarlis, M.C. Constantinou and A.M. Reinhorn, July 2, 2013.

MCEER-13-0012 "Theoretical Framework for the Development of MH-LRFD," by G.C. Lee (coordinating author), H.A Capers, Jr., C. Huang, J.M. Kulicki, Z. Liang, T. Murphy, J.J.D. Shen, M. Shinozuka and P.W.H. Yen, July 31, 2013.

MCEER-13-0013 "Seismic Protection of Highway Bridges with Negative Stiffness Devices," by N.K.A. Attary, M.D. Symans, S. Nagarajaiah, A.M. Reinhorn, M.C. Constantinou, A.A. Sarlis, D.T.R. Pasala, and D.P. Taylor, September 3, 2014.

MCEER-14-0001 "Simplified Seismic Collapse Capacity-Based Evaluation and Design of Frame Buildings with and without Supplemental Damping Systems," by M. Hamidia, A. Filiatrault, and A. Aref, May 19, 2014.

MCEER-14-0002 "Comprehensive Analytical Seismic Fragility of Fire Sprinkler Piping Systems," by Siavash Soroushian, Emmanuel "Manos" Maragakis, Arash E. Zaghi, Alicia Echevarria, Yuan Tian and Andre Filiatrault, August 26, 2014.

MCEER-14-0003 "Hybrid Simulation of the Seismic Response of a Steel Moment Frame Building Structure through Collapse," by M. Del Carpio Ramos, G. Mosqueda and D.G. Lignos, October 30, 2014.

MCEER-14-0004 "Blast and Seismic Resistant Concrete-Filled Double Skin Tubes and Modified Steel Jacketed Bridge Columns," by P.P. Fouche and M. Bruneau, June 30, 2015.

MCEER-14-0005 "Seismic Performance of Steel Plate Shear Walls Considering Various Design Approaches," by R. Purba and M. Bruneau, October 31, 2014.

MCEER-14-0006 "Air-Blast Effects on Civil Structures," by Jinwon Shin, Andrew S. Whittaker, Amjad J. Aref and David Cormie, October 30, 2014.

MCEER-14-0007 "Seismic Performance Evaluation of Precast Girders with Field-Cast Ultra High Performance Concrete (UHPC) Connections," by G.C. Lee, C. Huang, J. Song, and J. S. O'Connor, July 31, 2014.

MCEER-14-0008 "Post-Earthquake Fire Resistance of Ductile Concrete-Filled Double-Skin Tube Columns," by Reza Imani, Gilberto Mosqueda and Michel Bruneau, December 1, 2014.

MCEER-14-0009 "Cyclic Inelastic Behavior of Concrete Filled Sandwich Panel Walls Subjected to In-Plane Flexure," by Y. Alzeni and M. Bruneau, December 19, 2014.

MCEER-14-0010 "Analytical and Experimental Investigation of Self-Centering Steel Plate Shear Walls," by D.M. Dowden and M. Bruneau, December 19, 2014.

MCEER-15-0001 "Seismic Analysis of Multi-story Unreinforced Masonry Buildings with Flexible Diaphragms," by J. Aleman, G. Mosqueda and A.S. Whittaker, June 12, 2015.

MCEER-15-0002 "Site Response, Soil-Structure Interaction and Structure-Soil-Structure Interaction for Performance Assessment of Buildings and Nuclear Structures," by C. Bolisetti and A.S. Whittaker, June 15, 2015.

MCEER-15-0003 "Stress Wave Attenuation in Solids for Mitigating Impulsive Loadings," by R. Rafiee-Dehkharghani, A.J. Aref and G. Dargush, August 15, 2015.

MCEER-15-0004 "Computational, Analytical, and Experimental Modeling of Masonry Structures," by K.M. Dolatshahi and A.J. Aref, November 16, 2015.

MCEER-15-0005 "Property Modification Factors for Seismic Isolators: Design Guidance for Buildings," by W.J. McVitty and M.C. Constantinou, June 30, 2015.

MCEER-15-0006 "Seismic Isolation of Nuclear Power Plants using Sliding Bearings," by Manish Kumar, Andrew S. Whittaker and Michael C. Constantinou, December 27, 2015.

MCEER-15-0007 "Quintuple Friction Pendulum Isolator Behavior, Modeling and Validation," by Donghun Lee and Michael C. Constantinou, December 28, 2015.

MCEER-15-0008 "Seismic Isolation of Nuclear Power Plants using Elastomeric Bearings," by Manish Kumar, Andrew S. Whittaker and Michael C. Constantinou, December 29, 2015.

MCEER-16-0001 "Experimental, Numerical and Analytical Studies on the Seismic Response of Steel-Plate Concrete (SC) Composite Shear Walls," by Siamak Epackachi and Andrew S. Whittaker, June 15, 2016.

MCEER-16-0002 "Seismic Demand in Columns of Steel Frames," by Lisa Shrestha and Michel Bruneau, June 17, 2016.

MCEER-16-0003 "Development and Evaluation of Procedures for Analysis and Design of Buildings with Fluidic Self-Centering Systems" by Shoma Kitayama and Michael C. Constantinou, July 21, 2016.

MCEER-16-0004 "Real Time Control of Shake Tables for Nonlinear Hysteretic Systems," by Ki Pung Ryu and Andrei M. Reinhorn, October 22, 2016.

MCEER-16-0006 "Seismic Isolation of High Voltage Electrical Power Transformers," by Kostis Oikonomou, Michael C. Constantinou, Andrei M. Reinhorn and Leon Kemper, Jr., November 2, 2016.

MCEER-16-0007 "Open Space Damping System Theory and Experimental Validation," by Erkan Polat and Michael C. Constantinou, December 13, 2016.

MCEER-16-0008 "Seismic Response of Low Aspect Ratio Reinforced Concrete Walls for Buildings and Safety-Related Nuclear Applications," by Bismarck N. Luna and Andrew S. Whittaker.

MCEER-16-0009 "Buckling Restrained Braces Applications for Superstructure and Substructure Protection in Bridges," by Xiaone Wei and Michel Bruneau, December 28, 2016.

MCEER-16-0010 "Procedures and Results of Assessment of Seismic Performance of Seismically Isolated Electrical Transformers with Due Consideration for Vertical Isolation and Vertical Ground Motion Effects," by Shoma Kitayama, Michael C. Constantinou and Donghun Lee, December 31, 2016.

MCEER-17-0001 "Diagonal Tension Field Inclination Angle in Steel Plate Shear Walls," by Yushan Fu, Fangbo Wang and Michel Bruneau, February 10, 2017.

MCEER-17-0002 "Behavior of Steel Plate Shear Walls Subjected to Long Duration Earthquakes," by Ramla Qureshi and Michel Bruneau, September 1, 2017.

MCEER-17-0003 "Response of Steel-plate Concrete (SC) Wall Piers to Combined In-plane and Out-of-plane Seismic Loadings," by Brian Terranova, Andrew S. Whittaker, Siamak Epackachi and Nebojsa Orbovic, July 17, 2017.

MCEER-17-0004 "Design of Reinforced Concrete Panels for Wind-borne Missile Impact," by Brian Terranova, Andrew S. Whittaker and Len Schwer, July 18, 2017.

MCEER-17-0005 "A Simple Strategy for Dynamic Substructuring and its Application to Soil-Foundation-Structure Interaction," by Aikaterini Stefanaki and Metttupalayam V. Sivaselvan, December 15, 2017.

MCEER-17-0006 "Dynamics of Cable Structures: Modeling and Applications," by Nicholas D. Oliveto and Mettupalayam V. Sivaselvan, December 1, 2017.

MCEER-17-0007 "Development and Validation of a Combined Horizontal-Vertical Seismic Isolation System for High-Voltage-Power Transformers," by Donghun Lee and Michael C. Constantinou, November 3, 2017.

MCEER-18-0001 “Reduction of Seismic Acceleration Parameters for Temporary Bridge Design,” by Conor Stucki and Michel Bruneau, March 22, 2018.

MCEER-18-0002 “Seismic Response of Low Aspect Ratio Reinforced Concrete Walls,” by Bismarck N. Luna, Jonathan P. Rivera, Siamak Epackachi and Andrew S. Whittaker, April 21, 2018.

MCEER-18-0003 “Seismic Damage Assessment of Low Aspect Ratio Reinforced Concrete Shear Walls,” by Jonathan P. Rivera, Bismarck N. Luna and Andrew S. Whittaker, April 16, 2018.

ISSN 1520-295X